

REPORT DOCUMENTATION PAGE		READ INSTRUCTIONS BEFORE COMPLETING FORM
1. REPORT NUMBER R85-922617-1	2. GOVT ACCESSION NO.	3. RECIPIENT'S CATALOG NUMBER
4. TITLE (and Subtitle)  Investigation of Plasma Processes in Electronic Transition Lasers		5. TYPE OF REPORT & PERIOD COVERED Final Report June 1, 1976-May 30, 1985
		6. PERFORMING ORG. REPORT NUMBER R85-922617-1
7. AUTHOR(s)  William L. Nighan		8. CONTRACT OR GRANT NUMBER(s)  N00014-76-C-0847
9. PERFORMING ORGANIZATION NAME AND ADDRESS United Technologies Research Center Silver Lane East Hartford, CT 06108		10. PROGRAM ELEMENT, PROJECT, TASK AREA & WORK UNIT NUMBERS Prog. Element No.: 61153N Proj. Task Area No.: RR011-07-01 Work Unit No.: NR395-026
11. CONTROLLING OFFICE NAME AND ADDRESS Office of Naval Research Physics Program Office (Code 412) 800 N. Quincy St., Arlington, VA 22217		12. REPORT DATE May 30, 1985
		13. NUMBER OF PAGES 128
14. MONITORING AGENCY NAME & ADDRESS (if different from Controlling Office)		15. SECURITY CLASS. (of this report)  Unclassified
		15a. DECLASSIFICATION/DOWNGRADING SCHEDULE
16. DISTRIBUTION STATEMENT (of this Report) Approved for public release; distribution unlimited		
17. DISTRIBUTION STATEMENT (of the abstract entered in Block 20, if different from Report)		
18. SUPPLEMENTARY NOTES This report is comprised of reprints of published papers.		
19. KEY WORDS (Continue on reverse side if necessary and identify by block number) excimer lasers, rare gas-halide lasers, mercury-halide lasers, XeF(C→A) laser, Xe <sub>2</sub> Cl laser, HgBr(B→X) laser, XeCl(B→K) laser, UV lasers, visible lasers, blue-green lasers, transient absorption, e-HgBr <sub>2</sub> cross sections, e-F <sub>2</sub> cross sections, e-HCl attachment, e-beam sustained discharges, dis- charge stability		
20. ABSTRACT (Continue on reverse side if necessary and identify by block number) United Technologies Research Center has conducted an investigation of the fundamental processes affecting the operation and performance of electrically excited lasers having potential utility in a variety of areas of importance to the Navy. Particular attention in this investigation has been focused on lasers of the rare gas-halide and mercury-halide classes which have very promising potential for development as efficient, scalable optical sources for the UV/visible regions of the spectrum. In recent years (Continued)		

## 20. ABSTRACT (Continued)

this research has been closely coordinated with a complementary ONR-supported program at Rice University. This Final Report is comprised of reprints of papers published during the course of the investigation, in which specific results and conclusions of the research are described in detail.

# INVESTIGATION OF PLASMA PROCESSES IN ELECTRONIC TRANSITION LASERS

**Final Report**

**May 30, 1985**

**William L. Nighan  
Principal Investigator**

**Sponsored by The Office of Naval Research  
Contract: N00014-76-C-0847**

APPROVED FOR PUBLIC RELEASE  
DISTRIBUTION UNLIMITED



**UNITED  
TECHNOLOGIES  
RESEARCH  
CENTER.**

East Hartford, Connecticut 06108

R85-922617-1

Investigation of Plasma Processes in Electronic Transition Lasers

Final Report  
May 30, 1985

William L. Nighan  
Principal Investigator

Sponsored by the Office of Naval Research  
Contract: N00014-76-C-0847

Approved for Public Release; Distribution Unlimited

## PREFACE

United Technologies Research Center has conducted an investigation of the fundamental processes affecting the operation and performance of electrically excited lasers having potential utility in a variety of areas of importance to the Navy. Particular attention in this investigation has been focused on lasers of the rare gas-halide and mercury-halide classes which have very promising potential for development as efficient, scalable optical sources for the UV/visible regions of the spectrum. In recent years this research has been closely coordinated with a complementary ONR-supported program at Rice University. This Final Report is comprised of reprints of papers published during the course of the investigation, in which specific results and conclusions of the research are described in detail.

The research was performed under the direction of Dr. H. S. Pilloff of the Office of Naval Research. His interest and support are gratefully acknowledged as is that of R. H. Bullis, A. J. DeMaria, F. J. Leonberger, G. A. Peterson and E. Snitzer of United Technologies. It is also a pleasure to acknowledge the contributions of my United Technologies colleagues R. T. Brown, R. J. Hall, J. J. Hinchey, H. H. Michels, L. A. Newman, R. Tripodi, and W. J. Wiegand, and also those of D. W. Setser of Kansas State University, A. Herzenberg of Yale University, Y. Nachshon of the Technion and G. Marowsky of Max-Planck Institute fur biophysikalische Chemie. Finally, a special working relationship with F. K. Tittel and his Rice University co-workers, W. L. Wilson and R. Sauerbrey, has contributed significantly to the success of this work and has resulted in an effective industry-university collaboration that has proven to be both productive and enjoyable.

William L. Nighan

## TABLE OF CONTENTS

	<u>Page</u>
PREFACE . . . . .	i
I. INTRODUCTION . . . . .	I-1
II. BROADBAND TUNABLE EXCIMER LASERS . . . . .	II-1
A. XeF(C+A) Laser . . . . .	II-2
B. Xe <sub>2</sub> Cl Laser . . . . .	II-22
III. RARE GAS-HALIDE AND MERCURY HALIDE LASERS . . . . .	III-1
A. HgBr(B+X) Laser . . . . .	III-2
B. XeCl(B+X) Laser . . . . .	III-29
IV. BASIC PROCESSES IN RARE GAS-HALIDE LASERS . . . . .	IV-1
A. KrF(B+X) Laser . . . . .	IV-2
B. Laser Discharge Stability . . . . .	IV-19
C. Electron-F <sub>2</sub> Collision Processes . . . . .	IV-27

## DISTRIBUTION LIST

## I. INTRODUCTION

The advent of the rare gas-halide laser in 1975 represented a dramatic breakthrough in the quest for a short wavelength laser having an efficiency and scalability comparable to the IR CO<sub>2</sub> laser. Although a decade has passed since the discovery of the rare gas-halide laser, developments in this area continue to evolve at a rapid pace, propelled by significant advances in understanding of excited state chemistry, electron-halogen attachment, discharge and optical physics, and by development of sophisticated computer models of laser media. Throughout this period United Technologies Research Center has been conducting an investigation of fundamental processes affecting the operation of electrically excited rare gas-halide lasers and the closely related mercury-halide laser.

This Final Report is comprised of papers published during the course of the investigation. Section II covers broadband, tunable rare gas-halide lasers, particularly the blue-green XeF(C+A) laser having a wavelength centered near 480 nm. An important aspect of this portion of the research was the development of "mixture synthesis" concepts based on the fact that use of two rare gases combined in specific proportions to form an effective buffer species, and/or two molecular halogen species combined to form an effective halogen donor, result in unique mixture characteristics not attainable using either a single rare gas or a single halogen donor alone. As applied to the XeF(C+A) laser, use of Ar and Kr as a buffer and NF<sub>3</sub> and F<sub>2</sub> as the F-donor resulted in significantly improved XeF(C) formation and reduced transient absorption in e-beam excited gas mixtures. In experiments conducted at Rice University XeF(C+A) laser pulse energy density and intrinsic efficiency obtained using this approach have been found to be comparable to values typical of UV B-X rare gas-halide lasers.

The 502 nm HgBr(B+X) laser and 308 nm XeCl(B+X) laser are the subject of Section III. Therein particular attention is focused on dissociative attachment, vibrational excitation and dissociative electronic excitation of HgBr<sub>2</sub> by low energy electrons in HgBr(B)/HgBr<sub>2</sub> laser media; cross sections for these processes are presented. Additionally, it is shown that HCl vibrational excitation by electrons, resulting in greatly enhanced dissociative attachment, is a fundamental process in discharge excited XeCl(B+X) lasers.

Section IV is focused on basic kinetic processes that control the operation and performance of electron-beam sustained rare gas-halide laser discharges, particularly the 248 nm KrF(B+X) laser. Special emphasis is placed on the causes of instability in such laser discharges and on means to suppress instabilities. In addition, the effects of electron-F<sub>2</sub> dissociative attachment, vibrational excitation and dissociation on KrF laser discharge performance are considered in detail, and cross sections for these processes are reported.

II. BROADBAND TUNABLE EXCIMER LASERS

II-A. XeF(C+A) Laser

- Efficient XeF(C+A) Laser Oscillation Using Electron-Beam Excitation
- Synthesis of Rare Gas-Halide Mixtures Resulting in Efficient XeF(C+A) Laser Oscillation
- Optimization of Electrically Excited XeF(C+A) Laser Performance

Y. Nachshon, F. K. Tittel, and W. L. Wilson, Jr.

*Electrical Engineering Department and Rice Quantum Institute, Rice University, Houston, Texas 77251*

W. L. Nighan

*United Technologies Research Center, East Hartford, Connecticut 06108*

(Received 15 November 1983; accepted for publication 6 February 1984)

Significantly improved XeF( $C \rightarrow A$ ) laser energy density and efficiency have been obtained using electron-beam excited Ar-Xe gas mixtures at pressures up to 10 atm which contain both NF<sub>3</sub> and F<sub>2</sub>. Maximum blue-green laser pulse energy density in excess of 1.0 J/liter was obtained, corresponding to an intrinsic electrical-optical energy conversion efficiency estimated to be in the 0.5%–1.0% range. Comprehensive, time-resolved absolute measurements of XeF( $C \rightarrow A$ ) fluorescence, laser energy, and gain were carried out for a wide variety of experimental conditions. Analysis of these data has resulted in identification of the dominant transient absorbing species in the laser medium. For the laser mixtures investigated in this work, the primary blue/green absorption processes have been identified as photoionization of the 4p, 3d, and higher lying states of Ar, and of the Xe 6p and 5d states, and photodissociation of Ar<sub>2</sub>(<sup>3</sup>Σ<sub>u</sub><sup>+</sup>) and Ar<sub>3</sub><sup>+</sup>.

## I. INTRODUCTION

Of the rare-gas halide molecules, XeF is unique in that the two lowest Coulombic states  $B$  ( $\Omega = 1/2$ ) and  $C$  ( $\Omega = 3/2$ ) are separated in energy by nearly 0.1 eV, XeF( $C$ ) being lower in energy of the two,<sup>1</sup> as illustrated in Fig. 1. Therefore, in thermal equilibrium at 300 °K more than 95% of the combined population of the  $B$  and  $C$  states resides in the latter. For this reason the broadband XeF( $C \rightarrow A$ ) transition, centered near 490 nm, has potential for development of efficient tunable lasers in the blue/green region of the spectrum. Laser oscillation has been reported by a number of investigators using electron-beam excitation<sup>2,3</sup> or discharge excitation<sup>4,5</sup> of high-pressure gas mixtures containing Xe and a fluorine donor such as F<sub>2</sub> or NF<sub>3</sub>. Additionally, laser oscillation based on photolytic pumping of a gas containing XeF<sub>2</sub> has been demonstrated.<sup>6–8</sup> For the conditions of these studies the laser output has been found to be continuously tunable in the 450–520 nm wavelength region.<sup>7,9,10</sup>

Although the XeF( $C$ ) excimer can be formed efficiently under conditions typical of these experiments, the large ( $\sim 70$  nm)  $C \rightarrow A$  bandwidth and relatively long  $C$ -state lifetime ( $\sim 100$  nsec) result in a cross section for stimulated emission<sup>7</sup> that, at  $\sim 10^{-17}$  cm<sup>2</sup>, is more than an order of magnitude smaller than that of the highly efficient 351-nm  $B \rightarrow X$  laser transition.<sup>11</sup> Thus, development of adequate gain on the  $C \rightarrow A$  transition requires very intense pumping, a circumstance that results in high concentrations of electrons and of excited and ionized species when electrical excitation is used. The electrons tend to mix and quench the closely spaced  $B$  and  $C$  states, an effect strongly favoring the UV  $B \rightarrow X$  transition at the expense of the blue/green  $C \rightarrow A$  transition. More importantly, certain excited and ionized species typical of the laser medium absorb in the blue/green region of the spectrum. Until recently these and related factors have limited the efficiency of the electrically excited XeF( $C \rightarrow A$ ) laser to unacceptably low levels.<sup>2–5</sup> Photolytic pumping of XeF<sub>2</sub>-containing mixtures has been successful at circumventing certain of these effects, but at the expense of an increase in system complexity.<sup>8</sup>

Recently we reported results<sup>12</sup> demonstrating that by judicious tailoring of kinetic processes in electron-beam excited laser mixtures containing *both* NF<sub>3</sub> and F<sub>2</sub>, the concentrations of electrons and of absorbing species could be significantly reduced. The resulting increase in laser pulse energy density and intrinsic efficiency to  $\sim 0.1$  J/liter and  $\sim 0.1\%$ , respectively, represented an improvement of nearly two orders of magnitude over previously reported results. Herein we report further improvements in laser energy density and efficiency, based primarily on increased  $e$ -beam energy deposition in the laser mixture and optimization of the output coupling. Additionally, analysis of comprehensive time-resolved measurements of gain and absorption for a wide variety of mixture conditions has provided insight as to the identity of the primary absorbing species and, in certain cases, has permitted estimation of their absorption cross sections.

The details of the experimental arrangement and related diagnostic apparatus used in this investigation are summarized in Sec. II. In Sec. III experimental results are presented; therein are described the specific conditions resulting in an increase in XeF( $C \rightarrow A$ ) laser pulse energy density to the

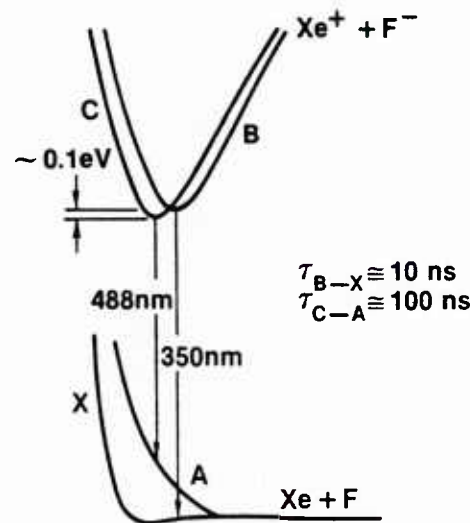


FIG. 1. Schematic XeF energy level diagram.

1.0–2.0 J/liter level, corresponding to an intrinsic efficiency estimated to be in the 0.5%–1.0% range. Our analysis and interpretation of those results is presented in Sec. IV–VI, wherein particular emphasis is placed on identification of the ionized and excited species dominating transient absorption in the  $\text{XeF}(\text{C} \rightarrow \text{A})$  laser mixture. Additionally, remaining factors that presently limit laser performance are discussed, along with possibilities for further improvement.

## II. EXPERIMENT

### A. Electron-beam and reaction cell

The overall experimental arrangement used in this investigation is illustrated in Fig. 2. A Physics International Pulserad 110 electron beam generator was used to transversely excite the high pressure laser mixtures through a 50- $\mu\text{m}$  titanium foil (Fig. 3). The electron beam energy was 1 MeV and the pump pulse duration was 10 nsec (FWHM), producing a current density at the center of the optical axis of 200–400  $\text{A cm}^{-2}$  as measured with a Faraday cup probe. A stable, intracell optical resonator was used consisting of a totally reflecting ( $R > 99.6\%$ ) mirror having a radius of curvature of 0.5 m, separated by 12.5 cm from a flat output mirror. The output mirrors had a reflectivity of either 95% or 98% between 460 and 510 nm, thereby providing an optimum wavelength match with the  $\text{XeF}(\text{C} \rightarrow \text{A})$  gain profile. The active region was the cylindrical 28  $\text{cm}^3$  volume defined by the clear aperture (1.9 cm diam) and the pumped length (10 cm), as confirmed by photographs of the near field laser output. Use of a tightly focused resonator permits a higher level of initial flux arising from spontaneous emission, a factor contributing to rapid buildup of intracavity laser flux.

The stainless-steel reaction cell was well passivated by prolonged exposure to  $\text{F}_2$  prior to any experiments. High-purity gas mixtures of research grade Ar, Xe, Kr,  $\text{NF}_3$ , and  $\text{F}_2$  were used, with the  $\text{F}_2$  in a 10–90  $\text{F}_2$ -He mixture. Good mixing of the different gas components was achieved by tur-

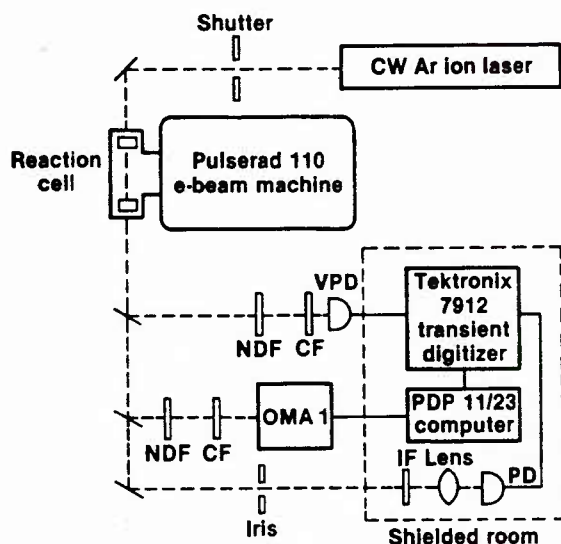


FIG. 2. Schematic illustration of experimental arrangement. NDF = neutral density filter, CF = color-glass filter, VPD = vacuum photodiode, PD = pin diode.

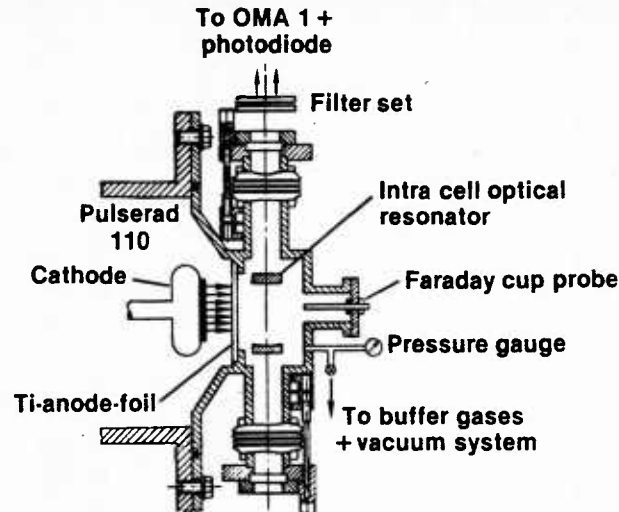


FIG. 3. Illustration of the transverse, e-beam excited high pressure reaction cell with an intracell optical cavity.

bulent flow of the high pressure gas components into the reaction cell. The concentration of  $\text{F}_2$  in the cell was verified by absorption of a HeCd laser probe<sup>13</sup>; the partial pressure of each gas is estimated to be accurate to within 2%. A fresh gas mixture was used for each shot. Repetitive pumping of the mixture resulted in a decrease in laser energy of about 20% per shot due to contamination and surface reaction processes of the foil window.

### B. Diagnostics

The temporal evolution of the fluorescence and the laser output were monitored by a fast vacuum photodiode detector (ITT:F4000 S5). Neutral density, interference, and color glass filters were used to define the spectral region of interest. Signals with a time resolution of better than 2 nsec were recorded by a Tektronix 7904 Transient Digitizer. The temporally integrated, spectrally resolved fluorescence was recorded by an optical multichannel analyzer (OMA I), using a Jarrell-Ash 0.25 m spectrometer; the spectral resolution was  $\sim 2$  nm. Data from the Transient Digitizer and the OMA I were processed using a PDP 11/23 minicomputer.

Absolute power measurements were made using calibrated vacuum photodiode detectors (with an effective aperture of 38 mm), and appropriate interference and color glass filters. The power was calculated using the temporally integrated OMA measurements and the calibration verified by means of a Sciencetech volume absorbing disc calorimeter model 38-0101 as well as with Polaroid film No. 42. The film was exposed to the laser output using neutral density and color glass filters to achieve a density of 0.5. These two methods of power determination were found to agree to within the estimated experimental error.

The laser beam divergence was also measured using two different methods. The first method used Polaroid film exposed to the laser light at different distances using neutral density and color glass filters, keeping the film density 0.5, and measuring the beam diameters. The second method measures the laser power at different distances along the optic axis for different size apertures. Both methods indicated a laser beam divergence of  $\sim 40$  mrad.

A measurement of the temporal evolution of the  $\text{XeF(C)}$  population for different gas mixture conditions was carried out by monitoring the  $\text{XeF(C} \rightarrow \text{A)}$  fluorescence at a distance 125 cm from the center of the laser cell along the optical axis using collimating optics with an effective aperture of 6.35 mm diam. The absolute value of the  $\text{XeF(C)}$  state population was then obtained using the integrated fluorescence spectrum from the OMA and the spectrally calibrated vacuum photodiode detector.

### C. Gain/absorption measurement

The experimental arrangement for measuring the optical gain (absorption) is also shown in Fig. 2. A cw Ar-ion laser and an R 6G dye laser were used to measure gain at eight different wavelengths: 514.5, 501.7, 496.5, 488.0, 476.5, 472.7, 457.9, and 590 nm. Either one or three passes of the probe beam through the cell was used, depending on the magnitude of the gain/absorption, in order to maximize the signal-to-noise ratio. The laser probe signal was focused on a Lasermetrics 3117 PIN detector (HP5082-4200) via a narrow-band interference filter, color-glass filter, and an iris located 10 m from the laser cell. The detector was located inside a Faraday cage to minimize electrical noise pickup and stray fluorescence. A mechanical shutter was used to produce a 4-msec laser probe pulse to avoid saturation of the detector. The electron-beam pulse was synchronized to appear in the middle of the laser probe pulse. In the cw mode, the detector diode is linear with input power for output currents up to 4 mA. However, the time response of the detector for currents above 2 mA started to deteriorate. Therefore, the detector current was always maintained below 1 mA, where the time response is estimated to be better than 2 nsec.

## III. EXPERIMENTAL RESULTS

Normalized temporal characteristics of the  $e$ -beam excitation pulse,  $\text{XeF(C} \rightarrow \text{A)}$  fluorescence and laser output for representative conditions are presented in Fig. 4. Formation of the  $\text{XeF(C)}$  state occurs during and after the excitation pulse, with the fluorescence peak occurring about 10 nsec after the peak in the  $e$ -beam current. Since there is strong absorption during the early phase of  $\text{XeF(C)}$  formation (a topic to be discussed in detail in subsequent sections), laser oscillation does not begin until after the peak fluorescence. The peak in the laser output occurs between 20 and 35 nsec after the fluorescence peak depending on the magnitude of the peak gain, the shorter time corresponding to higher gain, and therefore higher laser output. Laser oscillation continues for 20–30 nsec after termination of the  $\text{XeF(C} \rightarrow \text{A)}$  fluorescence, a reflection of the cavity resonator decay time.

### A. Laser pulse energy

The improvement in magnitude and duration of the net gain resulting from a two component halogen donor mixture ( $\text{NF}_3/\text{F}_2$ ) has been shown to result in a significant increase in laser pulse energy.<sup>12</sup> Figure 5 presents the laser pulse energy density (based on a 28 cm<sup>3</sup> active volume) as a function of either  $\text{F}_2$  pressure or  $\text{NF}_3$  pressure for 10 atm of Ar containing 16 Torr Xe; a 2% output coupler was used. The maxi-

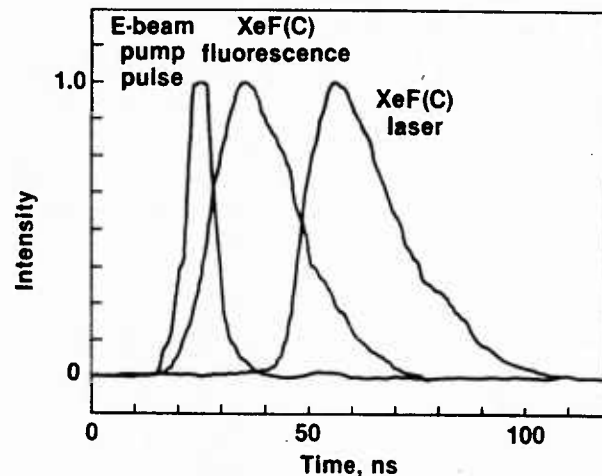


FIG. 4. Normalized temporal characteristics of the  $e$ -beam excitation pulse,  $\text{XeF(C} \rightarrow \text{A)}$  fluorescence, and laser pulse for a mixture comprised of 10 atm Ar, 16 Torr Xe, 8 Torr  $\text{NF}_3$ , and 8 Torr  $\text{F}_2$ . The  $e$ -beam current density on the optical axis was approximately  $400 \text{ A cm}^{-2}$ , and the transmission of the output mirror was 2%.

imum output of 0.5 J/liter for these specific conditions is observed to occur for a mixture containing 8 Torr of  $\text{NF}_3$  and 8 Torr of  $\text{F}_2$ , and is particularly sensitive to the concentration of the latter, a reflection of the fact that  $\text{F}_2$  has substantially larger excited state (i.e., absorber) quenching coefficients than does  $\text{NF}_3$ .<sup>14,15</sup> For conditions similar to those of Fig. 5 maximum laser pulse energy density values of 1.5 J/liter were achieved using a 5% output coupler.

Optimum mixtures were always found to contain about 8 Torr  $\text{NF}_3$ , 8 Torr  $\text{F}_2$ , and 16 Torr Xe, regardless of the cavity optics,  $e$ -beam current density, or Ar pressure. Thus, the concentrations of  $\text{NF}_3$ ,  $\text{F}_2$ , and Xe are essentially optimized for the present conditions. However, the  $e$ -beam current density ( $\sim 400 \text{ A cm}^{-2}$  max) and Ar pressure (10 atm max), corresponding to the highest measured laser output ( $\sim 1.5 \text{ J/liter}$ ), represent experimental limitations and are not optimum values. For values of  $e$ -beam current density between 200 and  $400 \text{ A cm}^{-2}$  and Ar pressures between 6 and 10 atm, laser pulse energy density increased somewhat faster than linearly with each of these parameters. However, for values below about  $200 \text{ A cm}^{-2}$  and 6 atm, laser pulse

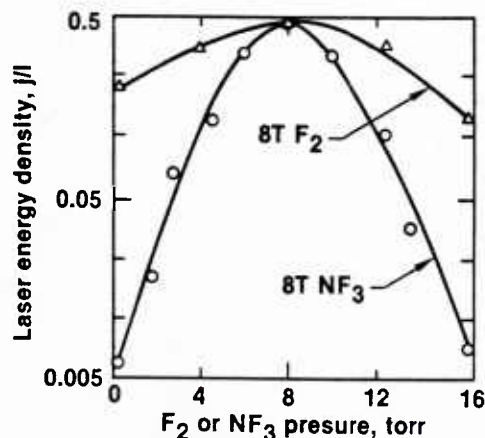


FIG. 5. Laser pulse energy density as a function of either  $\text{NF}_3$  pressure or  $\text{F}_2$  pressure for conditions otherwise the same as Fig. 4.

energy was found to decrease very rapidly due to the lower gain under these conditions.

### 1. Buffer gas variation

Use of Ne as the buffer gas in place of Ar resulted in laser pulse energy much lower than that of Fig. 5, almost certainly a reflection of the fact that Ne is about an order of magnitude less effective than Ar at mixing the *B* and *C* states of XeF,<sup>16</sup> and is also less effective at relaxing the XeF(*B,C*) vibrational manifolds. The use of Kr in place of Ar was reported<sup>3</sup> to result in much better laser performance for values of *e*-beam current density and total pressure much lower and excitation pulses much longer than those of the present investigation. However, we have found that use of Kr as the buffer at half the Ar pressure, so as to provide about the same *e*-beam energy deposition, resulted in significantly lower laser output energy. Experimentation using Kr as an *additive* at concentrations in the 0–760 Torr range was also found to result in lower laser output, except for Kr pressures in the 40–70 Torr range for which the laser output was about the same as without Kr present. However, measured gain profiles in laser mixtures containing Kr feature certain distinctive characteristics that may ultimately permit higher laser pulse energy, a topic to be discussed in subsequent sections.

### 2. Laser spectra

Although the laser output was found to be quite sensitive to mixture variations, the XeF(*C*→*A*) fluorescence was not, a circumstance indicating that changes in the absorption characteristics of the medium are largely responsible for changes in laser output. Examination of laser spectra supports this conclusion. Figure 6 shows measured laser spectra for an Ar-Xe mixture at 6 atm containing 8 Torr NF<sub>3</sub>, and 8 Torr each of F<sub>2</sub> and NF<sub>3</sub>, excited at an *e*-beam current density level of about 200 A cm<sup>-2</sup>, conditions for which the laser pulse energy density was about 0.1 J/liter for the two-halogen mixture.<sup>12</sup> The discrete absorption lines that appear in the NF<sub>3</sub> spectrum [Fig. 6(a)], due principally to transitions between Xe excited states,<sup>17</sup> vanish [Fig. 6(b)] with F<sub>2</sub> added to the mixture for laser output energy up to about 0.1 J/liter. For higher laser pulse energy (e.g., Fig. 5) the structure in the laser spectrum is again apparent even with F<sub>2</sub> present in the mixture, although to a much lesser degree than with NF<sub>3</sub> alone. For this case the laser pulse peaks at an earlier time at which the absorber concentrations are higher than those typical of Fig. 6(b).

It should be pointed out that the effect of broadband absorption on laser output energy is far more significant than that of the discrete absorption that is readily apparent in the laser spectrum [Fig. 6(a)]. However, many of the same species contributing to broadband absorption also exhibit discrete absorption. For this reason the appearance of structure and/or changes therein in XeF(*C*→*A*) laser spectra [Figs. 6(a) and 6(b)] are also symptomatic of the occurrence of the more severe broadband absorption.

### B. Gain and absorption

Figure 7 presents the temporal evolution of net gain at 488 nm (measured using the cw Ar-ion laser probe) for a laser

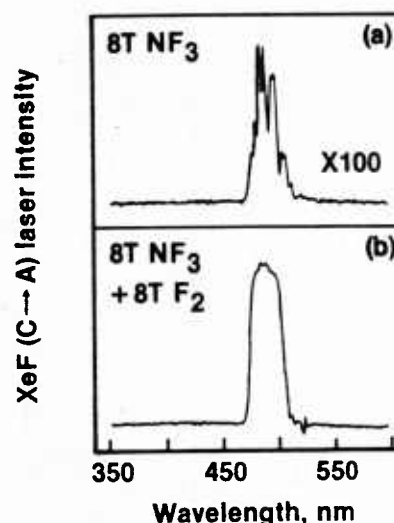


FIG. 6. XeF(*C*→*A*) laser spectra for a mixture of 6 atm Ar and 16 Torr Xe containing 8 Torr NF<sub>3</sub> (a), or 8 Torr NF<sub>3</sub> and 8 Torr F<sub>2</sub> (b). The *e*-beam current density on the optical axis was approximately 200 A cm<sup>-2</sup> and the transmission of the output coupler was 5%. For these conditions, the laser pulse energy density was about 0.1 J/liter.

mixture for which the Ar pressure was 6 atm. Under these conditions laser output energy density was about 0.25 J/liter. This figure shows that severe transient absorption occurs during the excitation pulse, a circumstance found to be typical of all Ar-Xe-NF<sub>3</sub>-F<sub>2</sub> laser mixtures. The net gain does not become positive until slightly before the peak in the fluorescence. For an Ar pressure of 10 atm, corresponding to ~1.0–2.0 J/liter laser output, the peak absorption rises to nearly 4% cm<sup>-1</sup> and the peak gain increases to almost 3% cm<sup>-1</sup> (Fig. 8). The peak values of the XeF(*C*) population deduced from the gain measurements (and predicted analytically) typically were about 25% larger than those determined from the calibrated fluorescence measurements, a difference within the combined uncertainty limits of both experimental techniques.

For the conditions of Fig. 7 (e.g., peak gain > 2% cm<sup>-1</sup>) the maximum intracavity laser flux corresponds to values equal to or greater than the saturation flux, *I*<sub>sat</sub> ~ 6 MW cm<sup>-2</sup>. Thus, while the laser output energy continues to

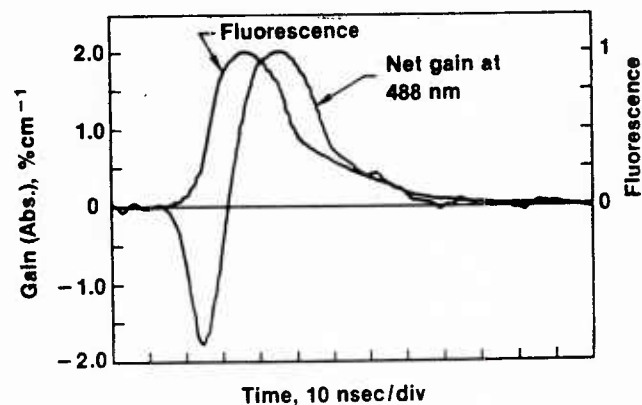


FIG. 7. Temporal evolution of the net gain measured at 488 nm and of the fluorescence for a mixture comprised of 6 atm Ar, 16 Torr Xe, 8 Torr NF<sub>3</sub>, and 8 Torr F<sub>2</sub>; the *e*-beam current density on the optical axis was approximately 300 A cm<sup>-2</sup>.

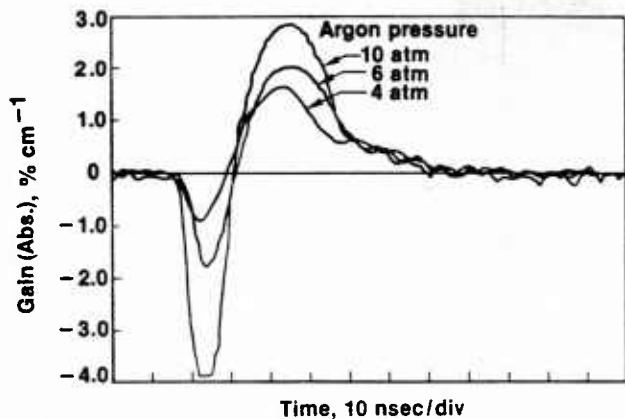


FIG. 8. Temporal evolution of the net gain measured at 488 nm for various Ar pressures, and conditions otherwise the same as those of Fig. 7.

increase significantly for peak gain levels higher than those of Fig. 7, for lower gain values (e.g.,  $< 1.5\% \text{ cm}^{-1}$ ) the laser output energy decreases precipitously. Figure 9 compares the gain for the two-halogen mixture of Fig. 7 with that of a mixture containing only  $\text{NF}_3$ , both excited under similar conditions. In the latter case the broadband absorption is more severe resulting in a gain peak of about  $1.5\% \text{ cm}^{-1}$ . However, because these gain values are relatively low, considering the 30 nsec during which gain persists, the difference in laser pulse energy between the  $\text{F}_2 + \text{NF}_3$  and  $\text{NF}_3$  mixtures is approximately two orders of magnitude (Fig. 5).

Although Kr did not improve laser performance for the conditions of this experiment, the addition of Kr to the laser mixture was found to have a striking effect on the temporal evolution of the gain-absorption profile under certain circumstances. Presented in Fig. 10 is the net gain at 488 nm for the mixture of Fig. 7, to which was added 0.2 atm Kr. While the peak value of gain is essentially the same for both cases, the strong initial absorption during the excitation pulse almost vanishes entirely. This was found to be the case for all Kr concentrations in the 0.2–1.0 atm pressure range. For Kr pressures above 1.0 atm the initial absorption was found to return to significant levels, and the peak gain decreased. With the Ar replaced entirely by 3 atm Kr, the initial absorption increased to nearly  $1.0\% \text{ cm}^{-1}$  and the peak value of gain decreased to approximately  $1.5\% \text{ cm}^{-1}$ . Thus, for the

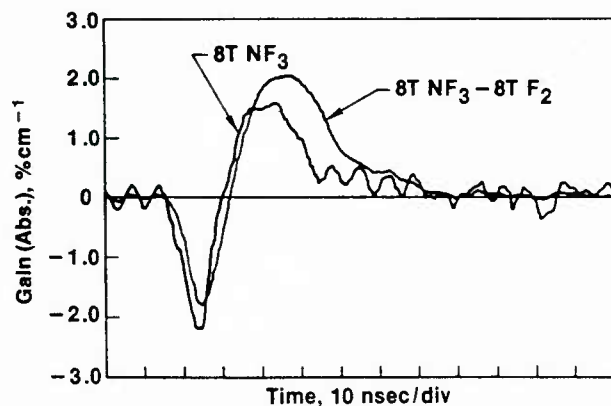


FIG. 9. Temporal evolution of the net gain at 488 nm for the conditions of Fig. 7, and for those conditions with no  $\text{F}_2$  in the mixture.

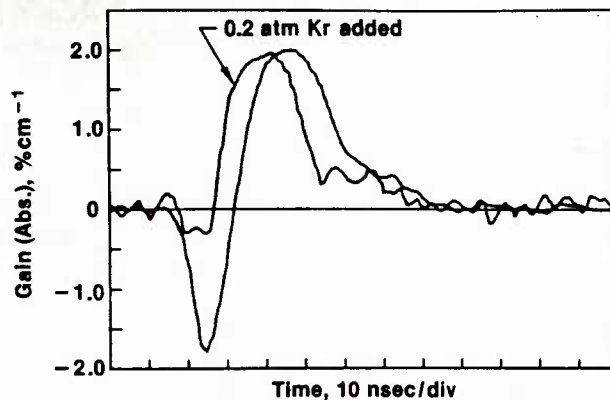


FIG. 10. Temporal evolution of the net gain at 488 nm for the conditions of Fig. 7, and for those conditions with 0.2 atm Kr added to the mixture.

conditions of this experiment, the use of Kr as an *additive* rather than as the buffer has an interesting and potentially significant effect on blue/green absorption during the excitation pulse, a topic to be explored in subsequent sections.

### 1. Wavelength dependence

As mentioned earlier, broadband absorption is of central importance to laser performance. For this reason gain/absorption measurements of the type discussed above were carried out for seven wavelength values available from the cw Ar-ion laser, and for the 590-nm R 6G dye laser wavelength. Presented in Fig. 11 is the wavelength dependence of the peak gain and peak absorption for the mixture and excitation conditions of Fig. 7, measured using the Ar-ion laser. The curve in this figure is the  $\text{XeF}(\text{C} \rightarrow \text{A})$  stimulated emission cross section reported in Ref. 7, normalized to the measured peak gain value at 480 nm. With the exception of the point at 514.5 nm,<sup>18</sup> the peak absorption is found to be essentially independent of wavelength. Thus, the decrease in the peak value of net gain on either side of 480 nm is primarily a reflection of the wavelength dependence of the  $\text{C} \rightarrow \text{A}$  cross section for stimulated emission.

## IV. $\text{XeF}(\text{C} \rightarrow \text{A})$ LASER KINETICS

In recent years kinetic processes controlling the  $\text{XeF}(\text{B}, \text{C})$  population in laser media have been the subject of

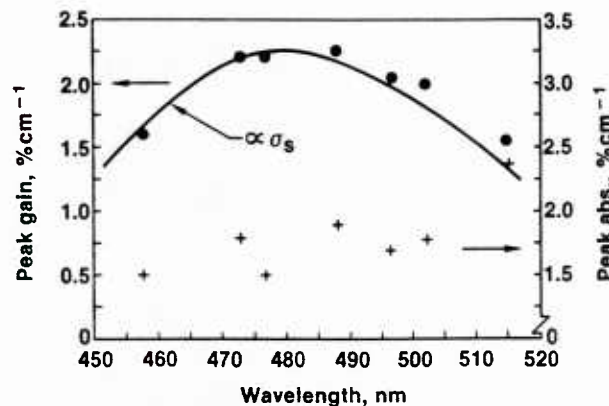


FIG. 11. Wavelength dependence of the peak gain and peak absorption for the conditions of Fig. 7. The curve refers to the wavelength dependence of the  $\text{XeF}(\text{C} \rightarrow \text{A})$  cross section for stimulated emission reported in Ref. 7.

considerable attention. Consequently, relatively complete rate coefficient data are available for  $\text{XeF}(B,C)$  formation processes such as ion-ion recombination<sup>19,20</sup> and halogen reactive quenching of rare-gas excited states<sup>14,15</sup> and for mixing and quenching of the  $B$  and  $C$  states.<sup>16,21</sup> Additionally, the body of related data pertaining to ion charge exchange and rearrangement,<sup>22-24</sup> kinetic processes in rare gases and their mixtures,<sup>25,26</sup> and to electron-halogen dissociative attachment<sup>27</sup> has been expanded significantly in reaction to the importance of rare-gas-halide lasers. In the present investigation these data have been used in a self-consistent model of  $\text{XeF}(B,C)$  processes for the experimental conditions described in Sec. III. Analytical and numerical procedures of the type utilized have become well developed in recent years.<sup>28,29</sup> Thus, the discussion to follow will concentrate on modeling results with little emphasis on methods and procedures.

### A. Mixture composition

Selection of an optimum buffer gas for the  $\text{XeF}(C \rightarrow A)$  laser is dictated by several requirements: (1) mixing of the  $B$  and  $C$  states must occur in a time much less than the radiative lifetime of the former; (2) vibrational relaxation of the  $B$  and  $C$  states must be very fast; (3) collisional quenching of  $\text{XeF}$  by the buffer must be minimal; (4) transient absorption at the laser wavelength by buffer-related ionized and excited species must be held to an acceptable level; and (5) when  $e$ -beam excitation is used the buffer gas must have a relatively high stopping power. While there are several species possessing one or more of these characteristics, so far Ar has been found to exhibit the best overall combination of properties for the conditions of this experiment.

The molecular source of fluorine atoms should also possess properties (3) and (4) above, and since net gain and laser oscillation occur during the afterglow period and are strongly influenced by absorption in the relaxing medium, the halogen must play the very important role of reducing the concentrations of electrons and absorbing species as rapidly as possible. As mentioned previously and discussed in detail in Ref. 12, we have shown that  $\text{F}_2$  and  $\text{NF}_3$  together exhibit attachment and absorber quenching characteristics superior to either species alone, thereby permitting higher levels of net gain and very much higher laser pulse energies. Most recently, evidence has been obtained indicating that addition of Kr as a fifth component of the mixture may beneficially alter medium absorption characteristics. These reasons and supportive experimental evidence have resulted in selection of the particular mixture constituents and their fractional concentrations described previously in connection with the discussion of Figs. 5-11.

### B. $\text{XeF}(C)$ formation and loss

Figure 12 illustrates the major energy pathways to and away from the coupled  $\text{XeF}(B,C)$  vibrational manifolds, based on modeling of kinetic processes. Because of the very large fractional concentration of Ar, ionization and excitation of the Ar by primary and secondary  $e$ -beam electrons is dominant, followed by charge and excitation transfer to Xe, and by ion recombination and excited state quenching by  $\text{F}^-$

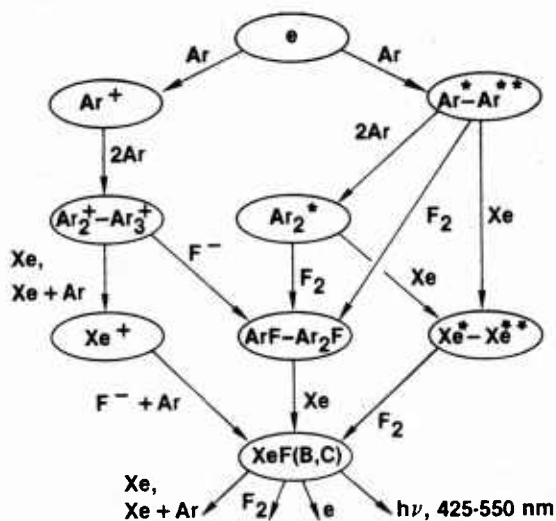


FIG. 12. Sequence diagram illustrating the  $\text{XeF}(B,C)$  formation and loss processes for the conditions of the present investigation.

and by  $\text{F}_2$  (and  $\text{NF}_3$ ), respectively. Those processes resulting in the formation of Xe ions and/or Xe excited states result in very efficient formation of  $\text{XeF}(B,C)$ .<sup>14,19</sup> However, the indicated paths leading to  $\text{ArF}$  and  $\text{Ar}_2\text{F}$  introduce inefficiency even though a fraction of that energy is also likely to result in  $\text{XeF}$  formation by way of displacement reactions. Nevertheless, modeling indicates that for the conditions of this experiment  $\text{XeF}(C)$  is produced with an efficiency of 5%-7% for a relatively wide range of experimental conditions.

The computed, time integrated fractional contributions to  $\text{XeF}(C)$  formation and loss are presented in Fig. 13, for conditions typical of Fig. 7. Because Ar mixes the  $\text{XeF}$  states on a sub-nsec time scale,<sup>16</sup> it doesn't matter whether the  $B$ ,  $C$  or  $D$  state of  $\text{XeF}$  is produced by the reactions indicated in Fig. 13(a). Of those reactions, the relative importance to  $\text{XeF}$  formation of the  $\text{Ar}_2\text{F-Xe}$  displacement reaction is least certain. A substantial fraction of the energy is channeled to  $\text{ArF}$  (Fig. 12) which is instantly converted to  $\text{Ar}_2\text{F}$  because of the high Ar pressure.<sup>30</sup> While there is evidence of displacement

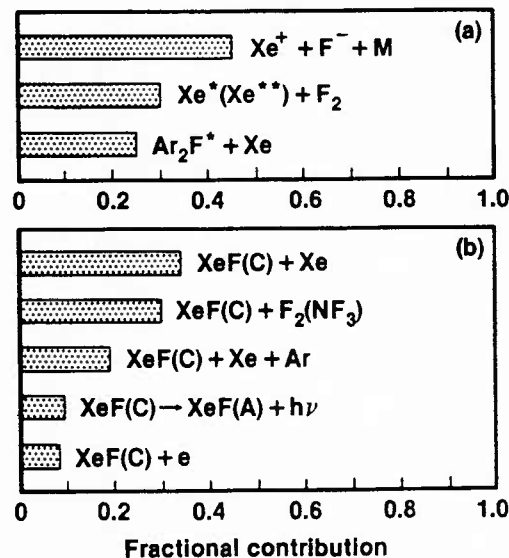


FIG. 13. Time integrated fractional contributions to  $\text{XeF}(C)$  formation (a), and loss (b), computed for the conditions of Fig. 7.

reactions involving diatomic rare-gas-halide molecules, there is very little information on the corresponding triatomic molecule reactions.<sup>29</sup> For the purposes of the present calculations the rate coefficient for the  $\text{Ar}_2\text{F} \rightarrow \text{XeF}$  displacement reaction was estimated to be  $2 \times 10^{-10} \text{ sec}^{-1} \text{ cm}^3$ .

The contributions to  $\text{XeF}(C)$  quenching are presented in Fig. 13(b), which shows that nearly 50% of the  $C$  state loss is due to two- and three-body quenching<sup>21</sup> by Xe, a factor that limits the Xe fractional concentration to a relatively low level. Also, in spite of the very large rate of dissociative attachment in the  $\text{NF}_3\text{-F}_2$  mixture, the intense  $e$ -beam pumping results in an electron density level such that electron quenching of the  $\text{XeF}(B,C)$  states is still significant.<sup>31</sup>

## V. ABSORPTION IN THE VISIBLE REGION

Although the kinetic efficiency for production of the upper laser level may be relatively high for excimer systems,  $\sim 5\%$ - $7\%$  in the present case, the overall laser efficiency can be severely limited by photoabsorption.<sup>32-35</sup> In recognition of this fact and the importance of UV rare-gas and rare-gas-halide lasers, in recent years there has been significant activity directed toward identification of species in laser media that absorb in the UV, and toward determination of their cross sections. For this reason transient absorption processes in electrically excited UV laser media are now relatively well understood.<sup>32</sup> Unfortunately, far less is known about the causes of the absorption observed in the visible region of the spectrum.<sup>36</sup> Since control of absorption in the blue/green region is absolutely critical to efficient operation of the  $\text{XeF}(C \rightarrow A)$  laser, we have endeavored to identify the specific causes of the broadband absorption observed in the present experiment. Progress toward this objective has been aided significantly by analysis of the absorption characteristics of specific rare gas mixtures in addition to the  $\text{XeF}$  laser mixtures of primary interest.

### A. Argon

Presented in Fig. 14 is the time dependence of the absorption measured at 488 nm in argon for conditions otherwise typical of the laser experiments discussed in Sec. III. The magnitude of the peak absorption,  $\sim 9\% \text{ cm}^{-1}$ , was found to be about the same at 457.9 nm and approximately 30% higher<sup>18</sup> at 514.5 nm, indicating that the absorption is essentially broadband in nature. Analysis of the decay of the absorption in Ar shows it to be composed of two components having characteristic times of approximately 15 and 50 nsec, respectively, a trend also observed by others<sup>36</sup> for generally similar conditions. Model calculations for the conditions of Fig. 14 provide valuable insight as to the excited and ionized species responsible for the Ar absorption, and permit first-order estimates of absorption cross sections for which data are unavailable.

Computed species concentrations corresponding to the conditions of Fig. 14 are presented in Fig. 15. Here  $\text{Ar}^*$  refers to the population of the  $\text{Ar}(4s)$  levels as indicated, while  $\text{Ar}^{**}$  refers to a single, effective higher-lying state representative of the grouped  $4p$ ,  $3d$  and higher levels. The computed concentration of the weakly bound ( $D_e \sim 0.22 \text{ eV}$ )  $\text{Ar}_3^+$

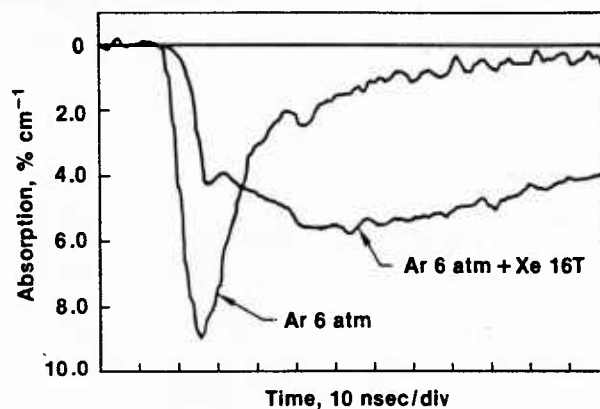


FIG. 14. Temporal evolution of the absorption measured at 488 nm in 6 atm Ar and in 6 atm Ar containing 16 Torr Xe. The  $e$ -beam current density was approximately  $300 \text{ A cm}^{-2}$ .

trimer ion is based on the forward and reverse rate coefficients reported by Turner and Conway,<sup>37</sup> and on the assumption that the rate coefficient for electron- $\text{Ar}_3^+$  recombination is five times larger<sup>38</sup> than that of  $\text{Ar}_2^+$ . Examination of Fig. 15 shows that, with the exception of  $\text{Ar}_2^+(^3\Sigma_u^+)$ , all other species essentially follow the temporal behavior of the  $e$ -beam excitation pulse, and decay with a time constant of about 10–20 nsec. In contrast, the long lived ( $\sim 3 \mu\text{sec}$ )  $\text{Ar}_2^+(^3\Sigma_u^+)$  state decays by way of electron mixing with the  $\text{Ar}_2^+(^1\Sigma_u^+)$  state, the latter having a lifetime of only 4 nsec.<sup>39</sup> Although the  $^1\Sigma_u^+$  concentration is always much smaller than that of  $^3\Sigma_u^+$ , spontaneous emission of the former provides the path through which the coupled (by electrons)  $^1\Sigma_u^+ - ^3\Sigma_u^+$  states decay. For these reasons the computed 40–50 nsec decay time constant of  $\text{Ar}_2^+(^3\Sigma_u^+)$  reflects the electron density decay rather than the  $^3\Sigma_u^+$  lifetime.

For the species of Fig. 15 the dominant broadband photoabsorption processes in the blue/green region are expected to be

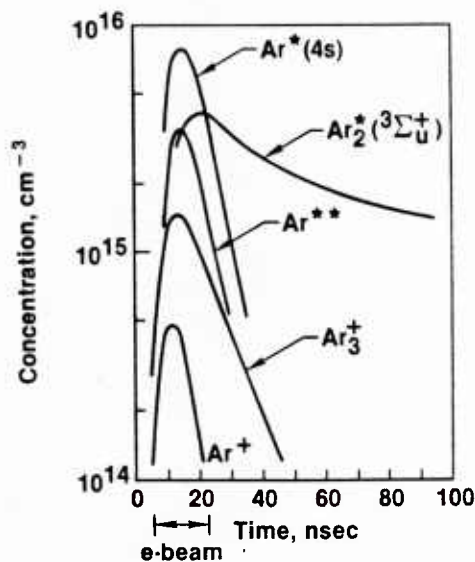


FIG. 15. Computed temporal evolution of the species concentrations in Ar for the conditions of Fig. 14. The peak value of the  $\text{Ar}_2^+$  concentration (not shown for the sake of clarity) is approximately three times larger than that of  $\text{Ar}_3^+$ .



Duzy and Hyman<sup>40</sup> have computed cross sections for the photoionization process, [Eq. (1)]. Although photons in the blue/green region have insufficient energy to ionize  $\text{Ar}^*(4s)$  atoms, they report photoionization cross sections of  $\sim 1.2 \times 10^{-17} \text{ cm}^2$  for  $\text{Ar}^{**}(4p)$  for  $\lambda \lesssim 460 \text{ nm}$ , and  $\sim 1.5 \times 10^{-17} \text{ cm}^2$  for  $\text{Ar}^{**}(3d)$  for  $430 < \lambda < 530 \text{ nm}$ . Presumably the cross sections for photoionization of higher excited states are somewhat larger. Cross sections for dimer ion ( $\text{Ar}_2^+$ ) photodissociation peak in the UV region.<sup>41</sup> Although absorption in the blue/green by  $\text{Ar}_2^+$  in high vibrational levels is possible, dimer ion absorption is not likely to be significant at the pressure levels of the present experiment. However, recent calculations by Michels, Hobbs, and Wright<sup>42</sup> and by Wadt<sup>43</sup> show that photodissociation of rare gas trimer ions is likely to be very strong and broadband throughout most of the visible region. Michels and co-workers report a cross section for  $\text{Ar}_3^+$  that is approximately  $10^{-17} \text{ cm}^2$  in the blue/green region, while Wadt's calculations suggest that the cross section may be substantially larger than that.<sup>44</sup> Although there are no reported cross sections for blue/green photoabsorption by  $\text{Ar}_2^+$ , recent calculations<sup>45</sup> by Yates and co-workers show that several molecular states correlating to  $\text{Ar-Ar}(4p)$  are highly repulsive in the region of the equilibrium internuclear separation of  $\text{Ar}_2^+ (^3\Sigma_u^+)$ , and have vertical transition energies in the 2-4 eV range. This suggests the possibility of significant broadband absorption by  $\text{Ar}_2^+$  in the visible region.

This information, considered in light of both the computed temporal evolution of excited and ionized species in Ar (Fig. 15), and of the measured absorption (Fig. 14), indicates that the strong initial absorption during the excitation pulse is caused by the combined effects of the  $4p$ ,  $3d$ , and higher excited states of Ar, by  $\text{Ar}_3^+$ , and by  $\text{Ar}_2^+ (^3\Sigma_u^+)$ , while the more slowly decaying component of the absorption is due almost entirely to  $\text{Ar}_2^+ (^3\Sigma_u^+)$  alone. Guided by the magnitudes of the cross sections reported for the excited states of Ar<sup>40</sup> and for Ar trimer ions,<sup>42-44</sup> numerical experimentation has shown that both the magnitude and two-phase time dependence of the observed broadband photoabsorption in Ar (Fig. 14) can be explained satisfactorily in terms of the computed temporal evolution of the species shown in Fig. 15 and the cross sections presented in Table I. Figure 16 shows the fractional contributions to Ar absorption for the conditions of Figs. 14 and 15.

## B. Argon-xenon mixtures

Both the magnitude and temporal variation of the measured absorption, particularly the latter, are changed significantly by the addition of a small amount ( $< 1\%$ ) of Xe to Ar. Figure 14 shows the measured absorption in Ar containing 16 Torr of Xe for conditions similar to those of pure Ar. The maximum value of the absorption is lowered slightly to about  $7\% \text{ cm}^{-1}$  with Xe present, and occurs about  $\sim 40\text{--}50 \text{ ns}$  after the excitation pulse. Moreover, the change in the

TABLE I. Blue-green photoabsorption cross sections.\*

Species	Estimates based on this work	Theoretical calculations
$\text{Ar}^{**}$	1.5	1.2 [ $\text{Ar}(3d)$ ] <sup>b</sup>
$\text{Xe}^{**}$	2.0	2.3 [ $\text{Xe}(6p)$ ], 2.7 [ $\text{Xe}(5d)$ ] <sup>b</sup>
$\text{Ar}_2(^3\Sigma_u^+)$	1.0	...
$\text{Ar}_3^+$	2.5	$\sim 1.0$ , <sup>c</sup> $\sim 3.0\text{--}4.0$ <sup>d</sup>

\*Units are  $10^{-17} \text{ cm}^2$ .

<sup>b</sup>Reference 40.

<sup>c</sup>Reference 42.

<sup>d</sup>Reference 44.

decay of the absorption is strikingly different from that of Ar alone. Figure 14 shows that the absorption is essentially constant for about the first  $\sim 100 \text{ nsec}$  after termination of the pulse, subsequently decaying with a time constant of approximately 300 nsec. This behavior can be explained on the basis of the computed excited and ionized species concentrations in the Ar-Xe mixture, which are shown in Fig. 17; the  $\text{Xe}^{**}$  concentration in this figure represents the grouped  $6s'$ ,  $6p$ ,  $5d$ , and higher lying levels of Xe.

Although the peak values of  $\text{Ar}^{**}$ ,  $\text{Ar}_2^+$ , and  $\text{Ar}_3^+$  are reduced significantly due to rapid excitation and charge transfer to Xe, these species still make an important contribution to absorption during the excitation pulse as shown in Fig. 18. However, upon termination of the pulse, all Ar-related species decay on a  $\sim 10 \text{ nsec}$  timescale due to strong quenching by Xe. Corresponding Xe-related molecular species that might be expected to exhibit broadband absorption in the visible region, such as  $\text{Xe}_2^+$  and  $\text{Xe}_3^+$ , are present only in very small quantities reflecting the small Xe fractional concentration.

Although the  $\text{Xe}^*(6s)$  concentration (not shown in Fig. 17) has essentially the same time dependence as that of  $\text{Xe}^{**}$ , and an even larger concentration ( $\sim 10^{16} \text{ cm}^{-3}$ ), blue/green photons have insufficient energy to photoionize  $\text{Xe}^*(6s)$ .

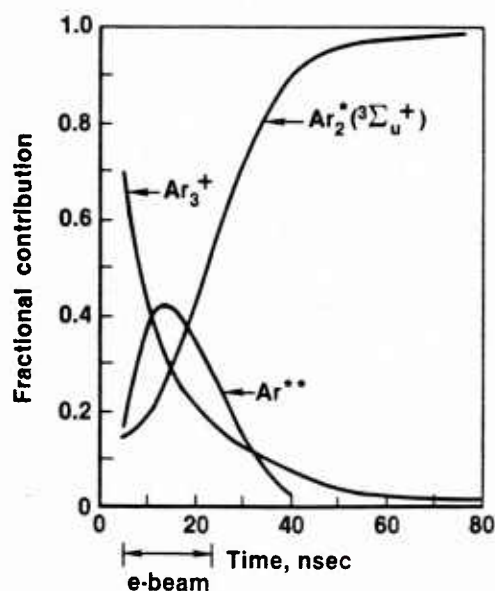


FIG. 16. Computed fractional contributions to the absorption in Ar (Fig. 14), based on the species concentrations of Fig. 15 and the cross sections of Table I.

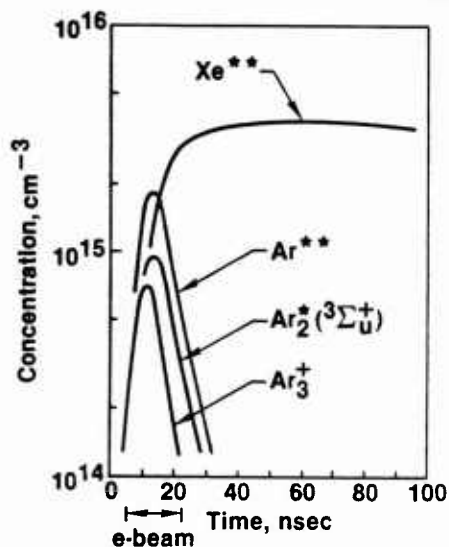


FIG. 17. Computed temporal evolution of certain species concentrations for the Ar-Xe mixture conditions of Fig. 14.

Thus, although discrete phototransitions from  $\text{Xe}^*(^3P_2, ^3P_1)$  to higher levels can be readily identified in the structured spectrum of  $\text{XeF}(C \rightarrow A)$  lasers,<sup>17</sup> the very large  $\text{Xe}^*(6s)$  concentration does not contribute *directly* to broadband absorption. However, Duzy and Hyman<sup>40</sup> compute photoionization cross sections for  $\text{Xe}^{**}(6p)$  and  $\text{Xe}^{**}(5d)$  that are approximately  $2$  and  $3 \times 10^{-17} \text{ cm}^2$ , respectively, at about 480 nm, varying only slightly throughout the wavelength range of present interest. When these cross section values are considered along with the computed magnitude and time dependence of the  $\text{Xe}^{**}$  population (Fig. 17), it becomes clear that the observed absorption in the Ar-Xe mixture of Fig. 14 is dominated by photoionization of Xe excited states, most probably those of the  $6p$  and  $5d$  manifolds. The computed fractional contributions to absorption in the Ar-Xe

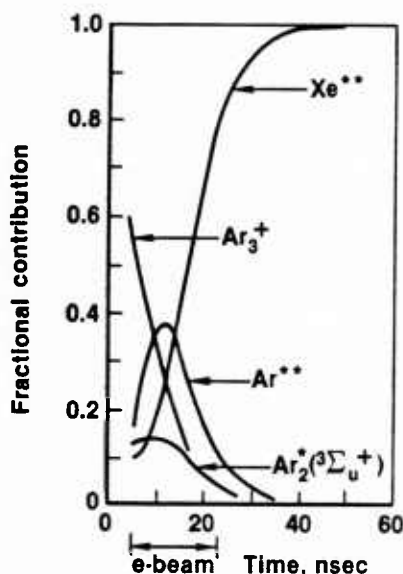


FIG. 18. Computed fractional contributions to the absorption in the Ar-Xe mixture of Fig. 14, based on the species concentrations of Fig. 17 and the cross sections of Table I.

mixture of Fig. 14, based on the cross sections of Table I, and presented in Fig. 18.

There are several reasons for the unusually large, slowly varying  $\text{Xe}^*$  and  $\text{Xe}^{**}$  populations for the present Ar-Xe mixture conditions. Modeling shows that the dominant ionized and excited species in the afterglow are atomic (i.e.,  $\text{Xe}^+$ ,  $\text{Xe}^*$ , and  $\text{Xe}^{**}$ ), even though the total pressure is very high. Since the Xe fractional concentration is small ( $< 0.01$ ), the rates of formation of the molecular species  $\text{Xe}_2^*(^1,3\Sigma_u^+)$  and  $\text{Xe}_2^+$  are much less than those for the corresponding reactions in pure Ar. Further, the heteronuclear species  $\text{ArXe}^+$  and  $\text{ArXe}^*$  are bound by only 0.14 eV<sup>46</sup> and  $< 0.1$  eV,<sup>26d</sup> respectively, so that the reverse rates for production of  $\text{Xe}^+$  and  $\text{Xe}^*$  from these molecular species are large. Consequently, the relative populations of Xe-related molecular species are much smaller than would be expected considering the high total pressure. Because the dominant ion is  $\text{Xe}^+$ , the electron loss by dissociative recombination is slow, with the result that the electron density in the Ar-Xe mixture remains high after termination of the excitation pulse, unlike the situation in pure Ar. The electrons collisionally mix  $\text{Xe}^*$  and  $\text{Xe}^{**}$  thereby establishing a quasiequilibrium condition, and, since *both* the production and loss of  $\text{Xe}^*$  and  $\text{Xe}^{**}$  are dominated by electron collisions, the concentrations of these species are practically time independent in the early afterglow. Therefore, the only significant reaction path away from the coupled  $\text{Xe}^*$ - $\text{Xe}^{**}$  system is the relatively slow formation of the excimer  $\text{Xe}_2^*(^1,3\Sigma_u^+)$ . This process is characterized by a  $\sim 300$  nsec time constant for the present conditions, a value very close to that observed for the absorption decay in the Ar-Xe mixture (Fig. 14).

### C. $\text{XeF}(C \rightarrow A)$ laser mixtures

Of course, the excited and ionized species discussed in connection with absorption in Ar and Ar-Xe mixtures will be present in  $\text{XeF}$  laser mixtures, albeit at significantly lower concentrations. Additionally, there will be other transient species related to  $\text{F}_2$  and/or  $\text{NF}_3$  such as various rare-gas halides. However, modeling shows that the only additional species having concentration levels that could lead to significant absorption (given appreciable blue/green photoabsorption cross sections) are the triatomic rare-gas halides,  $\text{Ar}_2\text{F}$  and  $\text{Xe}_2\text{F}$ . Calculations by Wadt<sup>47</sup> show that there are several allowed transitions between the lowest energy  $\text{RG}_2\text{X}(2^2B_2)$  state and higher energy states, with peak absorption wavelengths throughout the UV/visible region. However, only the UV transitions analogous to the corresponding  $\text{RG}_2^+$  absorption have large oscillator strengths, and are therefore expected to have significant absorption cross sections. Visible transitions in  $\text{RG}_2\text{X}$ , although broadband, have computed oscillator strengths more than one hundred times less than those of the UV transitions, implying peak absorption cross sections having values well below  $10^{-18} \text{ cm}^2$ . For this reason broadband visible absorption due to the presence of  $\text{Xe}_2\text{F}$  and/or  $\text{Ar}_2\text{F}$  is likely to be unimportant. Thus, we conclude that the same species causing the absorption in Ar and Ar-Xe mixtures (Table I) dominate the absorption in  $\text{XeF}(C \rightarrow A)$  laser mixtures.

## 1. Computed net gain

Presented in Fig. 19 is the net gain computed for conditions similar to those of Fig. 7. The various contributions to the absorption are presented in Fig. 20. Examination of Fig. 19 shows that the net gain for laser conditions can be computed in good qualitative and quantitative agreement with experimental observations using the absorption cross sections inferred by analysis of the absorption in Ar and Ar-Xe mixtures (Table I). Further, it is clear that while all the species identified as absorbers in Ar and Ar-Xe mixtures contribute significantly to absorption in the laser mixture (Fig. 20), photoionization of Xe\*\* is the most important absorption process.

Additional support for this conclusion is provided by absorption measurements using the 590-nm dye laser probe, which indicate a peak absorption of  $2.5\% \text{ cm}^{-1}$ . Since there is no contribution to net gain/absorption from XeF(C) at this wavelength, the measured  $2.5\% \text{ cm}^{-1}$  is actually the total absorption coefficient, a value significantly lower than the  $4.0\% - 5.0\% \text{ cm}^{-1}$  peak value found to be typical of the blue/green region (Fig. 19). However, the 590-nm photon energy is insufficient to ionize either the Xe(6p) levels or the first four Xe(5d) levels. Because relaxation of the higher excited states of Xe by Ar is very fast,<sup>26</sup> it is probable that the 6p and 5d levels dominate the calculated Xe\*\* population. Simply subtracting the Xe\*\* contribution (Fig. 20) reduces the peak absorption coefficient from  $\sim 4.0\% \text{ cm}^{-1}$  (Fig. 19) to about  $2.5\% \text{ cm}^{-1}$ , a value in good agreement with the 590 nm absorption measurement.

## D. Laser mixtures with krypton

Figure 10 shows that addition of Kr to the optimum laser mixture reduces the peak absorption from about  $2\% \text{ cm}^{-1}$  to  $\sim 0.25\% \text{ cm}^{-1}$ . Addition of the same amount of Kr to Ar and to the Ar-Xe mixture was found to reduce the absorption of the former by over 50% and to have little effect on the latter. This suggests that the presence of Kr in the laser mixture reduces the initial absorption caused by Ar-related species. Excitation transfer from Ar\*\* to Kr results

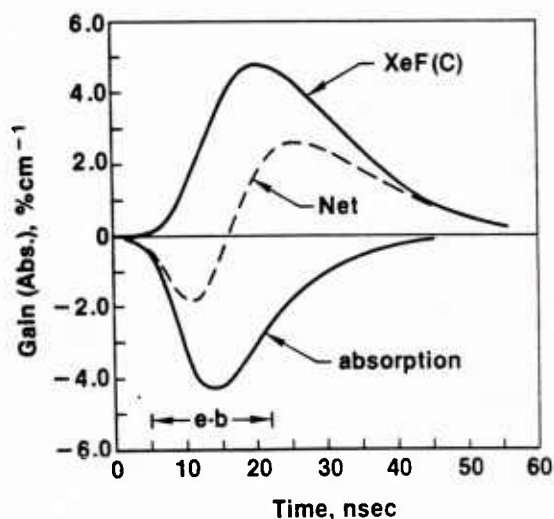


FIG. 19. Gain and absorption at 488 nm for the conditions of Fig. 7, based on computed species concentrations and the cross sections of Table I.

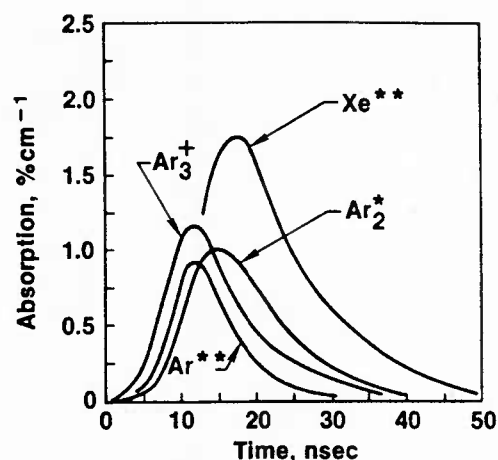


FIG. 20. Computed contributions to the absorption at 488 nm corresponding to the conditions of Fig. 19.

in the production of higher excited states of Kr that have photoionization cross sections somewhat larger than those of the corresponding Ar states.<sup>40</sup> However, excitation transfer from  $\text{Ar}_2^+(^3\Sigma_u^+)$  can only result in  $\text{Kr}(5s, s')$  states, while  $\text{Ar}_2^+$  and  $\text{Ar}_3^+$  charge exchange results in the formation of  $\text{Kr}^+$  (or  $\text{ArKr}^+$ ) ions. Calculations show that 0.2 atm Kr added to the XeF(C) laser mixture reduces the  $\text{Ar}_2^+(^3\Sigma_u^+)$  population by approximately a factor of two and the  $\text{Ar}_3^+$  population by over an order of magnitude. Examination of Fig. 20 indicates that the corresponding reduction in the contributions of  $\text{Ar}_2^+$  and  $\text{Ar}_3^+$  to absorption could easily account for the experimental observations. However, a comparison of the temporal evolution of the fluorescence for laser mixtures with and without Kr shows that the  $C \rightarrow A$  fluorescence rises somewhat faster in the Kr-containing mixture. Krypton is known to be faster than Ar at both relaxing the XeF(B,C) vibrational manifold and at mixing the two states,<sup>16</sup> although it is somewhat surprising if these effects are responsible for the faster XeF(C) fluorescence rise, given the fact that the Ar-Kr ratio was very large in these experiments. In any case, it appears that the dramatic reduction in initial absorption of XeF(C) laser mixtures containing Kr is due primarily to a reduction in the concentrations of Ar-related molecular absorbers, and possibly to an increase in the production rate of XeF(C) as well. Unfortunately, both gain and fluorescence data also show that quenching of XeF(C) is faster with Kr present. Nonetheless the near absence of early absorption with Kr added and peak net gain values comparable to the highest measured may have significant implications for improving laser extraction efficiency.

## VI. LASER EFFICIENCY

### A. e-beam energy deposition

Determination of the electrical-optical energy conversion efficiency corresponding to the measured laser pulse energy requires knowledge of the e-beam energy deposition in the gas. Several three-dimensional computer models<sup>48-50</sup> of e-beam energy deposition, and measurements<sup>48</sup> of gas pressure rise, all show that the energy deposited under conditions similar to those of this investigation typically is from

two to four times greater than that computed on the basis of simple stopping power calculations. The difference is due largely to backscatter from the cell walls and to multiple scattering in the foil separating the low and high pressure regions of the cell. To account for such effects, in this work we have used a factor of three correction to a stopping power calculation based on the Berger and Seltzer data<sup>51</sup> in order to obtain a reasonable estimate of the *e*-beam energy deposited in the active volume. Measured current density levels on the optical axis were found to vary from 200 to 400 A cm<sup>-2</sup>, depending on *e*-beam control parameters and unpredictable shot to shot variations. This range of current density, combined with Ar pressures in the 6-10 atm range, corresponds to energy deposition levels ranging from approximately 100 to 300 J/liter depending upon the specific combination of conditions. Therefore, our highest measured laser pulse energies of 1.0-2.0 J/liter correspond to an intrinsic laser efficiency of about 0.5%-1.0%. Although such estimates of *e*-beam energy deposition have to be considered somewhat uncertain, calculations of peak XeF(C) population, net gain, and the temporal relationship among laser medium properties, all of which depend on the modeling of *e*-beam energy deposition, are found to be in good agreement with experimental observations. Thus, we conclude that the *e*-beam energy deposition so estimated is probably accurate to within about  $\pm 35\%$ , a level of uncertainty that must also be assigned to the inferred value of intrinsic laser efficiency.

## B. Optical extraction efficiency

Presented in Fig. 21 is the computed temporal evolution of the intracavity optical flux for typical conditions. The relationship between fluorescence, net gain and laser pulse intensity in this figure is found to be in very good agreement with experiment. This figure shows that although the intracavity flux eventually reaches a level about three times the  $\sim 6 \text{ MW cm}^{-2}$  saturation flux, resulting in a significant depletion of the tail of the XeF(C) population profile, collisional deactivation of the C state still dominates the time integrated XeF(C) population decay. Thus, although the XeF(C) formation efficiency is 5%-7%, the overall optical extraction efficiency is only about 10%, a factor presently limiting the intrinsic laser efficiency to a value somewhat less than 1%.

The key factor limiting extraction efficiency is the strong initial absorption occurring during the excitation pulse. In spite of a significant increase in net gain and gain-absorption ratio over prior levels, even for conditions for which the highest output energy has been obtained, the gain does not become positive until after the excitation pulse is terminated. Further, the maximum value of gain is only slightly higher than one half that based on the XeF(C) population alone (Fig. 19). Calculations show that in the absence of such absorption, the intracavity flux would rise rapidly to a level approximately ten times the saturation flux at about the time the maximum zero-field XeF(C) population is achieved, a circumstance that would result in an extraction efficiency of approximately 40% for the conditions of this experiment. This suggests that even though addition of Kr to the optimum Ar-Xe-NF<sub>3</sub>-F<sub>2</sub> mixture did not increase the

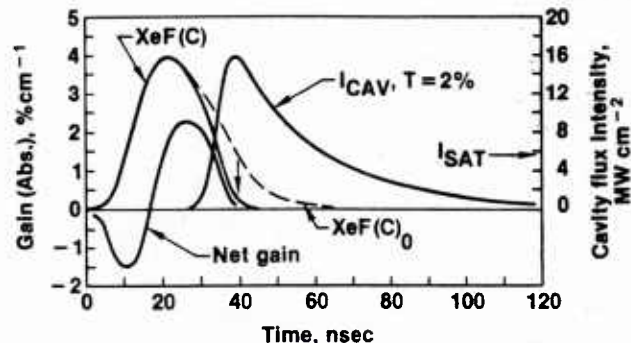


FIG. 21. Temporal evolution of net gain, intracavity optical flux, and XeF(C) population with and without the cavity flux, computed for conditions similar to those of Figs. 7 and 19. The transmission of the output mirror was 2%.

single pulse laser energy density, the near absence of initial absorption (Fig. 10) in certain Kr-containing mixtures may permit significant improvement in extraction efficiency if a multiple pulse excitation scheme is utilized to prolong the gain duration. For example, with a dual-pulse technique, the first pulse would be used to produce a high intracavity flux level prior to initiation of a second, higher energy pulse. Because there is very little initial absorption in Kr-containing mixtures, initiation of the second pulse near the time of the peak flux produced by the first should produce no significant detrimental effect. However, the high cavity flux present at the onset of the second pulse would ensure more efficient energy extraction. Preliminary modeling of conditions representative of this variation on the laser pulse-injection scheme indicate that extraction efficiency levels significantly larger than those obtained to date may be possible.

### 1. Bleaching of absorbing species

It is interesting to note that because the relevant photoabsorption cross sections (Table I) are significantly larger than the XeF(C $\rightarrow$ A) stimulated emission cross section, the saturation fluxes for the transient absorbers are about the same as that of XeF(C), in striking contrast to the situation typical of the rare-gas-halide B $\rightarrow$ X lasers. Thus, optical bleaching of the absorbing species is significant for the intracavity flux levels achieved in these experiments. For the conditions of Fig. 21 calculations indicate that the peak cavity flux (and both the laser output energy and efficiency) reach levels approximately 50% higher than would be the case without bleaching of the absorbers.

## VII. SUMMARY

Electron-beam excitation of a unique two-halogen gas mixture has been shown to be an effective way to obtain efficient, broadband XeF(C $\rightarrow$ A) excimer laser oscillation in the blue/green spectral region. Such a laser can now operate at intrinsic energy conversion efficiency approaching one percent with output pulse energy in excess of 1.0 J/liter. These greatly improved laser characteristics have been achieved by careful optimization of the components of the rare-gas-halide mixture, increased electron beam energy deposition, and improved optical resonator design.

Temporal and spectral gain/absorption, laser energy,

and fluorescence measurements under a variety of experimental conditions have provided good insight into the underlying kinetic and spectroscopic processes which control the performance of the  $\text{XeF}(C \rightarrow A)$  laser. Excellent agreement between experiment and theory has been demonstrated. The contributions to the major energy pathways resulting in the formation and loss of  $\text{XeF}(C)$ , and to transient photoabsorption in the visible region of the spectrum have been studied in order to characterize the optical extraction and intrinsic laser efficiency.

Broadband molecular and atomic absorption is the most important factor limiting the efficiency of electrically excited  $\text{XeF}(C \rightarrow A)$  lasers. For the laser mixtures investigated in this work, the primary absorption processes have been identified as photoionization of the  $4p$ ,  $3d$ , and higher lying states of Ar, and of the Xe  $6p$  and  $5d$  states, and photodissociation of  $\text{Ar}_2(^3\Sigma_u^+)$  and  $\text{Ar}_3^+$ . These saturable absorbers have blue/green photoabsorption cross sections comparable in magnitude to the  $\text{XeF}(C \rightarrow A)$  stimulated emission cross section, and are bleached for intracavity flux levels  $> 3.0 \text{ MW cm}^{-2}$ , an effect resulting in a prolongation of the gain duration thereby enhancing optical extraction efficiency. Quenching of some of the absorbing species by the addition of  $\text{F}_2$  to the Ar-Xe- $\text{NF}_3$  mixture increases the laser efficiency and the output power considerably. Further improvements, such as controlled optical bleaching of the absorbers, additional kinetic refinements, or double pumping, may lead to even higher  $\text{XeF}(C \rightarrow A)$  laser efficiencies. Indeed, intrinsic efficiency values approaching those of the UV  $B \rightarrow X$  rare-gas-halide lasers seem a distinct possibility.

The stimulated emission cross section for the  $\text{XeF}(C \rightarrow A)$  transition is an order of magnitude smaller than that of the  $B \rightarrow X$  transition, and, since  $> 95\%$  of the excited state population of  $\text{XeF}(B, C)$  is in the  $\text{XeF}(C)$  level, superradiance in a large scale laser device should be relatively small. Calculations and calibrated fluorescence measurements show that the  $\text{XeF}(C)$  formation efficiency is  $5\% - 7\%$  for the present conditions. Therefore, the  $\text{XeF}(C \rightarrow A)$  excimer medium has the potential to become an efficient wideband, high-power laser amplifier in the blue/green region that could be used as a final amplifier in conjunction with another laser oscillator.

## ACKNOWLEDGMENTS

It is a pleasure to acknowledge the contributions of Professor D. W. Setser of Kansas State University and those of Dr. R. Tripodi and Dr. H. H. Michels of UTRC. This work was supported in part by the Office of Naval Research, the National Science Foundation and the Robert A. Welch Foundation.

- <sup>1</sup>(a) D. Kligler, H. H. Nakano, D. L. Huestis, W. K. Bischel, R. M. Hill, and C. K. Rhodes, *Appl. Phys. Lett.* **33**, 39 (1978); (b) H. Helm, D. L. Huestis, M. J. Dyer, and D. C. Lorents, *J. Chem. Phys.* **79**, 3220 (1983).
- <sup>2</sup>W. E. Ernst and F. K. Tittel, *Appl. Phys. Lett.* **35**, 36 (1979).
- <sup>3</sup>J. D. Campbell, C. H. Fisher, and R. E. Center, *Appl. Phys. Lett.* **37**, 348 (1980).
- <sup>4</sup>R. Burnham, *Appl. Phys. Lett.* **35**, 48 (1979).
- <sup>5</sup>C. H. Fisher, R. E. Center, G. J. Mullaney, and J. P. McDaniel, *Appl. Phys. Lett.* **35**, 26 (1979).
- <sup>6</sup>W. K. Bischel, H. H. Nakano, D. J. Eckstrom, R. M. Hill, D. L. Huestis, and D. C. Lorents, *Appl. Phys. Lett.* **34**, 565 (1979).
- <sup>7</sup>W. K. Bischel, D. J. Eckstrom, H. C. Walker, Jr., and R. A. Tilton, *J. Appl. Phys.* **52**, 4429 (1981).
- <sup>8</sup>D. J. Eckstrom and H. C. Walker, *IEEE J. Quantum Electron.* **QE-18**, 176 (1982).
- <sup>9</sup>C. H. Fisher, R. E. Center, G. J. Mullaney and J. P. McDaniel, *Appl. Phys. Lett.* **35**, 901 (1979).
- <sup>10</sup>J. Liegel, F. K. Tittel, and W. L. Wilson, Jr., *Appl. Phys. Lett.* **39**, 369 (1981).
- <sup>11</sup>J. C. Hsia, J. A. Mangano, J. H. Jacob, and M. Rokni, *Appl. Phys. Lett.* **34**, 208 (1979).
- <sup>12</sup>W. L. Nighan, Y. Nachshon, F. K. Tittel, and W. L. Wilson, Jr., *Appl. Phys. Lett.* **42**, 1006 (1983).
- <sup>13</sup>D. J. Spencer, *J. Appl. Phys.* **49**, 3729 (1978).
- <sup>14</sup>J. E. Velazco, J. H. Kolts, and D. W. Setser, *J. Chem. Phys.* **69**, 4357 (1978).
- <sup>15</sup>J. E. Velazco, J. H. Kolts, and D. W. Setser, *J. Chem. Phys.* **65**, 3468 (1976).
- <sup>16</sup>(a) H. C. Brashears and D. W. Setser, *J. Chem. Phys.* **76**, 4932 (1982); (b) Y. C. Yu, D. W. Setser, and H. Horiguchi, *J. Phys. Chem.* **87**, 2199 (1983).
- <sup>17</sup>R. Sauerbrey, F. K. Tittel, W. L. Wilson, Jr., and W. L. Nighan, *IEEE J. Quantum Electron.* **QE-18**, 1336 (1982).
- <sup>18</sup>We observe higher peak absorption at 514.5 nm than at any other wavelength both in Ar and in laser mixtures (Fig. 11). Zamir and co-workers (Ref. 36) report similar behavior in  $e$ -beam excited Ar at high pressure. They suggest that the structure observed at 514.5 nm is due to the bound-bound  $4s^3\Sigma_u^+ - 5p^3\pi_g$  transition in Ar. Although the time dependence of the 514.5 nm absorption reported in Ref. 36 seems to be consistent with the anticipated  $^3\Sigma_u^+$  decay, it is difficult to assign the absorption to the  $^3\Sigma_u^+ - ^3\pi_g$  transition in view of the potential curves reported by Yates *et al.* (Ref. 45).
- <sup>19</sup>M. R. Flannery and T. P. Tang, *Appl. Phys. Lett.* **32**, 327, 356 (1978).
- <sup>20</sup>W. Lowell Morgan, B. L. Whitten, and J. N. Bardsley, *Phys. Rev. Lett.* **45**, 2021 (1980).
- <sup>21</sup>R. Sauerbrey, W. Walter, F. K. Tittel, and W. L. Wilson, Jr., *J. Chem. Phys.* **78**, 735 (1983).
- <sup>22</sup>D. K. Bohme, N. G. Adams, M. Moseman, D. B. Dunkin, and E. E. Ferguson, *J. Chem. Phys.* **52**, 5094 (1970).
- <sup>23</sup>C. B. Collins and F. W. Lee, *J. Chem. Phys.* **71**, 184 (1979).
- <sup>24</sup>W. J. Wiegand, Jr., in *Applied Atomic Collision Physics; Volume 3: Gas Lasers*, edited by H. S. W. Massey, E. W. McDaniel, and B. Bederson (Academic, New York, 1982), Chap. 3 and references cited therein.
- <sup>25</sup>(a) P. Millet, A. Birot, H. Brunet, H. Dijols, J. Galy, and Y. Salamero, *J. Phys. B* **15**, 2935 (1982); (b) H. Brunet, A. Birot, H. Dijols, J. Galy, P. Millet, and Y. Salamero, *J. Phys. B* **15**, 2945 (1982); (c) Y. Salamero, A. Birot, H. Brunet, H. Dijols, J. Galy, P. Millet, and J. P. Montagne, *J. Chem. Phys.* **74**, 288 (1981).
- <sup>26</sup>(a) H. Horiguchi, R. S. F. Chang, and D. W. Setser, *J. Chem. Phys.* **75**, 1207 (1981); (b) R. S. F. Chang and D. W. Setser, *J. Chem. Phys.* **69**, 3885 (1978); (c) R. S. F. Chang, H. Horiguchi, and D. W. Setser, *J. Chem. Phys.* **73**, 778 (1980); (d) J. H. Kolts and D. W. Setser, *J. Chem. Phys.* **68**, 4848 (1978).
- <sup>27</sup>P. J. Chantry, in *Applied Atomic Collision Physics; Volume 3: Gas Lasers*, edited by H. S. W. Massey, E. W. McDaniel, and B. Bederson (Academic, New York, 1982), Chap. 2.
- <sup>28</sup>(a) W. L. Nighan, *IEEE J. Quantum Electron.* **QE-14**, 714 (1978); (b) M. Rokni, J. A. Mangano, J. H. Jacob, and J. C. Hsia, *IEEE J. Quantum Electron.* **QE-14**, 464 (1978); (c) D. L. Huestis, R. M. Hill, H. H. Nakano, and D. C. Lorents, *J. Chem. Phys.* **69**, 5133 (1978).
- <sup>29</sup>(a) W. L. Morgan and A. Szoke, *Phys. Rev. A* **23**, 1256 (1981); (b) D. Klimmek and J. C. Hsia, *J. Appl. Phys.* **52**, 5361 (1981).
- <sup>30</sup>G. Marowsky, G. P. Glass, F. K. Tittel, K. Hohla, W. L. Wilson, Jr., and H. Weber, *IEEE J. Quantum Electron.* **QE-18**, 898 (1982).
- <sup>31</sup>A. V. Hazi, T. N. Rescigno, and A. E. Orel, *Appl. Phys. Lett.* **35**, 477 (1979).
- <sup>32</sup>L. F. Champagne, in *Applied Atomic Collision Physics; Volume 3: Gas Lasers*, edited by H. S. W. Massey, E. W. McDaniel, and B. Bederson (Academic, New York, 1982), Chap. 12 and references cited therein.
- <sup>33</sup>M. Rokni and J. H. Jacob, in *Applied Atomic Collision Physics; Volume 3: Gas Lasers*, edited by H. S. W. Massey, E. W. McDaniel, and B. Bederson (Academic, New York, 1982), Chap. 10.
- <sup>34</sup>G. M. Schindler, *IEEE J. Quantum Electron.* **QE-16**, 546 (1980).

- <sup>35</sup>D. Eimerl, J. Appl. Phys. **51**, 3008 (1980).
- <sup>36</sup>E. Zamir, D. L. Huestis, H. H. Nakano, R. M. Hill, and D. C. Lorents, IEEE J. Quantum Electron. **QE-15**, 281 (1979).
- <sup>37</sup>D. L. Turner and D. C. Conway, J. Chem. Phys. **71**, 1899 (1979).
- <sup>38</sup>J. A. MacDonald, M. A. Biondi, and R. Johnsen, J. Phys. B **16**, 4273 (1983). The electron recombination coefficient for  $\text{Ne}_3^+$  has been measured and found it to be approximately five times larger than that of  $\text{Ne}_2^+$ , the recombination coefficients for both ions having about the same electron temperature dependence. In the present work, we have assumed that the recombination coefficients for  $\text{Ar}_3^+$  and  $\text{Ar}_2^+$  are in the same ratio as those of the Ne ions.
- <sup>39</sup>J. W. Keto, R. E. Gleason, Jr., and G. K. Walters, Phys. Rev. Lett. **33**, 1365 (1974).
- <sup>40</sup>C. Duzy and H. A. Hyman, Phys. Rev. A **22**, 1878 (1980).
- <sup>41</sup>H. H. Michels, R. H. Hobbs, and L. A. Wright, J. Chem. Phys. **71**, 5053 (1979).
- <sup>42</sup>H. H. Michels, R. H. Hobbs, and L. A. Wright, Appl. Phys. Lett. **35**, 153 (1979).
- <sup>43</sup>W. R. Wadt, Appl. Phys. Lett. **38**, 1030 (1981).
- <sup>44</sup>The  $\text{Ar}_3^+$  photoabsorption cross section estimate reported in Ref. 42 is based on a triangular ionic structure. However, there is evidence that the most stable structure for  $\text{Ar}_3^+$  is linear (Refs. 37 and 43). On this basis the cross section for photodissociation of  $\text{Ar}_3^+$  is estimated to be approximately  $3\text{--}4 \times 10^{-17} \text{ cm}^2$  in the blue/green region [H. H. Michels (private communication)].
- <sup>45</sup>J. H. Yates, W. C. Ermler, N. W. Winter, P. A. Christiansen, Y. S. Lee, and K. S. Pitzer, J. Chem. Phys. **79**, 6145 (1983).
- <sup>46</sup>C. Y. Ng, P. W. Tiedeman, B. H. Mahan, and Y. T. Lee, J. Chem. Phys. **66**, 5737 (1977).
- <sup>47</sup>W. R. Wadt and P. J. Hay, J. Chem. Phys. **68**, 3850 (1978).
- <sup>48</sup>D. J. Eckstrom and H. C. Walker, Jr., J. Appl. Phys. **51**, 2458 (1980).
- <sup>49</sup>G. A. Hart and S. K. Searles, J. Appl. Phys. **47**, 2033 (1976).
- <sup>50</sup>K. S. Jancaitis and H. T. Powell (unpublished).
- <sup>51</sup>M. J. Berger and S. M. Seltzer, in *Studies in Penetration of Charged Particles in Matter*, Nuclear Science Series Report No. 10, NAS-NRC Publ. No. 1133 (National Academy of Sciences, Washington, D. C., 1964).

# Synthesis of rare gas-halide mixtures resulting in efficient $\text{XeF}(C \rightarrow A)$ laser oscillation

W. L. Nighan

United Technologies Research Center, East Hartford, Connecticut 06108

F. K. Tittel, W. L. Wilson, Jr., N. Nishida, Y. Zhu, and R. Sauerbrey

Electrical Engineering Department and Rice Quantum Institute, Rice University, Houston, Texas 77251

(Received 9 July 1984; accepted for publication 8 August 1984)

Significantly improved  $\text{XeF}(C \rightarrow A)$  laser performance has been achieved using electron beam excitation of complex, multicomponent gas mixtures specifically tailored so as to reduce medium transient absorption in the blue-green region. Use of Ar and Kr together as the effective rare gas buffer-energy transfer species, along with a combination of  $\text{NF}_3$  and  $\text{F}_2$  to produce the desired F-donor molecule characteristics, has permitted synthesis of near optimum medium properties for which  $\text{XeF}(C)$  is produced efficiently while transient absorption is minimized. With this technique we have achieved laser pulse energy density and intrinsic efficiency of  $2.2 \pm 0.3 \text{ J/l}$  and  $\sim 1.5\%$ , respectively, values that are comparable to those of the  $B \rightarrow X$  rare gas-halide lasers.

Short pulse electron beam ( $e$ -beam) excitation of the blue-green  $\text{XeF}(C \rightarrow A)$  laser transition is characterized by a period of strong transient absorption during the excitation pulse, followed by the development of net gain and subsequent laser oscillation in the afterglow regime.<sup>1</sup> Until recently, the combination of a relatively short duration of the net gain region ( $\leq 50 \text{ ns}$ ) and a relatively low value of the peak gain ( $\leq 2\% \text{ cm}^{-1}$ ) has limited the efficiency of this tunable laser to unacceptably low levels. However, by selectively tailoring kinetic processes through the use of a unique two-halogen mixture containing both  $\text{NF}_3$  and  $\text{F}_2$  so as to reduce transient absorption, a very significant improvement in  $\text{XeF}(C \rightarrow A)$  laser performance has been achieved.<sup>1,2</sup> Indeed,  $e$ -beam excitation of such two-halogen Ar-Xe mixtures has yielded laser pulse energy density in excess of  $1.0 \text{ J/l}$ , corresponding to intrinsic electrical-optical energy conversion efficiency estimated to be in the  $0.5\%$ – $1.0\%$  range. In this letter we report further improvement in  $\text{XeF}(C \rightarrow A)$  laser performance resulting from the addition of Kr to an Ar-Xe- $\text{NF}_3$ - $\text{F}_2$  mixture. This multicomponent mixture has permitted synthesis of near optimum medium properties resulting in  $\text{XeF}(C \rightarrow A)$  laser pulse energy density and intrinsic efficiency of  $2.2 \pm 0.3 \text{ J/l}$  and  $\sim 1.5\%$ , respectively. This improvement was obtained without increasing the energy deposited in the gas by the  $e$ -beam. Thus, a level of  $\text{XeF}(C \rightarrow A)$  laser performance has been achieved which, for the first time, is comparable to that typical of UV  $B \rightarrow X$  rare gas-halide laser transitions.

In this investigation laser excitation was provided by an electron beam having an energy of  $1 \text{ MeV}$  and a pulse duration of  $10 \text{ ns}$  (full width at half-maximum). The  $e$ -beam current density at the center of the optical axis was  $\sim 250$ – $300 \text{ A cm}^{-2}$ , as measured with a Faraday probe. A stable, intracell optical resonator was used consisting of a totally reflecting ( $R > 99.6\%$ ) mirror having a radius of curvature of either  $0.5$  or  $1.0 \text{ m}$ , separated by  $12.5 \text{ cm}$  from a flat output mirror having a reflectivity of  $95\%$ , a value found to be optimum for the present conditions. The active region was the  $\sim 28 \text{ cm}^3$  volume defined by the clear aperture ( $1.9 \text{ cm}$  diameter) and the pumped length ( $10 \text{ cm}$ ). Specific details of this experi-

mental arrangement and related diagnostic apparatus are described in Ref. 1.

A cw Ar-ion laser was used<sup>1</sup> to measure the temporal evolution of the gain/absorption at several wavelengths throughout the blue-green region. Figure 1 shows a representative gain-absorption profile at  $488 \text{ nm}$  for an optimized Ar-Xe- $\text{NF}_3$ - $\text{F}_2$  mixture under conditions for which the laser pulse energy density and intrinsic efficiency were typically  $1.5 \pm 0.3 \text{ J/l}$  and  $\sim 1.0\%$ , respectively. Comprehensive analysis<sup>1</sup> of medium kinetic processes indicates that for these conditions the initial period of strong absorption is primarily the result of photoionization of the  $4p$ ,  $3d$ , and higher lying states of Ar, and of the Xe  $6p$ , and  $5d$  states, along with photodissociation of  $\text{Ar}_2(^3\Sigma_u^+)$  and  $\text{Ar}_3^+$ . These broadband absorption processes more than offset the positive contribution of  $\text{XeF}(C)$  excimer molecules during and immediately following the period of  $e$ -beam excitation. Although the Ar-related absorption processes decay rapidly, photoionization of Xe excited states is very significant even after the gain

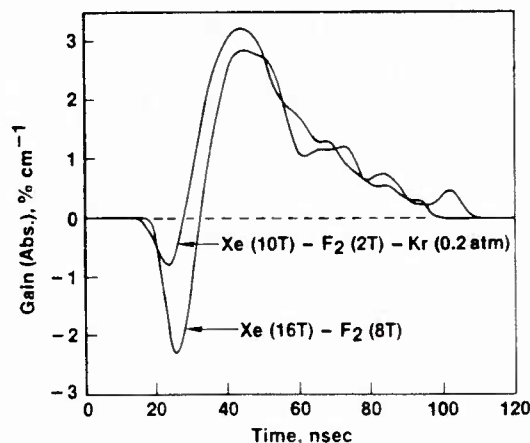


FIG. 1. Temporal evolution of the net gain measured at  $488 \text{ nm}$  for mixtures comprised of  $6.5 \text{ atm Ar}$ ,  $8 \text{ Torr NF}_3$ , and partial pressures of Xe and  $\text{F}_2$  optimized with and without Kr as indicated. The measured  $e$ -beam current density on the optical axis for these conditions was typically  $275 \pm 25 \text{ A cm}^{-2}$ , corresponding to a volumetric energy deposition estimated to be  $\sim 150 \text{ J/l}$  (Ref. 1).

II-16

becomes positive, thereby substantially reducing the peak gain value from that possible due to  $\text{XeF(C)}$  alone.<sup>1</sup>

During the course of this work it was found that addition of Kr dramatically reduced the initial absorption of the previously optimized Ar-Xe-NF<sub>3</sub>-F<sub>2</sub> mixture.<sup>1</sup> Based on our analysis of the change in measured absorption in pure Ar and in Ar-Xe mixtures, it appeared that the most likely explanation for this observation was that Kr reduced the concentrations of both  $\text{Ar}_2(^3\Sigma_u^+)$  and  $\text{Ar}_3^+$  during the *e*-beam excitation pulse, while providing additional decay channels for the Xe 6*p* and 5*d* states. Both gain and fluorescence data indicated that the additional quenching of  $\text{XeF(C)}$  by Kr was also significant, however, so that the magnitude and duration of the gain typical of our initial experimentation with Kr were not improved. Thus, in these early studies, no increase in laser pulse energy/efficiency was achieved with mixtures containing Kr.<sup>1</sup>

Because the influence of Kr on the measured blue-green absorption in various mixtures was found to be so pronounced, recent efforts have focused on systematic measurement and evaluation of gain temporal profiles and laser pulse energy, while varying the fractional concentrations of Xe, F<sub>2</sub>, and NF<sub>3</sub> in mixtures of Ar and Kr at a total pressure<sup>3</sup> of 6.5 atm. Although the Kr pressure was varied from a few Torr to several atm, particular emphasis was placed on Kr pressures in the 0.1–1.0-atm range for which the absorption peak during the *e*-beam excitation pulse was found to be minimized. Presented in Fig. 1 is the measured gain profile for a reoptimized mixture containing 0.2 atm Kr, excited under conditions essentially identical to those of the mixture without Kr, also shown in the figure. The significant reduction in absorption during the excitation pulse with Kr in the mixture is readily apparent, as is the higher value of peak gain and the increase in gain duration to about 80 ns. These features were found to be typical of Kr pressures throughout the entire 0.1–1.0-atm range.

Measurements show that the magnitude of the absorption minimum (Fig. 1) with Kr in the mixture is relatively insensitive to the specific values of Xe or F<sub>2</sub> pressure, but that the peak gain (and its rate of decay) is dependent on the concentrations of these species. Indeed, the optimum concentrations of both Xe and F<sub>2</sub> are found to be significantly lower than their values in the absence of Kr.

Although our measurements indicate that the primary role of Kr is reduction of the concentrations of Ar and Xe related species that absorb in the blue-green region,<sup>1</sup> the measured rate of rise of the  $\text{XeF(C} \rightarrow \text{A)}$  fluorescence and its peak value both are significantly higher with Kr in the mixture, particularly for large F<sub>2</sub> concentrations. Analysis shows that these effects are much more pronounced than would be expected on the basis of faster  $\text{XeF(B/C)}$  state mixing<sup>4</sup> due to Kr, suggesting that  $\text{XeF(B, C)}$  formation is enhanced when Kr is present. One possible explanation for this observation is that Xe displacement reactions involving either KrF or Kr<sub>2</sub>F are more effective than their Ar counterparts.<sup>5</sup> However, the enhancement in  $\text{XeF(C)}$  formation with Kr in the mixture appears to be of less importance than the reduction in transient absorption.

Presented in Fig 2 is the dependence of laser pulse ener-

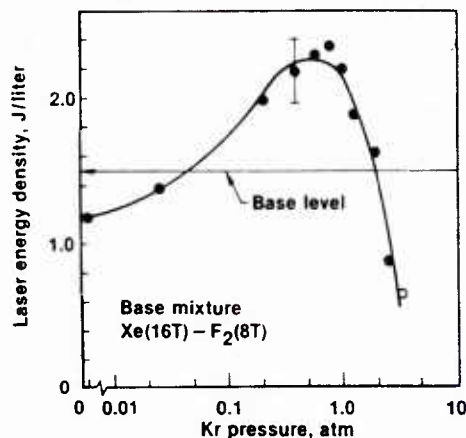


FIG. 2. Laser pulse energy density dependence on Kr pressure as measured using a calibrated vacuum photodiode detector. The mixture was comprised of Ar and Kr at a total pressure of 6.5 atm, 8 Torr NF<sub>3</sub>, 10 Torr Xe, and 2 Torr F<sub>2</sub>. The indicated base level refers to the mixture optimized in the absence of Kr; the symbol (O) indicates the measured laser energy with no Ar in the mixture.

gy density on Kr pressure for the specific Ar-Xe-F<sub>2</sub>-NF<sub>3</sub> mixture found to be optimum for Kr pressures in the 0.1–1.0-atm range.<sup>3</sup> The four-component mixture optimized in the absence of Kr consistently results in laser pulse energy density values of  $1.5 \pm 0.3$  J/l for the present conditions, a value not unduly sensitive to either the radius of curvature of the total reflector or of the transmission of the output coupler. Figure 2 shows that as the Kr pressure is increased above  $\sim 0.05$  atm for the reoptimized mixture, the laser pulse energy increases above the  $\sim 1.5$  J/l base level of the reference no-Kr mixture. For Kr pressures in the 0.4–0.9-atm range, a broad maximum in laser energy density is achieved, corresponding to  $\sim 50\%$  increase over that of the reference mixture, a result that is consistent with the trend exhibited by the measured gain/absorption profiles. The maximum  $2.2 \pm 0.3$  J/l laser energy density typical of these conditions corresponds to an intrinsic energy conversion efficiency estimated<sup>1</sup> to be approximately 1.5%.

Measurements were also carried out for Kr pressures in the 3–4-atm range with no Ar in the mixture, a condition for which the energy deposited by the *e*-beam would be very nearly equivalent to Ar-buffered mixtures at a total pressure of 6.5 atm.<sup>3</sup> In these tests, with the Xe and F<sub>2</sub> pressures again reoptimized, the maximum laser energy density was in the 0.5–0.7-J/l range, a value much lower than that of either the no-Kr reference mixture or the optimized mixture with Kr present.<sup>6</sup> With the Kr pressure in the 3–4-atm range, addition of varying amounts of either Ne or Ar up to pressures of several atm resulted in laser pulse energy values about the same as those using Kr alone, although the energy deposited in such cases was substantially increased. This is in contrast to the situation for either the Ar-buffered reference mixture or the optimized Ar-Kr mixture, for which it was found that increasing the energy deposition by increasing either the *e*-beam current density or the Ar pressure resulted in higher laser output. Indeed, for the optimum conditions of Fig. 2, but with the Ar pressure increased from  $\sim 6.5$  to 8.5 atm, the laser pulse energy was found to increase from 2.2 J/l to  $\sim 3.0$  J/l. Thus, all of our evidence indicates that the use of Ar and

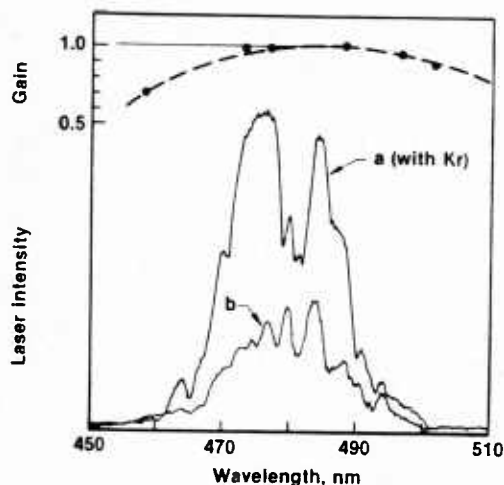


FIG. 3.  $\text{XeF}(\text{C} \rightarrow \text{A})$  laser spectra for (a) the mixture optimized with Kr present and (b) for the optimum mixture in the absence of Kr. Also shown is the wavelength dependence of peak zero-field gain normalized to its value at 488 nm.

Kr together as an effective buffer-energy transfer species results in a medium that, when electrically excited, is characterized by significantly lower concentrations of excited-ionized species that absorbed in the blue-green region than is the case using either Ar or Kr alone.

Presented in Fig. 3 are the time integrated laser spectra for optimum mixtures with and without Kr for conditions similar to those in Fig. 1. Although there are some differences, the two spectra are generally similar except for a somewhat deeper absorption valley centered near 480 nm in the Ar-Kr mixture. Also shown in this figure is the measured wavelength dependence of the peak value of the zero-field gain,<sup>1</sup> normalized to its value at 488 nm. The relatively weak wavelength dependence of the gain suggests that *efficient tuning*<sup>7</sup> of the electrically excited  $\text{XeF}(\text{C} \rightarrow \text{A})$  laser may be possible throughout a large portion of the 450–510-nm range.

This investigation has shown that a combination of rare gases (Ar + Kr) and fluorine molecules ( $\text{NF}_3 + \text{F}_2$ ) permits synthesis of near optimum  $\text{XeF}(\text{C} \rightarrow \text{A})$  laser properties for which  $\text{XeF}(\text{C})$  can be produced efficiently (5%–10%) while transient absorption is minimized. The resulting optical extraction efficiency of 20%–25% is unique for an electrically

excited  $\text{XeF}(\text{C} \rightarrow \text{A})$  laser. Indeed, the values of laser energy density (2–3 J/l) and intrinsic efficiency (1%–2%) typical of the present electron beam excited  $\text{XeF}(\text{C} \rightarrow \text{A})$  laser medium are comparable to those of other blue-green lasers such as  $\text{HgBr}(\text{B} \rightarrow \text{X})$  and wavelength shifted  $\text{XeCl}(\text{B} \rightarrow \text{X})$  or  $\text{XeF}(\text{B} \rightarrow \text{X})$ . If comparable performance levels can be achieved using discharge excitation, the  $\text{XeF}(\text{C} \rightarrow \text{A})$  laser may become a competitive, tunable optical source for the blue-green region of the spectrum. Additionally, it is likely that mixture synthesis of the type employed in this investigation will find application as a means to improve the performance of other laser systems.<sup>8</sup>

It is a pleasure to acknowledge the contributions to this work of our colleagues: Dr. Y. Nachshon of The Technion, Dr. G. Marowsky of the Max-Planck Institut für Biophysikalische Chemie, and Mr. F. Emmert of the University of Würzburg. This work was supported in part by the Office of Naval Research, the National Science Foundation, and the Robert A. Welch Foundation.

<sup>1</sup>Y. Nachshon, F. K. Tittel, W. L. Wilson, Jr., and W. L. Nighan, *J. Appl. Phys.* **56**, 36 (1984).

<sup>2</sup>W. L. Nighan, Y. Nachshon, F. K. Tittel, and W. L. Wilson, Jr., *Appl. Phys. Lett.* **42**, 1006 (1983).

<sup>3</sup>With an Ar pressure of 6.5 atm the addition of Kr up to pressures of  $\sim 0.3$  atm results in an insignificant increase in *e*-beam energy deposition. In order to account for the effect of Kr at higher pressures, the Ar partial pressure was reduced so as to maintain a total pressure of 6.5 atm. This approximation to constant energy deposition becomes relatively poor for Kr pressures  $\geq 1.0$  atm since the *e*-beam stopping power of Kr is about twice that of Ar. However, our experiments show that, for Kr pressures above  $\sim 2.0$  atm, the maximum attainable laser energy ( $< 1.0$  J/l) for an optimized mixture is relatively insensitive to either the partial pressures of various rare gas buffer species, the total pressure, or the energy deposited. See text.

<sup>4</sup>H. C. Brashears and D. W. Setser, *J. Chem. Phys.* **76**, 4932 (1982).

<sup>5</sup>The rate coefficient for quenching of  $\text{Kr}_2\text{F}$  by Xe has been measured and is found to be approximately 2.5 times larger than the corresponding  $\text{Ar}_2\text{F}$  reaction. These results will be published elsewhere.

<sup>6</sup>J. D. Campbell, C. H. Fisher, and R. E. Center, *Appl. Phys. Lett.* **37**, 348 (1980). These investigators found that use of Kr instead of Ar as an  $\text{XeF}(\text{C} \rightarrow \text{A})$  laser buffer resulted in improved performance, but their experimental conditions were very different than those of the present work.

<sup>7</sup>J. Liegel, F. K. Tittel, W. L. Wilson, Jr., and G. Marowsky, *Appl. Phys. Lett.* **39**, 369 (1981); C. H. Fisher, R. E. Center, G. J. Mullaney, and J. P. McDaniel, *Appl. Phys. Lett.* **35**, 901 (1979); W. K. Bischel, D. J. Eckstrom, H. C. Walker, Jr., and R. A. Tilton, *J. Appl. Phys.* **52**, 4429 (1981).

<sup>8</sup>W. Walter, H. Langhoff, and R. Sauerbrey, *Appl. Phys. B* **34** (1984).

# Optimization of electrically excited XeF( $C \rightarrow A$ ) laser performance

W. L. Nighan

United Technologies Research Center, East Hartford, Connecticut 06108

Y. Nachshon, F. K. Tittel, and W. L. Wilson, Jr.

Electrical Engineering Department, Rice University, Houston, Texas 77251

(Received 28 January 1983; accepted for publication 28 March 1983)

Significantly improved output power and spectral characteristics have been obtained for an electron beam-pumped XeF( $C \rightarrow A$ ) laser by selective tailoring of kinetic processes. Using a high pressure Ar-Xe mixture containing both NF<sub>3</sub> and F<sub>2</sub> in combination, a laser pulse energy density of 0.1 J/l was obtained corresponding to an electrical-optical conversion efficiency of approximately 0.1%. Modeling of kinetic processes and analysis of laser spectral output confirm that the improved laser efficiency is primarily a consequence of reduced absorption by Xe-related excited species.

PACS numbers: 42.55.Fn, 42.60.By

With broadband fluorescence spanning the 400–550-nm range, the XeF( $C \rightarrow A$ ) excimer transition has potential for the development of efficient, tunable lasers in the blue-green region of the spectrum. Laser oscillation near 480 nm has been reported by investigators using electron beam excitation<sup>1,2</sup> or discharge excitation<sup>3,4</sup> of mixtures containing Xe and a fluorine donor such as NF<sub>3</sub> or F<sub>2</sub> in a background gas at several atm pressure. Additionally, laser oscillation based on photolytic pumping of a gas containing XeF<sub>2</sub> has been demonstrated.<sup>5–7</sup> Although the XeF( $C$ ) excimer can be formed efficiently under the conditions typical of these experiments, the large ( $\sim 70$  nm)  $C \rightarrow A$  bandwidth and relatively long  $C$ -state lifetime ( $\sim 100$  ns) result in a cross section for stimulated emission<sup>6</sup> that, at  $\sim 10^{-17}$  cm<sup>2</sup>, is more than an order of magnitude smaller than that of the 351-nm  $B \rightarrow X$  laser transition. Thus, the development of adequate gain on the  $C \rightarrow A$  transition requires very intense pumping, a circumstance that usually results in high concentrations of electrons and of excited and ionized species when electrical excitation is used. The electrons tend to mix the closely spaced ( $\sim 0.1$  eV)  $B$  and  $C$  states,<sup>8</sup> an effect strongly favoring UV laser oscillation at the expense of the visible  $C \rightarrow A$  transition. More importantly, certain excited and ionized species typical of the laser medium absorb at the laser wavelength. To date, these two factors combined have limited the efficiency of the electrically excited XeF( $C \rightarrow A$ ) laser to levels much less than 0.1%. Photolytic pumping of XeF<sub>2</sub>-containing mixtures has been shown to minimize these effects, but at the expense of a significant increase in system complexity.<sup>7</sup> In this letter we report the results of an investigation directed toward tailoring kinetic processes in electrically excited XeF( $C \rightarrow A$ ) laser mixtures in such a way as to overcome the aforementioned problems.

Most previous investigations have used NF<sub>3</sub> as the source of fluorine in the XeF( $C \rightarrow A$ ) laser. Nitrogen trifluoride has a high rate coefficient for dissociative electron attachment for electron energies of a few eV. The F<sup>-</sup> resulting from this reaction recombines rapidly with Xe<sup>+</sup> yielding XeF( $B, C$ ).<sup>9</sup> However, the rate coefficients for NF<sub>3</sub> quenching of Xe\*, Xe<sub>2</sub><sup>+</sup>, and similar species are relatively small ( $\sim 10^{-10}$  cm<sup>3</sup> s<sup>-1</sup>) for a halogenated molecule,<sup>10</sup> with the

result that the concentrations of absorbing species reach very high levels when NF<sub>3</sub> is used under conditions of intense electrical excitation. Indeed, in all cases with NF<sub>3</sub> as the F donor,<sup>1–3</sup> the  $C \rightarrow A$  laser spectrum has been found to be severely structured, and the dominant absorption features readily identified with known transitions between atomic Xe-excited states.<sup>11,12</sup> In contrast, F<sub>2</sub> has an attachment coefficient that is much smaller than that of NF<sub>3</sub> for average electron energy above one eV, and a quenching coefficient for absorbers such as Xe\* that is typically an order of magnitude larger.<sup>10,13</sup> This suggests that use of NF<sub>3</sub> and F<sub>2</sub> together in electrically excited lasers may result in improved laser performance by maintaining the concentrations of both the electrons and excited species at acceptably low levels.

Presented in Fig. 1 are the rate coefficients for dissociative attachment of NF<sub>3</sub> and F<sub>2</sub> as a function of electron mean energy<sup>14</sup>; F<sup>-</sup> is the negative ion produced in both cases. Also shown is the effective attachment coefficient resulting from combination of the two species in equal proportions. Clearly the attachment coefficient of such a mixture is very much higher than that of either NF<sub>3</sub> or F<sub>2</sub> alone. In addition, for such a mixture, the effective rate coefficient for quenching of potential absorbers is even higher than that of F<sub>2</sub> alone due to the contribution of NF<sub>3</sub>. That F<sub>2</sub> quenching of XeF\* is also much higher than that of NF<sub>3</sub> (Ref. 15) tends to be offset

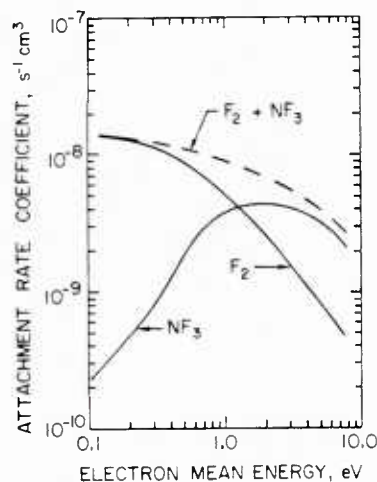


FIG. 1. Electron attachment coefficients for NF<sub>3</sub>, F<sub>2</sub>, and NF<sub>3</sub> + F<sub>2</sub> as a function of the electron mean energy [adapted from Chantray (Ref. 14)].

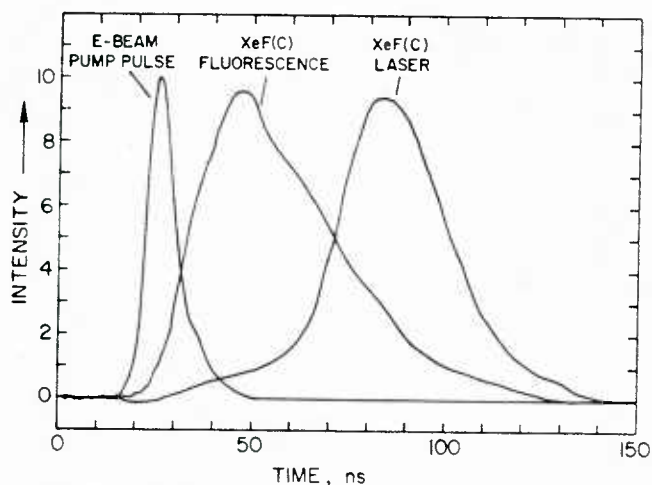


FIG. 2. Normalized temporal characteristics of the  $e$ -beam excitation pulse and  $\text{XeF}(\text{C} \rightarrow \text{A})$  fluorescence and laser output for a mixture of 6 atm Ar, 16 Torr Xe, 8 Torr  $\text{NF}_3$ , and 8 Torr  $\text{F}_2$ .

since the product of reactive quenching of  $\text{Xe}^*$  by  $\text{F}_2$  is  $\text{XeF}^*$ .<sup>13</sup> Indeed, an analysis of kinetic processes for conditions typical of  $e$ -beam excitation<sup>11</sup> indicated that in mixtures containing approximately equal concentrations of  $\text{NF}_3$  and  $\text{F}_2$ , the  $\text{XeF}^*$  population would be essentially unchanged by the presence of  $\text{F}_2$ , but that the concentrations of excited Xe atomic and molecular states would be reduced significantly.

In order to evaluate the *two-halogen* concept, mixtures of high-purity gases were transversely pumped by a 10-ns full width at half-maximum electron beam pulse.<sup>11,12</sup> The maximum beam energy was 1 MeV and the current density on the optical axis was typically  $100 \text{ A/cm}^2$ . A stable, intra-cell optical resonator was used consisting of a mirror having a radius of curvature of 1 m ( $R > 99.6\%$ ) and a flat output mirror having a reflectivity of 95% between 480 and 520 nm. The active region was the cylindrical volume defined by the mirror size and spacing, 1.9 cm in diameter and 10 cm long, as confirmed by photographs of the near-field laser output.

The optical emission from the reaction cell was monitored by a fast, calibrated vacuum photodiode (ITT F4000S5). Color glass and interference filters were used to observe only the emission from the  $\text{XeF}(\text{C} \rightarrow \text{A})$  transition. The photodiode signals were recorded by a Tektronix R7912

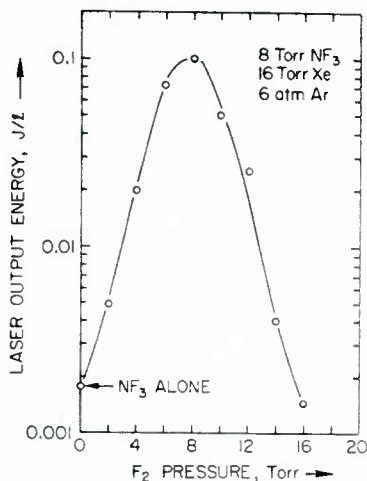


FIG. 3.  $\text{XeF}(\text{C} \rightarrow \text{A})$  laser energy density as a function of  $\text{F}_2$  pressure for a mixture containing 6 atm Ar, 16 Torr Xe, and 8 Torr  $\text{NF}_3$ .

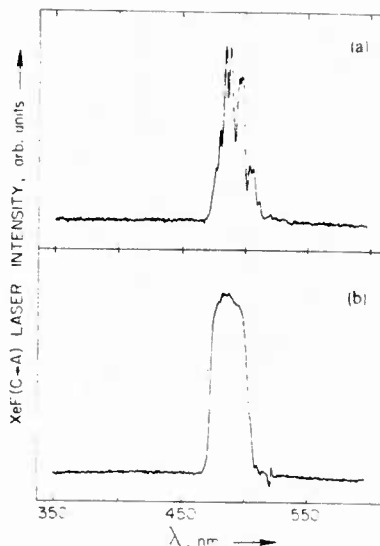


FIG. 4.  $\text{XeF}(\text{C} \rightarrow \text{A})$  laser spectra for a mixture of (a) 8 Torr  $\text{NF}_3$ , 16 Torr Xe, and 6 atm Ar; and (b) for the same mixture with 8 Torr  $\text{F}_2$  added.

Transient Digitizer. A 0.25-m Jarrel-Ash spectrometer in conjunction with an OMA1 optical multichannel analyzer was used to observe the temporally integrated emission spectra with a resolution of 1 nm.

Typical gas mixtures consisted of 6 atm Ar, 16 Torr Xe, and varying amounts of  $\text{NF}_3$  and  $\text{F}_2$ , individually or in combination. The variations of the  $\text{XeF}(\text{C} \rightarrow \text{A})$  fluorescence and laser output power for several mixtures were studied in detail. Peak laser emission, centered at 480 nm, occurred  $\sim 35$  ns after the  $\text{C} \rightarrow \text{A}$  fluorescence peak as shown in Fig. 2. The time-integrated laser output was found to increase from the 0.002-j/l level typical of our previous studies<sup>1,11</sup> using  $\text{NF}_3$  as the halogen donor, to 0.03 j/l using an optimum 8 Torr  $\text{F}_2$  in place of  $\text{NF}_3$ . Moreover, as shown in Fig. 3, an additional increase in laser output to 0.1 j/l was obtained for a mixture containing 8 Torr  $\text{F}_2$  and 8 Torr  $\text{NF}_3$ . Based on an estimate of  $e$ -beam energy deposited in the active volume ( $\sim 28 \text{ cm}^3$ ), a laser output of 0.1 j/l corresponds to an intrinsic efficiency of approximately 0.1%.

The absorption characteristics of the mixture were profoundly altered by the presence of  $\text{F}_2$ . Figure 4 shows measured laser spectra for mixtures containing optimum amounts of  $\text{NF}_3$ , and of  $\text{NF}_3$  and  $\text{F}_2$  in combination. The distinct absorption lines that appear in the  $\text{NF}_3$  laser spectrum of Fig. 4(a), principally due to transitions between Xe-excited states, vanish with  $\text{F}_2$  added to the mixture [Fig. 4(b)]. For the latter circumstances our calculations show that the concentrations of Xe-metastable atoms, higher excited states of Xe, and  $\text{Xe}_2^*$  dimers are reduced by approximately an order of magnitude. Thus, the nearly two orders-of-magnitude increase in laser power and efficiency is due primarily to a reduction of both atomic and molecular absorption by Xe-related excited species. Laser spectra typical of Fig. 4(b) are the first essentially absorption-free spectra ever reported for electrically excited  $\text{XeF}(\text{C} \rightarrow \text{A})$  laser media.

The results of this investigation demonstrate that by selective tailoring of kinetic processes in electrically excited  $\text{XeF}(\text{C} \rightarrow \text{A})$  laser mixtures, the concentrations of electrons

and of absorbing species can be maintained at levels compatible with efficient laser oscillation. Although the observed laser efficiency has been increased significantly from prior levels to a value of about 0.1%, our calculations indicate that the  $\text{XeF}(C)$  formation efficiency is in the 5–10% range for the conditions of this experiment, implying that the optical extraction efficiency is still only a few percent. This suggests that by optimization of the optical cavity and/or by laser pulse injection, operation of electrically excited  $\text{XeF}(C \rightarrow A)$  lasers with output energies of 1 J/l at efficiency levels on the order of one percent or more is a distinct possibility.

This work was supported in part by the Office of Naval Research, the National Science Foundation, and the Robert A. Welch Foundation.

<sup>1</sup>W. E. Ernst and F. K. Tittel, *Appl. Phys. Lett.* **35**, 36 (1979).

<sup>2</sup>J. D. Campbell, C. H. Fisher, and R. E. Center, *Appl. Phys. Lett.* **37**, 348 (1980).

<sup>3</sup>R. Burnham, *Appl. Phys. Lett.* **35**, 48 (1979).

<sup>4</sup>C. H. Fisher, R. E. Center, G. J. Mullaney, and J. P. McDaniel, *Appl. Phys. Lett.* **35**, 26 (1979).

<sup>5</sup>W. K. Bischel, H. H. Nakamo, D. J. Eckstrom, R. M. Hill, D. L. Huestis, and D. C. Lorents, *Appl. Phys. Lett.* **34**, 565 (1979).

<sup>6</sup>W. K. Bischel, D. J. Eckstrom, H. C. Walker, Jr., and R. A. Tilton, *J. Appl. Phys.* **52**, 4429 (1981).

<sup>7</sup>D. J. Eckstrom and H. C. Walker, *IEEE J. Quantum Electron.* **QE-18**, 176 (1982).

<sup>8</sup>W. Walter, R. Sauerbrey, F. K. Tittel, and W. L. Wilson, Jr., *Appl. Phys. Lett.* **41**, 387 (1982).

<sup>9</sup>M. R. Flannery and T. P. Tang, *Appl. Phys. Lett.* **32**, 327 (1978); **32**, 356 (1978).

<sup>10</sup>J. E. Velazco, J. H. Kolts, and D. W. Setser, *J. Chem. Phys.* **69**, 4357 (1978).

<sup>11</sup>F. K. Tittel, G. Marowsky, W. L. Wilson, Jr., and M. C. Smayling, *IEEE J. Quantum Electron.* **QE-17**, 2268 (1981).

<sup>12</sup>R. Sauerbrey, F. K. Tittel, W. L. Wilson, Jr., and W. L. Nighan, *IEEE J. Quantum Electron.* **QE-18**, 1336 (1982).

<sup>13</sup>J. E. Velazco, J. H. Kolts, and D. W. Setser, *J. Chem. Phys.* **65**, 3468 (1976).

<sup>14</sup>P. J. Chantry, in *Applied Atomic Collision Physics: Volume 3 Gas Lasers*, edited by H. S. W. Massey, E. W. McDaniel, and B. Bederson (Academic, New York, 1982), Chap. 2.

<sup>15</sup>H. C. Brashears and D. W. Setser, *J. Chem. Phys.* **76**, 4932 (1982).

II-B.  $\text{Xe}_2\text{Cl}$  Laser

- Effect of Nitrogen on  $\text{XeF}(\text{C}^+\text{A})$  and  $\text{Xe}_2\text{Cl}$  Laser Performance

# Effect of Nitrogen on $\text{XeF}(C \rightarrow A)$ and $\text{Xe}_2\text{Cl}$ Laser Performance

ROLAND SAUERBREY, FRANK K. TITTEL, SENIOR MEMBER, IEEE,  
WILLIAM L. WILSON, JR., MEMBER, IEEE, AND WILLIAM L. NIGHAN

**Abstract**—Experiments demonstrating the effect of nitrogen on electron-beam pumped  $\text{XeF}(C \rightarrow A)$  and  $\text{Xe}_2\text{Cl}$  laser performance are reported. The laser power of the  $\text{XeF}(C \rightarrow A)$  laser decreased with increasing nitrogen pressure, whereas the  $\text{Xe}_2\text{Cl}$  laser power increased by a factor of three at an optimum nitrogen pressure of 200 torr. Atomic absorptions in both laser spectra are decreased by the addition of nitrogen. The kinetic mechanisms leading to the observed behavior are discussed.

## I. INTRODUCTION

RECENTLY, broadband rare gas halide lasers utilizing either the  $C \rightarrow A$  transition of diatomic  $\text{XeF}^*$  [1]–[4] centered around 480 nm or trimers, such as  $\text{Xe}_2\text{Cl}$  at about 520 nm [5], have been developed. For the  $\text{XeF}(C \rightarrow A)$  laser, high power output and wavelength tunability have been demonstrated [6]–[8]. In the case of  $\text{Xe}_2\text{Cl}$ , gain measurements [9] and laser action [5] were reported.

Both excimer lasers suffer from absorptions by metastable xenon species [7], [10] which reduce their output power and impair their tuning capability. Recently, Eckstrom *et al.* [6], [7] demonstrated that these absorptions can be eliminated in the  $\text{XeF}(C \rightarrow A)$  laser spectrum when  $\text{XeF}_2$  is excited photochemically to form  $\text{XeF}^*$  and nitrogen is used instead of argon as the buffer gas. In this work the effects of adding nitrogen to  $\text{Ar/Xe/NF}_3$  and  $\text{Ar/Xe/CCl}_4$  mixtures on the electron beam-

pumped  $\text{XeF}(C \rightarrow A)$  and  $\text{Xe}_2\text{Cl}$  laser performance are reported. The fluorescence and laser output characteristics for both laser mixtures are described.

## II. EXPERIMENTAL SETUP

Details of the experimental arrangement were the same as those described in [10]. Mixtures of high purity gases were transversely pumped by an electron beam. In the case of  $\text{XeF}(C \rightarrow A)$ , 8 torr  $\text{NF}_3$ , 16 torr Xe, and varying amounts of nitrogen were mixed in 6 atm of argon buffer gas. Typical gas mixtures for  $\text{Xe}_2\text{Cl}$  were 1.5 torr  $\text{CCl}_4$ , 300 torr Xe, 6 atm Ar, and varying amounts of nitrogen. The maximum electron beam energy was 1 MeV and the pump pulse duration was 10 ns. The typical maximum electron beam current density, measured by a Faraday cup on the optical axis of the reaction cell was 200 A/cm<sup>2</sup>. An area of 10 cm × 2 cm was pumped by the e-beam.

The optical emission from the reaction cell was monitored by two fast vacuum photodiodes (ITT F 4000S). Color glass filters were used to reject the strong fluorescence from the  $\text{XeF}(B \rightarrow X)$  or  $\text{XeCl}(B \rightarrow X)$  transitions. The photodiode signals were recorded by a Tektronix R7912 Transient Digitizer. The rise time of the detection system was about 2 ns. A 0.25 m Jarrel Ash spectrometer in conjunction with an OMA 1 optical multi-channel analyzer was used to observe the temporally integrated emission spectra.

For the  $\text{XeF}(C \rightarrow A)$  laser experiments, mirrors with a reflectivity of 98 percent between 420 nm and 500 nm and radii of curvature of 1 and 10 m, respectively, were used. In the case of the  $\text{Xe}_2\text{Cl}$  laser, a mirror with a reflectivity of greater than 99.5 percent at 520 nm and a radius of 5 m and an output coupler with 98 percent reflectivity at 520 nm and a radius of curvature of 10 m were mounted inside the laser cell. In both cases the distance between the mirrors was 14 cm.

Manuscript received April 19, 1982. This work was supported by the Office of Naval Research, the National Science Foundation, the Robert A. Welch Foundation, and the Deutsche Forschungsgemeinschaft.

R. Sauerbrey is with the Physikalisches Institut der Universität Würzburg, Würzburg, Germany.

F. K. Tittel and W. L. Wilson are with the Department of Electrical Engineering and Rice Quantum Institute, Rice University, Houston, TX 77251.

W. L. Nighan is with the United Technologies Research Center, East Hartford, CT 06108.

## III. RESULTS

A.  $\text{XeF}(\text{C} \rightarrow \text{A})$ 

The variation of the time-integrated  $\text{XeF}(\text{C} \rightarrow \text{A})$  laser output power with the addition of small amounts of nitrogen was studied. When the entire spectral range of the laser pulse was considered, the laser power decreased monotonically with nitrogen up to 200 torr (Fig. 1). However, when only the short wavelength portion of the laser pulse was considered (453 to 470 nm), the laser power increased when up to 20 torr  $\text{N}_2$  was added. Thus, although the reflectivity of the laser mirrors decreased to about 97 percent at 460 nm, the output power from the  $\text{XeF}(\text{C} \rightarrow \text{A})$  laser increased by about 30 percent in this spectral region. The laser power decreased, however, when additional  $\text{N}_2$  was added to the  $\text{Ar/Xe/NF}_3$  laser mixture. Because the laser temporal pulse shape did not change with the addition of nitrogen, the peak laser power behaved the same as the laser energy. When pure nitrogen was used as a buffer gas, no laser action was observed for the pump power density available. Furthermore, the fluorescence from the  $\text{XeF}(\text{C})$  state around 480 nm decreased when the nitrogen pressure increased. This fluorescence decrease was less pronounced when higher amounts of xenon were used.

The laser spectrum changes considerably when  $\text{N}_2$  is added to the gas mixture. Fig. 2(a) shows a laser spectrum without nitrogen, while in Fig. 2(b), 50 torr  $\text{N}_2$  was added to a standard gas mixture. Besides the increase of the laser power in the short wavelength part of the spectrum, the absorption features in Fig. 2(b) are considerably richer than in Fig. 2(a).

Many of the absorptions in Fig. 2(a) have been attributed to absorption of metastable xenon species mainly into the Xe-Rydberg series. With no nitrogen present in the gas mixture and in agreement with earlier observations [7], [10], only absorptions from the  $\text{Xe}(6s^3P_0)$ -level and the  $\text{Xe}(6s^3P_1)$ -level (weaker) are observed. However, when nitrogen is added [Fig. 2(b)] absorption lines beyond the ionization limit of the  $3P_0 \rightarrow nf$  ( $\frac{3}{2}$ ) Rydberg series at 462.4 nm [11] can be observed because the laser spectrum now extends to shorter wavelengths. Most of these lines can be attributed to transitions from the  $\text{Xe}(6s^3P_2)$ -level into various  $\text{Xe}(6p)$  and  $\text{Xe}(7p)$ -states. Several absorption lines are probably due to xenon and argon ions [12].

The absorption valleys observed in the laser spectrum with nitrogen are not quite as deep as in the absence of nitrogen. However, no complete elimination of the absorption lines could be achieved as observed by Bischel *et al.* [7] with photolytic pumping.

B.  $\text{Xe}_2\text{Cl}$ 

The  $\text{Xe}_2\text{Cl}$  fluorescence and laser characteristics behaved quite differently compared with  $\text{XeF}(\text{C} \rightarrow \text{A})$ . First the fluorescence intensity was independent of the nitrogen admixture up to  $\text{N}_2$  pressures of 1 atm in a normal  $\text{Xe}_2\text{Cl}$  gas mixture. With an admixture of 50 torr nitrogen the  $\text{Xe}_2\text{Cl}$  fluorescent intensity as a function of  $\text{CCl}_4$  donor pressure was the same as in the absence of nitrogen. Furthermore, only very weak additional quenching of  $\text{Xe}_2\text{Cl}$  fluorescence by  $\text{N}_2$  was observed. The quenching rate constant for  $\text{Xe}_2\text{Cl}$  by  $\text{N}_2$  was determined to be  $(7 \pm 2) \times 10^{-14} \text{ cm}^3 \cdot \text{s}^{-1}$ .

Considerable improvement of the  $\text{Xe}_2\text{Cl}$  laser output was

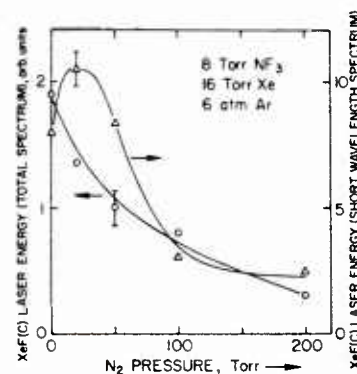


Fig. 1.  $\text{XeF}(\text{C} \rightarrow \text{A})$  laser energy as a function of the nitrogen admixture. The curve corresponding to the left vertical scale depicts the total laser energy. For the curve corresponding to the right vertical scale, the laser energy spectrum was integrated between 453 and 470 nm.

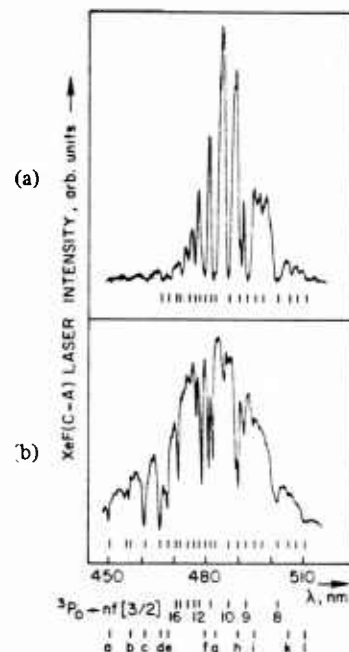


Fig. 2.  $\text{XeF}(\text{C} \rightarrow \text{A})$  laser spectra for a mixture of 8 torr  $\text{NF}_3$ , 16 torr  $\text{Xe}$ , and 6 atm  $\text{Ar}$  (a) and for the same mixture with 50 torr  $\text{N}_2$  added (b). Besides the  $3P_0 \rightarrow nf$  ( $\frac{3}{2}$ ), Rydberg series ( $n$  is the principal quantum number) the following absorption lines were identified:

- |   |   |   |
|---|---|---|
| a) $3P_0 \rightarrow 6p'$ [ $\frac{3}{2}$ ] | e) $3P_2 \rightarrow 6p'$ [ $\frac{3}{2}$ ] | i) $\text{Ar}^+$                            |
| b) $\text{Xe}^+$                            | f) $3P_2 \rightarrow 7p$ [ $\frac{3}{2}$ ]  | k) $3P_0 \rightarrow 11p$ [ $\frac{3}{2}$ ] |
| c) $\text{Xe}^+$                            | g) $3P_1 \rightarrow 7p$ [ $\frac{3}{2}$ ]  | l) $\text{Xe}^+$                            |
| d) $3P_2 \rightarrow 7p$ [ $\frac{5}{2}$ ]  | h) $3P_1 \rightarrow 6p'$ [ $\frac{3}{2}$ ] |   |

observed, however, when nitrogen was added to the gas mixture as shown in Fig. 3. A threefold increase of the laser power could be achieved by the addition of 200 torr of nitrogen. The decrease in laser power with increasing  $\text{N}_2$  pressure above 200 torr is consistent with earlier results where a failure of the  $\text{Xe}_2\text{Cl}$  laser using nitrogen as a buffer gas was reported [10]. In order to get reliable results, several shots with different gas mixtures were used for every experimental data point depicted in Fig. 3. The error bar gives the statistical error in the maximum of the curve.

As in the case of fluorescence, the  $\text{Xe}_2\text{Cl}$  laser intensity shows the same dependence on the  $\text{CCl}_4$  pressure with and without the admixture of 200 torr nitrogen. Intense UV-superradiance

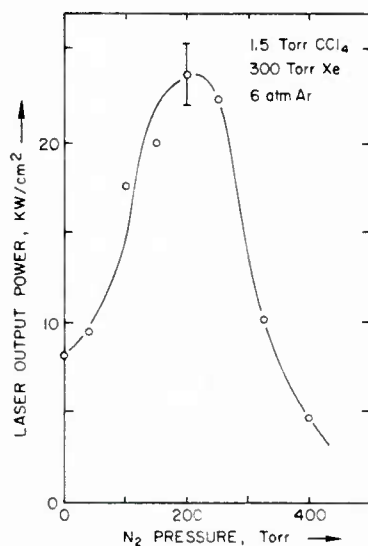


Fig. 3.  $\text{Xe}_2\text{Cl}$  laser power as a function of nitrogen pressure.

on the  $\text{XeCl}(B \rightarrow X)$ -transition at 308 nm which was observed for  $\text{CCl}_4$  pressures of more than 1.5 torr without nitrogen was strongly quenched by 50 torr of nitrogen. When neon was used as a buffer gas, no laser action could be observed. The addition of nitrogen did not alter this behavior.

The time-integrated laser spectrum of  $\text{Xe}_2\text{Cl}$  was strongly influenced by nitrogen (Fig. 4). Without nitrogen, the laser spectrum shows deep absorption valleys [Fig. 4(a)]. The most distinct absorption line is due to the transition between the  $\text{Xe}(6s^3P_0)$  and the  $\text{Xe}(7f \frac{3}{2})$  level at 516.4 nm [10]. When 200 torr nitrogen is added, this absorption line is eliminated completely [Fig. 4(b)]. The  $\text{Ar}^+$  absorption line at 514.5 nm is, however, not affected by nitrogen admixture. The absorption decrease of the xenon line is fully saturated at less than 100 torr of  $\text{N}_2$ . The laser power, however, increases up to 200 torr of nitrogen in the gas mixture.

#### IV. DISCUSSION

The primary role of  $\text{N}_2$  as an additive in the present  $\text{XeF}(\text{C})$  and  $\text{Xe}_2\text{Cl}$  laser experiments can be best understood by consideration of two factors: 1) the influence of  $\text{N}_2$  on the production of  $\text{XeF}$  and  $\text{Xe}_2\text{Cl}$  and 2) the effect of  $\text{N}_2$  on the production and loss of the primary absorbing species  $\text{Xe}^*$ ,  $\text{Xe}_2^*$ , and  $\text{Xe}_2^+$ . Evaluation of the loss of the neutral absorbers is relatively straightforward. Assuming that the measured [13] quenching coefficient of  $1.9 \times 10^{-11} \text{ s}^{-1} \text{ cm}^3$  for  $\text{Xe}(^3P_2)$  by  $\text{N}_2$  is also representative of the other  $\text{Xe}(6s)$  levels,  $\text{N}_2$  pressure of 100 torr results in a  $\text{Xe}^*$  quenching time constant of about 20 ns, a time characteristic of the observed lasing onset for the present conditions. Further, since the dimer  $\text{Xe}_2^+$  is produced from  $\text{Xe}^*$ , it follows that the presence of  $\text{N}_2$  will also result in a reduction of both the production and loss of this broadband absorber. For these reasons, the presence of  $\text{N}_2$  at the levels typical of this experiment is expected to reduce both discrete and broadband absorption resulting from  $\text{Xe}^*$  and  $\text{Xe}_2^+$  in both laser mixtures. However, a comparison of Figs. 2 and 4 reveals significant qualitative differences in the changes in absorption observed when  $\text{N}_2$  is added to  $\text{XeF}(\text{C})$  and  $\text{Xe}_2\text{Cl}$  mixtures. Additionally,  $\text{XeF}(\text{C})$  fluorescence and laser output was found to decrease in the presence

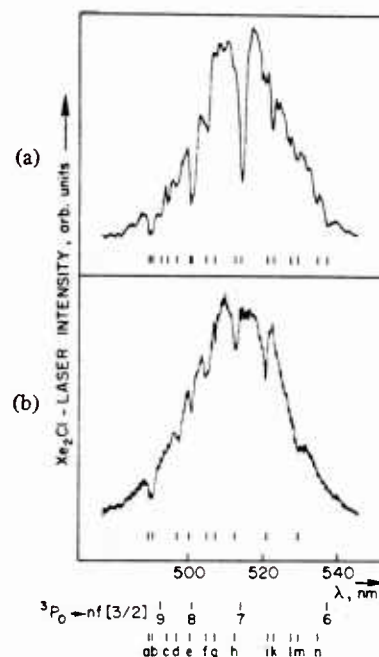


Fig. 4.  $\text{Xe}_2\text{Cl}$  laser spectra for a mixture of 1.5 torr  $\text{CCl}_4$ , 300 torr  $\text{Xe}$ , and 6 atm  $\text{Ar}$  (a) and for the same mixture with 200 torr  $\text{N}_2$  added (b). Besides the  $^3P_0 \rightarrow nf \frac{3}{2}$ , Rydberg series of  $\text{Xe}^*$  the following absorption lines have been identified [12]:

- |  |  |   |
|--|--|---|
| a) $^3P_0 \rightarrow 13p \frac{1}{2}$ | f) $\text{Ar}^*$                       | l) $\text{Xe}^+$                              |
| b) $^3P_2 \rightarrow 7p \frac{5}{2}$  | g) $^3P_0 \rightarrow 11p \frac{3}{2}$ | m) $\text{Xe}^+$                              |
| c) $\text{Ar}^+$                       | h) $\text{Ar}^+$                       | n) $^3P_0 \rightarrow ^\circ 10d \frac{3}{2}$ |
| d) $^3P_0 \rightarrow 12p \frac{1}{2}$ | i) $\text{Ar}^+$                       |   |
| e) $\text{Ar}^+$                       | k) $\text{Xe}^+$                       |   |

of  $\text{N}_2$  while  $\text{Xe}_2\text{Cl}$  laser output increased although  $\text{Xe}_2\text{Cl}$  fluorescence remained relatively unaffected. These observations are best explained by considering the effect of  $\text{N}_2$  addition on charged particle loss processes in the two laser mixtures.

Fig. 5 shows the electron energy dependence of the rate coefficient for dissociative electron attachment [14] to  $\text{NF}_3$  and  $\text{CCl}_4$ . In the absence of  $\text{N}_2$  the electron mean energy for both the  $\text{XeF}$  and  $\text{Xe}_2\text{Cl}$  laser mixtures is expected to be in the 2-3 eV range, typical of  $e$ -beam excited rare gases [15]. This is a mean energy for which the attachment coefficients for  $\text{NF}_3$  and  $\text{CCl}_4$  are both very large and of comparable magnitude. Under these circumstances ion production by the  $e$ -beam is balanced almost entirely by ion-ion recombination in both laser mixtures. Modeling of the present experimental conditions shows that for a quasi-steady electron mean energy of about 2-3 eV during and slightly after the  $e$ -beam excitation pulse, the negative ions  $\text{F}^-$  and  $\text{Cl}^-$  resulting from  $\text{NF}_3$  and  $\text{CCl}_4$  dissociative attachment recombine with  $\text{Xe}^+$  and  $\text{Xe}_2^+$  to form  $\text{XeF}$  and  $\text{XeCl}$ , respectively, the latter being the precursor of  $\text{Xe}_2\text{Cl}$  [10]. Thus, in the absence of  $\text{N}_2$ , attachment is balanced by positive ion-negative ion recombination in both mixtures.

Upon addition of  $\text{N}_2$  to these laser mixtures at the 1-5 percent fractional concentration levels of this experiment, calculations show that the electron mean energy will be substantially lower (a few tenths of an eV) during and after the excitation pulse as a result of electron cooling due to  $\text{N}_2$  vibrational excitation. Examination of Fig. 5 shows that the effect of such a reduction in electron temperature on negative ion pro-

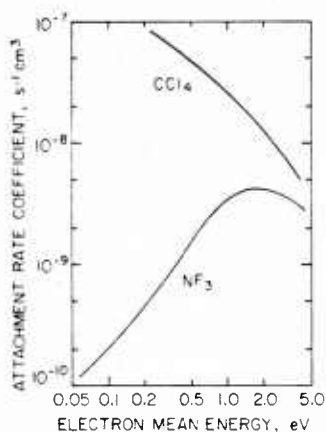


Fig. 5. Electron attachment coefficients for  $\text{NF}_3$  and  $\text{CCl}_4$  as a function of the mean electron energy (adapted from Chantry [14]).

duction (electron loss) is dramatically different in the  $\text{XeF}(\text{C})$  and  $\text{Xe}_2\text{Cl}$  mixtures containing  $\text{NF}_3$  and  $\text{CCl}_4$ , respectively. In the former, electron cooling from the few eV range to a few tenths of an eV results in an order-of-magnitude decrease in the rate coefficient for  $\text{NF}_3$  dissociative attachment with the result that  $\text{F}^-$  production and subsequently  $\text{XeF}$  formation decreases, a result consistent with our observation that  $\text{XeF}(\text{C} \rightarrow \text{A})$  fluorescence decreases as the  $\text{N}_2$  concentration increases. The quenching of  $\text{XeF}(\text{C})$  by  $\text{N}_2$  should be negligible even at nitrogen pressures of the order of 100 torr [16]. Additionally, in this case the decreased attachment results in a much larger electron density so that electron dissociative recombination with  $\text{Xe}_2^+$  dominates the charged particle loss, i.e., in the limit of a very low attachment coefficient ion, production by the  $e$ -beam is balanced by electron-ion recombination rather than by attachment. Since the product of  $e + \text{Xe}_2^+$  recombination [17] is  $\text{Xe}^*$ , although  $\text{N}_2$  serves to quench  $\text{Xe}^*$  and  $\text{Xe}_2^+$ , its presence in the  $\text{XeF}$  mixtures also contributes to an increase in the production of these absorbers. While the net effect of  $\text{N}_2$  on the density of absorbing species may be beneficial, when considered in light of the large decrease in  $\text{Xe}^+ - \text{F}^-$  recombination, addition of  $\text{N}_2$  results in a decrease in  $\text{XeF}(\text{C})$  laser output.

In marked contrast to the situation in  $\text{XeF}$  mixtures in which  $\text{NF}_3$  is the halogen donor, Fig. 5 shows that electron cooling in the  $\text{Xe}_2\text{Cl}$  mixture due to  $\text{N}_2$  addition results in an order-of-magnitude increase in the  $\text{CCl}_4$  attachment coefficient. Although the rate coefficient for  $\text{Cl}^-$  production increases sharply as the electron energy decreases, the net effect of this increase on the absolute magnitude of ion-ion recombination (and therefore  $\text{XeCl}$  production) is of second-order importance since for this mixture attachment is the dominant electron loss process throughout the entire 0.2–2.0 eV electron energy range of importance. Thus, for the conditions of the  $\text{Xe}_2\text{Cl}$  mixture with or without  $\text{N}_2$ ,  $\text{XeCl}$  formation by way of ion-ion recombination is sensibly constant, being determined by the magnitude of the  $e$ -beam excitation pulse. That is, so long as attachment is always the dominant electron loss process, the magnitude of the attachment coefficient itself is not particularly important. This interpretation is consistent with our observation that  $\text{Xe}_2\text{Cl}$  fluorescence is relatively insensitive to  $\text{N}_2$  addition over a broad range of  $\text{N}_2$  fractional concentration. Although an enhanced electron attachment coefficient does not affect the

$\text{XeCl}^*$  production, modeling of the present experimental conditions shows that  $\text{Xe}_2^+$ ,  $\text{Xe}^*$ , and  $\text{Xe}_2^+$  populations decrease with increasing electron attachment coefficient. Therefore, discrete and broadband absorption by these species are reduced by the addition of nitrogen, causing a significant increase in the  $\text{Xe}_2\text{Cl}$  laser output. These absorption processes are particularly important because recent calculations by Stevens and Krauss [19] show that the absorption of  $\text{Xe}_2\text{Cl}$  laser light by the  $\text{Xe}_2\text{Cl}$  molecule is negligibly small.

Clearly, high energy pulsed  $e$ -beam excitation of the high pressure mixtures typical of the  $\text{XeF}$  and  $\text{Xe}_2\text{Cl}$  lasers considered here results in a highly ionized, highly excited plasma medium of a type for which there is relatively little experience. Nonetheless, the differences in the magnitude and the electron energy dependence of the attachment coefficients in  $\text{NF}_3$  and  $\text{CCl}_4$  in response to the electron cooling certain to occur with  $\text{N}_2$  addition to rare gas mixtures are so large as to dominate over other known reactions. In conclusion, the present observations accompanying the addition of  $\text{N}_2$  to  $\text{XeF}(\text{C})$  and  $\text{Xe}_2\text{Cl}$  laser mixtures using  $\text{NF}_3$  and  $\text{CCl}_4$ , respectively, can be interpreted in a satisfactory manner on the basis of changes associated with the different attachment characteristics of the two laser mixtures and the quenching of absorbers by nitrogen.

#### REFERENCES

- [1] W. K. Bischel, H. H. Nakano, D. J. Eckstrom, R. M. Hill, D. L. Huestis, and D. C. Lorents, "New blue-green excimer laser in  $\text{XeF}$ ," *Appl. Phys. Lett.*, vol. 34, pp. 565–567, 1979.
- [2] C. H. Fisher, R. E. Center, G. J. Mullaney, and J. P. McDaniel, "A 490 nm  $\text{XeF}$  discharge laser," *Appl. Phys. Lett.*, vol. 35, pp. 26–28, 1979.
- [3] W. E. Ernst, F. K. Tittel, "A new electron-beam pumped  $\text{XeF}$  laser at 486 nm," *Appl. Phys. Lett.*, vol. 35, pp. 36–37, 1979.
- [4] R. Burnham, "A discharge pumped laser on the  $\text{C} \rightarrow \text{A}$  transition of  $\text{XeF}$ ," *Appl. Phys. Lett.*, vol. 35, pp. 48–49, 1979.
- [5] F. K. Tittel, W. L. Wilson, Jr., R. E. Stickel, G. Marowsky, and W. E. Ernst, "A triatomic  $\text{Xe}_2\text{Cl}$  excimer laser in the visible," *Appl. Phys. Lett.*, vol. 36, pp. 405–407, 1980.
- [6] D. J. Eckstrom and H. C. Walker, "Multijoule performance of the photolytically pumped  $\text{XeF}(\text{C} \rightarrow \text{A})$  laser," *IEEE J. Quantum Electron.*, vol. QE-18, pp. 176–181, Feb. 1982.
- [7] W. K. Bischel, D. J. Eckstrom, H. C. Walker, and R. A. Tilton, "Photolytically pumped  $\text{XeF}(\text{C} \rightarrow \text{A})$  laser studies," *J. Appl. Phys.*, vol. 52, pp. 4429–4434, 1981.
- [8] J. Liegel, F. K. Tittel, W. L. Wilson, Jr., and G. Marowsky, "Continuous broadband tuning of an electron beam pumped  $\text{XeF}(\text{C} \rightarrow \text{A})$  laser," *Appl. Phys. Lett.*, vol. 39, pp. 369–371, 1981.
- [9] K. Y. Tang, D. C. Lorents, and D. L. Huestis, "Gain measurement on the triatomic excimer  $\text{Xe}_2\text{Cl}$ ," *Appl. Phys. Lett.*, vol. 36, pp. 347–349, 1980.
- [10] F. K. Tittel, G. Marowsky, W. L. Wilson, Jr., and M. C. Smayling, "Electron beam pumped broadband diatomic and triatomic excimer lasers," *IEEE J. Quantum Electron.*, vol. QE-17, pp. 2268–2281, Dec. 1981.
- [11] R. F. Stebbings, C. J. Latimer, W. P. West, F. B. Dunning, and T. B. Cook, *Phys. Rev. A*, vol. 12, pp. 1453–1458, 1975.
- [12] A. R. Stigamow and N. S. Svenskii, *Tables of Spectral Lines*. New York: Plenum, 1968.
- [13] J. E. Velasco, J. H. Kolts, and D. W. Setser, "Rate constants and quenching mechanisms for the metastable states of argon, krypton, and xenon," *J. Chem. Phys.*, vol. 69, pp. 4357–4373, 1978.
- [14] P. J. Chantry, "Negative ion formation in gas lasers," *Applied Atomic Collision Physics: Gas Lasers*, H. S. W. Massey, E. W. McDaniel, and B. Bederson, Eds. New York: Academic, 1982, pp. 35–71.
- [15] C. J. Elliott and A. E. Greene, "Electron energy distributions in  $e$ -beam generated  $\text{Xe}$  and  $\text{Ar}$  plasmas," *J. Appl. Phys.*, vol. 47, pp. 2946–2953, 1976.
- [16] H. C. Brashears and D. W. Setser, "Transfer and quenching rate constants for  $\text{XeF}(\text{B})$  and  $\text{XeF}(\text{C})$  state in low vibrational levels," *J. Chem. Phys.*, to be published.

- [17] Y. J. Shin, M. A. Biondi, and D. P. Sipler, "Dissociative recombination in Xe: Variation of the total rate coefficient and excited state production with electron temperature," *Phys. Rev. A*, vol. 15, pp. 484-498, 1977. For conditions typical of the present XeF\*(C) and Xe<sub>2</sub>Cl\* laser experiments, the ion Xe<sup>+</sup> is produced on a very short time scale by charge transfer from the argon ions produced initially by the e-beam.
- [18] H. H. Michels, R. H. Hobbes, and L. A. Wright, "Electron structure of the noble gas dimer ions II, theoretical absorption spectrum for the A<sup>2</sup>σ<sub>1/2μ</sub><sup>+</sup> - D<sup>2</sup>σ<sub>1/2g</sub><sup>+</sup> system," *J. Chem. Phys.*, vol. 71, pp. 5053-5062, 1979.
- [19] W. J. Stevens and M. Krauss, "Absorption in the triatomic excimer Xe<sub>2</sub>Cl," *Appl. Phys. Lett.*, to be published.

III. RARE GAS-HALIDE AND MERCURY-HALIDE LASERS

III-A. HgBr(B+X) Laser

- Kinetic Processes in the HgBr(B+X)/HgBr<sub>2</sub> Dissociation Laser
- Efficient HgBr(B+X) Laser Oscillation in Electron-Beam-Controlled-Discharge-Excited Xe/HgBr<sub>2</sub> Mixtures
- Kinetic Processes in the Electrically Excited Mercuric-Bromide Dissociation Laser
- Low Energy Electron Collision Phenomena in HgBr<sub>2</sub>

# Kinetic processes in the $\text{HgBr}(B \rightarrow X)/\text{HgBr}_2$ dissociation laser

William L. Nighan and Robert T. Brown

United Technologies Research Center, East Hartford, Connecticut 06108

(Received 17 May 1982; accepted for publication 7 July 1982)

Results are reported of an investigation of fundamental kinetic processes influencing discharge and laser properties typical of the 502-nm  $\text{HgBr}(B \rightarrow X)/\text{HgBr}_2$  dissociation laser. Specific attention is focused on conditions representative of electron-beam-controlled discharges. Experimental results and corresponding analysis and interpretation are presented for several laser mixtures, focusing particularly on the factors affecting discharge characteristics and  $\text{HgBr}(B)$  formation. A set of *phenomenological* electron- $\text{HgBr}_2$  cross sections inferred on the basis of analysis of experimental observations is presented, along with a discussion of the effect of electron-electron collisions on medium properties at the level of fractional ionization typical of the  $\text{HgBr}(B)/\text{HgBr}_2$  laser.

PACS numbers: 42.55.Hq, 52.80. — s, 41.80.Dd

## I. INTRODUCTION

The blue/green 502-nm  $\text{HgBr}(B \rightarrow X)$  laser is a leading candidate for applications requiring an efficient ( $> 1\%$ ) visible laser capable of generating relatively high average power ( $> 100$  W).<sup>1</sup> Efficient  $\text{HgBr}(B \rightarrow X)$  oscillation has been demonstrated recently<sup>2,3</sup> using a variety of discharge-excited mixtures containing 0.2–1.0% mercuric bromide  $\text{HgBr}_2$ . Under such conditions the excited mercurous bromide molecule  $\text{HgBr}(B)$  is produced as the result of dissociative excitation of  $\text{HgBr}_2$  by either electron impact or reactive quenching of certain excited atoms or molecules.<sup>4</sup>

In this paper we report the results of an investigation of fundamental kinetic processes influencing both discharge and laser properties typical of the  $\text{HgBr}(B)/\text{HgBr}_2$  system. Specific attention is focused on conditions representative of electron-beam-controlled discharges, an excitation method capable of generating high pressure, volume-dominated glow discharges that are quasisteady. Because of these characteristics, such discharges can provide a rich source of fundamental information difficult to obtain by other means.<sup>4</sup> Section II presents a description of the electron-beam-controlled discharge experiment and related diagnostic apparatus, along with examples of representative current, voltage, and fluorescence characteristics. A detailed discussion of our analysis of these characteristics is presented in Sec. III. Therein attention is focused on charged-particle production and loss processes and their influence on the dependence of discharge current density on variations in applied electric field. The factors affecting  $\text{HgBr}(B)$  formation are treated in Sec. IV, wherein the effects of gas-mixture variation are analyzed and a comparison of measured and computed values of 502 nm gain discussed. This investigation and a related study<sup>5</sup> have shown that virtually all aspects of electron- $\text{HgBr}_2$  collision phenomena affect laser/discharge performance. The discussion of Sec. V deals with this aspect of the subject, focusing particularly on electron- $\text{HgBr}_2$  collision processes such as vibrational and electronic excitation. Therein a set of phenomenological electron- $\text{HgBr}_2$  cross sections inferred on the basis of analysis of experimental observations is presented, along with a discussion of the role of electron-electron collisions for conditions typical of  $\text{HgBr}(B)/\text{HgBr}_2$  laser discharges.

## II. ELECTRON-BEAM-CONTROLLED DISCHARGE EXPERIMENTS

### A. Discharge cell

The present experiments were carried out using an *e*-beam-controlled discharge having a  $1.5 \times 1.7 \times 50$  cm active volume, enclosed within a heated chamber as shown in Fig. 1. Because of the reactive nature of  $\text{HgBr}_2$ , proper cell design was critical in order to maintain purity of the gas mixtures and to minimize surface reactions. In the cell used in this investigation, the only materials in contact with the  $\text{HgBr}_2$  containing gas mixture were type 316 stainless steel, Pyrex, Viton, and dielectric coated mirrors.  $\text{HgBr}_2$  crystals were contained in a Pyrex reservoir positioned in a sidearm as shown in the figure. The main cell structure was maintained at a temperature of 195 °C; variation of the reservoir temperature in the 150–190 °C range provided a corresponding variation in  $\text{HgBr}_2$  partial pressure from approximately 1 to 12 Torr.<sup>6</sup> The electron-beam system and discharge driver are described elsewhere.<sup>2</sup>

The discharge voltage was provided by a low-inductance capacitor of a size so as to produce only a very slight decrease in voltage (i.e.,  $E/n$ ) during the pulse. Additionally,

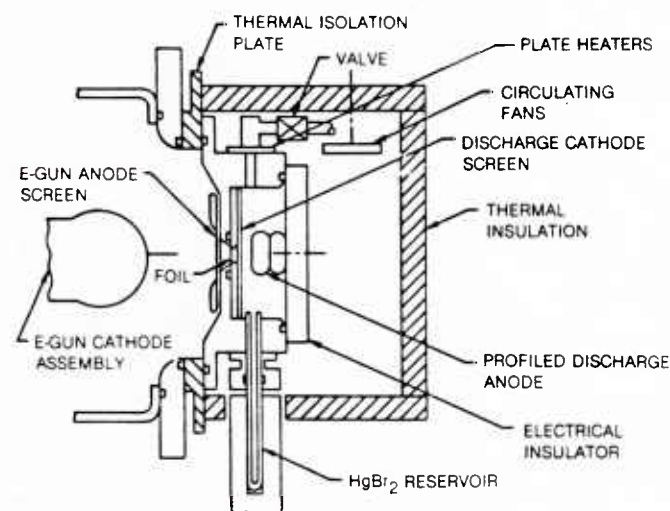


FIG. 1. Schematic illustration of the heated  $\text{HgBr}(B)/\text{HgBr}_2$  *e*-beam-controlled laser discharge cell.

the electron beam was initiated 200 nsec prior to the onset of the discharge voltage and provided a constant  $e$ -beam current density of  $0.5 \text{ A cm}^{-2}$  for  $1.2 \mu\text{s}$ . With this arrangement it was possible to produce a highly uniform plasma medium that was essentially quasisteady, a circumstance greatly facilitating detailed comparison of experimental observations with the predictions of our discharge/laser kinetics model.

### 1. $V$ - $I$ characteristics

In the work reported here, all measurements were carried out with a reservoir temperature of  $170^\circ\text{C}$  at a total cell pressure of 2.0 atm. Both neon and argon were used as buffers, with and without the addition of 5–10% of an excitation transfer species such as  $\text{N}_2$  and/or Xe. In order to ensure true equilibrium between the  $\text{HgBr}_2$  density and the reservoir temperature, the desired  $\text{HgBr}_2$  density was established in the pre-evacuated cell prior to the admission of the buffer gas mixture. For each gas mixture, shots were made over a range of applied voltages, starting at a level below that for which any significant  $\text{HgBr}(B \rightarrow X)$  fluorescence was observed and proceeding to the point at which nearly instantaneous discharge instability occurred.

Presented in Fig. 2 are representative voltage, current, and fluorescence data for Ne containing 0.35%  $\text{HgBr}_2$ , corresponding to  $E/n$  values for which the fluorescence was relatively intense. For the lower  $E/n$  value a stable, uniform discharge could be maintained for  $1 \mu\text{s}$  until the  $e$  beam was terminated. However, as  $E/n$  was increased, the discharge and fluorescence terminated prematurely due to the occurrence of ionization instability.<sup>2,7</sup> This general behavior was found to be typical of all mixtures and conditions examined.

### B. Gain measurement

In order to obtain a quantitative relationship between the relative fluorescence and the  $\text{HgBr}(B)$  density, and to relate discharge current, voltage, and fluorescence to mea-

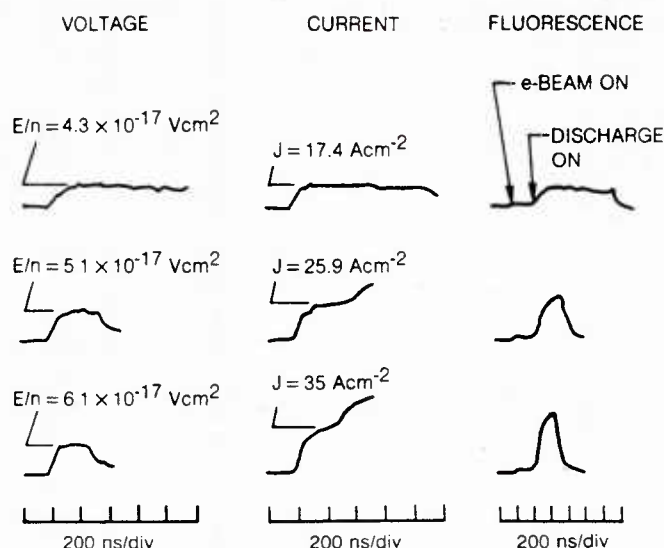


FIG. 2. Representative voltage, current, and  $\text{HgBr}(B \rightarrow X)$  fluorescence characteristics for an  $e$ -beam-controlled discharge excited Ne-0.35%  $\text{HgBr}_2$  mixture at a pressure of 2 atm and a cell temperature of  $190^\circ\text{C}$ . The  $e$ -beam current density, at  $0.5 \text{ A cm}^{-2}$ , was constant for  $1.2 \mu\text{s}$  and was initiated 200 ns prior to application of the discharge voltage.

sured laser performance, the arrangement shown in Fig. 3 was used to make small-signal gain measurements. A nitrogen-pumped dye laser (Molelectron model DL-14) was used in a standard two-beam configuration with the probe and reference pulse energies detected using pyroelectric joulemeters (Molelectron model J3). A photodetector was used to monitor the superimposed fluorescence and probe laser signals and to verify the temporal location of the probe pulse. Since the probe pulse was short ( $\sim 5 \text{ nsec}$ ) compared to the discharge duration, shot-to-shot measurements were used to determine the temporal variation of the gain during the discharge pulse. In the present study all small-signal gain data were obtained at  $502.2 \text{ nm}$  (i.e., at the wavelength exhibiting

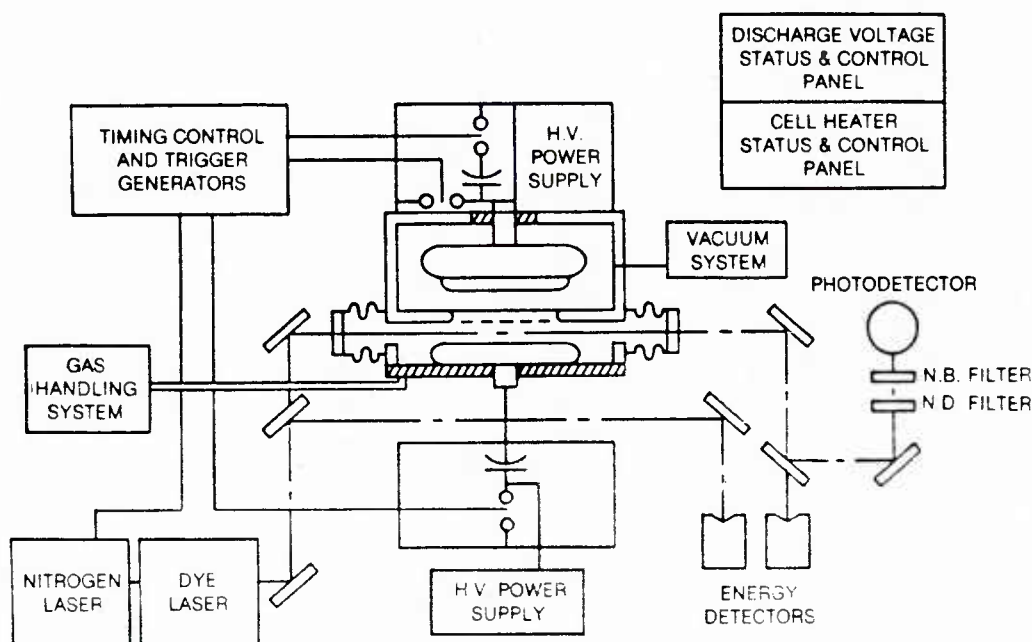


FIG. 3. Diagram of small-signal gain experiment and related apparatus.

strongest lasing when the discharge was operated with an optical cavity).

Detailed gain measurements were carried out for selected gas mixtures and discharge voltages. Qualitatively, the present studies yielded results in good agreement with those reported by other investigators<sup>5</sup> and showed that relative changes in measured small-signal gain correlated very closely with variations in relative fluorescence. On the basis of these findings, the fluorescence data were interpreted as relative small-signal gain, even for gas mixtures and voltage ranges for which gain measurements were not actually carried out.

### III. DISCHARGE KINETICS

#### A. Analysis of $V$ -variations

Although accurate measurement of discharge voltage and current is relatively straightforward for conditions typical of those presented in Fig. 2, quantitative computation of these properties is quite difficult, even though the  $e$ -beam-controlled discharge medium closely approximates a quasi-steady, spatially uniform medium. Accurate prediction of the variation of discharge current density  $J$  with  $E/n$  requires knowledge of the electron drift velocity and all important charged particle production and loss processes. Depending on mixture conditions, the drift velocity is very sensitive to low-energy electron-HgBr<sub>2</sub> collision processes, such as vibrational and electronic excitation, and to the effect of electron-electron collisions on the electron energy distribution function,<sup>7</sup> a topic to be discussed in Sec. V. Although charged-particle production is dominated by the  $e$ -beam source for low  $E/n$  values, direct and multistep ionization by low-energy discharge electrons invariably become important as  $E/n$  is increased, ultimately resulting in discharge instability. Both HgBr<sub>2</sub> dissociative attachment and electron-ion recombination are found to contribute to the loss of electrons for the conditions of interest.

##### 1. Computed drift velocity and attachment coefficient

Presented in Figs. 4 and 5 are electron drift velocities and attachment coefficients for the mixtures examined in this investigation, computed<sup>8</sup> using reported cross sections for Ne,<sup>9</sup> Xe,<sup>10</sup> N<sub>2</sub>,<sup>11</sup> and for HgBr<sub>2</sub>.<sup>5</sup> Clearly there are substantial mixture-to-mixture variations in the drift velocity over the 1–10 Td  $E/n$  range. Figure 5 indicates that the attachment coefficient is less sensitive to mixture variation, with the exception of mixtures containing N<sub>2</sub>. In the latter case, the resonance in the  $e$ -N<sub>2</sub> vibrational cross sections near 2.0 eV truncates the electron energy distribution,<sup>11</sup> so that there are very few electrons with energy above the 3.1 eV threshold for dissociative attachment.<sup>5</sup> Thus, for low  $E/n$  values, the HgBr<sub>2</sub> attachment coefficient is unusually low with N<sub>2</sub> in the mixture.

##### 2. $J$ vs $E/n$ variation

Measured and computed variations of discharge current density with  $E/n$  are presented in Figs. 6 and 7 for Ne and Ar containing 0.35% HgBr<sub>2</sub> and for Ne-0.35% HgBr<sub>2</sub> mixtures containing either 5% N<sub>2</sub> or 10% Xe. Both mea-

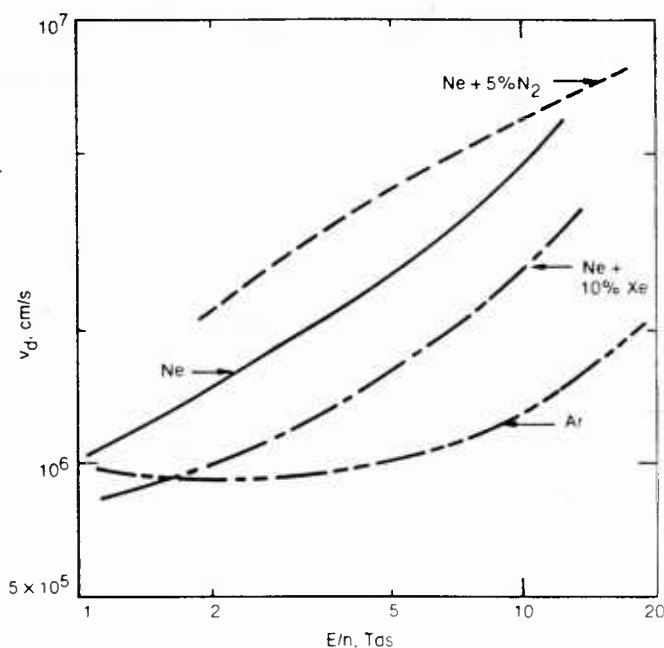


FIG. 4. Computed electron drift velocity for the indicated mixtures containing 0.35% HgBr<sub>2</sub>. The drift velocity (and the electron energy distribution function) was computed for a fractional ionization level of  $2 \times 10^{-6}$ , using the cross sections shown in Fig. 12 as discussed in Sec. V.

sured and computed values refer to a time 200 ns after application of the discharge voltage pulse. For these conditions the ratio of discharge power input to that of the  $e$ -beam ranges from about 2 to 20 for the Ne, Ar, and Ne + Xe-HgBr<sub>2</sub> mixtures, and from 20 to 60 for the Ne-N<sub>2</sub>-HgBr<sub>2</sub> mixture, reflecting the high current density and  $E/n$  values typical of the latter. Calculations show that, for the lowest  $E/n$  values in all four mixtures, the only ionization is pro-

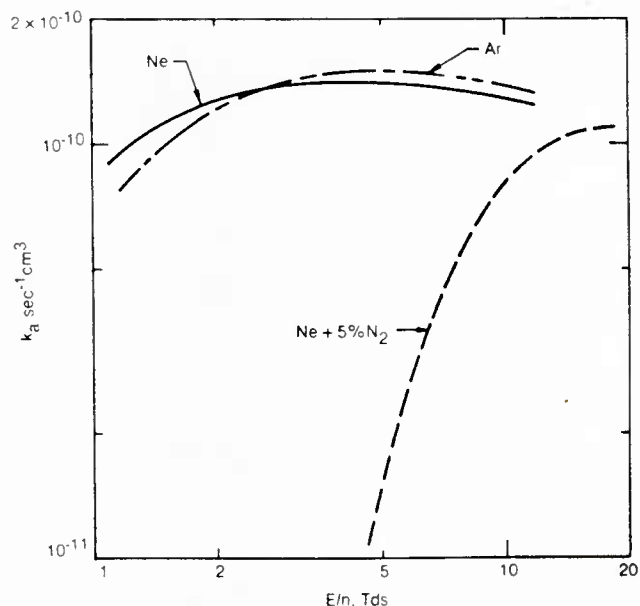


FIG. 5. Computed electron-HgBr<sub>2</sub> dissociative attachment coefficients for the conditions of Fig. 4. The attachment coefficient for the Ne-Xe-HgBr<sub>2</sub> mixture falls between the curves for the Ne and Ar mixtures and has been omitted for the sake of clarity.

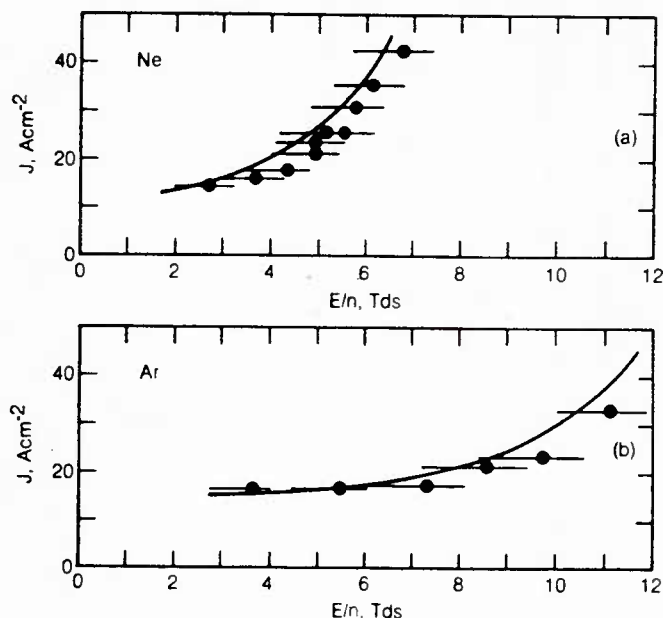


FIG. 6. Measured and computed discharge current density for (a) Ne and (b) Ar containing 0.35%  $\text{HgBr}_2$  at the cell conditions of Fig. 2. Because medium properties are particularly sensitive to variations in  $E/n$  the uncertainty in the measured values of this parameter is indicated.

vided by the electron beam either directly or by way of Penning ionization reactions. In mixtures not containing  $\text{N}_2$ , the principle electron-loss process is dissociative attachment, with electron-ion recombination representing between 25 and 50% of the total loss depending on specific conditions. Thus, for low  $E/n$  values the agreement between the measured and computed current density, along with mixture-to-mixture consistency, is indicative of the accuracy with which the electron drift velocity and attachment coefficients can be computed (Figs. 4 and 5).

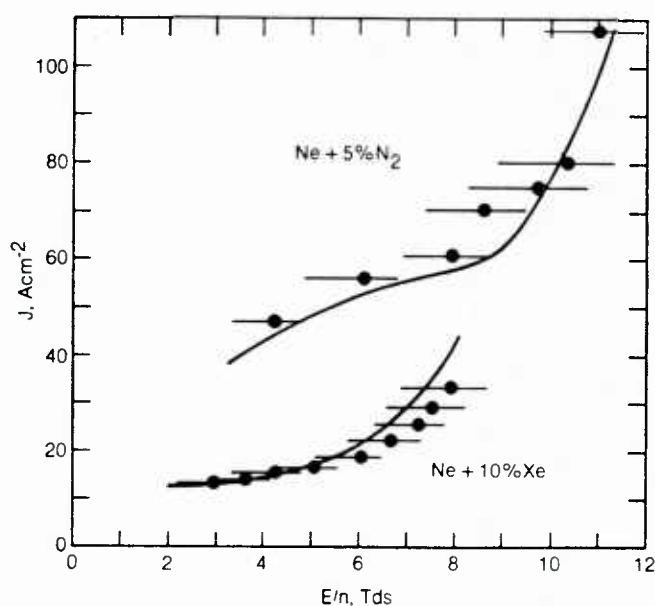


FIG. 7. Measured and computed discharge current density for a Ne-5%  $\text{N}_2$  mixture and a Ne-10% Xe mixture, both containing 0.35%  $\text{HgBr}_2$ , and cell conditions otherwise similar to those of Figs. 2 and 6.

Examination of Figs. 6 and 7 shows that the current density increases as  $E/n$  is increased for all mixtures, as expected. However, the data exhibit substantially different variations, primarily indicative of the dependence of the drift velocity on  $E/n$  (Fig. 4) and on the increasing importance of direct and multistep ionization at higher  $E/n$  values. For the Ar- $\text{HgBr}_2$  mixture and the Ne- $\text{HgBr}_2$  mixture containing Xe, the present calculations show that the sharp rise in the current density, ultimately resulting in discharge instability, is a consequence of multistep ionization of the metastable and higher excited states<sup>7</sup> of Ar and Xe, respectively. In contrast to this situation, direct electron-impact ionization of  $\text{HgBr}_2$  dominates in the Ne- $\text{HgBr}_2$  mixture with or without  $\text{N}_2$  present. Whether dominated by multistep or direct ionization, the calculated  $E/n$  for instability onset was found to be in satisfactory agreement with experimental observations for all mixtures examined.

### 3. Electron-ion recombination

Because attachment is not significant for low  $E/n$  values in the mixture containing  $\text{N}_2$ , the measured current density in this case provides a means for estimating an effective electron-recombination coefficient for  $\text{HgBr}_2$ -related ions. The present modeling of ion-species concentrations included the ions  $\text{Ne}^+$ ,  $\text{Ne}_2^+$ ,  $\text{Ar}^+$ ,  $\text{Ar}_2^+$ ,  $\text{N}_2^+$ ,  $\text{N}_4^+$ ,  $\text{Xe}^+$ ,  $\text{Xe}_2^+$ ,  $\text{HgBr}_2^+$ , and the product ions  $\text{HgBr}^+$ ,  $\text{Hg}^+$ , and  $\text{Br}^+$ . For the conditions of Figs. 6 and 7, calculations indicate that  $\text{HgBr}_2^+$  is usually dominant, followed by the sum of the indicated product ions. Satisfactory agreement between theory and experiment is obtained using a value of  $2 \pm 1 \times 10^{-7} \text{ s}^{-1} \text{ cm}^3$  for the electron-ion recombination coefficient for all  $\text{HgBr}_2$ -related ions. This value is probably representative of  $\text{HgBr}_2^+$ ,  $\text{HgBr}^+$ , and/or these ions clustered to  $\text{HgBr}_2$ ,<sup>12</sup> for average electron energy values in the 2–4 eV range.

### IV. $\text{HgBr}(B)$ FORMATION

A large number of  $\text{HgBr}_2^*$  states<sup>4,13</sup> can be produced either by direct electron impact or by  $\text{HgBr}_2$  reactive quenching of excited states of species such as Ne, Ar,  $\text{N}_2$ , and Xe. However, only the  $^3,1\Sigma_u^+$  state of  $\text{HgBr}_2$  predissociates to form  $\text{HgBr}(B)$ .<sup>13</sup> Further, available evidence indicates that this state can be collisionally produced in substantial quantity only by electrons and/or by the excited states of  $\text{N}_2$ <sup>14,15</sup> or Xe.<sup>14,16</sup>

Figure 8 illustrates the general sequence of events resulting in  $\text{HgBr}(B)$  formation in discharge excited lasers. The large Franck-Condon shift between the  $B$  and  $X$  states of  $\text{HgBr}$  is such that the laser transitions terminate on high vibrational levels of the  $X$  state. These levels are rapidly deactivated by collisions with the background gas,<sup>17</sup> thereby permitting efficient optical extraction. Following laser oscillation, the  $\text{HgBr}(X)$  state recombines with Br atoms to reform  $\text{HgBr}_2$ , the final step in a reaction sequence that appears to be nearly completely cyclic under carefully controlled conditions.

The laser/discharge medium produced using the  $e$ -beam-controlled discharge excitation technique is especially well suited for evaluation of the  $\text{HgBr}(B)$  production reactions illustrated in Fig. 8. In order to study both electron-

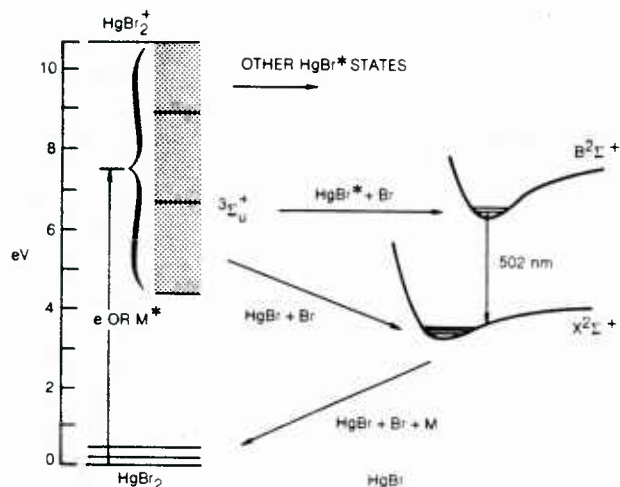


FIG. 8. Sequence diagram illustrating the dominant steps in  $\text{HgBr}(B)$  formation in the  $\text{HgBr}_2$  dissociation laser. Both electrons ( $e$ ) and certain excited species ( $M^*$ ) can excite the  $3^1\Sigma_u^+$  states of  $\text{HgBr}_2$  that predissociate to form  $\text{HgBr}(B)$ . In addition, many  $\text{HgBr}_2$  states are excited which do not yield  $\text{HgBr}(B)$  upon predissociation.

impact excitation and excitation transfer reactions,  $\text{HgBr}(B)$  fluorescence and gain were examined for several mixtures over a range of discharge conditions.

#### A. Ne and Ar- $\text{HgBr}_2$ mixtures

Both Ne and Ar have been used as the background gas in the present study and by other investigators as well.<sup>3</sup> Although rare gas metastable atoms and higher excited states are produced both by the electron beam and by low-energy electron collisions in such mixtures, reactive quenching of these species by  $\text{HgBr}_2$  results in little or no  $\text{HgBr}(B)$  formation.<sup>14,16</sup> In the present analysis  $\text{HgBr}_2$  quenching rate coefficients for the excited states of Ne and Ar have been taken to be  $2 \times 10^{-10}$  and  $3 \times 10^{-10} \text{ sec}^{-1} \text{ cm}^3$ , respectively. For  $\text{Ne}^*$  quenching, all the reaction products have been assumed to be ions, i.e., the products of Penning reactions, while for  $\text{Ar}^*$ , two-thirds of the reaction species have been assumed to be ions and one-third neutral fragments. While use of these rate coefficients and branching fractions has been found to be consistent with the observed  $I$ - $V$  characteristics, the agreement between the computed and measured values of current density (Fig. 6) is not unduly sensitive to the values chosen.

Figure 9 shows the measured and computed values of small signal gain in Ne and Ar containing 0.35%  $\text{HgBr}_2$ . Under these conditions, our analysis shows that  $\text{HgBr}(B)$  is produced as the result of direct electron-impact dissociative excitation of  $\text{HgBr}_2$ . The agreement between the computed and measured values of gain is satisfactory lending support to the electron- $\text{HgBr}_2$  cross sections used in the calculation, a topic to be discussed in Sec. V. For the higher  $E/n$  values, calculations show that the  $\text{HgBr}(B)$  formation efficiency for the Ne and Ar- $\text{HgBr}_2$  mixture conditions of Fig. 9 is in the 2.5–3.0% range.

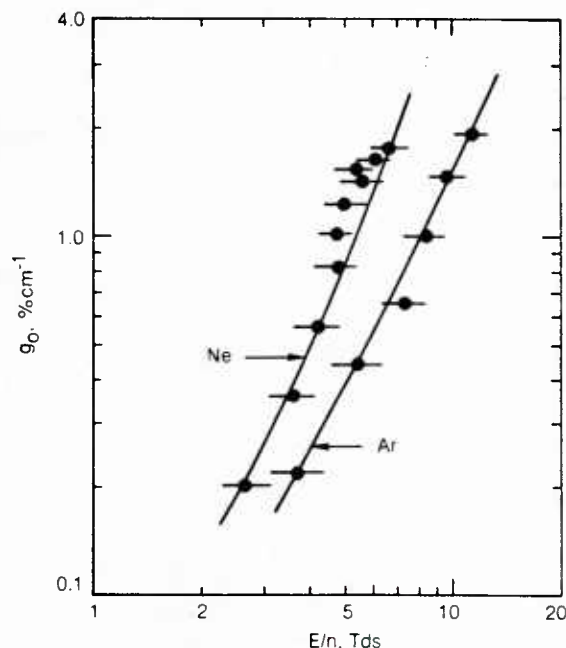


FIG. 9. Measured and computed small-signal gain for Ne and Ar containing 0.35%  $\text{HgBr}_2$  excited under the  $e$ -beam-controlled discharge conditions of Figs. 2 and 6.

#### 1. Ion recombination

Very weak fluorescence was observed with Ne and Ar mixtures and  $e$ -beam excitation alone (Fig. 2), most likely the result of  $\text{HgBr}_2^+$  recombination with electrons and/or  $\text{Br}^-$ . Analysis indicated that these reactions had comparable rates during the 200-ns period prior to initiation of the discharge. However, the  $\text{HgBr}_2^+ \cdot \text{Br}^-$  recombination reaction is not expected to produce the  $1,3\Sigma_u^+$  state and, in turn,  $\text{HgBr}(B)$ .<sup>13</sup> While electron-ion recombination is not state selective, this reaction may produce some higher lying  $\text{HgBr}_2^*$  states<sup>13</sup> which correlate with the  $B$  state of  $\text{HgBr}$ . Nonetheless, the magnitude of the  $e$ -beam-produced  $\text{HgBr}(B \rightarrow X)$  fluorescence observed in this investigation can be accounted for by assuming only a 10%  $B$  state branching fraction for electron- $\text{HgBr}_2^+$  recombination. Apparently, direct branching to  $\text{HgBr}(B)$  following recombination and cascade from higher lying  $\text{HgBr}$  states produced by recombination are both small.

#### B. Ne- $\text{N}_2$ - $\text{HgBr}_2$ mixtures

With  $\text{N}_2$  added to the Ne- $\text{HgBr}_2$  mixtures, discharge and laser properties are changed dramatically, primarily as a consequence of  $\text{N}_2$  vibrational and electronic excitation.<sup>11</sup> Of course, direct electron excitation of  $\text{HgBr}_2$  resulting in  $\text{HgBr}(B)$  still occurs, but calculations show that the magnitude of the rate coefficient for this reaction is reduced somewhat from its value in a Ne- $\text{HgBr}_2$  mixture. Offsetting this decrease are excitation transfer reactions involving  $\text{N}_2(4^3\Sigma_u^+)$  and higher  $\text{N}_2$  excited states.<sup>15</sup> Unfortunately, the branching<sup>15</sup> to  $\text{HgBr}(B)$  upon reactive quenching of  $\text{N}_2(4)$  by  $\text{HgBr}_2$  is only 15%. This reaction combined with direct electron dissociative excitation of  $\text{HgBr}_2$  is insufficient

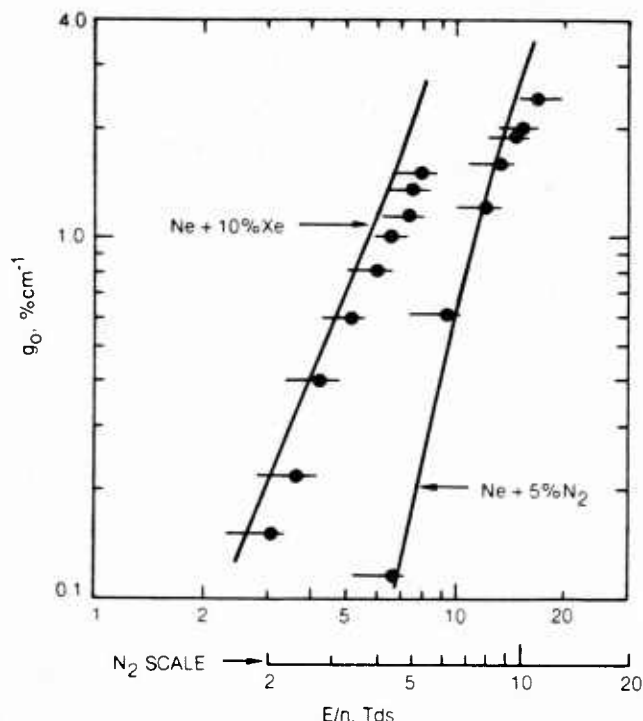


FIG. 10. Measured and computed small-signal gain for a Ne-10% Xe mixture and a Ne-5%  $N_2$  mixture, both containing 0.35%  $HgBr_2$ , excited under the  $e$ -beam-controlled discharge conditions of Figs. 2 and 7. Note that the  $E/n$  scale for the  $N_2$  mixture has been shifted for the sake of clarity.

to account for the gain observed in the  $N_2$  mixture. However, electron excitation of  $N_2(A)$  represents only 20–40% of the total  $N_2$  electronic excitation,<sup>18</sup> and there is evidence that a higher  $N_2$  excited state(s) also contributes to  $HgBr(B)$  formation.<sup>15</sup> Thus, in the present analysis, another  $N_2$  excited state was considered in addition to  $N_2(A)$ .

### 1. $N_2^*-HgBr_2$ branching to $HgBr(B)$

The rate coefficient for electron-impact excitation of the higher-energy  $N_2$  electronic state was taken as the sum of those of nine other  $N_2$  states for which cross sections have been reported.<sup>19</sup> Assuming that the total  $HgBr_2$  quenching coefficient for this single effective state is  $2 \times 10^{-10} \text{ s}^{-1} \text{ cm}^3$ , a value typical of  $N_2(A)$ , an  $HgBr(B)$  branching fraction of  $25 \pm 10\%$  is found to result in satisfactory agreement between measured and computed gain as shown in Fig. 10. Most probably  $HgBr(B)$  is produced primarily as a consequence of an  $HgBr_2$  reaction with  $N_2(B^3\Pi_g)$ ,<sup>18</sup> the highly populated and closely coupled  $B^3\Pi_g$  and  $W^3\Delta_u$  states of  $N_2$  being produced both by electron impact on ground state  $N_2$  and by cascade from higher lying levels. For the conditions of the  $N_2$  mixture of Fig. 10, approximately 50% of the  $HgBr(B)$  production results from  $N_2$  excitation transfer [one-third of that from  $N_2(A)$ ], and 50% from direct electron-impact excitation of  $HgBr_2$ . The computed  $HgBr(B)$  formation efficiency for the higher  $E/n$  values of Fig. 10 is in the 1.0–1.5% range.

### C. Ne-Xe- $HgBr_2$ mixtures

As is typical of the rare gases, the two lowest Xe( $6s$ ) states,  $^3P_2$  and  $^3P_1$ , can be produced very efficiently in an  $e$ -

beam-controlled electric discharge. Additionally, these Xe states are strongly quenched by  $HgBr_2$  resulting in  $HgBr(B)$  formation with an efficiency of about 80%.<sup>14,16</sup> For these reasons, Xe would seem to be the ideal excitation transfer species for the  $HgBr(B)/HgBr_2$  laser, and initial calculations<sup>2</sup> indicated that the  $HgBr(B)$  formation efficiency in mixtures containing Xe could be on the order of 10%. Unfortunately, such has not been found to be the case. Indeed, the Xe- $HgBr_2$  laser mixtures examined to date are not as efficient as others under  $e$ -beam-controlled discharge excitation, although their performance is comparable. Absorption in the blue/green region may contribute to a lower optical extraction efficiency in mixtures containing Xe. However, for the present conditions, measured absorption at 520 nm was found to be less than  $0.1\% \text{ cm}^{-1}$ . Further, since the observed  $B \rightarrow X$  fluorescence was substantially less than predicted, it appears that the explanation probably lies with the  $HgBr(B)$  formation sequence itself, a factor prompting more detailed examination of  $Xe^*-HgBr_2$  kinetics.

### 1. $Xe^*$ kinetics

Figure 11 shows the Xe electronic levels of significance in the present context. The two  $6s$  states at about 8.3 and 8.5 eV are efficiently excited by electron impact on ground state Xe, as are many higher lying Xe states. In the present analysis, it is assumed that the closely spaced  $^3P_2$  and  $^3P_1$  levels are completely mixed by electron and neutral collisions and constitute a single level. The  $6s'$ ,  $6p$ , and all higher lying states are also closely coupled together<sup>20</sup> and are assumed to be coupled to the lower-energy  $6s$  levels only by electron collisions as indicated in the figure. In addition, the single, effective upper state ( $6s', 6p, \dots$ ) so comprised is assumed to be strongly quenched by  $HgBr_2$  with no branching to  $HgBr(B)$ . Even on the basis of these rather conservative assumptions, the computed  $HgBr(B)$  fluorescence and formation efficiency are found to be higher than measured values. Consideration of the factors contributing to this situation shows that the underlying reason is a computed  $Xe(6s)$  population which is apparently too large. One explanation for this discrepancy is an unaccounted-for  $Xe(6s)$  loss mechanism, with three-body quenching by Ne a likely possibility.

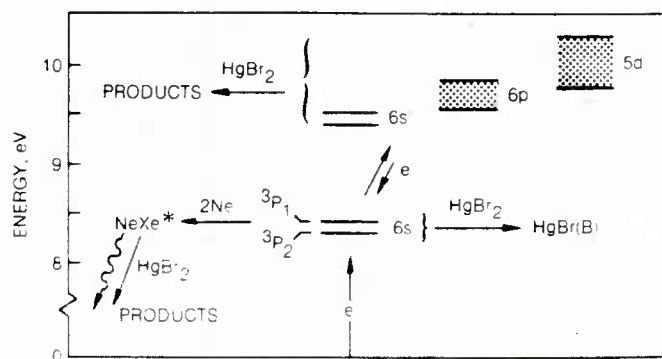


FIG. 11. Simplified Xe energy-level diagram showing the excited states of primary importance in the present context and indicating the dominant production and loss processes for each group of states as discussed in the text.

## 2. Xe(6s) three-body quenching

Based on the relatively small ( $\sim 10^{-32} \text{ s}^{-1} \text{ cm}^6$ ) rate coefficient for the reaction  $\text{Xe}(^3\text{P}_2) + \text{Xe} + \text{M} \rightarrow \text{Xe}_2(^3\Sigma_u^+) + \text{M}$ , three-body quenching of  $\text{Xe}^*$  would be insignificant for the conditions of this experiment. However, measurements<sup>21</sup> indicate that the reaction  $\text{Xe}(^3\text{P}_1) + \text{Xe} + \text{Ar} \rightarrow \text{Xe}_2(^1\Sigma_u^+) + \text{Ar}$  has a rate coefficient of  $2 \times 10^{-31} \text{ s}^{-1} \text{ cm}^6$ , a factor of 10 times higher than the analogous  $^3\text{P}_2$  reaction. Nevertheless, even with this value for the rate coefficient, merely substituting Ne as the third body has little effect on the computed  $\text{Xe}(6s)$  population because the Xe fractional concentration is only 10%. However, if it is assumed that two Ne atoms are involved, then reasonable agreement between computed and measured gain can be obtained. For example, the computed gain shown in Fig. 10 for the 10% Xe mixture was generated on this basis using a rate coefficient of  $2 \times 10^{-31} \text{ s}^{-1} \text{ cm}^6$  for the proposed three-body  $\text{Xe}(^3\text{P}_1) \rightarrow \text{NeXe}^*$  reaction. The hypothesis that Ne three-body quenching of the coupled  $^3\text{P}_1$  and  $^3\text{P}_2$  states of Xe proceeds at a rate much faster than suggested by the value of the rate coefficient measured for  $\text{Xe}(^3\text{P}_2)$  alone is also consistent with recent observations<sup>22</sup> of increased  $\text{Xe}(^3\text{P}_1)$  decay in Ne at lower pressures.

Although the  $\text{NeXe}^*$  molecule so produced is likely to be weakly bound, implying a large rate coefficient for the reaction back to  $\text{Xe}(^3\text{P}_1)$ , radiative decay and  $\text{HgBr}_2$  quenching may compete strongly with the reverse reaction. The  $^3\text{P}_1$  component of Xe forms a molecule having an allowed transition to the ground state, with the result that the lifetime of  $\text{NeXe}^*$  will be typical of that of  $\text{Xe}_2(^1\Sigma_u^+)$ ,  $\sim 10$  nsec. Quenching by  $\text{HgBr}_2$  will also have a characteristic time of several nanoseconds for the  $\text{HgBr}_2$  concentrations of interest. Further, the very efficient reaction channel resulting in the formation of  $\text{HgBr}(B)$  following  $\text{Xe}(^3\text{P}_{2,1})$  quenching by  $\text{HgBr}_2$  is thought<sup>16</sup> to involve the charge transfer potential  $\text{Xe}^+ - \text{HgBr}_2^-$ , which subsequently evolves specifically to  $\text{HgBr}(B) + \text{Xe} + \text{Br}$ , probably by way of the predissociating intermediate  $\text{Xe} - \text{HgBr}^*$ . However,  $\text{NeXe}^*$  (and/or  $\text{Xe}_2^*$ ) may have lower branching to  $\text{HgBr}(B)$  upon quenching by  $\text{HgBr}_2$  because of reduced efficiency of the charge transfer step, or for the subsequent evolution of the charge transfer intermediate.<sup>16</sup> For these reasons conversion of  $\text{Xe}(6s)$  atoms to  $\text{NeXe}^*$  (or other similar molecular species) may significantly lower the effective  $\text{HgBr}(B)$  branching fraction.

Additional clarification of the factors controlling the  $\text{Xe}(^3\text{P}_{2,1})$  population in discharges of the type under consideration may provide the basis for devising means to take advantage of the highly efficient formation of  $\text{HgBr}(B)$  following reactive quenching of  $\text{Xe}(^3\text{P}_{2,1})$  by  $\text{HgBr}_2$ . Clearly, additional experimentation in this area would be most helpful.

## V. ELECTRON COLLISION PROCESSES

### A. Electron- $\text{HgBr}_2$ electronic cross sections

As discussed earlier, reactive quenching of Ne and Ar metastable atoms by  $\text{HgBr}_2$  results in little or no  $\text{HgBr}(B)$  formation. For this reason, the present observations and those of McGeoch, Hsia and Klimek,<sup>23</sup> of strong

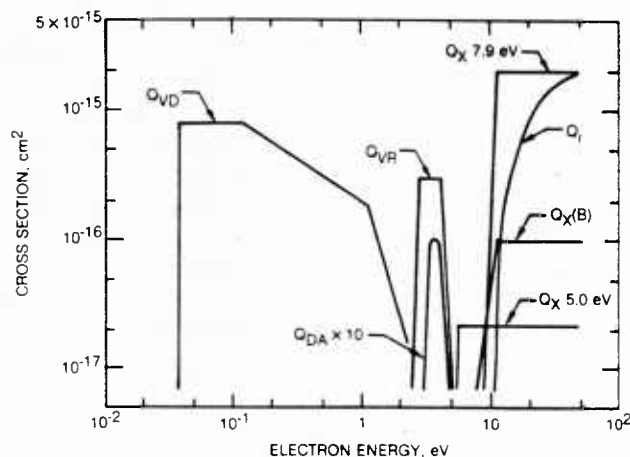


FIG. 12. Measured electron cross sections for  $\text{HgBr}_2$  dissociative attachment  $Q_{DA}$  and ionization  $Q_i$  as reported in Refs. 5 and 23, along with the cross sections for direct  $Q_{VD}$  and resonant  $Q_{VR}$  vibrational excitation as inferred from analysis of electron swarm experiments (Ref. 5). Also shown are the electronic cross sections inferred as part of the present investigation as discussed in Sec. V.

$\text{HgBr}(B \rightarrow X)$  fluorescence in  $e$ -beam-controlled discharge excited mixtures with Ne or Ar as the buffer, suggested that direct electron-impact excitation of  $\text{HgBr}_2$  is an important reaction leading to  $\text{HgBr}(B)$ . Under these circumstances, the electron-ion recombination rate is insufficient to account for the observed blue/green fluorescence. Further, the dissociative attachment rate is also too low and at low  $E/n$  values has a qualitative variation<sup>5,24</sup> inconsistent with that of the observed fluorescence. Thus,  $\text{HgBr}(B)$  is apparently not the dominant neutral fragment of the  $e$ - $\text{HgBr}_2$  attachment reaction as once suggested.<sup>25</sup> On the other hand, a relatively modest rate coefficient (i.e., cross section) for dissociative excitation of  $\text{HgBr}_2$ , branching to  $\text{HgBr}(B)$ , easily accounts for the observed fluorescence. On this basis, a phenomenological cross section for  $\text{HgBr}(B)$  formation was inferred as part of the present investigation and independently by McGeoch, Hsia, and Klimek,<sup>23</sup> both by analyzing  $e$ -beam-controlled laser discharge characteristics. The present cross section for  $\text{HgBr}(B)$  formation  $Q_X(B)$ , as determined in this manner, is shown in Fig. 12.

More difficult than determining the approximate magnitude and  $E/n$  variation of the  $e$ - $\text{HgBr}_2$  rate coefficient for  $\text{HgBr}(B)$  production, is generation of a self-consistent set of companion cross sections representative of  $\text{HgBr}_2$  vibrational<sup>5</sup> and electronic excitation that are capable of predicting the mixture-to-mixture variation of both discharge and laser properties in a satisfactory way. Cross sections for direct  $e$ - $\text{HgBr}_2$  vibrational excitation  $Q_{VD}$ , with an energy loss of 0.035 eV, and for resonant vibrational excitation  $Q_{VR}$ , with an effective energy loss of 0.25 eV, have been recently inferred from an analysis of data obtained using an electron swarm experiment.<sup>5</sup> These cross sections are also shown in Fig. 12, along with those for  $\text{HgBr}_2$  dissociative attachment and ionization.<sup>5,24</sup> In addition to  $Q_X(B)$ , two other  $e$ - $\text{HgBr}_2$  electronic cross sections have been used in this analysis, one having a threshold of 5.0 eV,  $Q_X(5.0)$ , the approximate threshold for  $\text{HgBr}_2$  electronic excitation,<sup>13</sup> and a higher-energy cross section with a threshold of 7.9 eV,  $Q_X(7.9)$ . Of

course there are many  $\text{HgBr}_2$  electronic states<sup>13</sup> that can be excited by electrons, but for the present purposes, use of three effective cross sections is sufficient to explain experimental observations of discharge/laser performance.

The magnitude of the electronic cross section  $Q_x(5.0)$  was adjusted so that, in combination with the resonant vibrational cross section  $Q_{VR}$ , the low  $E/n$  behavior of  $\text{HgBr}(B)$  fluorescence computed using  $Q_x(B)$  was in satisfactory agreement with experiment. As indicated in Fig. 8, the  $\text{HgBr}_2$  5.0-eV process results in  $\text{HgBr}(A,X)$  upon predissociation. However, a much larger cross section,  $Q_x(7.9)$ , most likely representative of a number of  $\text{HgBr}_2^*$  states, is required to predict both discharge characteristics, particularly instability onset, and fluorescence in agreement with experimental observation. This finding is in agreement with the observations of McGeoch, Hsia, and Klimek,<sup>23</sup> and also with recently measured<sup>26</sup> electron energy loss spectra in  $\text{HgBr}_2$ , which indicate the existence of a large cross section with a corresponding energy loss of about 7.9 eV.

### 1. Numerical experimentation with trial cross sections

Considerable numerical experimentation involving variations in both the magnitude and threshold slopes of the cross sections  $Q_x(5.0)$ ,  $Q_x(B)$ , and  $Q_x(7.9)$  indicated that the computed laser/discharge properties are not particularly sensitive to the magnitude of the cross sections above the threshold region. For example, increasing or decreasing the constant portion of any of the three electronic cross sections of Fig. 12 by a factor of two or more has little significant effect on computed gain or  $\text{HgBr}(B)$  formation efficiency for the conditions of this investigation. However, these laser properties are very sensitive to the *relative* threshold slopes of  $Q_x(B)$  and  $Q_x(7.9)$ . Because the 7.9-eV cross section tends to block the  $B$ -state cross section in the threshold region, changes in the initial slopes of either of these cross sections result in significant changes in the computed values of both gain and  $B$ -state formation efficiency. The relationship between these two cross sections, as shown in Fig. 12, was found to yield satisfactory agreement between the computed and measured laser and discharge properties of the present investigation. However, with the exception of the cross sections for ionization and attachment, the phenomenological cross sections shown in Fig. 12 are inferred and therefore should be considered provisional, pending measurement of the individual  $e\text{-HgBr}_2$  cross sections.

### 2. Attachment and ionization in Ne-HgBr<sub>2</sub> mixtures

Computed  $\text{HgBr}_2$  attachment and ionization coefficients for the Ne-HgBr<sub>2</sub> mixture conditions discussed earlier are shown in Fig. 13 and serve to illustrate the importance of  $Q_x(7.9)$ . Since the threshold for electronic excitation of Ne is well above the 10.62-eV  $\text{HgBr}_2$  ionization potential, in Ne-HgBr<sub>2</sub> mixtures, the effect of electronic excitation of  $\text{HgBr}_2$  alone determines the  $E/n$  value for which  $\text{HgBr}_2$  ionization becomes important relative to attachment. Since the  $\text{HgBr}_2$  cross sections for attachment and ionization are well-known,<sup>5,24</sup> calculations show that the magnitude and energy variation of the cross section  $Q_x(7.9)$  determines the  $E/n$

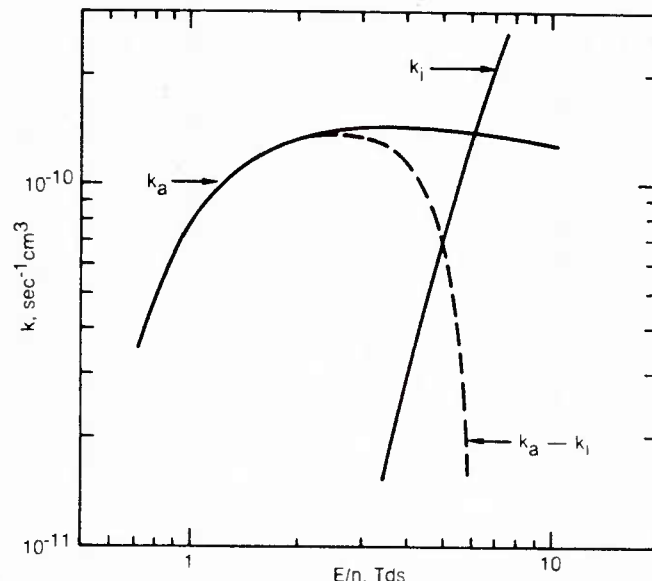


FIG. 13. Attachment rate coefficient  $k_a$  and ionization rate coefficient  $k_i$  for a Ne-0.35%  $\text{HgBr}_2$  mixture computed using the cross sections of Fig. 12 and a fractional ionization value of  $2 \times 10^{-6}$ . Also shown is the difference or net attachment coefficient  $k_a - k_i$ .

value for which the *net* attachment,  $k_a - k_i$ , begins to decrease rapidly, leading to  $e$ -beam-controlled discharge current runaway. In the present investigation, the magnitude and, more importantly, the slope of  $Q_x(7.9)$  were adjusted until the  $E/n$  variation of discharge current density, including instability onset, could be predicted in Ne-HgBr<sub>2</sub> mixtures, along with the  $E/n$  variation of the gain based on  $Q_x(B)$ . The resulting  $Q_x(7.9)$  so determined was also found to be consistent with observations in an electron swarm experiment<sup>5</sup> under conditions very different from those of the present  $e$ -beam-controlled laser discharge.

### 3. Fractional power transfer—Ne-HgBr<sub>2</sub>

Various contributions to the electron fractional power transfer (FPT) for the Ne-HgBr<sub>2</sub> conditions discussed above, computed using the cross sections of Fig. 12, are presented in Fig. 14. Over a relatively broad range of  $E/n$ , the FPT associated with  $\text{HgBr}(B)$  formation is in the 7–8% range for the present conditions, which, upon consideration of the quantum efficiency, results in a maximum  $\text{HgBr}(B)$  formation efficiency of about 3%. Numerical experimentation shows that this value is very sensitive to the slope of  $Q_x(B)$  (Fig. 12) because of the *blocking* effect of the 7.9-eV cross section. For these mixture conditions, by far the largest contribution to FPT is the combined effect of the 5.0- and 7.9-eV electronic cross sections, particularly the latter. Indeed, with the computed FPT for the effective 7.9-eV process five to ten times larger than that of  $\text{HgBr}(B)$  formation, it seems highly likely that excitation of higher lying  $\text{HgBr}_2$  states (as represented by the 7.9-eV process) also contribute significantly to  $\text{HgBr}(B)$  formation. Even if the  $\text{HgBr}(B)$  branching fraction associated with the 7.9-eV process is as low as 5%,  $\text{HgBr}(B)$  formation efficiency and gain will be affected significantly. For this reason, assignment of all  $\text{HgBr}(B)$  formation to a

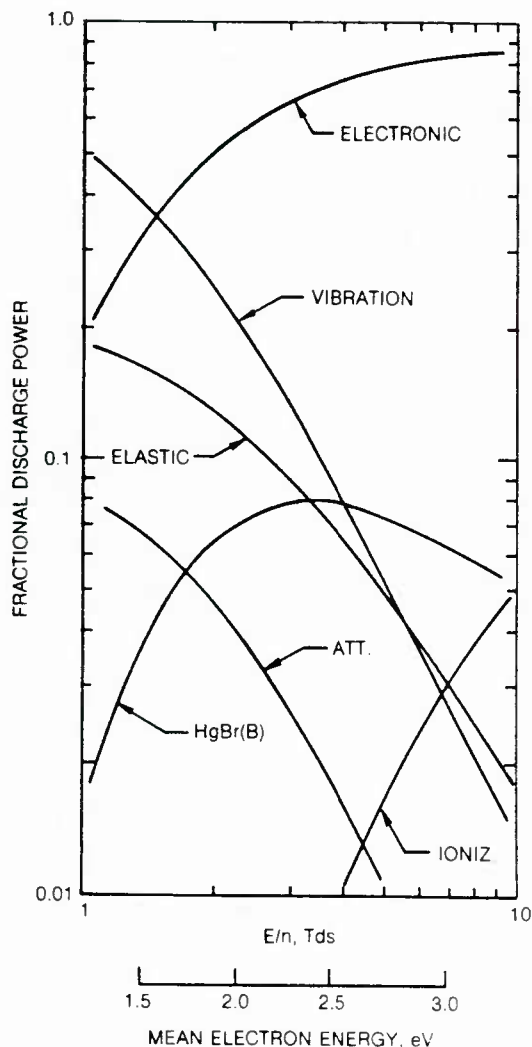


FIG. 14. Various contributions to the electron fractional power transfer (FPT) for a Ne-0.35% HgBr<sub>2</sub> mixture computed for the conditions of Fig. 13.

single cross section  $Q_x(B)$ , while convenient, is probably not correct.

Figure 14 shows that the FPT due to vibrational excitation of HgBr<sub>2</sub> is also significant. For the present mixture conditions, vibrational excitation represents about a 10% electron energy loss, a value which increases rapidly for lower  $E/n$  values. In addition, by depressing the tail of the electron energy distribution, the resonant vibrational cross section  $Q_{VR}$  significantly affects the magnitude and variation of the attachment coefficient at low  $E/n$  values<sup>5</sup> (Fig. 5).

## B. Electron-electron collisions

Although the electron energy distribution function is non-Maxwellian for the glow discharge conditions typical of the present investigation, the fractional ionization  $\alpha = n_e/n$  is at least  $10^{-6}$  and usually higher. At this fractional ionization level, it has been shown<sup>7,27</sup> that electron-electron collisions exert an important influence on the electron distribution function, particularly the high-energy region. All electron transport properties and rate coefficients are affected by the change in the distribution function, most signifi-

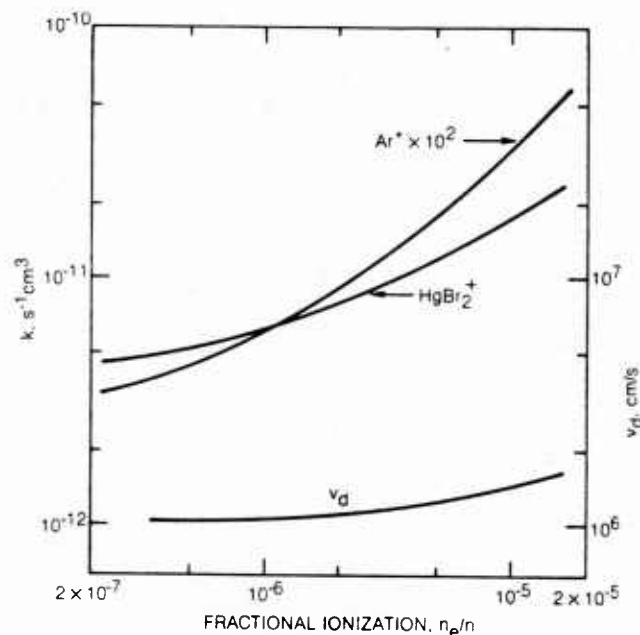


FIG. 15. Dependence of the electron drift velocity  $v_d$ , HgBr<sub>2</sub> ionization coefficient, and Ar metastable production coefficient on fractional ionization  $\alpha = n_e/n$ , computed for an  $E/n$  value of 7 Td s. The dependence of these properties on  $\alpha$  is stronger for lower  $E/n$  values and weaker for higher values.

cantly processes having an energy threshold much higher than the 2–3-eV mean electron energy typical of HgBr(B)/HgBr<sub>2</sub> laser discharge. As an illustration of the importance of this effect in the present context, Fig. 15 presents the computed fractional ionization dependence of electron drift velocity, the HgBr<sub>2</sub> ionization coefficient, and the Ar metastable production coefficient computed for an Ar-0.35% HgBr<sub>2</sub> mixture at a constant  $E/n$  value of 7 Td s. These results show that processes such as excitation and ionization can exhibit a significant dependence on fractional ionization for values of this variable above  $10^{-6}$ ; even the electron drift velocity changes substantially for  $\alpha > 10^{-6}$ . Calculations show that the effect of  $e$ - $e$  collisions is most pronounced when the background gas has an electron momentum transfer cross section exhibiting a strong energy variation, such as Ar. Additionally, the sensitivity of transport properties and rate coefficients to increases in fractional ionization is larger the lower the  $E/n$  value, reflecting the strong increase in the cross section for electron-electron collisions with decreasing electron energy.<sup>28</sup>

Since the electron distribution function exhibits a dependence on fractional ionization, it is particularly important to include the effect of electron-electron collisions in analyses of discharge conditions for which  $\alpha \gtrsim 10^{-6}$ . Electron cross sections inferred on the basis of analysis of  $e$ -beam-controlled laser/discharge performance will be affected unless the dependence of the electron energy distribution on both  $E/n$  and fractional ionization is taken into account.

## VI. SUMMARY

In the present investigation, measurements of  $e$ -beam-controlled discharge current density, HgBr(B $\rightarrow$ X) fluores-

cence, and 502-nm small-signal gain, obtained for several gas mixtures and a large range of  $E/n$  values, have been analyzed in detail. Satisfactory agreement between measured and computed discharge current density has been obtained, due in large measure to consideration of both vibrational excitation<sup>5</sup> of  $\text{HgBr}_2$  by low-energy electrons and the influence of electron-electron collisions on the electron energy distribution and, subsequently, on computed electron drift velocity and rate coefficients. Once able to predict discharge current density over a wide range of experimental variables, attention was directed toward analysis of  $\text{HgBr}(B)$  reaction kinetics. In mixtures comprised of Ne or Ar and  $\text{HgBr}_2$ , direct electron-impact dissociative excitation of  $\text{HgBr}_2$  is found to dominate  $\text{HgBr}(B)$  formation, a conclusion also reported by other investigators.<sup>3,23</sup> With  $\text{N}_2$  or Xe added to the mixture, dissociative excitation transfer contributes to  $\text{HgBr}(B)$  production. In  $\text{N}_2$  containing mixtures,  $\text{N}_2(A^3\Sigma_u^+)$  and a higher  $\text{N}_2^*$  state(s) (probably  $\text{B}^3\Pi_g$ ) are reactively quenched by  $\text{HgBr}_2$ , resulting in  $\text{HgBr}(B)$  formation with branching fractions of 15% and  $25 \pm 10\%$ , respectively. Excitation transfer from  $\text{Xe}(^3P_2)$ , following quenching by  $\text{HgBr}_2$ , results in  $\text{HgBr}(B)$  formation with near-unit branching and is an important reaction in mixtures containing Xe. However, for the conditions examined to date, a competitive  $\text{Xe}(^3P_2)$  loss channel appears to significantly limit the efficiency of  $\text{HgBr}(B)$  formation and thus laser performance. We suggest Ne three-body quenching of the closely coupled  $^3P_1$  state as a likely possibility. In any case, with the exception of Xe mixtures, the present analysis shows that the  $\text{HgBr}(B)$  formation pathway is not very selective, a factor likely to limit the efficiency of  $\text{HgBr}(B)$  formation to a maximum value of approximately 5% even under the most optimum of conditions.

In conjunction with a closely related study,<sup>5</sup> a set of self-consistent  $e\text{-HgBr}_2$  cross sections for attachment, ionization, vibrational excitation, and electronic excitation has been determined. When used to model laser/discharge kinetics, this cross-section set results in satisfactory agreement between measured and computed properties. However, it should be recognized that only the cross sections for  $\text{HgBr}_2$  ionization and attachment have been actually measured,<sup>5,24</sup> while the phenomenological cross sections for vibrational and electronic excitation have been inferred on the basis of related experimental observations. Although very useful in the present context, such inferred cross sections should be considered provisional, pending the availability of measured cross sections.

## ACKNOWLEDGMENTS

It is a pleasure to acknowledge the helpful discussions

with our UTRC colleagues J. J. Hinchey, H. H. Michels, and W. J. Wiegand, and with Professor D. W. Setser of Kansas State University. The expert technical assistance of R. Preisach is also much appreciated.

This work was supported in part by the Naval Ocean Systems Center and by the Office of Naval Research.

- <sup>1</sup>R. Burnham and E. J. Schimitschek, *Laser Focus* **17**, 54 (1981) and references cited therein.
- <sup>2</sup>R. T. Brown and W. L. Nighan, *Appl. Phys. Lett.* **37**, 1057 (1980).
- <sup>3</sup>M. McGeoch, J. Hsia, and D. Klimek, *Bull. Am. Phys. Soc.* **27**, 102 (1982); C. H. Fisher, I. Smilanski, T. DeHart, J. P. McDaniel, and J. J. Ewing, *ibid.* **27**, 102 (1982); E. J. Schimitschek and J. E. Celto, *Appl. Phys. Lett.* **36**, 176 (1978).
- <sup>4</sup>W. L. Nighan, in *Applied Atomic Collision Physics*, edited by H. S. W. Massey, E. W. McDaniel, and B. Bederson (Academic, New York, 1982), Chap. 11 and references cited therein.
- <sup>5</sup>W. L. Nighan, J. J. Hinchey, and W. J. Wiegand, *J. Chem. Phys.* **77**, 3442 (1982).
- <sup>6</sup>L. Brewer, in *The Chemistry and Metallurgy of Miscellaneous Materials*, edited by L. L. Quill (McGraw-Hill, New York, 1950), pp. 183-274.
- <sup>7</sup>W. L. Nighan, *IEEE J. Quantum Electron.* **QE-14**, 714 (1978).
- <sup>8</sup>Techniques used in modeling discharge and laser properties have become well developed in recent years in connection with investigations of excimer lasers. Specific details of the methods used in the present investigation can be found in Refs. 4, 5, and 7 and will not be repeated herein.
- <sup>9</sup>A. G. Robertson, *J. Phys. B* **5**, 648 (1972).
- <sup>10</sup>L. S. Frost and A. V. Phelps, *Phys. Rev.* **136**, A1538 (1964).
- <sup>11</sup>A. G. Engelhardt, A. V. Phelps, and C. G. Risk, *Phys. Rev.* **135**, A1566 (1964).
- <sup>12</sup>R. Johnson and M. A. Biondi, *J. Chem. Phys.* **73**, 5048 (1980).
- <sup>13</sup>W. Wadt, *J. Chem. Phys.* **72**, 2469 (1980).
- <sup>14</sup>R. S. F. Chang and R. Burnham, *Appl. Phys. Lett.* **36**, 397 (1980).
- <sup>15</sup>T. D. Dreiling and D. W. Setser, *Chem. Phys. Lett.* **74**, 211 (1980).
- <sup>16</sup>T. D. Dreiling, D. W. Setser, and S. Ferrero, *J. Chem. Soc., Faraday Trans. II* (in press).
- <sup>17</sup>H. Helvajian and C. Wittig, *Appl. Phys. Lett.* **38**, 731 (1981).
- <sup>18</sup>W. L. Nighan, *Appl. Phys. Lett.* **36**, 173 (1980).
- <sup>19</sup>D. C. Cartwright, S. Trajmar, A. Chutjian, and W. Williams, *Phys. Rev. A* **16**, 1041 (1977).
- <sup>20</sup>H. Horiguchi, R. S. F. Chang, and D. W. Setser, *J. Chem. Phys.* **75**, 1207 (1981).
- <sup>21</sup>R. E. Gleason, T. D. Bonifield, J. W. Keto, and G. K. Walters, *J. Chem. Phys.* **66**, 1589 (1977).
- <sup>22</sup>W. Wieme and J. Lenaerts, *J. Chem. Phys.* **72**, 2708 (1980).
- <sup>23</sup>M. W. McGeoch, J. C. Hsia, and D. E. Klimek, *J. Chem. Phys.* (in press); also Avco Everett Research Laboratory Final Technical Report under Contract N000123-80-C-1135, October 1981.
- <sup>24</sup>W. J. Wiegand and L. R. Boedeker, *Appl. Phys. Lett.* **40**, 225 (1982).
- <sup>25</sup>J. Degani, M. Rokni, and S. Yatsiv, *J. Chem. Phys.* **75**, 164 (1981).
- <sup>26</sup>D. Spence and M. A. Dillon (unpublished).
- <sup>27</sup>W. H. Long, *J. Appl. Phys.* **50**, 168 (1979), *Phys. Lett.* **31**, 391 (1977).
- <sup>28</sup>I. P. Shkarofsky, T. W. Johnston, and M. P. Bachynski, *The Particle Kinetics of Plasmas* (Addison-Wesley, Reading, Massachusetts, 1966), Chap. 7.

# Efficient HgBr ( $B \rightarrow X$ ) laser oscillation in electron-beam-controlled-discharge-excited Xe/HgBr<sub>2</sub> mixtures

Robert T. Brown and William L. Nighan  
United Technologies Research Center, East Hartford, Connecticut 06108

(Received 11 August 1980; accepted for publication 7 October 1980)

This letter reports the results of an investigation of HgBr( $B^2\Sigma^+ \rightarrow X^2\Sigma^+$ ) laser oscillation at 502 nm in Xe-HgBr<sub>2</sub> mixtures excited using an electron-beam-controlled discharge. Measured values of instantaneous electrical-optical energy conversion efficiency were 2%, a level substantially higher than that typical of N<sub>2</sub>-HgBr<sub>2</sub> mixtures. Calculations show that efficiencies of 5–10% may be possible under optimized conditions.

PACS numbers: 42.55.Hq, 52.80. — s, 41.80.Dd

The HgBr( $B^2\Sigma^+ \rightarrow X^2\Sigma^+$ ) laser operating at 502 nm promises to be an important optical source in the blue/green region of the spectrum. Excitation of this laser transition has been achieved by dissociative excitation of the mercuric-bromide molecule, HgBr<sub>2</sub>, in an electric discharge.<sup>1</sup> Using N<sub>2</sub>-HgBr<sub>2</sub> mixtures, electrical-optical energy conversion efficiencies in the 0.5–1.0% range have been obtained.<sup>1</sup> Analysis of the kinetics of electrically excited N<sub>2</sub>-HgBr<sub>2</sub> mixtures has shown that the HgBr( $B^2\Sigma^+$ ) laser molecule is formed following predissociation of HgBr<sub>2</sub>( $^3\Sigma_u^+$ ), the latter produced as a result of N<sub>2</sub>( $A^3\Sigma_u^+$ ) quenching by HgBr<sub>2</sub> molecules.<sup>2</sup> However, calculations show that the production efficiency of N<sub>2</sub>( $A^3\Sigma_u^+$ ) in N<sub>2</sub>-HgBr<sub>2</sub> discharges is about 10–15%, and recent measurements indicate that the N<sub>2</sub>( $A^3\Sigma_u^+$ )-HgBr<sub>2</sub> branching fraction for HgBr( $B^2\Sigma^+$ ) formation is only 15–20%.<sup>3</sup> These factors may limit the efficiency of the discharge-excited HgBr( $B$ )/HgBr<sub>2</sub> dissociation laser to a value of approximately 1% when N<sub>2</sub> is used as the energy transfer molecule.

By way of contrast, recent measurements show that the Xe( $^3P_2$ ) metastable atom has a large rate coefficient for HgBr<sub>2</sub> dissociative excitation and that HgBr( $B^2\Sigma^+$ ) is formed with near unit efficiency.<sup>4</sup> In addition, the present calculations show that Xe( $^3P_2$ ) metastable atoms can be produced with high efficiency (> 50%) over a broad range of electric discharge conditions. For these reasons Xe has unusual potential as an energy transfer species in the HgBr( $B$ )/HgBr<sub>2</sub> dissociation laser. In this letter we report the results of efficient HgBr( $B \rightarrow X$ ) laser oscillation in Xe-HgBr<sub>2</sub> mixtures using an electron-beam-controlled discharge.

The present experiments were carried out using a 1.5 × 1.7 × 50-cm active volume within the heated discharge cell shown schematically in Fig. 1. Previous investigations<sup>5</sup> have shown that proper cell design is critical in order to maintain chemical purity of the gas mixture. In order to keep HgBr<sub>2</sub>-surface interactions to a minimum, in this cell the only materials in contact with the working gas mixture were type 316 stainless-steel, Pyrex, Kalrez, and dielectric-coated mirrors. HgBr<sub>2</sub> crystals were contained in a Pyrex reservoir positioned in a side arm as shown in the figure. Variation of the cell (and reservoir) temperature in the 150–200 °C range provided a corresponding variation in HgBr<sub>2</sub> partial pres-

sure from about 1 Torr to approximately 15 Torr. The electron beam system and discharge driver utilized in this investigation have been described previously.<sup>6</sup>

Presented in Fig. 2 are representative measured characteristics for a mixture containing 10% Xe in a Ne buffer at a total pressure of 2 atm and a temperature of 185 °C. Based on available vapor pressure data,<sup>7</sup> the HgBr<sub>2</sub> concentration for these conditions was  $2.4 \times 10^{17}$  cm<sup>-3</sup>, corresponding to a mixture fraction of approximately 0.007. In this case the electron beam was initiated 200 ns before the discharge voltage and provided a constant  $e$ -beam current density of 0.5 A cm<sup>-2</sup> for 1.2  $\mu$ sec. The discharge voltage was provided by a low-inductance capacitor of a size so as to produce only a very slight decrease in voltage (i.e.,  $E/n$ ) during the pulse. With this arrangement it was possible to produce a highly uniform plasma medium which was essentially quasisteady. For the conditions of Fig. 2 the measured current and voltage exhibited essentially steady-state behavior for over 0.5  $\mu$ sec, at which time the discharge was terminated by arcing.

Time-dependent discharge and laser properties were modeled numerically using procedures which have been described previously.<sup>2,6</sup> Computed current-voltage characteristics were found to be in very good qualitative and quantitative agreement with measured values over a range of  $E/n$  values and HgBr<sub>2</sub> concentrations. In addition, the onset of arcing could be predicted and was shown to be due to volu-

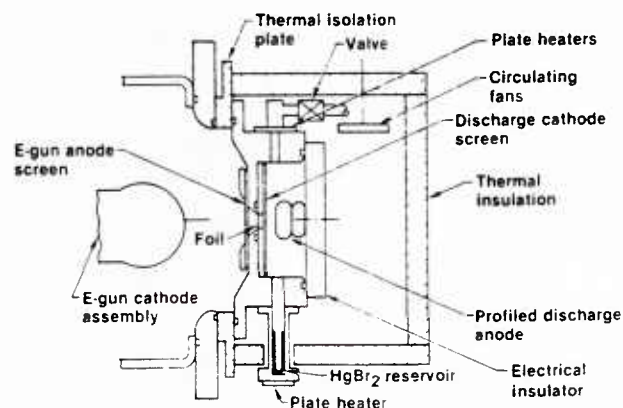


FIG. 1. Illustration of heated HgBr( $B$ )/HgBr<sub>2</sub> laser discharge cell.

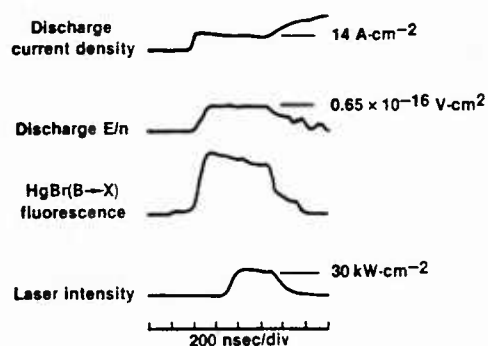
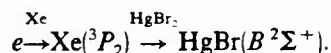


FIG. 2. Representative characteristics for an *e*-beam-controlled-discharge-excited mixture comprised of 10% Xe in a Ne buffer at a total pressure of 2 atm and a temperature of 185 °C. For these conditions the HgBr<sub>2</sub> concentration in the cell was  $2.4 \times 10^{17} \text{ cm}^{-3}$ , approximately 0.7% of the total mixture. The *e*-beam current density (at the center of the discharge) was  $0.5 \text{ A cm}^{-2}$ .

metric ionization instability.<sup>6</sup> Prior to the onset of arcing the discharges were found to operate in a high-impedance ( $2\text{--}3 \Omega$ ), externally controlled mode. Modeling of discharge properties indicated that for conditions typical of this investigation (e.g., Fig. 2) 80–90% of the deposited energy was provided by the discharge, and 60–70% of the ionization was provided by the *e*-beam, values found to be consistent with experimental observations. Thus the Ne/Xe/HgBr<sub>2</sub> discharges examined in this investigation were *e*-beam controlled and exhibited a high discharge:*e*-beam energy enhancement factor.

The HgBr<sub>2</sub>( $B^2\Sigma^+ \rightarrow X^2\Sigma^+$ ) fluorescence was found to be a relatively sensitive function of applied voltage, reflecting the strong dependence of Xe( $^3P_2$ ) metastable production of  $E/n$ . Modeling of discharge characteristics indicated that HgBr( $B^2\Sigma^+$ ) was produced with an efficiency typically in the 15–20% range by way of the reaction sequence<sup>8</sup>



Computed zero-field gain based on the calculated HgBr( $B^2\Sigma^+$ ) concentration and using a stimulated emission cross section of  $2.4 \times 10^{-16} \text{ cm}^2$  was approximately  $0.03 \text{ cm}^{-1}$  for the conditions of Fig. 2.

Using an internally mounted optical cavity consisting of a 4.0-m max *R* mirror and a flat 90% *R* output coupler, the laser pulse shown in Fig. 2 was obtained. The output beam imaged the full  $1.5 \times 1.7\text{-cm}$  discharge cross section and was found to be very uniform. Although the onset of laser oscillation was delayed, Fig. 2 shows that a uniform laser pulse of almost 400-nsec duration was obtained. More-

over, the instantaneous electrical-optical energy conversion efficiency was found to be 2.0%, a level substantially higher than that typical of N<sub>2</sub>/HgBr<sub>2</sub> laser mixtures. However, calculations show that in the absence of appreciable volumetric absorption (i.e., for gain/absorption ratios greater than 10) laser efficiencies greater than 5% should be attainable for these conditions. Both the delayed onset and the apparently low optical extraction efficiency are suggestive of a *net* gain lower than the computed value, and/or a relatively high level of volumetric absorption. With an HgBr<sub>2</sub> concentration in excess of  $10^{17} \text{ cm}^{-3}$ , even a low level of surface reactions and/or impurities introduced with the HgBr<sub>2</sub> could result in a substantial level of neutral impurities, one or more of which may either absorb at the laser wavelength or quench HgBr(*B*). Additionally, ionic or excited states of HgBr<sub>2</sub> itself may absorb in the blue/green region of the spectrum. These possibilities are presently being studied in more detail.

The present investigation has shown that use of Xe as the primary energy receptor-transfer species in *e*-beam-controlled-discharge-excited HgBr(*B*)/HgBr<sub>2</sub> dissociation lasers permits laser efficiency higher than reported for N<sub>2</sub>-HgBr<sub>2</sub> mixtures. More importantly, calculations show that electrically excited Xe-HgBr<sub>2</sub> mixtures have the potential for development as blue/green sources with efficiencies even higher than those measured in the present experiments. Modeling of discharge/laser properties for a variety of conditions suggests that electrical-optical energy conversion efficiencies of 5–10% may be possible under optimized conditions.

The authors acknowledge helpful discussions with their UTRC colleagues L. A. Newman, W. J. Wiegand, and H. H. Michels, and also with D. W. Setser. In addition, the expert assistance of R. Preisach and L. Bromson is greatly appreciated. This work was supported by the Naval Ocean Systems Center and by the Office of Naval Research.

<sup>1</sup>E. J. Schimitschek and J. E. Celto, Appl. Phys. Lett. **36**, 176 (1980), and references cited therein.

<sup>2</sup>W. L. Nighan, Appl. Phys. Lett. **36**, 173 (1980).

<sup>3</sup>T. D. Dreiling and D. W. Setser, Chem. Phys. Lett. (to be published).

<sup>4</sup>R. S. F. Chang and R. Burnham, Appl. Phys. Lett. **36**, 397 (1980).

<sup>5</sup>E. J. Schimitschek and J. E. Celto, Opt. Lett. **2**, 64 (1978).

<sup>6</sup>R. T. Brown and W. L. Nighan, Appl. Phys. Lett. **32**, 730, 1978; **35**, 144 (1979).

<sup>7</sup>L. Brewer, in *The Chemistry and Metallurgy of Miscellaneous Materials*, edited by L. L. Quill (McGraw-Hill, New York, 1950).

<sup>8</sup>Experimentation with neon-HgBr<sub>2</sub> mixtures yielded evidence of a direct HgBr(*B*) formation mechanism tentatively identified as electron impact dissociative excitation of HgBr<sub>2</sub>. The magnitude of the rate coefficient for this process, which is required to explain the experimental observation of HgBr(*B*→*X*) fluorescence in neon-HgBr<sub>2</sub> mixtures, suggests that a direct electron excitation of HgBr<sub>2</sub> resulting in HgBr(*B*) may also be significant reaction in mixtures containing either N<sub>2</sub> or Xe.

# Kinetic processes in the electrically excited mercuric-bromide dissociation laser

William L. Nighan

United Technologies Research Center, East Hartford, Connecticut 06108

(Received 26 September 1979; accepted for publication 19 November 1979)

This letter reports the results of an analysis of basic kinetic and plasma processes in fast-pulse ( $\sim 100$  nsec) electric discharges containing mixtures of the mercuric-bromide molecule,  $\text{HgBr}_2$ , and  $\text{N}_2$  in a Ne background. Formation of the laser molecule  $\text{HgBr}(B^2\Sigma^+)$  is shown to occur as a result of dissociative excitation transfer following quenching of  $\text{N}_2(A^3\Sigma_u^+)$  by  $\text{HgBr}_2$ .

PACS numbers: 42.55.Hq, 52.20.Hv, 82.30.Eh,

Excitation of the mercury-bromide  $B^2\Sigma^+ \rightarrow X^2\Sigma^+$  laser transition at 502 nm has been achieved by dissociative excitation of the mercuric-bromide molecule  $\text{HgBr}_2$  in an electric discharge.<sup>1,2</sup> Electrical-optical energy conversion efficiency in the 0.1–1.0% range has been obtained, suggesting that for optimized conditions, efficiency in excess of 1% may be achievable. Moreover, the required concentration of  $\text{HgBr}_2$  ( $\sim 2$  Torr) can be produced at a temperature ( $\sim 150^\circ\text{C}$ ) substantially lower than that typical of mercury-halide lasers using mercury-vapor-halogen mixtures. In this letter basic kinetic processes occurring in this new class of mercury-halide lasers will be examined.

Experimentation<sup>1,2</sup> using fast-pulse ( $\sim 100$  nsec) electric discharge excitation indicates an optimum  $\text{HgBr}_2$  fractional concentration in the 0.2–0.3% range with Ne (or He) serving as the buffer gas at a pressure near 1 atm. Addition of approximately 2–10%  $\text{N}_2$  to this mixture has been found to improve laser power and efficiency significantly. For this reason, analysis of  $\text{HgBr}(B^2\Sigma^+)$  formation kinetics in the  $\text{N}_2$  laser mixture has been emphasized in the present study. Electron- $\text{N}_2$  collision processes are expected to dominate discharge processes in the  $\text{HgBr}_2$ - $\text{N}_2$ -Ne mixture because of the large  $\text{N}_2$  :  $\text{HgBr}_2$  concentration ratio, the numerous  $\text{N}_2$  vibrational and electronic levels having large cross sections, and the high-energy threshold for electronic excitation of Ne. Indeed, the present calculations of electron energy distributions and electron-molecule energy transfer rates for the  $E/n$  range typical of the experiments of Refs. 1 and 2 show that over 95% of the total discharge energy is consumed by  $\text{N}_2$  vibrational and electronic excitation in approximately equal proportions. Recent measurements have shown that the rate coefficient for dissociative excitation transfer from  $\text{N}_2(A^3\Sigma_u^+)$  to  $\text{HgBr}_2$  is large,<sup>3</sup> and that the cross section for direct electron dissociative excitation of  $\text{HgBr}_2$  leading to  $\text{HgBr}(B^2\Sigma^+)$  is small.<sup>4</sup> These findings are consistent with the  $\text{HgBr}(B^2\Sigma^+)$  formation sequence illustrated in Fig. 1.

Figure 1 shows the principal  $\text{N}_2$  states excited directly by electron impact on ground state  $\text{N}_2$ . The shaded area refers to the  $\text{N}_2(B^3\Sigma_u^-)$ , ( $a^1\Sigma_u^-$ ), ( $a^1\Pi_g$ ), and ( $w^1\Delta_u$ ) group of states; and the percentages shown refer to the fractional electron energy initially transferred to each state (or group of states), computed for the experimental conditions of present interest.<sup>1,2</sup> There are numerous  $\text{HgBr}_2$  electronic states in the 4–10-eV range.<sup>5</sup> In this figure, the regions labeled *a*–*d*

refer to the experimentally determined photoabsorption bands of  $\text{HgBr}_2$ .<sup>1,5</sup> Available evidence indicates that only states in the *b* band, and particularly  $\text{HgBr}_2(3\Sigma_u^+)$  and ( $1\Sigma_u^+$ ), predissociate to form  $\text{HgBr}(B^2\Sigma^+)$ .

Measurements<sup>3</sup> of  $\text{N}_2(A^3\Sigma_u^+)$  quenching by  $\text{HgBr}_2$  yield a rate coefficient of  $1.0 \times 10^{-10} \text{ sec}^{-1} \text{ cm}^3$  for the formation of  $\text{HgBr}(B^2\Sigma_u^+)$ , and a total quenching coefficient of approximately  $3.0 \times 10^{-10} \text{ sec}^{-1} \text{ cm}^3$ , indicative of a branching ratio of about one-third. However, Fig. 1 shows that only 10% of the electron energy is transferred directly to  $\text{N}_2(A^3\Sigma_u^+)$ . Thus, a primary consideration in analysis of  $\text{HgBr}(B^2\Sigma^+)$  formation kinetics in the  $\text{HgBr}_2/\text{N}_2$  system is the ultimate redistribution of the large fraction ( $\sim 40\%$ ) of the discharge energy initially deposited in higher  $\text{N}_2$  electronic levels, particularly the coupled  $B^3\Pi_g$  and  $W^3\Delta_u$  states which are populated by electron impact and by cascade from higher levels. Under laser discharge conditions, excitation transfer from these states to  $\text{HgBr}_2$  is likely to occur in a time less than that required for either electronic relaxation to high vibrational levels of  $\text{N}_2(A^3\Sigma_u^+)$ , or for vibrational relaxation of the  $A^3\Sigma_u^+$  state. Michels<sup>6</sup> has carried out an analysis based on consideration of the energy defect corresponding to various  $\text{N}_2^+$ - $\text{HgBr}_2$  collision channels, and on correlations of the spin and symmetry of reaction products. This analysis shows that excitation transfer from  $\text{N}_2(A^3\Sigma_u^+)$  results in the formation of  $\text{HgBr}_2(3\Sigma_u^+)$ , which correlates diabatically with the  $\text{HgBr}(B^2\Sigma^+)$  laser state, with some branching to  $\text{HgBr}(A^2\Pi)$  and  $\text{HgBr}(X^2\Sigma^+)$  also probable. This conclusion is consistent with measure-

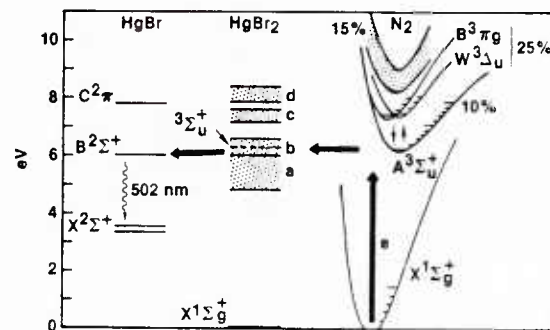


FIG. 1. Simplified energy level diagram illustrating the  $\text{HgBr}(B^2\Sigma^+)$  formation sequence in electrically excited mixtures of  $\text{HgBr}_2$  and  $\text{N}_2$ . The percentages shown refer to the fractional electron energy transfer to each state.

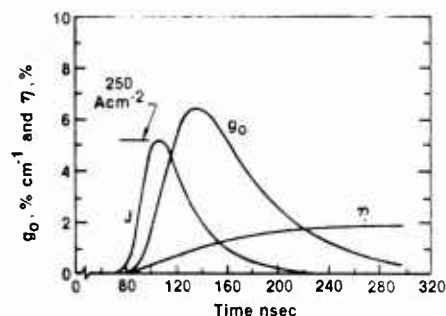


FIG. 2. Temporal variations of discharge current density, zero-field gain (assuming no lower laser level population), and HgBr( $B^2\Sigma^+$ ) formation efficiency computed for a Ne-N<sub>2</sub>-HgBr<sub>2</sub> mixture in the proportions 0.95 : 0.05 : 0.0025 at a pressure of 1.3 atm and conditions otherwise similar to the experiments of Ref. 1.

ments<sup>3</sup> of N<sub>2</sub>( $A^3\Sigma_u^+$ ) quenching by HgBr<sub>2</sub>. In contrast to this situation, excitation transfer from N<sub>2</sub>( $W^3\Delta_u$ ) leads to HgBr<sub>2</sub>( $^3\Delta_u$ ), and subsequently to HgBr( $A^2\Pi$ ) and HgBr( $C^2\Pi$ ), with no branching to HgBr( $B^2\Sigma^+$ ). In addition, excitation transfer from N<sub>2</sub>( $B^3\Pi_g$ ) leads to HgBr<sub>2</sub>( $^3\Pi_g$ ), which correlates diabatically with the HgBr( $C^2\Pi$ ) state, with branching to the  $A^2\Pi$ ,  $B^2\Sigma^+$ , and  $X^2\Sigma^+$  states of HgBr also possible. Thus, excitation transfer to HgBr<sub>2</sub> from the coupled  $B^3\Pi_g$  and  $W^3\Delta_u$  states of N<sub>2</sub> is expected to result in states of HgBr<sub>2</sub> which, for the most part, do not dissociate to produce the HgBr( $B^2\Sigma^+$ ) laser state. In the present analysis, the total rate coefficient for quenching of N<sub>2</sub>( $B^3\Pi_g$ ) and N<sub>2</sub>( $W^3\Delta_u$ ) was taken to be the same as the value measured for N<sub>2</sub>( $A^3\Sigma_u^+$ ), but branching to HgBr( $B^2\Sigma^+$ ) was assumed to be zero.

Because N<sub>2</sub> cross sections for vibrational and electronic excitation are well known, electron energy distributions and related rate coefficients could be calculated reliably for use as input in a self-consistent model of the time-dependent variation of electron, ion, and excited state processes for conditions typical of the fast-pulse discharge experiments of Refs. 1 and 2. For a Ne-N<sub>2</sub>-HgBr<sub>2</sub> mixture in the proportions 0.95 : 0.05 : 0.0025 at a pressure of 1.3 atm, the measured<sup>1</sup>  $E/n$  value at which breakdown occurred was found to be approximately  $3 \times 10^{-16}$  V cm<sup>2</sup>, subsequently decreasing to zero in about 150 nsec. For these conditions the present calculations show that the dominant contributions to ionization are Penning ionization of N<sub>2</sub> and HgBr<sub>2</sub> by Ne\* (~50%), direct electron impact ionization of N<sub>2</sub> (~35%), and direct electron impact ionization of HgBr<sub>2</sub> (~15%).<sup>7</sup> Ionization from the highly populated N<sub>2</sub>( $A^3\Sigma_u^+$ ), ( $B^3\Pi_g$ ), and ( $W^3\Delta_u$ ) states was found to be unimportant, a reflection of the relatively high ionization potentials of these excited species. This is significant, since cumulative ionization involving electronically excited species is usually a major contributor to the occurrence of ionization instability and subsequently, discharge arcing.<sup>8</sup>

Presented in Fig. 2 are temporal variations of discharge current density, zero-field gain (assuming no lower laser level population), and the energy efficiency of HgBr( $B^2\Sigma^+$ ) formation computed for conditions typical of those of Ref. 1. The HgBr( $B^2\Sigma^+$ ) formation efficiency at any point is simply

the time-integrated ratio of the energy flow through the HgBr( $B^2\Sigma^+$ ) state to the total energy deposited in the discharge up to that time. Both the peak values and temporal evolution of the computed current density and gain are in good agreement with measured values.<sup>1</sup> For the conditions of this example HgBr( $B^2\Sigma^+$ ) is produced by way of excitation transfer from the N<sub>2</sub>( $A^3\Sigma_u^+$ ) state alone as discussed previously, the latter produced by direct electron impact of N<sub>2</sub>, and to a lesser extent by N<sub>2</sub>( $B^3\Pi_g$ ) → N<sub>2</sub>( $A^3\Sigma_u^+$ ) transitions resulting from collisions with electrons and N<sub>2</sub> molecules. The primary loss of HgBr( $B^2\Sigma^+$ ) is due to spontaneous decay (~47%), and to collisions with HgBr<sub>2</sub> (~17%), Ne (~16%), electrons (~13%) and N<sub>2</sub> (~7%). These processes result in an effective upper level lifetime of about 10 nsec, corresponding to a saturation intensity of approximately 175 kW/cm<sup>2</sup>, which is also in good agreement with measured values.<sup>1</sup> Figure 2 indicates that HgBr( $B^2\Sigma^+$ ) formation efficiency reaches a maximum level of about 2.0% by the end of the pulse. Measured<sup>1</sup> laser efficiency under these conditions is typically 0.5%, a value consistent with an overall optical extraction efficiency of 25%.

Figure 3 shows the temporal variation of several major species corresponding to the conditions of Fig. 2. The concentrations of the N<sub>2</sub>( $A^3\Sigma_u^+$ ) and the coupled N<sub>2</sub>( $B^3\Pi_g$ ) and N<sub>2</sub>( $W^3\Delta_u$ ) states reach very high levels at about the time the current density reaches its peak, reflecting the relatively large values of N<sub>2</sub> concentration, electron density, and  $e$ -N<sub>2</sub> excitation rate coefficients. These N<sub>2</sub> states decay rather slowly, indicative of their rate of quenching by HgBr<sub>2</sub>, which is present in small concentration. In the present model the temporal decay of HgBr( $B^2\Sigma^+$ ) essentially follows the N<sub>2</sub>( $A^3\Sigma_u^+$ ) population as shown in the figure. However, vibrational redistribution within the N<sub>2</sub>( $A^3\Sigma_u^+$ ) state will occur as a function of time, particularly as the pumping decreases (decreasing  $n_e$  and  $E/n$ ). Indeed, both the total N<sub>2</sub>( $A^3\Sigma_u^+$ ) quenching rate and HgBr<sub>2</sub> product states may actually exhibit a dependence on N<sub>2</sub>( $A^3\Sigma_u^+$ ) vibrational level, and therefore on time.

Fractional dissociation of HgBr<sub>2</sub> reaches a value of approximately 10% for the present example, resulting in a significant concentration of HgBr( $X^2\Sigma^+$ ) by the end of the

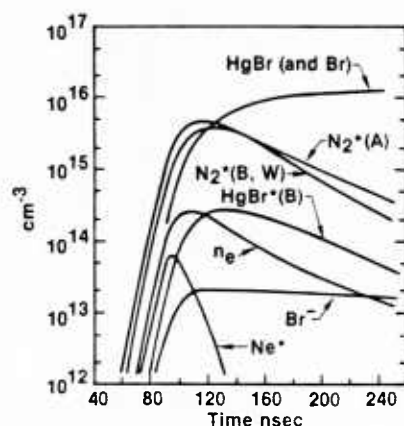


FIG. 3. Temporal variation of selected species concentrations corresponding to the conditions of Fig. 2.

pulse. A significant fraction of  $\text{HgBr}(X^2\Sigma^+)$  is initially produced in the  $v = 22$  terminal laser level which is apparently relaxed rather rapidly by collisions with neutrals. However, since the electron density and electron temperature remain relatively high throughout the entire pulse, vibrational excitation of  $\text{HgBr}$  by electrons may result in a vibrational temperature well above that typical of the gas temperature. Thus, it is probable that lower laser level buildup becomes significant at some time prior to the end of the pulse for the conditions examined here.

Although addition of  $\text{N}_2$  to the  $\text{Ne-HgBr}_2$  mixture results in a significant improvement in pulse energy and efficiency, particularly the former, the  $\text{HgBr}_2$  dissociation laser does operate at an efficiency above 0.1% without  $\text{N}_2$  in the mixture.<sup>1</sup> The present analysis shows that electron energy transfer, ionization, and  $\text{HgBr}(B^2\Sigma^+)$  formation processes are completely different in the absence of  $\text{N}_2$ . Calculations indicate that in  $\text{Ne-HgBr}_2$  mixtures, the dominant electron energy transfer processes are  $\text{Ne}$  metastable production followed by Penning ionization of  $\text{HgBr}_2$ , and direct electron impact ionization of  $\text{HgBr}_2$ .<sup>7</sup> Predissociating states of  $\text{HgBr}_2$  can be produced either by the ion-ion recombination reaction,  $\text{HgBr}_2^+ + \text{Br}^- + \text{Ne} \rightarrow \text{HgBr}_2^* + \text{Br} + \text{Ne}$ , or by electron-ion recombination,  $\text{HgBr}_2^+ + e \rightarrow \text{HgBr}_2^*$ . Based on estimates for ion loss rates,<sup>9</sup> the present calculations show that ion loss due to electron-ion recombination is 5–10 times larger than that due to ion-ion recombination. Since numerous excited states of  $\text{HgBr}_2$  can be formed by either recombination reaction, the branching ratio for  $\text{HgBr}(B^2\Sigma^+)$  formation is not likely to be very high. By assuming a branching ratio of 0.2 for  $\text{HgBr}(B^2\Sigma^+)$  formation via recombination reactions, values of peak gain ( $\sim 4\% \text{ cm}^{-1}$ ) and  $\text{HgBr}(B^2\Sigma^+)$  formation efficiency ( $\sim 1.75\%$ ) were computed for conditions generally similar to those of Fig. 2. These values are somewhat less than those typical of mixtures containing  $\text{N}_2$ , a result consistent with experimental observations.<sup>1</sup> However, for similar current density levels the total energy deposited in the gas is significantly less in the absence of  $\text{N}_2$ , reflecting substantial-

ly lower  $E/n$  levels typical of  $\text{Ne-HgBr}_2$  mixtures. It should also be pointed out that with  $\text{N}_2$  in the mixture, recombination reactions are insignificant compared to  $\text{N}_2(A^3\Sigma_u^+)$  excitation transfer insofar as  $\text{HgBr}(B^2\Sigma^+)$  formation is concerned.

Although the data base required for comprehensive modeling of mercuric-bromide dissociation lasers is far from complete, the present analysis shows that available experimental observations can be interpreted in a self-consistent manner for  $\text{HgBr}_2$  laser mixtures containing  $\text{N}_2$ . Analysis of  $\text{HgBr}(B^2\Sigma^+)$  formation kinetics and discharge characteristics indicate that the  $\text{HgBr}_2/\text{N}_2$  system has considerable potential for efficient scaling to energy levels substantially in excess of those reported to date.

The author acknowledges numerous helpful discussions with his colleagues particularly L.A. Newman and H.H. Michels. Also, the expert assistance of L. Bromson with the numerical work is much appreciated. Additionally, the author thanks E.J. Schimitschek and R. Burnham for access to experimental data prior to publication. This work was supported in part by the Office of Naval Research.

<sup>1</sup>E.J. Schimitschek and J.E. Celto, *Opt. Lett.* **2**, 64 (1978); *Appl. Phys. Lett.* **36**, (1980) (to be published).

<sup>2</sup>R. Burnham, *Appl. Phys. Lett.* **33**, 156 (1978).

<sup>3</sup>R.S.F. Chang and R. Burnham (unpublished).

<sup>4</sup>J. Allison and R.N. Zare, *Chem. Phys.* **35**, 263 (1978).

<sup>5</sup>K. Wieland, *Z. Phys.* **77**, 157 (1932); W.R. Wadt, *J. Chem. Phys.* (to be published).

<sup>6</sup>H.H. Michels (private communication).

<sup>7</sup>For the purpose of the present analysis, the ionization cross section for  $\text{HgBr}_2$  has been assumed to increase from threshold at 10.6 eV to a peak value of  $5 \times 10^{-16} \text{ V cm}^2$  in the 50–100-eV range. The rate coefficient for dissociative attachment of  $\text{HgBr}_2$  was taken as  $1 \times 10^{-10} \text{ sec}^{-1} \text{ cm}^3$ . The results presented in Figs. 2 and 3 were found to be relatively insensitive to variations in the  $\text{HgBr}_2$  ionization and attachment rate coefficients.

<sup>8</sup>R.T. Brown and W.L. Nighan, *Appl. Phys. Lett.* **32**, 730 (1978).

<sup>9</sup>In this analysis an effective electron-ion recombination coefficient of  $1.0 \times 10^{-7} \text{ sec}^{-1} \text{ cm}^3$  was used for  $\text{HgBr}_2^+$ , along with a value of  $3 \times 10^{-7} \text{ sec}^{-1} \text{ cm}^3$  for the reaction  $\text{HgBr}_2^+ + \text{Br}^- + \text{Ne} \rightarrow \text{HgBr}_2^* + \text{Br} + \text{Ne}$ , as recently computed by M.R. Flannery (private communication).

# Low energy electron collision phenomena in $\text{HgBr}_2$

William. L. Nighan, John J. Hinchey, and Walter J. Wiegand

United Technologies Research Center, East Hartford, Connecticut 06108

(Received 10 May 1982; accepted 18 June 1982)

Cross sections for mercuric bromide ( $\text{HgBr}_2$ ) dissociative attachment and ionization have been measured using an electron beam experiment. The dominant products of these reactions, as identified by mass analysis, are  $\text{Br}^-$  and  $\text{HgBr}_2^+$ . A complementary electron swarm experiment was used to determine the ion production coefficients in a variety of gas mixtures containing  $\text{HgBr}_2$ . The measured ion production coefficients were found to be in excellent agreement with the attachment and ionization coefficients computed using the measured cross sections. Additionally, analysis of the variations in the measured  $\text{HgBr}_2$  ion production coefficients along with measured electron drift velocity variations is found to be consistent with the interpretation that vibrational excitation of  $\text{HgBr}_2$  is dominated by a resonance in the 3–5 eV electron energy range for which dissociative attachment is observed to occur.

## I. INTRODUCTION

The 502 nm  $\text{HgBr}(B-X)$  laser is a leading candidate for applications requiring an efficient ( $>1\%$ ) visible laser capable of generating relatively high average power ( $>100$  W).<sup>1</sup> Mercuric bromide  $\text{HgBr}_2$  is the source of mercurous bromide in this electrically excited laser. Modeling of this laser requires knowledge of the low energy electron  $\text{HgBr}_2$  cross sections for such processes as attachment, ionization, and vibrational and electronic excitation. In this paper we report the results of an experimental and analytical investigation directed toward determination of certain of these cross sections.

Two entirely independent, albeit complementary, experimental techniques were used in this investigation<sup>2</sup>: low energy electron-beam measurements and electron swarm measurements. Section II presents a description of electron beam measurements of the  $e\text{-HgBr}_2$  cross sections for dissociative attachment and for ionization. The principal ion products of these reactions, as identified by mass analysis, were found to be  $\text{Br}^-$  and  $\text{HgBr}_2^+$ , respectively. A complementary electron swarm experiment used to determine the corresponding electron rate coefficients for attachment and ionization is described in Sec. III. The measured rate coefficients were found to be in excellent agreement with those computed using the  $e$ -beam measured cross sections. In addition, measurements of the electron drift velocity in rare gas- $\text{HgBr}_2$  mixtures were analyzed in order to obtain information concerning vibrational excitation of  $\text{HgBr}_2$  by electrons. This analysis showed that the measured variations in the electron drift velocity and attachment coefficient are consistent with the interpretation that vibrational excitation of  $\text{HgBr}_2$  is dominated by a resonant excitation process in the 3–5 eV electron energy range for which dissociative attachment is also observed to occur.

## II. ELECTRON BEAM MEASUREMENTS

### A. Technique

Refinements to the classic Tate-Smith<sup>3</sup> electron beam method by Rapp and co-workers<sup>4–6</sup> have provided an abundance of data concerning ionization and attachment

of numerous atmospheric and rare gases, while additional works by Chantry<sup>7</sup> and by Kurepa *et al.*,<sup>8,9</sup> report cross sections for several electronegative species.

The method consists of firing a magnetically collimated electron beam through a nearly electric field-free collision chamber containing the subject gas at a known concentration. Ions formed as a result of ionizing or attaching collisions are not greatly influenced by the applied magnetic field, and under the influence of a weak transverse electric field are collected on electrodes located at opposite sides of the collision chamber. Due to their small Larmor radii, scattered electrons cannot reach these collectors and are intercepted by the chamber end walls. The remaining beam electrons are collected on an electrode located beyond the chamber. The cross section  $Q$  for the process of interest is computed from the measured ion current  $I_I$ , electron-beam current  $I_e$ , gas concentration  $n$ , and beam path length  $L$ , using the simple expression:

$$Q = I_I / (I_e n L) . \quad (1)$$

Additional information regarding the ion formation processes is obtained by mass analysis of sampled product ions.

### B. Apparatus

In the present investigation a beam experiment in the Tate-Smith configuration was used, with ion analysis provided by a quadrupole mass spectrometer. The collision chamber and mass spectrometer were housed in a stainless steel vacuum chamber whose  $10^{-7}$  Torr base pressure was maintained by a  $\text{LN}_2$  trapped diffusion pump. The system including the collision chamber and spectrometer was superheated to 390 K to preclude the possibility of forming secondary  $\text{HgBr}_2$  reservoirs. The mercuric bromide powder initially was vacuum distilled into the primary reservoir where a temperature stabilized warm water bath controlled the  $\text{HgBr}_2$  vapor pressure<sup>10</sup> during subsequent data acquisition.

#### 1. Collision chamber design

The collision chamber assembly replaced the commercial ionizer section on the quadrupole mass spec-

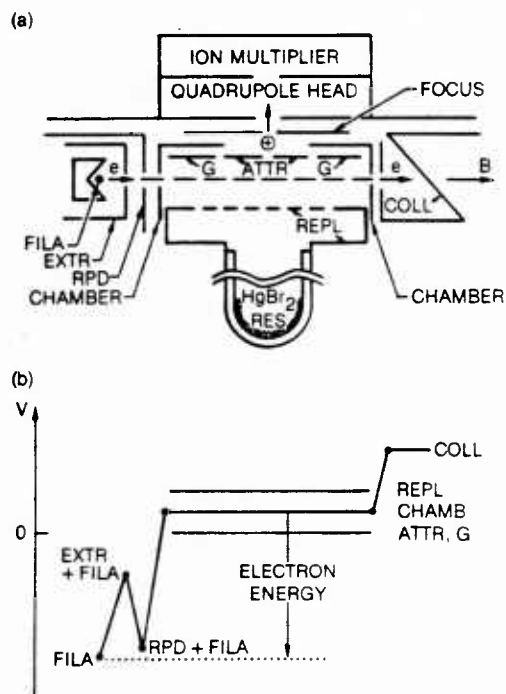


FIG. 1. Schematic illustration of the collision chamber (a), and typical voltage profile along the electron beam path (b). The voltage profile (b) is representative of a positive ion tune. For negative ion observation the polarities of REPL and CHAMB are reversed. Beam energy, sweep and RPD programming were keyboard controlled from a DEC PDP 11 computer which, in conjunction with a Tracor Northern multichannel analyzer, served to process the acquired data. An MKS Baratron capacitive pressure transducer measured the pressure at a location intermediate between the reservoir and the collision chamber.

trometer. The principal features of the chamber design are illustrated in Fig. 1 which also shows a typical potential profile. The source consisted of a dc heated thoriated iridium filament FILA, an electron extracting electrode EXTR, and a retarding potential difference plate RPD. The EXTR and RPD potentials were referenced with respect to the center potential of the filament, which was swept negatively relative to the collision chamber CHAMB to provide a beam of increasingly energetic electrons. Depending on the potential of the RPD plate relative to the filament voltage, the beam source could be operated as a conventional electron source or, for high resolution measurements in the RPD mode,<sup>11,12</sup> where the voltage increment was provided on alternate electron energy sweeps.

The electron beam was constrained to a nearly linear path in the collision chamber by a field of up to 600 gauss provided by external electromagnets. The collision chamber proper comprised four electrically isolated elements: the chamber piece CHAMB that contained the beam entrance and exit apertures at a separation of 3.34 cm; the repeller REPL that consisted of a perforated sidewall backed by a small plenum coupled to the reservoir tube; the attractor ATTR with its ion sampling aperture; and the split guard electrode G that minimized leakage currents and defined the 1.10 cm ion

collection length of the attractor. The chamber elements were precision formed from 0.25 mm stainless steel stock, insulated from each other by shielded alumina spacers and, when assembled into the collision chamber, constituted an enclosure from which the loss of vapor occurred principally through the beam apertures. Finally, the collector electrode COLL was configured such as to minimize the possibility of reflected or secondary electrons returning to the collision chamber.

Collision chamber electrode voltages were tuned to sustain the potential on the electron beam path within the chamber at a level equal to the potential applied to the chamber end faces, while a sufficient transverse field was maintained between the repeller and attractor/guard electrodes to saturate ion current collection. To permit observation of the ions by the quadrupole spectrometer whose entrance aperture was grounded, the chamber voltage was biased typically several volts positive or negative depending on the polarity of ions under study. The attractor and collector currents were measured with Keithley electrometers in series with a bias battery. Selectively, the output signals from either of the electrometers could be sent to a multichannel analyzer/DEC PDP 11 controller system for subsequent evaluation of the cross sections.

Products of the electron-HgBr<sub>2</sub> collisions were identified by extracting a portion of the attractor-directed ion current through an aperture in that electrode. The Electronic Associates Quad 200 Residual Gas Analyzer utilized for mass analysis was equipped with a Channeltron 4039 (Ruggedized) ion multiplier that was used in the pulse counting mode. Since multiplier gain deteriorated during measurements of HgBr<sub>2</sub> fragment ions, observation at the lowest feasible chamber pressure and sampling current level was required.

### C. System calibration

Absolute energy scales and magnitudes for the cross sections were established by system calibrations employing krypton and xenon, whose ionization cross sections are well known.<sup>4</sup> At the submillitorr pressures of these studies, free molecular flow considerations indicate that while the loss rate of gas from the chamber is mass dependent, the ratio of the pressure as measured at the Baratron gauge to that existing in the collision chamber remains species independent.<sup>4</sup> To determine this ratio, Xe and Kr were separately leaked through the reservoir into the chamber to various gauge pressures in the 10<sup>-4</sup>–10<sup>-2</sup> Torr range. The energy dependence of the measured attractor-to-beam current ratio ( $I_i/I_e \propto Q_i$ ) was found to duplicate that measured by Rapp and Englander-Golden.<sup>4</sup> Using the reported magnitudes of  $Q_i$  at 70 eV, the gas density  $n$  in the collision chamber was computed using Eq. (1). Comparison of this value with that determined from manometer readings established the apparatus calibration factor of  $0.33 \pm 0.03$ . Using this factor, HgBr<sub>2</sub> concentrations in the collision chamber were determined from capacitance manometer readings and measured temperatures during the mercuric bromide measurements.

The linear voltage sweep of the electron beam was calibrated to an absolute energy scale using current cut-off at zero energy and the well-established<sup>13</sup> ionization thresholds of Xe and Kr.

#### D. HgBr<sub>2</sub> ionization cross sections

The total electron impact cross section for ionization of mercuric bromide from threshold to 70 eV was determined from measurements using Eq. (1). Electron beam currents in the 10<sup>-8</sup> A to low 10<sup>-7</sup> A range were selected to eliminate space charge effects of the source. Attractor ion currents were limited to several percent of this beam current by setting reservoir temperatures to provide chamber densities between 10<sup>12</sup> and 10<sup>13</sup> cm<sup>-3</sup>. Over these ranges of parameters, for all magnetic fields above 200 gauss, and for reasonable variations in the chamber tune, the measured electron energy dependence of the HgBr<sub>2</sub> ionization cross section was repeatable to within  $\pm 3\%$  for all electron energies.

The measured total cross section for ionization of HgBr<sub>2</sub> is shown in Fig. 2 with tabulated values presented in Table I. As is typical of many gases, the ionization cross section is a generally featureless function of electron energy, rising nearly linearly from threshold (10.6 eV for HgBr<sub>2</sub>) toward a maximum value at an energy above 70 eV. The measured ionization cross section is found to be very large, reaching a peak of about  $2 \times 10^{-15}$  cm<sup>2</sup> at 70 eV. In contrast to the rare gas calibration measurements, the measured  $I_t/I_e$  ratio and the manometer readings exhibited considerable random scatter in the presence of HgBr<sub>2</sub> vapor. Consideration of the possible error in the instrument calibration factor discussed earlier ( $\pm 10\%$ ), variations in the ratio of the detected currents ( $\pm 12\%$ ), and the observed scatter in the measured pressure readings ( $\pm 20\%$ ) results in an estimated uncertainty of approximately  $\pm 25\%$  for the HgBr<sub>2</sub> ionization cross section.

There are several correlations between the ionization cross section and the electron polarizability of molecules.<sup>14,15</sup> Consideration of the large value of HgBr<sub>2</sub> polarizability<sup>16</sup> (11.5 Å<sup>3</sup>), in light of these correlations,

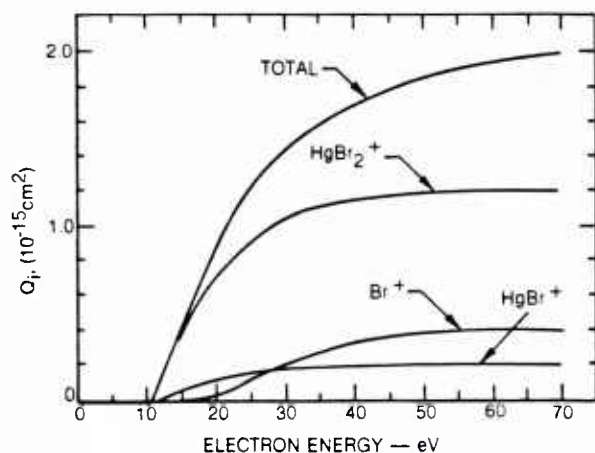


FIG. 2. Measured total and partial cross sections for electron impact ionization of HgBr<sub>2</sub>.

TABLE I. HgBr<sub>2</sub> cross sections for ionization and attachment.

Energy (eV)	$Q_i (10^{-15} \text{ cm}^2)$	Energy (eV)	$Q_a (10^{-17} \text{ cm}^2)$
10.62	0	3.1	0
12.5	0.18	3.2	0.18
15	0.41	3.3	0.4
17.5	0.64	3.4	0.7
20	0.88	3.5	0.9
22.5	1.09	3.6	0.98
25	1.23	3.7	1.0
30	1.44	3.8	0.96
35	1.58	3.9	0.85
40	1.7	4.0	0.67
45	1.79	4.1	0.5
50	1.85	4.2	0.35
55	1.91	4.3	0.22
60	1.95	4.4	0.1
70	2.0	4.5	0

suggests a peak HgBr<sub>2</sub> ionization cross section in the range of 1 to  $2 \times 10^{-15}$  cm<sup>2</sup>, a value in satisfactory agreement with the present measurement.

#### 1. Partial ionization cross sections

The simple appearance of the total ionization cross section belies the fact that it is a charge-weighted summation of a half dozen partial cross sections, each having its own threshold and energy dependence. From the mass spectrometer measurements information regarding the energy dependence of these partial cross sections was determined. Ionization processes leading to the production of the singly charged ions HgBr<sub>2</sub><sup>+</sup>, HgBr<sup>+</sup>, Br<sup>+</sup>, and Hg<sup>+</sup> contribute to the total ionization level at low electron energies, whereas HgBr<sub>2</sub><sup>2+</sup>, HgBr<sup>2+</sup>, and Br<sup>2+</sup> formation contribute to the net electron yield at high energies. Placing the partial cross sections on a true relative scale was not possible using the present beam experiment due to the unknown transmission efficiency of the ion extraction optics and the quadrupole mass spectrometer over such a broad ion mass range. However, relative abundances of HgBr<sub>2</sub><sup>+</sup>, HgBr<sup>+</sup>, Br<sup>+</sup>, and Hg<sup>+</sup> produced by 70 eV electrons impacting on mercuric bromide have been reported.<sup>17</sup> In the present study, these relative ion abundance values were used along with the measured cross section shapes to provide the approximate partial ion cross section estimates shown in Fig. 2.

#### E. HgBr<sub>2</sub> dissociative attachment

Operation of the beam experiment with key potentials reversed permitted determination of the cross sections for negative ion production processes having cross section values in excess of approximately  $3 \times 10^{-19}$  cm<sup>2</sup>. The total electron attachment cross section  $Q_a$ , in HgBr<sub>2</sub> was found to be resonant in character, consisting of a single peak located between 3.1 and 4.5 eV and centered at about 3.7 eV. Mass spectrometer analysis revealed that the process being observed was dissociative attachment leading to Br<sup>-</sup> formation. The measured electron energy dependence of the attachment cross section is presented in Fig. 3 and Table I. The peak value of 1

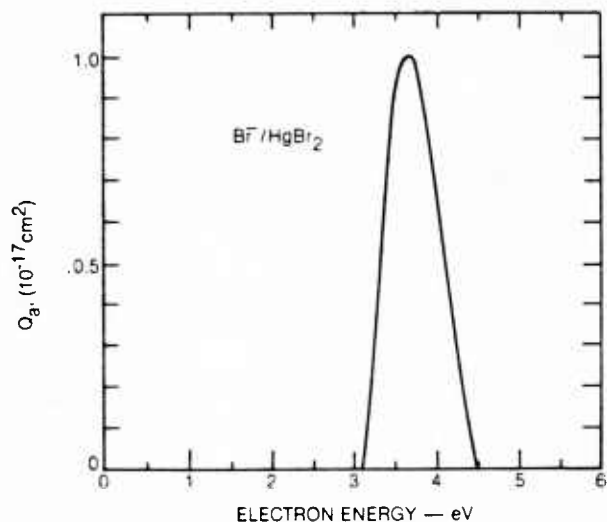


FIG. 3. Dissociative attachment cross section for electrons in  $\text{HgBr}_2$ ; the negative ion product of this reaction is  $\text{Br}^-$ .

$\times 10^{-17} \text{ cm}^2$  at 3.7 eV was determined in alternate calibrations of the peak attachment cross section and the total ionization cross section at 70 eV. These dual calibrations were obtained at common  $\text{HgBr}_2$  reservoir temperatures over a range of  $\text{HgBr}_2$  densities varying by a factor of 10 and centered at a vapor concentration of  $3 \times 10^{12} \text{ cm}^{-3}$ . Owing to uncertainties in the mercuric bromide chamber density  $n$  and the observed scatter in the  $I_t/I_e$  ratio ( $\pm 20\%$ ) at the less than  $10^{-11} \text{ A}$   $I_t$  current levels of these attachment measurements, the uncertainty of the peak attachment cross section is estimated to be approximately  $\pm 30\%$ .

### III. ELECTRON SWARM EXPERIMENTS

#### A. Technique

An electron swarm experiment was used to provide a direct measure of the rate coefficients  $k$  for production or loss of electrons due to ionization or attachment reactions in  $\text{HgBr}_2$ . This independent technique is complementary to the electron-beam measurements described in the preceding section, and is especially useful when the cross section for a particular process has a narrow energy width, and/or has a measurable value only near zero energy as is frequently the case for attachment. In these circumstances the measurement of the electron energy-weighted cross section (i.e., the rate coefficient) can often provide a more accurate measure of the effective cross section magnitude than can beam measurements which may suffer from resolution problems.

The pulsed swarm technique used in the present studies is based on the integral method pioneered by Grünberg.<sup>18</sup> In this approach a burst of electrons is introduced into a constant electric field region between two parallel electrodes by photoemission from one electrode using a suitable light source. When a proper mixture of the attaching gas and a buffer is present in the interelectrode gap, attachment and/or ionization reactions convert a portion of the rapidly drifting electron

group into much less mobile ions. The integral of the current induced in the external circuit by the motion of these electrons and ions has a very distinctive waveform which is readily interpreted in terms of the total ion production rate. By judicious selection of mixture composition, conditions can be identified for which *either* ionization or attachment dominates ion production. This method with refinements has recently been used in the study of attachment reactions in a number of halogen bearing molecules. A review<sup>19</sup> of this work by Nygaard, Brooks, and Hunter describes a typical apparatus and analysis of experimental waveforms.

#### B. Apparatus

##### 1. Measurement cell

A partial schematic of the swarm experiment used in this investigation is shown in Fig. 4. A spherical glass cell was provided with a quartz window permitting introduction of a UV light pulse, and with a set of identical planar electrodes for collection of ions and electrons. A vertical closed-end tube attached to the cell bottom served as the  $\text{HgBr}_2$  reservoir; a temporary glass appendage used to load  $\text{HgBr}_2$  into the reservoir by vacuum distillation was later sealed off. To minimize reaction with  $\text{HgBr}_2$ , the collection electrodes were gold plated and the cell was isolated from gas and vacuum manifolds by a magnetically actuated ground glass valve.

The buffer gas pressure was measured with a capacitance manometer separated from the cell by a valve that was normally closed to minimize exposure to  $\text{HgBr}_2$ . The concentration of mercuric bromide was determined from its vapor pressure<sup>10</sup> at the reservoir temperature which was maintained by an oil bath. The cell itself was electrically shielded by multiple layers of aluminum foil wrapped directly on the glass and superheated in a separate oven to control gas temperature. Thermocouples at three locations on the cell wall indicated a superheat temperature uniformity of better than 5 K at 420 K.

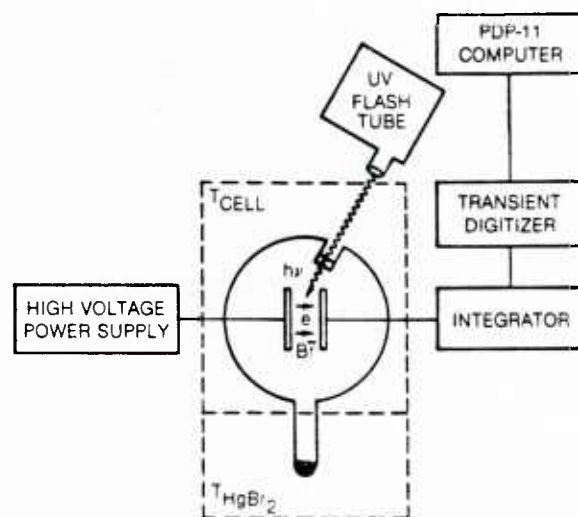


FIG. 4. Schematic illustration of the pulsed electron swarm experiment and related apparatus.

**HgBr<sub>2</sub> production.** The presence of even very small amounts of molecular impurities can have a pronounced effect on measured transport properties. For this reason mercuric bromide was synthesized by the reaction of an excess of bromine (99.999%) with mercury (99.99999%) at 60°C and then vacuum distilled three times before distillation transfer to the gas reservoir. The glass transfer tube was then sealed and this was followed by a final vaporization in vacuum.

**Photon source.** The photon source used in these studies was an EG&G FX-265 bulb-type xenon flashtube. Use of a 0.05 pf low inductance capacitor in the manufacturer's recommended circuit resulted in photoflashes of approximately 600 ns duration and of sufficient UV yield to provide the  $10^6$  photoelectrons required experimentally; larger quantities of photoelectrons caused space charge distortion of the applied electric field.

## 2. Current integrators

The electrodes were 2.5 cm in diameter and were fixed at a separation of 1.5 cm. Connected to the emitting electrode was a well-regulated dc power supply. The collecting electrode was connected through either of two integrating circuits to a Tektronix transient digitizer PDP-11 computer combination. Single pulse or average waveforms could be recorded; most of the data were obtained by averaging 64 waveforms for signal/noise improvement. The integration of the electron component of this small signal was performed on the 80 pf net capacitance of a short length of RG58 coaxial cable and the input capacitance of the amplifier plug-in. Typical electron transit times were several microseconds during which time a signal of several millivolts was developed on this integrator.

The 80  $\mu$ s RC time constant of the fast integrator made it unsuitable for observation of the ion component of the swarm signal which had a characteristic time scale of about 1 ms. However, the overall behavior of the swarm waveform was readily handled using an operational amplifier-based integrator with a feedback capacitor of 60 pf and a time constant of tens of milliseconds. Thus, electron transit times were determined from the fast integrator signal and the relative contributions of electron and ion components were obtained using the second integrator circuit. Typical integrated waveforms for electron and ion currents obtained with the transient digitizer (average of 64 waveforms) are shown in Fig. 5.

## C. Analysis of current waveforms

The pulsed swarm experiment is idealized by considering the electrons to move as a sheet between the two electrodes under the influence of an applied electric field. At pressures where gas collisions dominate and when the electron concentration is sufficiently low to avoid space charge effects, the electron drift velocity and the electron energy distribution are characterized by the gas mixture and the prevailing electric field-to-gas density ratio  $E/n$ . When attaching species are present in sufficient concentration in the gas mixture, and when the value of  $E/n$  is sufficient to ensure the

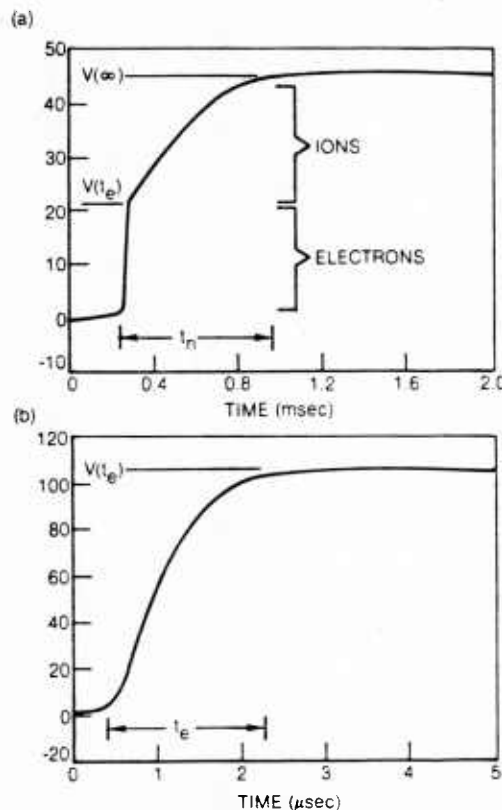


FIG. 5. Typical integrated waveforms for the ion (a) and electron (b) currents obtained with the transient digitizer as discussed in the text. The ion transit time  $t_n$  and electron transit time  $t_e$  are indicated.

presence of electrons at energies above the threshold for attachment, conversion of electrons to negative ions will take place.<sup>19</sup> Under these conditions, an exponential attenuation of the number of electrons in the sheet will occur as it sweeps across the gap. Left behind will be a spatially distributed group of negative ions which also slowly drifts toward the collector. The current induced in the external circuit as a result of the motion of these charges consists of an initial several microsecond electron spike superimposed on a slowly declining, low current component due to the less mobile negative ions. Integration of this induced current waveform has two practical benefits. First, it converts the fast, low-level current pulse into an experimentally observable voltage waveform and secondly, it makes the extraction of the attachment rate data especially straightforward.

A typical integrated waveform is displayed in Fig. 5(a). The leading edge of a similar waveform is shown in Fig. 5(b) on an expanded time scale. Note that the initial rapid rise of the integrated current to a voltage level  $V(t_e)$  ends at the electron transit time  $t_e$ . This time corresponds to electrode separation  $L$  divided by the electron drift velocity  $v_{de}$ , i.e.,

$$t_e = L/v_{de} \quad (2)$$

A further slow increase in voltage follows until the last negative ions reach the collector from their origin near the emitter. At this time, which corresponds to the

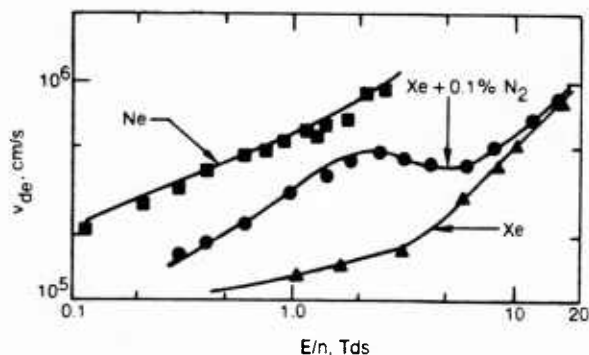


FIG. 6. Measured and computed electron drift velocity at 300 K. The drift velocity was measured at several pressures in the 50–200 Torr range and exhibited no pressure dependence.

electrode separation  $L$  divided by the negative ion drift velocity  $v_{dn}$ , i. e.,

$$t_n = L/v_{dn}, \quad (3)$$

the current integral has attained its saturated value  $V(\infty)$ . Mathematical modeling of the electron and negative ion currents and evaluation of their integrals reveals that the attachment rate coefficient  $k_a$ , the concentration of the attaching gas  $n_a$ , and the electron transit time  $t_e$ , are related to the observed voltages  $V(t_e)$  and  $V(\infty)$  by the expression<sup>19</sup>:

$$\frac{V(t_e)}{V(\infty)} = \frac{1 - \exp(-k_a n_a t_e)}{k_a n_a t_e}. \quad (4)$$

Thus, measurement of the two voltages  $V(t_e)$  and  $V(\infty)$  and the electron transit time  $t_e$ , along with a knowledge of  $n_a$  permits determination of  $k_a$ , the attachment rate coefficient. A more complex expression<sup>18</sup> for this voltage ratio applies when volume ionization augments the number of electrons in the swarm. However, in the limit where ionization greatly exceeds attachment, the shape of the integrated current is similar to that associated with attachment and

$$\frac{V(t_e)}{V(\infty)} = \frac{1 - \exp(-k_i n t_e)}{k_i n t_e}, \quad (5)$$

where  $k_i$  is the mixture weighted ionization rate coefficient and  $n$  is the total concentration of neutral species. Experimentally, the onset of ionization is readily distinguishable owing to the rapid increase in the saturation level  $V(\infty)$  with increasing  $E/n$ .

#### D. Electron drift velocity measurements

A key factor in the determination of the ion production coefficient as described above is accurate determination of the electron transit time  $t_e$  based on interpretation of the leading edge of the integrated current waveform [Fig. 5(b)]. In order to evaluate the accuracy of the present swarm experiment, the electron transit time was measured for several gases and mixtures (not containing  $\text{HgBr}_2$ ) for which the electron drift velocity is known or can be computed with high accuracy using known cross sections; gas pressure was varied in the

50–200 Torr range. The corresponding electron drift velocity data so obtained are shown in Fig. 6. Also shown is the drift velocity computed using the expression,<sup>20</sup>

$$v_{de} = -\left(\frac{2e}{m}\right)^{1/2} \frac{E/n}{3} \int_0^\infty \frac{u df/du}{Q_{em}} du, \quad (6)$$

in which  $e$  and  $m$  are the electron charge and mass,  $E$  is the electric field intensity,  $n$  is the total number density of neutrals,  $f$  is the isotropic component of the electron energy distribution function,  $Q_{em}$  is the mixture weighted momentum transfer cross section, and  $u$  is the electron energy expressed in eV. The electron distribution function was determined by numerical solution<sup>20</sup> of the Boltzmann equation for a uniform medium using the known cross sections for Xe,<sup>21</sup> Ne,<sup>22</sup> and  $\text{N}_2$ .<sup>23</sup> The observed agreement (Fig. 6) between the computed and measured drift velocity values in Ne and Xe essentially duplicates results reported by others<sup>21,22</sup> and is indicative of the degree to which the present experimental configuration simulates an infinite, uniform electron drift region. The ability to compute the drift velocity for mixtures such as Xe + 0.1%  $\text{N}_2$ , for which experimental data were not previously available, is more significant and provides an effective illustration of how observed variations in drift velocity can be interpreted in terms of fundamental electron collision processes involving both mixture constituents. For example, the particularly large increase in the drift velocity upon addition of 0.1%  $\text{N}_2$  to Xe is a consequence both of the Ramsauer minimum in the Xe momentum transfer cross section<sup>21</sup> in the vicinity of 0.5 eV, and the resonance in the  $\text{N}_2$  vibrational cross sections<sup>23</sup> near 2.0 eV. For  $E/n$  values of a few Tds in the Xe + 0.1%  $\text{N}_2$  mixture, resonant vibrational excitation of  $\text{N}_2$  results in a mean electron energy of a few tenths of an eV, an energy for which the Xe momentum transfer cross section is at its minimum. Since the drift velocity is inversely proportional to the momentum transfer cross section [Eq. (6)], this results in an unusually large increase in the drift velocity even though the  $\text{N}_2$  fractional concentration is only 0.001.

**Drift velocity in Xe- $\text{HgBr}_2$  mixtures.** Detailed measurements of electron drift velocity in Xe- $\text{HgBr}_2$  mixtures were carried out for a Xe pressure and temperature of 140 Torr and 140°C, respectively; these values specify a Xe neutral number density of about  $3 \times 10^{18} \text{ cm}^{-3}$ . Data were obtained over a wide range of  $E/n$  values for three  $\text{HgBr}_2$  reservoir temperatures corresponding to  $\text{HgBr}_2$  fractional concentrations of 0.067%, 0.135%, and 0.25%. For fixed  $E/n$  the change in the drift velocity as the  $\text{HgBr}_2$  concentration was increased (or decreased) was readily apparent. Figure 7 presents the  $E/n$  variation of the measured drift velocity for a mixture containing 0.135%  $\text{HgBr}_2$ . The error bars indicated in the figure are primarily the result of the uncertainty associated with determination of the electron transit time from the integrated current waveforms [Fig. 5(b)]. Clearly, the qualitative variation of the measured drift velocity in Xe containing 0.135%  $\text{HgBr}_2$  is significantly different from that observed with about the same amount of  $\text{N}_2$  in Xe (Fig. 6). However, the

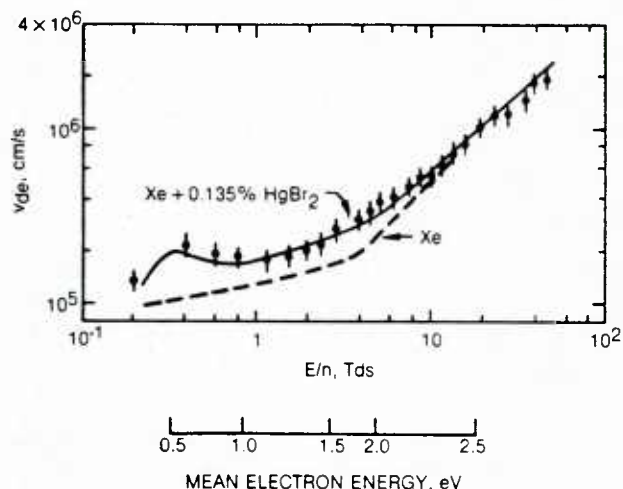


FIG. 7. Measured electron drift velocity in Xe at 140 Torr and 140 °C containing 0.135% HgBr<sub>2</sub>. Also shown is the drift velocity computed for this mixture using the cross sections shown in Fig. 12 as described in Sec. III F of the text. For comparison the drift velocity in Xe (Fig. 6) is also shown.

magnitude of the measured change in the drift velocity for  $E/n$  values of a few Tds is of approximately the same order as that observed with 0.1% N<sub>2</sub> in Xe. For HgBr<sub>2</sub> fractional concentrations higher (lower) than 0.135% the measured drift velocity variation as compared to Xe alone was greater (less) than that shown in Fig. 7.

Since the Xe:HgBr<sub>2</sub> concentration ratio is approximately 10<sup>3</sup> for these conditions, and since the momentum transfer cross section for Xe is relatively large even at its minimum value ( $\sim 10^{-17}$  cm<sup>2</sup>), the drift velocity in Xe-HgBr<sub>2</sub> mixtures is not significantly affected by  $e$ -HgBr<sub>2</sub> momentum transfer collisions. Rather, as is also the case for the Xe-0.1% N<sub>2</sub> mixture, the dependence of the drift velocity on HgBr<sub>2</sub> concentration reflects changes in the electron distribution function caused by low energy electron inelastic collisions with HgBr<sub>2</sub> [Eq. (6)]. The observed changes in the measured drift velocity can be interpreted on the basis of  $e$ -HgBr<sub>2</sub> vibrational excitation, a topic to be discussed in a subsequent section.

## E. Ion production rate measurements

### 1. Attachment in Xe-HgBr<sub>2</sub> mixtures

The electron attachment coefficient for Xe-HgBr<sub>2</sub> mixtures was determined by employing Eq. (4) in conjunction with measured drift velocity data (i.e., the electron transit time) (Fig. 7) and corresponding measurements of the voltages  $V(t_e)$  and  $V(\infty)$ , [Fig. 5(a)]. Measured values of the attachment coefficient so determined are presented in Fig. 8, along with values computed using the attachment cross section of Fig. 3 and the expression,<sup>20</sup>

$$k_a = \left(\frac{2e}{m}\right)^{1/2} \int_0^\infty u f Q_a(u) du. \quad (7)$$

For the purposes of this and subsequent calculations of

$k_a$  the magnitude of the attachment cross section of Fig. 3 was reduced by 12%, an adjustment well within the estimated  $\pm 30\%$  accuracy of the measured cross section.

The strong dependence of  $k_a$  on  $E/n$  at the lower values of the latter reflects the interaction of the tail of the electron energy distribution and the threshold region of the attachment cross section (Fig. 3). For higher  $E/n$  values the bulk of the electrons have energies of a few eV, the region where  $Q_a$  peaks (Fig. 3), and the attachment coefficient reaches a plateau as indicated. Throughout the entire  $E/n$  region, the measured and computed attachment coefficients are found to be in very good agreement up to a value of about 30 Tds for this mixture. Recall, however, that the present measurement technique is sensitive to the *total* ion production rate, not simply the production of negative ions. Indeed, calculations show that the sharp increase in the measured ion production rate coefficient for an  $E/n$  value above approximately 35 Tds reflects the onset of Xe ionization rather than a change in the nature of the production of Br<sup>-</sup> by way of the attachment reaction. Figure 8 shows that the computed value of the Xe<sup>+</sup> ion production coefficient, weighted to account for the Xe:HgBr<sub>2</sub> concentration ratio, is in excellent agreement with the observed increase in the measured total ion production coefficient for high  $E/n$  values. Comparison of the computed ionization rate coefficients for Xe and HgBr<sub>2</sub> shows that for this mixture the effect of Xe ionization is very much greater than that of HgBr<sub>2</sub>.

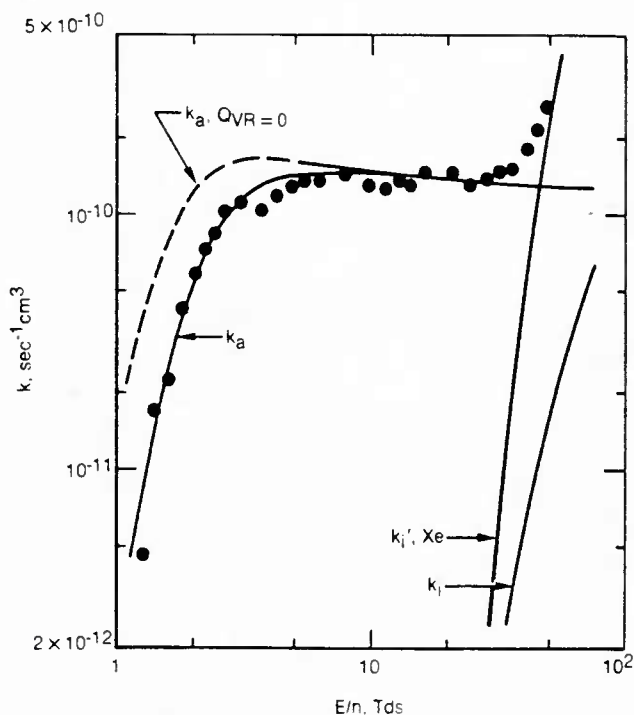


FIG. 8. Measured ion production coefficient for a Xe-0.135% HgBr<sub>2</sub> mixture at a total neutral number density of  $3 \times 10^{18}$  cm<sup>-3</sup> and a temperature of 140 °C. Also shown are computed rate coefficients for HgBr<sub>2</sub> attachment  $k_a$  and ionization  $k_i$  along with the Xe ionization coefficient  $k_i'$  mixture weighted to account for the Xe/HgBr<sub>2</sub> concentration ratio. The attachment coefficient labeled  $Q_{VR}=0$  was computed neglecting resonant vibrational excitation of HgBr<sub>2</sub> as discussed in the text.

## 2. Ionization in $N_2$ - $HgBr_2$ mixtures

Because of a rather fortuitous combination of circumstances, measurement of the ion production rate coefficient in  $N_2$ - $HgBr_2$  mixtures provides a means for determining the  $HgBr_2$  ionization rate coefficient rather than the attachment rate coefficient. The reason for this can be understood by examination of Fig. 9 showing measured values of the total ion production coefficient and computed values of both the  $HgBr_2$  attachment and ionization coefficient in an  $N_2$ - $HgBr_2$  mixture. Comparison of Figs. 8 and 9 reveals a marked qualitative and quantitative difference between the measured ion production coefficients and between the computed attachment coefficients in the  $N_2$ - $HgBr_2$  and  $Xe$ - $HgBr_2$  mixtures. Analysis of the calculated attachment coefficients shows that these differences are a reflection of important differences in the electron energy distribution functions for the two mixtures. For  $E/n$  values below about 50 Td in the  $N_2$ - $HgBr_2$  mixture, resonant vibrational excitation of  $N_2$  results in a truncated electron energy distribution function<sup>20,23</sup> at an energy of about 2.0 eV, a value less than the 3 eV required for  $HgBr_2$  dissociative attachment (Fig. 3). For this reason, at low  $E/n$  values the attachment rate coefficient is very much less in the  $N_2$ - $HgBr_2$  mixture than is the case for the  $Xe$ - $HgBr_2$  mixture. Indeed, the calculated rate coefficients of Fig. 9 indicate that by the time  $E/n$  is large enough in the  $N_2$ - $HgBr_2$  mixture to result in an attachment coefficient comparable to that of the  $Xe$ - $HgBr_2$

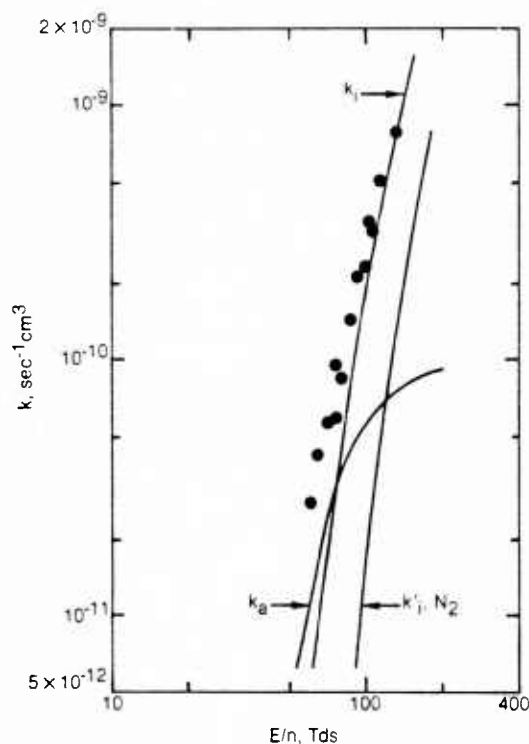


FIG. 9. Measured ion production coefficient for a  $N_2$ -2%  $HgBr_2$  mixture at a total neutral number density of  $1.9 \times 10^{18} \text{ cm}^{-3}$  and a temperature of  $170^\circ \text{C}$ . Also shown are computed rate coefficients for  $HgBr_2$  attachment  $k_a$  and ionization  $k_i$  along with the  $N_2$  ionization coefficient  $k_i'$  mixture weighted to account for the  $N_2$ - $HgBr_2$  concentration ratio.

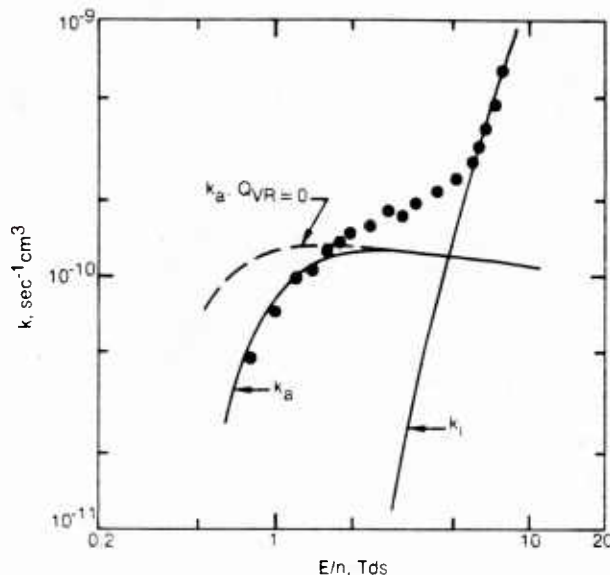


FIG. 10. Measured ion production coefficient for a  $Ne$ -0.2%  $HgBr_2$  mixture at a total neutral number density of  $3 \times 10^{18} \text{ cm}^{-3}$  and a temperature of  $140^\circ \text{C}$ . Also shown are the computed rate coefficients for  $HgBr_2$  attachment  $k_a$  and ionization  $k_i$ . The attachment coefficient labeled  $Q_{VR}=0$  was computed neglecting resonant vibrational excitation of  $HgBr_2$  as discussed in the text.

mixture ( $\sim 10^{-10} \text{ s}^{-1} \text{ cm}^3$ ), direct ionization of  $HgBr_2$  has already become the dominant  $HgBr_2$  ion production process. As shown in Fig. 9, ionization of  $N_2$  is not significant because of the high  $N_2$  ionization potential and relatively small ionization cross section. Thus, for this mixture the swarm experiment provides a means for determination of the  $HgBr_2$  ionization coefficient. Examination of Fig. 9 shows that the measured ion production coefficient in this  $N_2$ - $HgBr_2$  mixture is in very good agreement with the computed value of the  $HgBr_2$  ionization rate coefficient, the latter obtained using Eq. (7) and the measured ionization cross section of Fig. 2.

## 3. $Ne$ - $HgBr_2$ mixtures

While the  $HgBr_2$  attachment coefficient can be determined using  $Xe$ - $HgBr_2$  mixtures (Fig. 8) and the  $HgBr_2$  ionization coefficient can be determined in  $N_2$ - $HgBr_2$  mixtures, both attachment and ionization of  $HgBr_2$  are found to be important in  $Ne$ - $HgBr_2$  mixtures. Presented in Fig. 10 is the measured ion production rate coefficient in a  $Ne$ - $HgBr_2$  mixture for conditions similar to those for Figs. 8 and 9, along with computed values of the rate coefficients for attachment and ionization of  $HgBr_2$ . Ionization of  $Ne$  is insignificant for these conditions. Comparison of the experimental and analytical ion production coefficients shows that for this mixture attachment is dominant for  $E/n$  values below about 3 Tds and  $HgBr_2$  ionization dominates for  $E/n$  above 5 Tds, with both processes contributing to ion production in the intermediate  $E/n$  regime.

Because  $Xe$  and  $N_2$  have thresholds for electronic excitation which are below the 10.62 eV ionization poten-

tial of  $\text{HgBr}_2$ , and are present in much larger concentrations, the  $E/n$  value for which ionization becomes important in those mixtures (Figs. 8 and 9) is largely determined by the electronic cross sections of Xe and/or  $\text{N}_2$ . However, the threshold for electronic excitation in Ne is well above 10.62 eV, with the result that the  $E/n$  value for which  $\text{HgBr}_2$  ionization becomes important in Ne- $\text{HgBr}_2$  mixtures is determined in large measure by the cross sections for  $\text{HgBr}_2$  electronic excitation. For this reason the  $E/n$  variation of the measured ion production coefficient in Ne/ $\text{HgBr}_2$  mixtures provides valuable information concerning the magnitude of the  $\text{HgBr}_2$  cross sections for electronic excitation. Indeed, the  $\text{HgBr}_2$  electronic cross sections used in the computation of  $k_a$  and  $k_i$  for the conditions of Fig. 10 were inferred on the basis of the present swarm measurements in conjunction with analysis of the properties of electron-beam controlled discharges in Ne- $\text{HgBr}_2$  mixtures.<sup>24</sup> These latter results will be reported elsewhere.

### F. Vibrational excitation of $\text{HgBr}_2$

As discussed earlier in connection with Eq. (6) and Fig. 7, the electron drift velocity in atomic gases containing a small amount of a molecular additive is particularly sensitive to changes in the electron distribution function caused by inelastic electron collisions with the molecular species. Thus, when the qualitative and quantitative change in the drift velocity can be measured accurately over a wide range of conditions, the drift velocity itself can be used as a diagnostic to obtain information concerning the nature of the inelastic electron-molecule collision processes.<sup>21-23</sup> As part of the present study the observed changes in the drift velocity in Xe containing variable amounts of  $\text{HgBr}_2$  were analyzed in order to investigate electron- $\text{HgBr}_2$  inelastic collision processes, particularly vibrational excitation.

Electron cross sections for electronic excitation of  $\text{HgBr}_2$  have been recently inferred in connection with  $\text{HgBr}/\text{HgBr}_2$  laser studies.<sup>24,25</sup> Although the inferred electronic cross sections are found to be large ( $>10^{-17} \text{ cm}^2$ ), computation of the electron distribution function for the conditions of Fig. 7 using these  $\text{HgBr}_2$  electronic cross sections alone shows that the resultant change in the drift velocity is quite a bit less than that measured in the present investigation, and that the qualitative variation of the drift velocity with  $E/n$  is substantially different from that observed. Additionally, the  $E/n$  dependence of the computed attachment coefficient in Xe and Ne- $\text{HgBr}_2$  mixtures differs substantially from measured values. Considering that the mean electron energy is approximately one eV for these conditions, the most probable explanation for such discrepancies is the effect on the electron energy distribution of low energy electron collision processes, particularly  $\text{HgBr}_2$  vibrational excitation.

#### 1. Resonant e- $\text{HgBr}_2$ vibrational excitation

The large body of evidence concerning electron vibrational excitation of molecules indicates that vibrational excitation is often likely to proceed by way of resonant

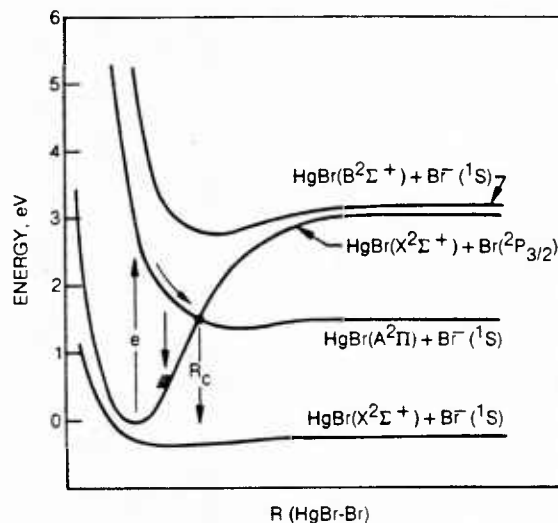
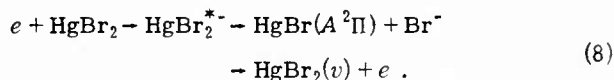


FIG. 11. Illustration showing representative  $\text{HgBr}_2^{*-}$  potential energy curves. The two exit channels corresponding to  $\text{HgBr}_2$  vibrational excitation and attachment following resonant excitation of the lowest energy  $\text{HgBr}_2^{*-}$  state are illustrated. Dissociative attachment cannot occur unless the attached electron survives until the critical separation distance  $R_c$  is reached.

electron capture by the molecule.<sup>23,26,27</sup> The intermediate resonant molecular negative ion state so formed subsequently decays through a number of exit channels resulting principally in vibrational excitation and dissociative attachment in those situations for which a stable negative ion can be formed. For this reason our observation of a resonant character in the  $\text{HgBr}_2$  cross section for dissociative attachment provides a very valuable clue to the occurrence of resonant vibrational excitation of  $\text{HgBr}_2$ .

Figure 11 shows that the observation of a resonance in the attachment cross section in the 3-5 eV range is consistent with  $\text{HgBr}_2^{*-}$  states likely to be formed<sup>28,29</sup> from  $\text{HgBr}$  and  $\text{Br}^-$ . This figure illustrates the two  $\text{HgBr}_2^{*-}$  states that correlate with  $\text{HgBr}(B^2\Sigma^+)$  and  $\text{HgBr}(A^2\Pi)$ , respectively. Although it has been suggested<sup>30</sup> that the primary neutral fragment of  $\text{HgBr}_2$  dissociative attachment is  $\text{HgBr}(B^2\Sigma^+)$ , interpretation of the  $\text{HgBr}(B-X)$  fluorescence characteristics in electron-beam controlled discharges<sup>24</sup> indicates that the dominant neutral fragment is  $\text{HgBr}(A,X)$ . Thus, it seems likely that excitation of the lower energy  $\text{HgBr}_2^{*-}$  state indicated in Fig. 11 dominates resonant electron capture, i.e.,



On the basis of the preceding arguments trial cross sections for resonant  $\text{HgBr}_2$  vibrational excitation were constructed for use in solution of the Boltzmann equation for the conditions of Figs. 7, 8, and 10 following the usual iterative procedure.<sup>22,23</sup> These trial cross sections were adjusted until satisfactory agreement between the measured and computed electron drift velocity and attachment coefficient was obtained. The computed

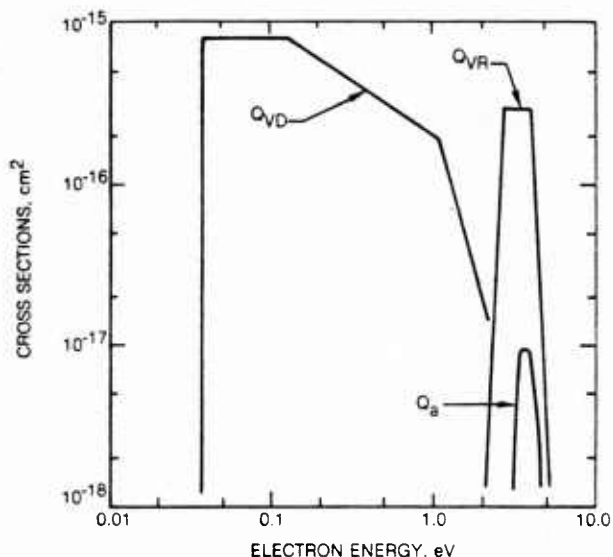


FIG. 12. Inferred cross sections for vibrational excitation of  $\text{HgBr}_2$  by direct processes  $Q_{VD}$  having an energy loss of 0.035 eV, and by resonant excitation,  $Q_{VR}$ , with an effective energy loss taken to be 0.25 eV. The measured cross section for dissociative attachment (Fig. 3) is also shown for comparison.

curves shown in Figs. 7, 8, and 10 are the result of this procedure and the cross sections used in the calculation are presented in Fig. 12. The effective electron energy loss used in conjunction with the resonant vibrational cross section,  $Q_{VR}$ , shown in Fig. 12 was 0.25 eV. Thus, the effective energy loss-cross section product of approximately  $10^{-16} \text{ cm}^2 \text{ eV}$  is intended to reflect the combined effect of excitation of a great many  $\text{HgBr}_2$  vibrational levels.

Figures 8 and 10 show that the strong increase in the computed attachment coefficient as  $E/n$  is increased is particularly sensitive to the nature of  $Q_{VR}$ . These figures show that for the lower  $E/n$  values the attachment coefficient computed using all  $\text{HgBr}_2$  cross sections except  $Q_{VR}$  is a factor of two-to-three times higher than the measured values of the ion production coefficients. However, inclusion of the cross section  $Q_{VR}$  in the calculation depresses the tail of the electron energy distribution in the threshold region of the attachment cross section, significantly affecting the  $E/n$  variation of the attachment coefficient.

## 2. Direct vibrational excitation

Calculations show that the computed electron drift velocity in the  $\text{Xe-HgBr}_2$  mixture of Fig. 7 is sensitive to the resonant portion of the vibrational cross section  $Q_{VR}$  in the 1.0–7.0 Td  $E/n$  range. Below about 1 Td  $Q_{VR}$  has very little effect on the drift velocity. Thus, in order to account for the observed distinctive drift velocity variation in  $\text{Xe-HgBr}_2$  mixture for  $E/n$  below 1 Td (Fig. 7), a low energy electron  $\text{HgBr}_2$  inelastic process, assumed to be direct (i.e., nonresonant) vibrational excitation, was taken into account.

Only the fundamental bending and asymmetric stretch modes<sup>31</sup> of  $\text{HgBr}_2$ , having excitation energies of 0.005

and 0.035 eV, have transition dipole moments. Thus, assuming that electric dipole scattering dominates non-resonant vibrational excitation, only these modes are expected to have appreciable cross sections for electron energy well above threshold. However, calculations show that even the lowest  $E/n$  values of the present experiment correspond to mean electron energies very much higher than the 0.035 eV threshold of the asymmetric stretch mode. For this reason the present experimental data do not permit separation of direct vibrational excitation into its various components (nor is it possible to determine the influence of rotational and/or elastic energy loss). Therefore, a single cross section  $Q_{VD}$  was used for analysis of the low  $E/n$  drift velocity data, having a threshold of 0.035 eV and the energy variation shown in Fig. 12. The magnitude of this cross section was adjusted until satisfactory agreement between the measured and computed drift velocity data for low  $E/n$  values in  $\text{Xe-HgBr}_2$  mixtures was obtained (Fig. 7).

## IV. SUMMARY

In this investigation an electron beam experiment has been used to measure the cross sections for  $\text{HgBr}_2$  dissociative attachment and ionization to an accuracy estimated to be  $\pm 25\%$ . The dominant ion products of these reactions have been determined from mass analysis to be  $\text{Br}^-$  and  $\text{HgBr}_2^+$ . Measurement of the total positive and negative ion production coefficients in several gas mixtures containing  $\text{HgBr}_2$  using an electron swarm experiment has revealed dramatic differences in the nature of  $\text{HgBr}_2$  related ion production processes (Figs. 8–10). Detailed analysis shows that the observed sensitivity of  $\text{HgBr}_2$  ion production to the nature of the background gas is a manifestation of a sensitivity to the electron energy distribution. The sensitivity to the electron distribution function arises from the facts that the energy thresholds for  $\text{HgBr}_2$  attachment and ionization are relatively high and low, respectively; and the electron cross sections for both processes are relatively large.

Very good agreement between measured and computed attachment coefficients is obtained over a wide range of  $E/n$  values and mixture conditions if vibrational excitation of  $\text{HgBr}_2$  is taken into account. Indeed, the best agreement between measured and computed attachment coefficients and electron drift velocity data is obtained if it is assumed that vibrational excitation of  $\text{HgBr}_2$  is dominated by a resonant excitation process in the 3–5 eV electron energy range for which dissociative attachment is also observed to occur. On the basis of this interpretation an effective cross section for resonant vibrational excitation of  $\text{HgBr}_2$  has been determined by iterative solution of the Boltzmann equation for the conditions of the present experiments. The cross section so determined is assigned an energy loss of 0.25 eV so that the inferred peak cross section-energy loss product of approximately  $1 \times 10^{-16} \text{ cm}^2 \text{ eV}$  represents the combined effect of excitation of a great many  $\text{HgBr}_2$  vibrational levels. The computed attachment coefficients and drift velocities are not unduly sensitive to specific details of either the magnitude of the vibrational cross section so inferred or the effective energy loss, so long

as the energy loss-cross section product is about  $10^{-16}$  cm<sup>2</sup> eV and the effective cross section has an energy width of approximately 1–2 eV centered in the 3–4 eV range. In this connection it is important to re-emphasize that only the cross sections for attachment and ionization of HgBr<sub>2</sub> have been measured. The present inference of resonant vibrational excitation, although consistent with the experimental observations of this investigation, should be considered provisional pending actual measurement of *e*-HgBr<sub>2</sub> cross sections for vibrational excitation.

## ACKNOWLEDGMENTS

It is a pleasure to acknowledge helpful discussions with our UTRC colleagues R. T. Brown, H. H. Michels, and L. R. Boedeker, and with Professor D. W. Setser of Kansas State University and Professor A. Herzenberg of Yale University who provided valuable insight as to the likely nature of HgBr<sub>2</sub> vibrational excitation. Additionally, the expert technical assistance of W. E. Conklin, J. A. Post, and R. E. Cutting is greatly appreciated. This work was supported in part by the Naval Ocean Systems Center and by the Office of Naval Research.

- <sup>1</sup>R. Burnham and E. J. Schimitschek, *Laser Focus* 17, 54 (1981); E. J. Schimitschek and J. E. Celto, *Appl. Phys. Lett.* 36, 176 (1980); W. L. Nighan, *Appl. Phys. Lett.* 36, 173 (1980).
- <sup>2</sup>W. J. Wiegand and L. R. Boedeker, *Appl. Phys. Lett.* 40, 225 (1982).
- <sup>3</sup>J. T. Tate and P. T. Smith, *Phys. Rev.* 39, 270 (1932).
- <sup>4</sup>D. Rapp and P. Englander-Golden, *J. Chem. Phys.* 43, 1464 (1965).
- <sup>5</sup>D. D. Briglia and D. Rapp, *J. Chem. Phys.* 42, 3201 (1965).
- <sup>6</sup>D. Rapp and D. D. Briglia, *J. Chem. Phys.* 43, 1480 (1965).
- <sup>7</sup>P. J. Chantry, *Phys. Rev.* 172, 125 (1968).
- <sup>8</sup>M. V. Kurepa and D. S. Belic, *J. Phys. B* 11, 3719 (1978).
- <sup>9</sup>M. V. Kurepa, V. M. Pejcev, and I. M. Cadez, *J. Phys. D* 9, 481 (1976).
- <sup>10</sup>Vapor pressures for HgBr<sub>2</sub> were computed from the JANAF thermochemical tables [(D. R. Stull and H. Prophet: *Nat. Stand. Ref. Data Ser.* 37, (1971)] for the range of temperatures 300 to 600 K. Pressure at 300 K is  $1.2 \times 10^{-4}$  Torr and at higher temperatures is consistent with the tabular data listed by L. Brewer in *The Chemistry and Metallurgy of Miscellaneous Materials*, edited by L. L. Quill (McGraw-Hill, New York, 1950).
- <sup>11</sup>R. E. Fox, W. M. Hickam, D. J. Grove, and T. Kjeldaa, *Rev. Sci. Instrum.* 26, 1101 (1955).
- <sup>12</sup>P. J. Chantry, *Rev. Sci. Instrum.* 40, 884 (1969).
- <sup>13</sup>H. M. Rosenstock, K. Draxl, B. W. Steiner, and J. T. Herron, *J. Phys. Chem. Ref. Data* 6, Suppl. 1, (1977).
- <sup>14</sup>R. E. Center and A. Mandl, *J. Chem. Phys.* 57, 4104 (1972).
- <sup>15</sup>F. W. Lampe, J. L. Franklin, and F. H. Field, Jr., *J. Am. Chem. Soc.* 79, 6129 (1957).
- <sup>16</sup>Landolt-Bornstein, *Zahlenwerte und Funktionen*, 6 *Auflage*, *Atom und Molecular-physik* (Springer, Berlin, 1951), Vol. 3, p. 514. The value of  $P_E$  reported therein was converted to polarizability  $\alpha$  using the expression  $\alpha = 0.3963 P_E$ .
- <sup>17</sup>R. W. Kiser, J. G. Dillard, and D. L. Dugger, *Ad. Chem. Ser.* 72, 153, (1968); The relative abundance of the product ions at 70 eV are: HgBr<sub>2</sub><sup>+</sup> (100.00), HgBr<sup>+</sup> (17.5), Br<sup>+</sup> (34.3), and Hg<sup>+</sup> (~0) as listed in Ref. 17.
- <sup>18</sup>R. Grünberg, *Z. Naturforsch. Teil A* 24, 1039 (1969).
- <sup>19</sup>K. J. Nygaard, H. L. Brooks, and S. R. Hunter, *IEEE J. Quantum Electron.* QE-15, 1216 (1979).
- <sup>20</sup>W. L. Nighan, *Phys. Rev. A* 2, 1989 (1970).
- <sup>21</sup>L. S. Frost and A. V. Phelps, *Phys. Rev.* 136, A1538 (1964); L. T. Specht, S. A. Lawton, and T. A. DeTemple, *J. Appl. Phys.* 51, 166 (1980).
- <sup>22</sup>A. G. Robertson, *J. Phys. B* 5, 648 (1972).
- <sup>23</sup>A. G. Engelhardt, A. V. Phelps, and C. G. Risk, *Phys. Rev.* 135, A 1566 (1946); D. C. Cartwright, S. Trajmar, A. Chutjian, and W. Williams, *Phys. Rev. A* 16, 1041 (1977).
- <sup>24</sup>W. L. Nighan and R. T. Brown, *J. Appl. Phys.* (in press).
- <sup>25</sup>M. W. McGeoch, J. C. Hsia, and D. E. Klimek (to be published).
- <sup>26</sup>G. J. Schulz, *Rev. Mod. Phys.* 45, 423 (1973).
- <sup>27</sup>D. Spence, J. L. Mauer, and G. J. Schulz, *J. Chem. Phys.* 57, 5516 (1972).
- <sup>28</sup>H. H. Michels (private communication).
- <sup>29</sup>A. Herzenberg (private communication).
- <sup>30</sup>J. Degani, M. Rokni, and S. Yatsiv, *J. Chem. Phys.* 75, 164 (1981). These investigators inferred the attachment rate in Xe-HgBr<sub>2</sub> mixtures by measuring the rate of electron density decay following an ionizing pulse of x-radiation. They report a  $k_a$  value of  $8.5 \pm 1.5 \times 10^{-11}$  s<sup>-1</sup> cm<sup>3</sup> for HgBr<sub>2</sub> fractional concentrations in the 0.02%–0.10% range and an  $E/n$  value of approximately 1.5 Td. Unfortunately, the present calculations show that  $k_a$  in Xe-HgBr<sub>2</sub> mixtures is especially sensitive to both HgBr<sub>2</sub> fractional concentration and  $E/n$  for these particular conditions (Fig. 8). Nonetheless, computation of the attachment coefficient for a variety of conditions similar to those of Ref. 30 using the cross sections of Fig. 12 results in  $k_a$  values in the range  $3.5$ – $8.0 \times 10^{-11}$  s<sup>-1</sup> cm<sup>3</sup>, in reasonable accord with the value reported by Degani and co-workers considering the sensitivity of  $k_a$  to the conditions of their experiment.
- <sup>31</sup>W. Klemperer and L. Linderman, *J. Chem. Phys.* 25, 397 (1956).

III-B. XeCl(B $\rightarrow$ X) Laser

- Properties of Electron-Beam Controlled XeCl(B $\rightarrow$ X) and HgBr(B $\rightarrow$ X) Laser Discharges
- Efficient XeCl(B) Formation in an Electron-Beam Assisted Xe/HCl Discharge

# 11

## *Properties of Electron-Beam Controlled $\text{XeCl}(B \rightarrow X)$ and $\text{HgBr}(B \rightarrow X)$ Laser Discharges*

**William L. Nighan**

United Technologies Research Center  
East Hartford, Connecticut

I. Introduction . . . . .	319
II. Electron-Beam Controlled Discharges . . . . .	321
A. Application to Electronic Transition Lasers . . . . .	322
III. Rare-Gas Halide and Mercury Halide Lasers . . . . .	325
A. $\text{XeCl}(B \rightarrow X)$ Laser Discharges . . . . .	325
B. $\text{HgBr}(B \rightarrow X)/\text{HgBr}_2$ Dissociation Laser Discharges . . . . .	328
IV. Excited State and Ionic Kinetics . . . . .	332
A. Ionic and Excited State Processes in $\text{XeCl}$ Laser Discharges . . . . .	333
B. Ionic and Excited State Processes in the $\text{HgBr}_2$ Dissociation Laser Discharge . . . . .	337
C. Halogen Dissociation . . . . .	341
D. Rare-Gas P-State Processes . . . . .	342
V. Summary . . . . .	344
References . . . . .	345

### **I. Introduction**

Electrically excited rare-gas halide lasers and their closely related mercury halide counterparts are leading candidates for the development of efficient, high energy optical sources in the UV and visible regions of the spectrum (Rokni and Jacob, 1982; Burnham and Schimitschek, 1981). The plasma medium typical of these lasers is created in a near atmospheric pressure gas

mixture containing a small ( $<1\%$ ) fractional concentration of a halogen-bearing molecule. Pulsed electrical excitation is provided by either a fast-pulse ( $\geq 100$ -ns duration), avalanche-type electric discharge, a beam of high intensity relativistic electrons, or an electron-beam stabilized electric discharge (Brau, 1979). In this chapter attention is focused on the latter excitation method; i.e., *e-beam stabilized laser discharges*, with particular emphasis on the properties of the ionized medium so created.

Electron-beam controlled discharge excitation provides selective (i.e., efficient) excitation of the working species, along with a degree of scalability that is not typical of avalanche discharges. In addition, there often results a significant reduction in the technology problems encountered when pure electron-beam pumping is utilized. Moreover, the e-beam controlled discharge excitation method is capable of generating high pressure, collision dominated glow discharges having exceptional diagnostic value. Thus such discharges provide a rich source of fundamental information difficult to obtain by other means. In Section II of this chapter the essential features of e-beam controlled discharges of the type common to rare-gas and mercury halide lasers are outlined. In addition, certain constraining factors that determine the range of accessible parameter space are considered in general terms as a prelude to more detailed discussion of the application of e-beam controlled discharges to xenon chloride and mercury bromide laser excitation.

Of the several rare-gas and mercury halide lasers under investigation, the  $\text{XeCl}(\text{B} \rightarrow \text{X})$  laser operating at 308 nm and the  $\text{HgBr}(\text{B} \rightarrow \text{X})$  laser at 502 nm have demonstrated unusual potential for a variety of applications (see, for example, Burnham and Schimitschek, 1981). These lasers also represent excellent contrasting examples of lasers excited in e-beam controlled discharges. The general characteristics of these lasers are presented in Section III along with a discussion of several unique features that set the XeCl and HgBr laser apart from others in this class. Since a primary purpose of this contribution is to elucidate the characteristics of the plasma medium typical of optimum laser performance, the dominant excited state and ionic processes occurring in XeCl and HgBr laser discharges are discussed in detail in Section IV. Particular emphasis is placed on analysis of the factors influencing the concentrations of excited and ionic species and their influence on laser/discharge properties. The accompanying discussion is presented within a framework intended to show the great progress that has recently been made in the understanding of the high pressure glow discharges common to electronic transition lasers, while at the same time indicating those areas requiring improvement in both basic data and understanding.

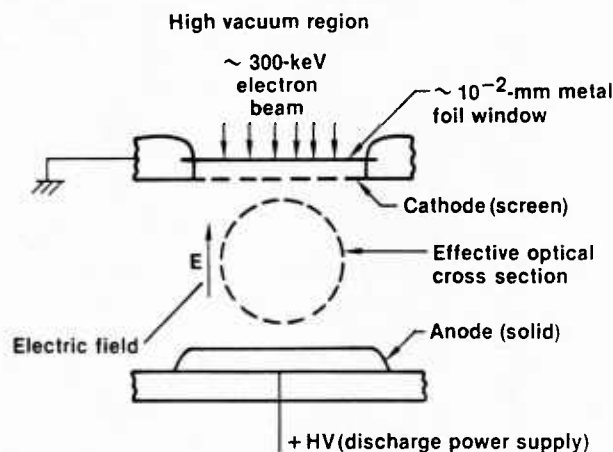


**Fig. 1.** Schematic illustration of the experimental arrangement common to e-beam controlled laser discharges. The cross-sectional area of the discharge region is typically in the 1–100 cm<sup>2</sup> range and the discharge length in the optical direction is typically on the order of 1 m. dimensions corresponding to active volumes in the 0.1–10.0 liter range.

## II. Electron-Beam Controlled Discharges

The electron-beam controlled<sup>†</sup> discharge technique was first devised and implemented about a decade ago as a means to overcome thermal instability in large volume, high energy CO<sub>2</sub> laser discharges. A comprehensive article on this subject by Daugherty (1976) provides a particularly informative survey of the background and early research leading to the successful development of the first high pressure, e-beam ionized glow discharges. Figure 1 illustrates the general features of the experimental arrangement common to such discharges. Ideally, ionization of the laser gas mixture is provided by uniform irradiation of the active volume by a large area electron beam. The physics of the resulting ionization/excitation process has been studied extensively in recent years (Elliott and Greene, 1976). Such an e-beam produced plasma has an electron temperature well below that required for regenerative or self-sustained ionization. The electron temperature is elevated to the level required for efficient excitation of the medium by application of a uniform electric field, as indicated in Fig. 1. Since the electron temperature

<sup>†</sup> The terms "electron-beam controlled discharge," "electron-beam sustained discharge," and "e-beam ionizer-sustainer discharge" are used interchangeably throughout the literature to describe discharges for which the e beam is used as a source of ionization for an electric discharge having an electric field below that required for avalanching or self-sustained operation.

needed for efficient excitation of the working species is below that required for self-sustained operation, this method results in a decoupling of the electron production process from the electric field. For this reason a host of plasma instabilities can often be eliminated or their effects greatly reduced (Nighan, 1977a,b). Indeed, this technique has proven successful as a means of producing uniform *glow* discharges in large volumes ( $\gtrsim 1$  liter) over a continuous range of pressures from a few tenths to several atmospheres, thereby advancing the state of the art in a very substantial way.

#### A. Application to Electronic Transition Lasers

The basic motivation underlying application of the e-beam controlled discharge technique to electronic transition lasers is the same as that for CO<sub>2</sub> lasers, i.e., creation of scalable, high pressure glow discharges. There the similarity ends, however. Because the CO<sub>2</sub> laser operates on relatively low energy vibrational transitions, the optimum electron temperature is always very much less than that required for self-sustained or regenerative operation. For this same reason the concentration of electronically excited species remains very low, and multistep ionization is unimportant. Thus in CO<sub>2</sub> lasers there are no significant ionization mechanisms other than those provided directly (or indirectly) by the e beam. By way of contrast, UV and/or visible lasers require efficient excitation of electronic levels very close to the ionization limit, i.e., a high electron temperature is required for efficient excitation. Additionally, large fractional concentrations of easily ionized excited species are invariably present, with the result that multistep ionization is usually significant and often dominant. Thus e-beam controlled electronic transition laser discharges are marginally stable at best, and utilization of this technique for electronic transition laser applications is confined to a relatively limited range of parameter space.

##### 1. Electron Production and Loss

For a spatially uniform, collision-dominated plasma medium typical of e-beam sustained electronic transition laser discharges, the electron conservation equation may be expressed in the following illustrative form:

$$\partial n_e / \partial t = n S_{eb} + n_e n k_i(E/N) + n_e n^* k_i^*(E/N) + \cdots - n_e n k_a(E/N) - \cdots \quad (1)$$

In this equation, in which only the processes usually dominant in rare-gas, mercury halide lasers are indicated,  $n_e$ ,  $n^*$ , and  $n$  are the number densities of electrons, electronically excited species (e.g., metastable atoms), and neutrals, respectively;  $k_i(E/N)$ ,  $k_i^*(E/N)$ , and  $k_a(E/N)$  are the *mixture weighted* rate coefficients for ionization from the ground state, for excited state ion-

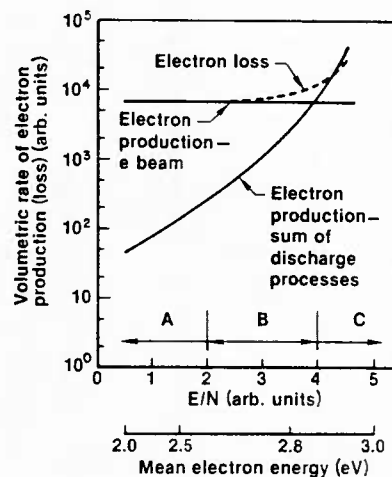


Fig. 2.  $E/N$  variation of the electron production and loss terms for quasisteady conditions representative of e-beam controlled rare-gas-mercury halide discharges.

ization, and for attachment, respectively; and  $S_{eb}$  is the rate of electron production due to the e beam. Penning ionization, electron-ion recombination, and negative ion detachment, although frequently important, have been omitted for the sake of clarity. As will be shown subsequently, it is often possible to obtain quasisteady conditions such that the temporal derivative on the left-hand side of Eq. (1) is small compared to the electron production and loss terms. In this circumstance it is instructional to plot the various contributions to electron production (loss) as a function of  $E/N$ . Presented in Fig. 2 is an illustration of the  $E/N$  variation of electron production and loss terms under quasisteady conditions that are typical of e-beam controlled rare-gas-mercury halide laser discharges. This figure indicates that for low values of  $E/N$ , ionization resulting from discharge processes<sup>\*</sup> is very small compared to that of the e beam (Region A). That is, as a consequence of the low electron temperature, ionization from the ground state is insignificant and excited state production is so low that multistep ionization is not important. In this low  $E/N$  regime the rate of electron production due to the e-beam electrons balances the rate of electron loss, the latter process usually dominated by halogen dissociative attachment (Chantry, 1982). Under these circumstances the discharge is truly electron-beam *controlled* and behaves much like a CO<sub>2</sub> laser discharge under otherwise similar conditions. Unfortunately, in this regime it usually is not possible to efficiently produce electronically excited species in the required numbers. Efficient excited state production requires that  $E/N$  (electron temperature) be increased, and along with such an increase there

<sup>\*</sup> Ionization processes other than the e-beam contribution in Eq. (1).

occurs a rapid increase in both direct ionization of neutrals from their ground states, and multistep ionization involving the electronically excited species participating in laser molecule formation. Under these circumstances discharge ionization processes become increasingly important, indeed comparable to the ionization produced by the e beam (Region B). Ultimately, an  $E/N$  value is reached above which the ionization process is no longer stable, Region C (Nighan, 1978a; Brown and Nighan, 1978; Long, 1979; Haas, 1982; Rokni and Jacob, 1982). Thus for e-beam ionized electronic transition laser discharges there exists a relatively narrow  $E/N$  "window," bounded at low  $E/N$ 's by a region of insufficient pumping intensity and at high  $E/N$ 's by discharge ionization instability. Optimum laser conditions are usually found to exist within the high  $E/N$  portion of the stable range, for which ionization by the e beam may be the largest single source of ionization, but for which the aggregate effect of discharge ionization mechanisms is comparable to or even larger than electron production due to the e beam alone.

In spite of the constraints discussed earlier, conditions can usually be found such that the generation of spatially and temporally uniform laser discharges becomes possible. Presented in Fig. 3 are voltage and current profiles representative of an e-beam controlled mercury bromide laser discharge at a pressure of 2.0 atm. This figure shows that following an initial transient during which the applied discharge voltage rises, there results a highly uniform discharge having a duration of almost 1  $\mu$ s, as evidenced by the essentially constant values of voltage and current. Since characteristic collision times are typically less than 0.1  $\mu$ s for such conditions, analysis shows that kinetic processes in the plasma medium are essentially quasi-steady throughout the discharge pulse, as suggested by the trend exhibited

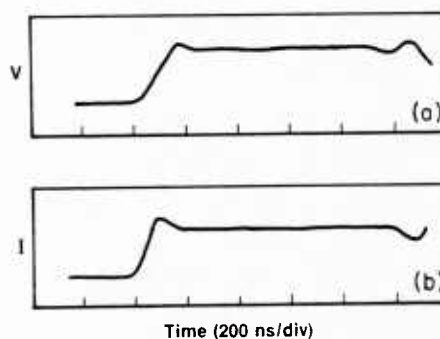


Fig. 3. Representative voltage-current characteristics for an e-beam controlled mercury bromide laser discharge: (a) voltage, (b) current.

by the V-I characteristics shown in the figure. Analysis of such a medium has proven invaluable as a tool to identify the mechanisms controlling both discharge and laser operation (Nighan, 1978a; Rokni *et al.*, 1978).

### III. Rare-Gas Halide and Mercury Halide Lasers

Because of their high efficiency (1–10%) and scalability, electrically excited rare-gas and mercury halide lasers have been the subject of intensive investigation in recent years. The characteristics and performance features of rare-gas halide lasers are treated in detail in the contribution to this volume by Rokni and Jacob (1982). Of the several members comprising this class of lasers, the XeCl (308 nm) laser using HCl as a halogen donor, and the HgBr (502 nm) laser utilizing dissociative excitation of the mercuric bromide molecule ( $\text{HgBr}_2$ ) have unusual promise for many applications (Burnham and Schimitschek, 1981). The primary reasons for the success of these lasers are favorable absorption characteristics permitting high optical extraction efficiency, combined with *relatively* minor volumetric and/or surface chemistry problems. These attributes are due in large measure to the use of HCl (Champagne, 1978) and  $\text{HgBr}_2$  (Schimitschek *et al.*, 1977; Schimitschek and Celto, 1978) as the respective halogen donors in XeCl and HgBr lasers. Indeed, the XeCl laser (McKee *et al.*, 1980; Gower *et al.*, 1980; Miller *et al.*, 1979) and the  $\text{H}_2\text{Br}/\text{HgBr}_2$  laser (Celto and Schimitschek, 1982) have demonstrated lifetime characteristics setting them apart from others of this general class.

In this section the basic kinetic sequences operative in e-beam ionized XeCl(B→X) and HgBr(B→X) laser discharges will be briefly outlined, emphasizing certain unique features characteristic of HCl and  $\text{HgBr}_2$ . Specifics of the XeCl and HgBr laser media will be discussed in Section IV.

#### A. XeCl(B→X) Laser Discharges

Although one of the first rare-gas halide lasers to exhibit oscillation, efficient XeCl laser operation was not achieved until HCl was used as the halogen donor. The reduction in absorption at the laser wavelength accompanying use of HCl in Xe-Ne mixtures resulted in the achievement of electrical-optical energy conversion efficiency in the 6–7% range using pure electron-beam excitation (Champagne, 1978), and in the 2–3% range using either the e-beam ionized discharge method of primary interest here (Nighan and Brown, 1980) or fast-pulse discharge excitation.

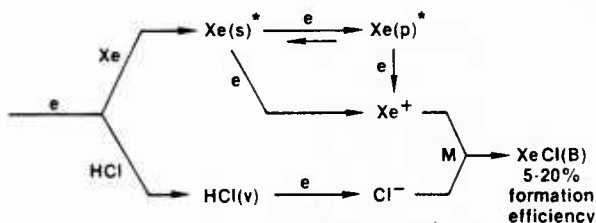


Fig. 4. Sequence diagram showing the dominant processes in the XeCl(B) formation chain in discharge excited Ne-Xe-HCl mixtures. [From Nighan and Brown (1980).]

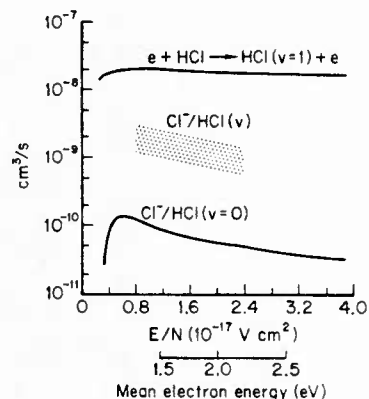
The sequence diagram of Fig. 4 illustrates the dominant features of the XeCl formation chain in *discharge excited* lasers. Under optimum conditions, calculations show that electron energy transfer is dominated by Xe metastable atom production and by subsequent excitation of metastable atoms to the higher lying manifold of Xe 6p states (Nighan and Brown, 1980). Production of the ion  $\text{Xe}^+$  then proceeds by way of electron impact ionization of both Xe metastable (6s) and p-state atoms. As indicated in the figure, the  $\text{Cl}^-$  negative ion is produced by dissociative attachment to vibrationally excited HCl and subsequently recombines with  $\text{Xe}^+$  in a three-body reaction resulting in formation of the laser molecule XeCl(B). Thus XeCl(B) is produced by way of an *ion-recombination channel* with an efficiency in the 5–20% range, depending on specific conditions.

#### 1. *Vibrational Excitation and Dissociative Attachment to HCl*

There are several important features, only recently understood, that set HCl apart from the halogen donors used in other rare-gas halide lasers. Unlike most chlorine donors, formation of XeCl(B) by way of  $\text{Xe}(^3\text{P}_2)\text{-HCl}$  reactions is slightly endothermic at 300 K, reflecting the large 4.45-eV HCl bond energy. Although  $\text{Xe}(^3\text{P}_1, ^3\text{P}_0, ^1\text{P}_1)\text{-HCl}$  reactions or  $\text{Xe}(^3\text{P}_2)\text{-HCl}(r \lesssim 1)$  reactions are energetically capable of XeCl(B) formation, available evidence indicates that such reactions are dominated almost entirely by the dissociation of HCl rather than by XeCl(B) formation<sup>†</sup> (Kolts *et al.*, 1979, Wren and Setser, 1981). Thus it can be concluded with reasonable certainty that  $\text{Xe}^*$  quenching by HCl is not a major XeCl(B) formation process in discharge excited lasers. Additionally, initial evaluation of the role of HCl attachment indicated that formation of  $\text{Cl}^-$  at a rate sufficient for XeCl(B) formation by way of the  $\text{Xe}^+ \text{-Cl}^-$  recombination channel was not possible. This conclusion was based largely on the relatively small

<sup>†</sup> Recent measurements by Chang (1981) indicate that quenching of  $\text{Xe}(^3\text{P}_2)$  by  $\text{HCl}(r = 1)$  results in XeCl(B) formation with a branching fraction of about one-third.

**Fig. 5.** Rate coefficients for vibrational excitation and dissociative attachment for HCl in the ground vibrational state, computed for a Ne(0.989)–Xe(0.01)–HCl(0.001) laser mixture. The shaded region is indicative of the magnitude of the *effective* rate coefficient for attachment to vibrationally excited HCl. [From Nighan and Brown (1980).]



$\text{Cl}^-/\text{HCl}$  cross section measured by Azria *et al.* (1974) and by others as well. However, HCl has an unusually large cross section for vibrational excitation (Rohr and Linder, 1976), a circumstance resulting in a very large fractional concentration of vibrationally excited HCl under XeCl laser discharge conditions. By considering this factor in an analysis of experimental data obtained using a variety of HCl-containing mixtures excited in e-beam controlled discharges, Nighan and Brown (1980) concluded that vibrational excitation of HCl resulted in more than an order-of-magnitude increase in  $\text{Cl}^-$  production over that to be expected from HCl in its ground vibrational state. This finding was subsequently confirmed by measurements of the threshold values of the cross sections for  $\text{Cl}^-/\text{HCl}(v=1,2)$  (Allan and Wong, 1981). Thus vibrational excitation of HCl has been found to be a fundamental process in XeCl lasers, acting as a precursor to production of  $\text{Cl}^-$  by way of dissociative attachment.

Presented in Fig. 5 are the rate coefficients for excitation of HCl from the ground state to the first vibrational level and for the  $\text{Cl}^-/\text{HCl}(v=0)$  dissociative attachment reaction, as computed for a Ne–Xe–HCl laser mixture. The measurements of Rohr and Linder (1976) indicate that the  $v=0 \rightarrow 2$  and  $v=0 \rightarrow 3$  transitions in HCl have cross sections very much smaller than the  $v=0 \rightarrow 1$  transition. Thus multiquantum vibrational transitions are unlikely to be important, and the rate coefficient for the  $v=0 \rightarrow 1$  transition shown in Fig. 5 is probably representative of single-quantum transitions involving higher HCl vibrational levels as well. On this basis Nighan and Brown (1980) have modeled XeCl e-beam controlled laser discharges and, based on analysis of laser/discharge characteristics, have inferred an *effective*<sup>\*</sup> rate coefficient for the reaction  $\text{Cl}^-/\text{HCl}(v)$ , the magnitude of

<sup>\*</sup> The effective attachment coefficient used here refers to the average over all HCl vibrational levels, i.e.,  $k_a(\text{eff}) \equiv [\text{HCl}]^{-1} \sum \text{HCl}(v)k_a(v)$ .

which is indicated by the shaded region of Fig. 5. Although the energy variation of the attachment cross sections for individual HCl vibrational levels are not yet known, Allan and Wong (1981) have observed an exceptionally strong dependence of the  $\text{Cl}^-/\text{HCl}$  attachment process on temperature and have inferred  $\sigma(v=1)/\sigma(v=0)$  and  $\sigma(v=2)/\sigma(v=0)$  ratios of approximately 38 and 880, respectively, at the energies corresponding to the thresholds for each attachment process. Numerical experimentation has shown that this finding is quantitatively consistent with the interpretation of Nighan and Brown (1980). Thus, there is ample evidence that HCl is unique among the rare-gas halide laser halogen donors, exhibiting *relatively* weak attachment until vibrationally excited, a characteristic impacting significantly on both discharge and laser properties.

### *B. HgBr(B $\rightarrow$ X)/HgBr<sub>2</sub> Dissociation Laser Discharges*

The closely related mercury halide lasers HgBr(B  $\rightarrow$  X) and HgCl(B  $\rightarrow$  X) exhibited relatively efficient laser oscillation shortly after rare-gas halide oscillation was demonstrated (Parks, 1977a,b). Initially the HgBr laser was excited using mixtures containing mercury and various bromine compounds. However, practical problems encountered at the high temperatures needed to produce the required concentration of Hg are formidable. Additionally, the reaction sequence typical of such mixtures is noncyclic, resulting in significant temporal changes in mixture composition. These factors significantly retarded progress in HgBr(B  $\rightarrow$  X) laser development. However, Schimitschek and Celto (1978, 1980) demonstrated that dissociative excitation of the mercuric bromide molecule (HgBr<sub>2</sub>) resulted in relatively efficient HgBr(B) formation. Moreover, the required concentrations of HgBr<sub>2</sub> can be obtained at temperatures of less than 200°C. Additionally, repetitive pulsing and related discharge lifetime tests demonstrated that volumetric and surface chemistry problems associated with the use of HgBr<sub>2</sub> are *relatively* minor compared to those encountered using mixtures containing mercury and bromine compounds, and that the HgBr(B)/HgBr<sub>2</sub> reaction sequence is cyclical. For these reasons use of a molecular species comprising the mercury halide molecule itself represented a significant step toward development of a practical visible wavelength laser.

#### *1. HgBr<sub>2</sub> Dissociative Excitation*

Efficient 502-nm HgBr(B  $\rightarrow$  X) oscillation has been demonstrated using a variety of discharge excited mixtures containing 0.2–1.0% HgBr<sub>2</sub> (Sch-

mitschek and Celto, 1980; Brown and Nighan, 1980; Burnham and Schimitschek, 1981). Analysis of discharge and laser properties shows that with either neon or argon as the buffer gas, HgBr(B) is produced as a consequence of electron impact dissociative excitation of HgBr<sub>2</sub> (McGeoch *et al*, 1982; Brown and Nighan, 1980). Additionally, with a few percent N<sub>2</sub> or Xe added to the mixture, HgBr(B) is also formed as a result of reactive quenching by HgBr<sub>2</sub> of either N<sub>2</sub>(A<sup>3</sup>Σ<sub>u</sub><sup>+</sup>) and higher energy N<sub>2</sub><sup>\*</sup> states (Nighan, 1980; Dreiling and Setser, 1980) or of Xe(<sup>3</sup>P<sub>2</sub>) (Brown and Nighan, 1980; Chang and Burnham, 1980). Calculations indicate that with an energy transfer species such as N<sub>2</sub> or Xe in the mixture, direct electron impact excitation of HgBr<sub>2</sub> and excitation transfer reactions contribute to HgBr(B) formation in approximately equal proportions. In any case, regardless of the specific discharge excitation technique or the gas mixture, HgBr(B) is produced by way of *dissociative excitation* reactions, in contrast the ion-ion recombination reaction dominating XeCl(B) formation in XeCl lasers.

The dominant processes in the HgBr(B  $\rightarrow$  X) laser are illustrated in Fig. 6. There is a large number of HgBr<sub>2</sub> electronic states between threshold at about 4.5 eV and the 10.62-eV ionization limit. However, only excitation of the predissociating <sup>3</sup>Σ<sub>u</sub><sup>+</sup> (or <sup>1</sup>Σ<sub>u</sub><sup>+</sup>) state of HgBr<sub>2</sub> results in HgBr(B) formation, as indicated in the figure (Wadt, 1980). The large Franck-Condon shift between the B and X states of HgBr is such that the laser transitions terminate on high vibrational levels of the X state. These levels are rapidly deactivated by collisions with the background gas (Helvajian and Wittig, 1981), thereby permitting efficient optical extraction as is the case for the rare-gas halide excimers such as XeCl. Following laser oscillation the HgBr(X) state recombines with Br atoms to reform HgBr<sub>2</sub>, the final step in a reaction sequence

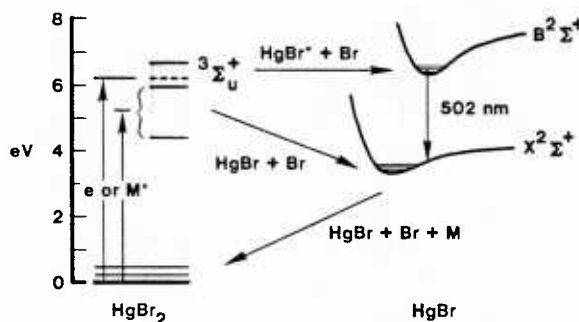


**Fig. 6.** Sequence diagram illustrating the dominant steps in the HgBr(B) formation sequence in the HgBr<sub>2</sub> dissociation laser. Both electrons (e) and certain excited species (M<sup>\*</sup>) can excite the <sup>3,1</sup>Σ<sub>u</sub><sup>+</sup> states of HgBr<sub>2</sub> that predissociate to form HgBr(B). In addition, HgBr<sub>2</sub> states are excited which do not yield HgBr(B) upon predissociation.

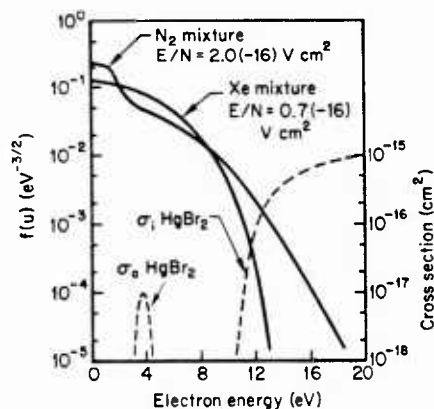


**Fig. 7.** Computed electron-energy distributions in Ne-HgBr<sub>2</sub> mixtures containing either 10% N<sub>2</sub> or 10% Xe. Also shown are the cross sections for HgBr<sub>2</sub> dissociative attachment and ionization. [From Wiegand and Boedeker (1982).]

that appears to be nearly completely reversible under carefully controlled conditions (Burnham and Schimitschek, 1981).

## 2. Ionization and Dissociative Attachment of HgBr<sub>2</sub>

Although both N<sub>2</sub> and Xe have been used as energy receptor-transfer species in HgBr(B) HgBr<sub>2</sub> dissociation lasers, many characteristics of the resulting laser discharges are far different than would be expected on the basis of the known differences between N<sub>2</sub> and Xe electron energy transfer processes alone. However, the observed differences are understood and provide a particularly interesting illustration of the importance to laser analysis of accurate and complete cross-section data.

Figure 7 presents computed electron energy distribution functions in two Ne-HgBr<sub>2</sub> mixtures, each containing either 10% N<sub>2</sub> or 10% Xe. It requires a significantly larger  $E/N$  value to produce the same mean electron energy<sup>†</sup> in the N<sub>2</sub> mixture, reflecting the large energy loss due to N<sub>2</sub> vibrational excitation. Thus for the purpose of this illustration,  $E/N$  has been chosen for both the Xe and N<sub>2</sub> mixtures to yield approximately the same mean electron energy. Figure 7 illustrates the familiar, albeit unusual, shape of the electron energy distribution in N<sub>2</sub> (Nighan, 1970). In N<sub>2</sub> the energy distribution is significantly depleted in the 2–5 eV range within which the N<sub>2</sub> vibrational cross sections are very large (Schulz, 1976). However, in the Xe mixture there is an excess of electrons in the 2–5 eV range but a severe depletion above the 8.3-eV Xe(<sup>3</sup>P<sub>2</sub>) excitation threshold. These characteristics of electron energy transfer collisions with N<sub>2</sub> and Xe, respectively, have a dramatic

<sup>†</sup> Mean electron energy as used here is defined as two-thirds the average electron energy: i.e.,  $kT_e$  for a Maxwellian energy distribution.

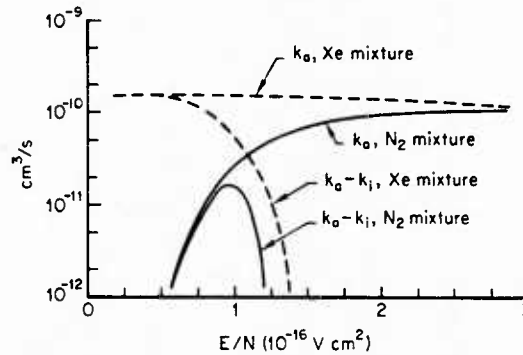


**Fig. 8.** Computed  $\text{HgBr}_2$  attachment coefficients in Ne- $\text{HgBr}_2$  mixtures containing either 10%  $\text{N}_2$  or 10% Xe. Also shown is the net or effective attachment coefficient for each mixture, as defined by the difference between the  $\text{HgBr}_2$  attachment and ionization coefficients,  $k_a - k_i$ .

effect on the electron energy distribution as  $E/N$  is varied, and on the effectiveness of  $\text{HgBr}_2$  as an attaching species under laser conditions.

Figure 7 also shows the cross sections for  $\text{HgBr}_2$  dissociative attachment and ionization (Wiegand and Boedeker, 1982). The  $\text{HgBr}_2$  attachment cross section has a relatively narrow energy width and happens to reach its peak value at an energy about 2.0 eV *higher* than the onset of the resonant portion of the  $\text{N}_2$  vibrational cross sections (i.e., in the region of electron depletion in the  $\text{N}_2$  laser mixture). Additionally,  $\text{HgBr}_2$  has a relatively low ionization potential (10.62 eV) and a very large ionization cross section in the region of depleted electrons in the Xe laser mixture. Thus, as  $E/N$  is varied, calculations show that *ionization* of  $\text{HgBr}_2$  is weighted much less heavily in the Xe mixture than in the  $\text{N}_2$  mixture, and *attachment* is weighted much less heavily in the  $\text{N}_2$  mixture than in the Xe mixture. The significance of this situation is vividly illustrated by comparing attachment coefficients and the net or *apparent* effect of attachment for Ne- $\text{HgBr}_2$  mixtures containing the same amount of  $\text{N}_2$  and Xe, respectively.

Presented in Fig. 8 are the results of such a calculation over the complete range of  $E/N$  appropriate for laser excitation of these mixtures. Figure 8 shows that the attachment coefficient in the Xe mixture is almost completely insensitive to  $E/N$ , reflecting the relatively small changes in the electron energy distribution in the 3–5 eV range as  $E/N$  is varied. However, since the  $\text{HgBr}_2$  ionization cross section is very large, the net effect of  $\text{HgBr}_2$  as a species contributing to electron *loss* in the Xe mixture diminishes rapidly as  $E/N$  is increased, as is evidenced by the decrease in the *difference* between the attachment and ionization coefficients  $k_a - k_i$ . Indeed, for  $E/N$  greater

than about  $1.4 \times 10^{-16} \text{ V cm}^2$  in the Xe mixture,  $\text{HgBr}_2$  ionization dominates over attachment; that is,  $\text{HgBr}_2$  makes a net contribution to electron production rather than loss. The behavior of the  $\text{N}_2$  mixture is markedly different qualitatively and quantitatively. For low  $E/N$  values in  $\text{N}_2$ -dominated mixtures, the electron distribution function is truncated at about 2.0 eV, the onset of the resonant portion of the  $\text{N}_2$  vibrational cross sections (Schulz, 1976). Eventually electrons penetrate the vibrational barrier at higher  $E/N$  values. However, the nature of the electron distribution function results in a strong  $E/N$  dependence of the  $\text{HgBr}_2$  attachment coefficient. More importantly, when the  $\text{HgBr}_2$  ionization coefficient in the  $\text{N}_2$  mixture is subtracted from the attachment coefficient, Fig. 8 shows that the net or *apparent* attachment coefficient has a very unusual behavior and is much smaller than the corresponding value in Xe over the entire  $E/N$  range. Indeed, with a maximum  $k_a - k_i$  value only slightly about  $1.0 \times 10^{-11} \text{ cm}^3/\text{s}$  in the  $\text{N}_2$  mixture (one-tenth of the maximum value in the Xe mixture),  $\text{HgBr}_2$  does not behave like an attaching species for the conditions typical of laser discharges. Calculations show that for the *same* ion densities and  $\text{HgBr}_2$  concentrations, attachment is the dominant electron loss process in the Ne-Xe- $\text{HgBr}_2$  laser mixture, and electron-ion recombination the dominant electron loss in the corresponding Ne- $\text{N}_2$ - $\text{HgBr}_2$  mixture. Clearly, interpretation of the resulting discharge/laser characteristics without benefit of the  $\text{HgBr}_2$  ionization and attachment cross sections would be a difficult task indeed.

#### IV. Excited State and Ionic Kinetics

Recognition of the potential of rare-gas halides as UV laser molecules and the following very rapid development of electrically excited lasers provided great stimulus for research in a number of important areas, particularly energy transfer reactions involving the rare-gas metastable states and halogenated molecules (Velazco *et al.*, 1978), electron-halogen dissociative attachment (Chantry, 1982), and high pressure ion-ion recombination reactions (Flannery, 1979, 1982). As a consequence, understanding of such processes has reached a new plateau, and a wealth of fundamental data has been generated, thereby providing the basis for development of sophisticated analytical models of laser-discharge characteristics (Rokni *et al.*, 1978; Nighan, 1978a). A very significant feature of such models is their ability to generate information relating to fundamental processes not easily accessed experimentally. For this reason interpretation of experimental results using analytical models has itself resulted in identification of many previously

unrecognized processes and has contributed to the generation of additional basic data as well (Nighan, 1978b; Nighan and Brown, 1980; Morgan and Szoke, 1981). As an illustration of the information typically obtained using the now well-developed kinetic modeling techniques, in this section results representative of e-beam ionized XeCl and HgBr laser discharges will be presented.

### *A. Ionic and Excited State Processes in XeCl Laser Discharges*

#### *1. General Characteristics*

As mentioned in Section I, rare-gas halide lasers are excited electrically using a variety of techniques. Although the resulting laser media share some common characteristics, specific differences in the excitation methods introduce substantial changes in important processes, including the rare-gas halide formation sequence itself. Nighan and Brown (1980) have modeled the characteristics of e-beam ionized XeCl laser discharges for conditions of relatively high gain and XeCl(B) formation efficiency, as verified by experimental observations. For conditions typical of this excitation technique, optimum laser characteristics are obtained using neon as a buffer gas at a total pressure of 3.0–5.0 atm, containing 1–2% Xe and approximately 0.1% HCl. In such a mixture the neon provides the stopping agent for the ionizing high energy beam electrons, and also serves to ensure effective vibrational relaxation of the XeCl(B) vibrational manifold. Additionally, volumetric absorption at the laser wavelength due to excited and ionic states of neon is minimal (Champagne, 1982). Although Xe is the working species, its concentration is limited to a very low level so as to prevent excessive formation of Xe<sub>2</sub><sup>+</sup>, which is a strong absorber at the 308-nm laser wavelength (Champagne, 1982; Michels *et al.*, 1979a,b). The optimum concentration of HCl results as a compromise between the formation of Cl<sup>-</sup> required for XeCl(B) production and HCl quenching of XeCl(B) and Xe\*, the latter species a precursor of Xe<sup>+</sup> (Fig. 4).

The fact that XeCl(B) is formed by way of an ion-ion recombination reaction, combined with the constraints on the mixture fractions discussed above, results in a low impedance discharge medium having a high current density and low  $E/N$  value. Nighan and Brown (1980) have shown that such e-beam ionized XeCl laser discharges actually operate in a quasi-avalanche mode, with only about 10% of the ionization provided by the e beam, the dominant ionization process being multistep ionization of Xe excited states by low energy discharge electrons (Fig. 4). For this reason

**TABLE I**  
**Representative Medium Properties for the Electron-Beam Assisted XeCl Laser Discharge Conditions**  
**of Nighan and Brown (1980)<sup>a</sup>**

Mixture	Pressure	E-beam current density	Discharge current density	$E/N$	Electric power density	XeCl(B) formation efficiency	Zero-field gain coefficient	Volumetric absorption coefficient
Ne: 0.989 Xe: 0.01 HCl: 0.001	3 atm	$1.5 \text{ A cm}^{-2}$	$189 \text{ A cm}^{-2}$	$1.95 \times 10^{-17} \text{ V cm}^2$	$288 \text{ kW cm}^{-3}$	17.2%	$6.7\% \text{ cm}^{-1}$	$0.67\% \text{ cm}^{-1}$

<sup>a</sup> The tabulated properties correspond to nearly quasisteady conditions at a time  $0.25 \mu\text{s}$  into a  $0.5\text{-}\mu\text{s}$  discharge pulse, at the end of which the time integrated XeCl(B) and electrical energy densities were 7.5 J/liter and 60 J/liter, respectively, and for which approximately 95% of both the ionization and energy deposition were provided by the discharge.

the term electron-beam *assisted* discharge has been used to describe this XeCl laser excitation procedure (Nighan and Brown, 1980). Other characteristics of this laser discharge are summarized in Table I.

## 2. Species Concentrations

Presented in Figs. 9 and 10 are computed concentrations of ionic and excited species corresponding to the conditions of Table I. Reflecting the relatively large current density—low  $E/N$  conditions, Fig. 9 shows that the electron density is approximately  $1 \times 10^{15} \text{ cm}^{-3}$ , a relatively high value for a large volume glow discharge of the type under consideration. Indeed,

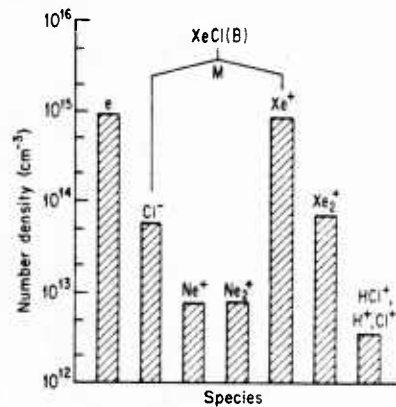


**Fig. 9.** Computed quasisteady charged particle concentrations for the e-beam assisted XeCl laser discharge conditions of Table I.

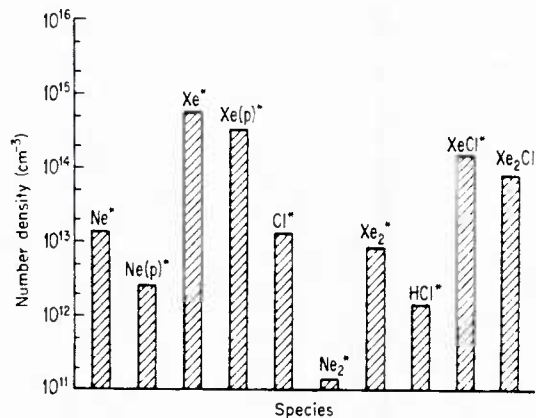


**Fig. 10.** Computed quasisteady excited state concentrations for the e-beam assisted XeCl laser discharge conditions of Table I.

electron quenching of the XeCl(B) laser molecule is comparable to the radiative loss for electron density values above approximately  $3 \times 10^{14} \text{ cm}^{-3}$  (Rokni and Jacob, 1982). This calculation indicates that the ion  $\text{Xe}^+$ , produced by multistep ionization, is the dominant positive ion in spite of the fact that the total pressure is 3 atm. This is a result of (and the reason for) the low fractional concentration of Xe that limits the rate of  $\text{Xe}_2^+$  dimer ion formation. Nonetheless, even though the  $\text{Xe}_2^+$  concentration is more than an order of magnitude less than that of  $\text{Xe}^+$ , volumetric absorption at the laser wavelength due to  $\text{Xe}_2^+$  photodissociation represents about one-third of the total absorption for these conditions. Thus increasing the Xe fractional concentration to a value much above 1% results in a nearly proportional increase in volumetric absorption, along with a decrease in optical extraction efficiency (McCusker, 1979; Rokni and Jacob, 1982).

Although  $\text{Cl}^-$  is produced at a rapid rate by dissociative attachment to vibrationally excited HCl, the relatively low HCl concentration combined with a very large  $\text{Cl}^-$  loss rate due to the  $\text{Cl}^- - \text{Xe}^+ \rightarrow \text{XeCl(B)}$  formation process results in a  $\text{Cl}^-$  concentration that is low compared to the electron and  $\text{Xe}^+$  densities. Even so, absorption at the laser wavelength due to electron photodetachment of  $\text{Cl}^-$  (Rothe, 1969) contributes about 15% to the total volumetric absorption for these conditions.

Figure 10 shows that the corresponding concentrations of  $\text{Xe}^*$  (representing the coupled  $^3\text{P}_2$  and  $^3\text{P}_1$  6s states) and the grouped levels of the 6p manifold are very high and of comparable magnitude. Ionization from these states dominates  $\text{Xe}^+$  formation, as discussed previously. The high  $\text{Xe}^*(\text{p})$  concentration impacts on laser/discharge properties in several ways: photoionization at the laser wavelength of p-state atoms (Hyman, 1977; Duzy and Hyman, 1980), a disproportionate contribution by p states to multistep ionization (Hyman, 1979; Nighan, 1978a), and energy loss by way of p-s relaxation by neutral collisions (Nighan, 1978a; and Section IV.D herein). The concentration of laser molecules,  $\text{XeCl}^*(\text{B})$ , is shown to exceed  $10^{14} \text{ cm}^{-3}$ , corresponding to a gain of over  $5\% \text{ cm}^{-1}$ ; calculations also indicate that the  $\text{XeCl(B)}$  formation efficiency is in the 15–20% range for these conditions (Table I). In addition, Fig. 10 shows that the concentration of the triatomic rare-gas halide molecule,  $\text{Xe}_2\text{Cl}^*$ , is almost as large as that of  $\text{XeCl}^*(\text{B})$ . The molecule  $\text{Xe}_2\text{Cl}^*$  is formed as a result of a three-body  $\text{XeCl}^*(\text{B})$  quenching reaction involving Xe (Marowsky *et al.*, 1981), and for these conditions is produced with an energy efficiency of approximately 1%. Although  $\text{Xe}_2\text{Cl}^*$  formation is a loss process in the  $\text{XeCl(B} \rightarrow \text{X)}$  laser, electrical excitation of similar mixtures containing 5–10% Xe have resulted in  $\text{Xe}_2\text{Cl}^*$  laser emission centered at 518 nm (Tittel *et al.*, 1980).

### ***B. Ionic and Excited State Processes in the HgBr<sub>2</sub> Dissociation Laser Discharge***

#### ***1. General Characteristics***

The blue/green HgBr(B  $\rightarrow$  X)/HgBr<sub>2</sub> dissociation laser operating at 502 nm is in a somewhat earlier stage of development than its UV XeCl(B  $\rightarrow$  X) counterpart. This laser, first excited electrically using a fast-pulse, avalanche discharge technique (Schimitschek and Celto, 1978, 1980), and more recently using the e-beam controlled discharge method (Brown and Nighan, 1980), operates with a buffer at a pressure of 1.5–3.0 atm at a temperature in the 150–200°C range. Neon is often used as the buffer for many of the same reasons discussed in connection with the XeCl laser. Variation of the temperature in the 150–200°C range results in an HgBr<sub>2</sub> vapor pressure variation in the range 2.0–20.0 Torr (Brewer, 1950). Both N<sub>2</sub> or Xe at fractional concentrations of 5–10% have been used successfully as excitation transfer species (Schimitschek and Celto, 1980; Brown and Nighan, 1980). As discussed previously, the principal factors determining the mixture constituents and their respective fractions in rare-gas halide lasers, such as XeCl, are absorption at the laser wavelength and collisional quenching of the laser molecule. However, the HgBr(B) molecule is apparently much less susceptible to collisional deactivation than the rare-gas halides (Roxlo and Mandl, 1980). Additionally, experiments indicate little transient absorption near 500 nm due to discharge produced species. For these reasons, mixture optimization of the HgBr<sub>2</sub> dissociation laser appears to be less critical than is the case for the XeCl laser, for example.

While many HgBr<sub>2</sub><sup>\*</sup> states are excited under electric discharge conditions, only the <sup>3,1</sup>Σ<sub>u</sub><sup>+</sup> states predissociate to form HgBr(B) (Wadt, 1980), indicating that the laser molecule production process is not highly selective. Electron impact excitation of HgBr<sub>2</sub> states below 6 eV results in HgBr(X) formation upon predissociation (Fig. 6), while electron excitation of HgBr<sub>2</sub> states above about 7 eV results in other HgBr excited states, e.g., HgBr(C). Thus for conditions typical of electric discharges the effective branching fraction for HgBr(B) formation following electron impact excitation of HgBr<sub>2</sub> is found to be approximately 20–25% (McGeoch *et al.*, 1982). This value of the HgBr(B) branching fraction is also representative of HgBr<sub>2</sub> reactive quenching of N<sub>2</sub> excited states (Dreiling and Setser, 1980). When considered along with other energy loss processes typical of electric discharge excitation, the lack of a selective HgBr(B) formation channel apparently limits laser efficiency to a value of about 2–3% in Ne(or Ar)–HgBr<sub>2</sub> mixtures, with or without an energy transfer species such as N<sub>2</sub> or Xe present (Burnham and

**TABLE II**  
Representative Medium Properties for the Electron-Beam Controlled HgBr Laser Discharge Conditions  
of Brown and Nighan (1980)<sup>a</sup>

Mixture	Temperature and pressure	E-beam current density	Discharge current density	$E/N$	Electric power density	HgBr(B) formation efficiency	Zero-field gain coefficient	Volumetric absorption coefficient
Ne: 0.895 Xe: 0.10 HgBr <sub>2</sub> : 0.005	185°C 2 atm	0.5 A cm <sup>-2</sup>	14.5 A cm <sup>-2</sup>	$7.5 \times 10^{-17}$ V cm <sup>2</sup>	37 kW cm <sup>-3</sup>	4.0%	2.0% cm <sup>-1</sup>	<0.1% cm <sup>-1</sup>

<sup>a</sup> The tabulated properties correspond to nearly steady state conditions at a time mid-way into a 0.5-μs discharge pulse, at the end of which the time integrated HgBr(B) and electrical energy densities were 1.0 J/liter and 20 J/liter, respectively, and for which the discharge accounted for approximately 90% of the energy deposited and 20% of the ionization. Electron-beam controlled discharges of this type using Ar-0.8% HgBr<sub>2</sub> mixtures have resulted in volumetric laser efficiency of 1.0 J/liter amagat and overall electrical-optical energy conversion efficiency of about 2% (McGeoch *et al.*, 1982; Burnham and Schimitschek, 1981).

Schimitschek, 1981). This value of efficiency is somewhat lower than that typical of rare-gas halide lasers excited under similar conditions.

The fact that the HgBr(B) molecule is produced by way of a dissociative excitation reaction relieves the *requirement* for high ion density typical of ion recombination lasers such as XeCl. For example, HgBr(B) production is possible for conditions such that an electron beam ionized discharge operates in a high impedance mode corresponding to a low current density and a high  $E/N$  value, a situation typical of the KrF\* laser discharge (Nighan, 1978a). For these circumstances the discharge ionization process is dominated by the e beam (Brown and Nighan, 1980), although discharge ionization processes are still significant for the reasons discussed in Section II. Typical characteristics of such a laser discharge are summarized in Table II. In order to facilitate comparison with the XeCl laser conditions treated earlier, the discussion to follow will focus attention on conditions typical of the e-beam discharge excited HgBr<sub>2</sub> dissociation laser using Xe an energy transfer species.

## 2. Species Concentrations

Figure 11 presents computed ion concentrations for the conditions of Table II. The most obvious manifestation of the high impedance mode of operation is an electron density much less than that of the XeCl laser (Fig. 9). Additionally, the dominant ion is a molecular species, HgBr<sub>2</sub><sup>+</sup>, which is produced primarily by direct electron impact on ground state HgBr<sub>2</sub>, and to a lesser extent by charge transfer reactions (Johnsen and Biondi, 1981). Although it is likely that there is some contribution to HgBr(B) formation by

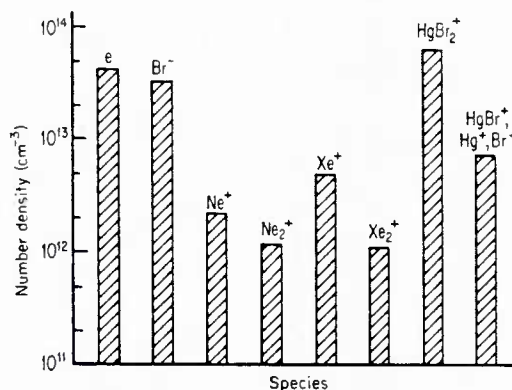


Fig. 11. Computed quasisteady charged particle concentrations for the e-beam controlled HgBr(B) dissociation laser discharge conditions of Table II.

either electron or  $\text{Br}^-$  ion recombination with  $\text{HgBr}_2^+$ , calculations show that such reactions are not important for the conditions of Fig. 11. Additionally, such recombination reactions are not selective, resulting in many  $\text{HgBr}_2$  states that do not predissociate with  $\text{HgBr(B)}$  as a product (Wadt, 1980). Thus ion reactions in the  $\text{HgBr(B)}/\text{HgBr}_2$  laser are much less important than is the case in the  $\text{XeCl}$  laser. However, should  $\text{HgBr}_2^+$  have an absorption cross section greater than  $1 \times 10^{-17} \text{ cm}^2$  near 500 nm, a large concentration of this ion as indicated in Fig. 11 would contribute significantly to volumetric absorption of the medium; thereby limiting optical extraction efficiency.

The corresponding excited state concentrations presented in Fig. 12 are more nearly comparable in magnitude to those in the  $\text{XeCl}$  laser (Fig. 10). For these conditions  $\text{Xe}^*(^3\text{P}_2)$  is produced very efficiently, subsequently transferring its energy to  $\text{HgBr}_2(^3\Sigma_u^+)$ , which predissociates to form  $\text{HgBr(B)}$ . This reaction accounts for about 60% of the  $\text{HgBr(B)}$  production; direct electron impact dissociative excitation accounting for about 40% for these conditions. Calculations indicate that the  $\text{HgBr(B)}$  formation efficiency via these reactions is almost 4% for the conditions of Fig. 12, and that the gain is approximately  $2.0^\circ \text{ cm}^{-1}$  (Table II). Reflecting the lower electron density, Fig. 12 also shows that the  $\text{Xe}^*(\text{p})$  concentration is lower relative to that of  $\text{Xe}^*(\text{s})$  than is the case in the  $\text{XeCl}$  laser. The relatively small concentration of  $\text{XeBr}^*$  indicated in Fig. 12 is a consequence of  $\text{Xe}^+$  and  $\text{Xe}_2^+$  recombination with  $\text{Br}^-$  (Flannery, 1982), while the concentration of unspecified excited products indicated results primarily from electron and  $\text{Br}^-$  recombination reactions involving  $\text{HgBr}_2^+$ .

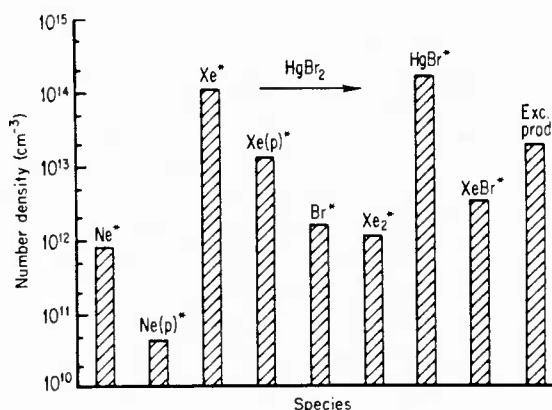
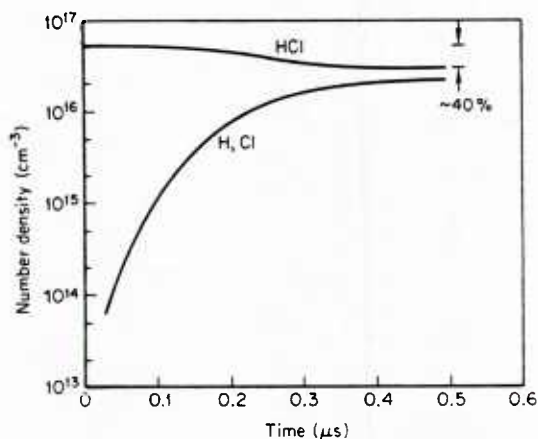


Fig. 12. Computed quasisteady excited state concentrations for the e-beam controlled  $\text{HgBr(B)}/\text{HgBr}_2$  dissociation laser discharge conditions of Table II.



**Fig. 13.** Computed temporal variation of the HCl dissociation products for the XeCl laser conditions of Figs. 9 and 10.

### C. Halogen Dissociation

For the relatively high pressure–high ion density conditions typical of e-beam controlled XeCl and HgBr laser discharges, characteristic excitation and ionization times are much less than the discharge–laser pulse duration. Thus medium kinetic processes are essentially quasisteady for most commonly encountered conditions. However, this does not imply that important temporal changes are not occurring. Indeed, it is clear from the previous discussion that the principal reactions resulting directly and indirectly in laser molecule formation involve dissociation of the halogenated species. Additionally, recombination of the dissociation fragments does not occur on the microsecond (or less) time typical of the pulse duration. Thus since virtually all aspects of discharge–laser characteristics are sensitive to halogen reactions, the properties of the medium typically change significantly throughout the pulse, albeit in a quasisteady manner.

Figures 13 and 14 present the computed temporal evolution of HCl and HgBr<sub>2</sub> dissociation fragments for the XeCl and HgBr laser conditions discussed previously. In both cases the dissociation products are shown to reach levels above 10<sup>16</sup> cm<sup>-3</sup> after a few hundred nanoseconds,<sup>†</sup> a value much higher than the concentrations of all excited and/or ionic species. For the pressures typical of these lasers there is little doubt that both positive and negative cluster ion species involving the dissociation products will be

<sup>†</sup> In fast-pulse electric discharge lasers, which are pumped more intensely, such changes occur on a much shorter time scale.

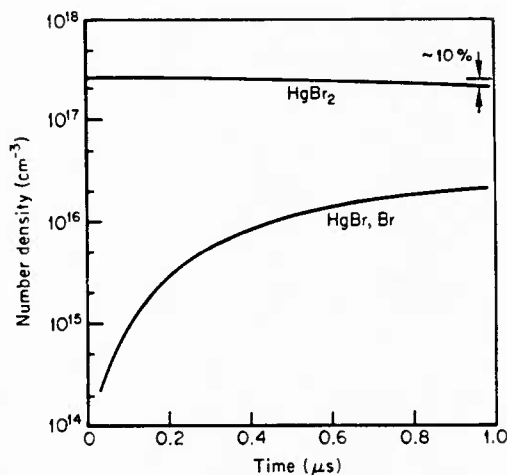


Fig. 14. Computed temporal variation of the  $\text{HgBr}_2$  dissociation products for the  $\text{HgBr(B)}$ ,  $\text{HgBr}_2$  laser conditions of Figs. 11 and 12.

formed (Wiegand, 1982). Other ion rearrangement and/or charge exchange reactions are likely, involving especially the chemically active H atom in XeCl lasers, and the easily ionized molecular fragment  $\text{HgBr}$  (I.P.  $\sim 9.0$  eV) in  $\text{HgBr}_2$  dissociation lasers. The success of laser modeling, which generally does not include such reactions, suggests that the primary effect of dissociation is simply loss of the original halogen fuel. Nonetheless, depending on conditions, there are several aspects of laser-discharge behavior that are only partially understood, which may be influenced significantly by reactions involving the products of halogen dissociation. Such effects are most likely to be of significance for repetitive pulse, closed gas flow cycle operation, an area for which there is very little experience.

#### D. Rare-Gas P-State Processes

As a consequence of the importance of excimer lasers, interest in electronically excited species, particularly the lowest excited states of the rare gases, has been intense. The physical similarities between the rare-gas metastable atoms and alkali metal atoms have significant implications for the laser applications of current interest (Velazco *et al.*, 1978). One such similarity is a very large low energy electron cross section for excitation from the rare-gas s states to the next higher energy manifold of p states (Hyman, 1978). For rare-gas s-state fractional populations greater than about  $10^{-5}$

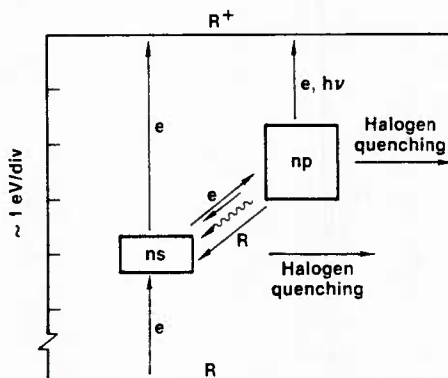
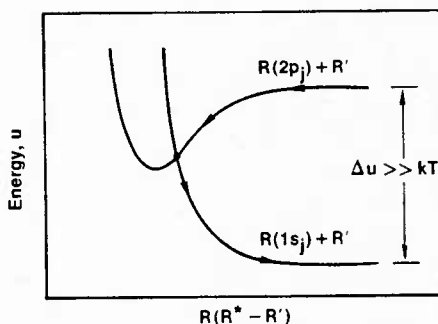


Fig. 15. Illustration of the approximate energy relationship and production and loss processes for rare-gas s- and p-state atoms.

the resulting electron energy loss is significant (Nighan, 1978a). Additionally, since ionization and photoabsorption from the p states is substantially greater than from the s states (Hyman, 1978, 1979; Duzy and Hyman, 1980), the resultant effects of p state processes on both discharge and laser properties can be quite important (Nighan, 1978a). For these reasons knowledge of the dominant factors controlling p-state population levels in rare-gas mixtures common to both rare-gas and mercury halide lasers is of considerable importance.

Presented in Fig. 15 is a simplified energy level diagram typical of the rare gases, which shows the approximate energy relationship between the s and p groups of states and indicates the processes coupling the groups together. On the basis of energy defect arguments alone, collisional deactivation of states of the p-state manifold to the s states, resulting from collisions with ground state rare-gas atoms, would not be expected to be significant. However, Setser and co-workers have recently shown that such intermultiplet energy transfer between rare-gas p and s states occurs by way of complex mechanisms involving curve crossings, in which attractive bound  $R_2^*$  potential curves from R and R(p) interact with the repulsive curves from R and R(s) (Chang and Setser, 1978, 1980; Chang *et al.*, 1980; and Horiguchi *et al.*, 1981). This sequence of events is illustrated in simplified form in Fig. 16. The rate constants for intermultiplet transfer of this type depend on the specific  $2p_j$  levels and on gas mixture. However, effective rate constants for relaxation of the p manifold to the s manifold have been found to be on the order of  $1.0 \times 10^{-11} \text{ s}^{-1} \text{ cm}^3$  for the rare gases and certain rare-gas mixtures. Thus at the high pressures typical of rare-gas and mercury halide lasers, the characteristic time for p  $\rightarrow$  s deactivation by collisions with rare-gas atoms



**Fig. 16.** Illustration of rare-gas intermultiplet  $2p_j-1s_j$  deactivation by collisions with ground state rare-gas atoms. [From Chang and Setser (1978).]

can be as short as 1 ns. In any case, modeling of laser characteristics has shown that this interesting relaxation mechanism usually controls the population of the p-state manifold, thereby exerting an important influence on laser-discharge properties (Nighan, 1978a; Nighan and Brown, 1980).

## V. Summary

The advent of the rare-gas halide laser in 1975 represented a dramatic breakthrough in the 10-yr quest for a short-wavelength laser having an efficiency and scalability comparable to the IR  $\text{CO}_2$  laser. Although little more than five years have passed since the discovery of the rare-gas halide laser, developments in this area have evolved at an extremely rapid pace, propelled by significant advances in understanding of excited state chemistry, electron-halogen attachment, discharge physics, and development of sophisticated computer models of laser-discharge properties.

Recently, research attention has been directed toward important practical considerations such as volumetric and surface chemistry and the resultant implications for laser short-term temporal behavior and overall laser system lifetime. For this reason the  $\text{XeCl(B)}/(\text{Xe-HCl})$  laser operating at 308 nm or Raman shifted to longer wavelengths (Trainor *et al.*, 1980; Burnham and Djeu, 1978), and the blue/green  $\text{HgBr(B)}/\text{HgBr}_2$  dissociation laser at 502 nm have emerged as leading candidates for a wide range of applications. Both lasers have exhibited favorable chemical characteristics and have demonstrated the potential for repetitive pulse, long-life operation. Additionally, the dominant processes in these lasers have been identified and, although data for certain reactions are still lacking, the general characteristics of  $\text{XeCl}$  and  $\text{HgBr}$  lasers operating in a laboratory environment can be predicted in a reasonably satisfactory way. However, there is essentially

no information on the effect of HCl or HgBr<sub>2</sub> dissociation fragments on excited state or ionic processes in the XeCl and HgBr lasers, respectively. Since the concentration of dissociation products often becomes comparable to that of the parent molecule during the discharge pulse, there is little doubt that their presence will influence discharge-laser properties, especially in closed gas-flow cycle operation. Clearly, a significantly improved understanding of the role of discharge generated neutral species would be useful.

One of the most significant factors in the emergence of both the XeF and XeCl lasers as efficient UV sources was recognition of the critical role of transient absorption at UV wavelengths by discharge produced species such as the rare-gas dimer ions. Surprisingly, very little is known about the visible absorption characteristics of the discharge produced excited and ionic species typical of mercury halide lasers such as HgBr or of other blue-green lasers such as XeF(C $\rightarrow$ A), Xe<sub>2</sub>Cl, and Kr<sub>2</sub>F (Tittel *et al.*, 1981). Past experience with the UV rare-gas halides strongly suggests that absorption at visible wavelengths will have an important effect on the optical extraction efficiency of such lasers. For this reason it is probable that knowledge of the 400–600 nm absorption cross sections for the ionic and excited species known to be present (e.g., Figs. 11 and 12) will lead to a rethinking of the importance of various mixture constituents in visible wavelength lasers, followed by improvements in optical extraction efficiency.

#### Acknowledgments

It is a pleasure to acknowledge the contributions to this work of my United Technologies colleagues R. T. Brown, H. H. Michels, L. A. Newman, and W. J. Wiegand, and also those of D. W. Setser of Kansas State University and A. Herzenberg of Yale University. The expert assistance of L. V. Bromson with the programming and numerical work is also much appreciated, as is the continued interest and support of R. H. Bullis, E. Snitzer, and A. J. DeMaria. In addition, the support of the Office of Naval Research is gratefully acknowledged.

#### References

- Allan, M., and Wong, S. F. (1981). *J. Chem. Phys.* **74**, 1687–1691.
- Azria, R., Roussier, L., Paineau, R., and Tronnec, M. (1974). *Rev. Phys. Appl.* **9**, 469–473.
- Brau, C. A. (1979). Excimer lasers, *Top. Appl. Phys.* **30**, 87–133.
- Brewer, L. (1950). In "The Chemistry and Metallurgy of Miscellaneous Materials" (L. L. Quill, ed.), pp. 193–274. McGraw-Hill, New York.
- Brown, R. T., and Nighan, W. L. (1978). *Appl. Phys. Lett.* **32**, 730–733.
- Brown, R. T., and Nighan, W. L. (1980). *Appl. Phys. Lett.* **37**, 1057–1059.
- Burnham, R., and Djeu, N. (1978). *Opt. Lett.* **3**, 215–217.
- Burnham, R., and Schimitschek, E. J. (1981). *Laser Focus* **17**, 54–66.
- Champagne, L. F. (1978). *Appl. Phys. Lett.* **33**, 523–525.
- Champagne, L. F. (1982). In "Applied Atomic Collision Physics" (H. S. W. Massey, E. W. McDaniell, and B. Bederson, eds.), this volume, pp. 349–386. Academic Press, New York.

- Chang, R. S. F. (1981). To be published.
- Chang, R. S. F., and Burnham, R. (1980). *Appl. Phys. Lett.* **36**, 397-400.
- Chang, R. S. F., and Setser, D. W. (1978). *J. Chem. Phys.* **69**, 3885-3897.
- Chang, R. S. F., and Setser, D. W. (1980). *J. Chem. Phys.* **72**, 4099-4110.
- Chang, R. S. F., Horiguchi, H., and Setser, D. W. (1980). *J. Chem. Phys.* **73**, 778-790.
- Chantry, P. J. (1982). In "Applied Atomic Collision Physics" (H. S. W. Massey, E. W. McDaniel, and B. Bederson, eds.), this volume, pp. 35-70. Academic Press, New York.
- Daugherty, J. D. (1976). In "Principles of Laser Plasmas" (G. Bekefi, ed.), pp. 369-419. Wiley, New York.
- Degani, J., Rokni, M., and Yatsiv, S. (1981). *J. Chem. Phys.* **75**, 164-171.
- Dreiling, T. D., and Setser, D. W. (1980). *Chem. Phys. Lett.* **75**, 211-217.
- Duzy, C., and Hyman, H. (1980). *Phys. Rev. A* **22**, 1878-1883.
- Elliott, C. J., and Greene, A. E. (1976). *J. Appl. Phys.* **47**, 2946-2953.
- Flannery, M. R. (1979). *Int. J. Quantum Chem. Symp.* **13**, 501-429.
- Flannery, M. R. (1982). In "Applied Atomic Collision Physics" (H. S. W. Massey, E. W. McDaniel, and B. Bederson, eds.), this volume, pp. 141-172. Academic Press, New York.
- Gower, M. C., Kearsley, A. J., and Webb, C. E. (1980). *IEEE J. Quantum Electron.* **QE-16**, 231-234.
- Haas, R. A. (1982). In "Applied Atomic Collision Physics" (H. S. W. Massey, E. W. McDaniel, and B. Bederson, eds.), this volume, pp. 423-452. Academic Press, New York.
- Helvajian, H., and Wittig, W. (1981). *Appl. Phys. Lett.* **38**, 731-733.
- Horiguchi, H., Chang, R. S. F., and Setser, D. W. (1981). *J. Chem. Phys.* **75**, 1207-1218.
- Hyman, H. (1977). *Appl. Phys. Lett.* **31**, 14-15.
- Hyman, H. (1978). *Phys. Rev. A* **18**, 441-446.
- Hyman, H. (1979). *Phys. Rev. A* **20**, 855-859.
- Johnsen, R., and Biondi, M. A. (1980). *J. Chem. Phys.* **73**, 5048-5050.
- Kolts, J. H., Velazco, J. E., and Setser, D. W. (1979). *J. Chem. Phys.* **71**, 1247-1263.
- Long, W. H. (1979). *J. Appl. Phys.* **50**, 168-172.
- Marowsky, G., Glass, G. P., Smayling, M., Fittell, F. K., and Wilson, W. L. (1981). *J. Chem. Phys.* **75**, 1153-1158.
- McCusker, M. (1979). Excimer Lasers. *Top. Appl. Phys.* **30**, 47-86.
- McGeoch, M., Hsia, J., and Klimek, D. (1982). To be published.
- McKee, T. J., James, D. J., Nip, W. S., Weeks, R. W., and Willis, C. (1980). *Appl. Phys. Lett.* **36**, 943-945.
- Michels, H. H., Hobbs, R. H., and Wright, L. A. (1979a). *J. Chem. Phys.* **71**, 5053-5062.
- Michels, H. H., Hobbs, R. H., and Wright, L. A. (1979b). *Appl. Phys. Lett.* **35**, 153-155.
- Miller, J. L., Dickie, J., Davin, J., Swingle, J., and Kan, T. (1979). *Appl. Phys. Lett.* **35**, 912-914.
- Morgan, W. L., and Szoke, A. (1981). *Phys. Rev. A* **23**, 1256-1265.
- Nighan, W. L. (1970). *Phys. Rev. A* **2**, 1989-2000.
- Nighan, W. L. (1977a). *Phys. Rev. A* **15**, 1701-1720.
- Nighan, W. L. (1977b). *Phys. Rev. A* **16**, 1209-1223.
- Nighan, W. L. (1978a). *IEEE J. Quantum Electron.* **QE-14**, 714-726.
- Nighan, W. L. (1978b). *Appl. Phys. Lett.* **32**, 297-300.
- Nighan, W. L. (1980). *Appl. Phys. Lett.* **36**, 173-175.
- Nighan, W. L., and Brown, R. T. (1980). *Appl. Phys. Lett.* **36**, 498-500.
- Parks, J. (1977a). *Appl. Phys. Lett.* **31**, 192-194.
- Parks, J. (1977b). *Appl. Phys. Lett.* **31**, 297-300.
- Rohr, K., and Linder, F. (1976). *J. Phys. B: At. Mol. Phys.* **9**, 2521-2536.

- Rokni, M., and Jacob, J. A. (1982). In "Applied Atomic Collision Physics" (H. S. W. Massey, E. W. McDaniel, and B. Bederson, eds.), this volume, pp. 273-293. Academic Press, New York.
- Rokni, M., Mangano, J. A., Jacob, J. H., and Hsia, J. C. (1978). *IEEE J. Quantum Electron.* **QE-14**, 464-481.
- Rothe, D. E. (1969). *Phys. Rev.* **177**, 93-99.
- Roxlo, C., and Mandl, A. (1980). *J. Chem. Phys.* **72**, 541-543.
- Schimtschek, E. J., and Celto, J. E. (1978). *Opt. Lett.* **2**, 64-66.
- Schimtschek, E. J., and Celto, J. E. (1980). *Appl. Phys. Lett.* **36**, 176-178.
- Schimtschek, E. J., Celto, J. E., and Trias, J. A. (1977). *Appl. Phys. Lett.* **31**, 608-610.
- Schulz, G. (1976). In "Principles of Laser Plasmas" (G. Bekefi, ed.), pp. 33-38. Wiley, New York.
- Tittel, F. K., Wilson, W. L., Stickel, R. E., Marowsky, G., and Ernst, W. E. (1980). *Appl. Phys. Lett.* **36**, 405-407.
- Tittel, F. K., Marowsky, G., Wilson, W. L., and Smayling, M. C. (1981). *IEEE J. Quantum Electron.* **QE-17**, 2268-2281.
- Trainor, D. W., Hyman, H., Itzhan, I., and Heinrichs, R. M. (1980). *Appl. Phys. Lett.* **37**, 440-442.
- Velazco, J. E., Kolts, J. H., and Setser, D. W. (1978). *J. Chem. Phys.* **69**, 4357-4373.
- Wadt, W. (1980). *J. Chem. Phys.* **72**, 2469-2478.
- Wiegand, W. J. (1982). In "Applied Atomic Collision Physics" (H. S. W. Massey, E. W. McDaniel, and B. Bederson, eds.), this volume, pp. 71-98. Academic Press, New York.
- Wiegand, W. J., and Boedeker, L. R. (1982). *Appl. Phys. Lett.* **40**, 225-227.
- Wren, D. J., and Setser, D. W. (1982) *J. Phys. Chem.* **86**, 284-291.

# Efficient $\text{XeCl}(B)$ formation in an electron-beam assisted Xe/HCl laser discharge

William L. Nighan and Robert T. Brown

United Technologies Research Center, East Hartford, Connecticut 06108

(Received 17 December 1979; accepted for publication 15 January 1980)

$\text{XeCl}(B)$  formation processes are examined for conditions typical of a discharge-excited laser using HCl as the chlorine donor. It is shown that vibrational excitation of HCl followed by dissociative attachment is a primary step in the reaction sequence resulting in  $\text{Cl}^-$ .  $\text{XeCl}(B)$  formation is the result of a three-body  $\text{Xe}^+ - \text{Cl}^-$  recombination reaction. Experimental results are presented which demonstrate efficient ( $\sim 2\%$ )  $\text{XeCl}$  laser operation in an  $e$ -beam assisted discharge in which over 75% of the energy was deposited by the discharge.

PACS numbers: 42.55.Hq, 42.60.By

Recently, efficient ( $\sim 5\%$ ) laser oscillation on the  $\text{XeCl}(B \rightarrow X)$  transition (308 nm) has been reported using both pure electron-beam excitation<sup>1,2</sup> and an electron-beam controlled discharge.<sup>2</sup> In both cases, the observation of efficient operation with little or no long-term degradation in laser performance is attributed to the use of HCl as the halogen donor.<sup>1-3</sup> However, relatively little is known about HCl reaction kinetics in the  $\text{XeCl}$  laser medium, a factor which has hampered development of a good understanding of basic processes in this laser. The present letter addresses this problem, and reports results of an investigation of  $\text{XeCl}(B)$  formation kinetics and plasma processes in an electron-beam assisted discharge for total volumetric energy loading comparable to that reported previously,<sup>1,2</sup> but under conditions such that electrical energy input was dominated by the discharge.

There are several important features which set HCl apart from other effective halogen donors: (1) a high dissociation energy (4.45 eV), (2) a very high cross section for vibrational excitation by electrons,<sup>4</sup> and (3) a cross section for dissociative attachment from the ground vibrational level which is substantially lower than that of the halogen donors typically used in rare-gas fluoride lasers. Formation of  $\text{XeCl}(B)$  by way of  $\text{Xe}(^3P_2)$ -HCl reactions is slightly endothermic at 300 °K,<sup>5</sup> reflecting the strong HCl bond energy. Thus the large measured<sup>5</sup>  $\text{Xe}(^3P_2)$  quenching rate by HCl is apparently a purely dissociative reaction and does not result in formation of the  $\text{XeCl}(B)$  upper laser level. Although quenching of  $\text{Xe}(^3P_1, ^3P_0, ^1P_1)$  by HCl may result in  $\text{XeCl}(B)$  formation, at present there are no data for such reactions. In addition, while the large cross section for HCl vibrational excitation ensures the presence of a high fractional concentration of vibrationally excited HCl in laser plasmas, there is no evidence suggesting efficient  $\text{XeCl}(B)$  formation by way of  $\text{Xe}(^3P_2)$ -HCl( $v$ ) reactions.

A more likely consequence of HCl vibrational excitation is enhanced dissociative attachment. Indeed, our analysis of current-voltage characteristics for electron-beam controlled discharges in a variety of rare-gas-HCl mixtures indicate the occurrence of an electron loss process which increases with time throughout the discharge pulse. Modeling studies show that this enhanced electron loss correlates

with the growth in the concentration of vibrationally excited HCl. Further, without taking this effect into account, it is not possible to quantitatively model either discharge characteristics or laser properties in  $\text{XeCl}$  laser mixtures on the basis of other *known* reactions alone.

Presented in Fig. 1 are the rate coefficients for vibrational excitation and attachment for HCl in the ground vibrational level, computed for a Ne(0.989)-Xe(0.01)-HCl(0.001) laser mixture. The vibrational cross section of Rohr and Linder<sup>4</sup> was used in the calculation, and the shape of the attachment cross section of Ziesel, Nenner, and Schulz<sup>6</sup> was used, adjusted in magnitude to yield a rate coefficient consistent with our experimental observations in vibrationally cold HCl. The shaded region in this figure is indicative of the 10- to 20-fold increase in the *effective* attachment rate of HCl resulting from vibrational excitation, as deduced from the present modeling of the characteristics of rare-gas-HCl discharges.<sup>7</sup> Very recent measurements by Wong<sup>8</sup> indicate an increase of more than an order of magnitude in the attachment cross section due to HCl vibrational excitation, a result that provides additional support for the present conclusions.

On the basis of the interpretation discussed above, it is concluded that vibrational excitation of HCl is a fundamental process in  $\text{XeCl}$  lasers using HCl as the chlorine donor. For discharge-excited lasers, modeling studies indicate that  $\text{XeCl}(B)$  formation proceeds by way of the sequence illustrated in Fig. 2. In this sequence, electron energy transfer is

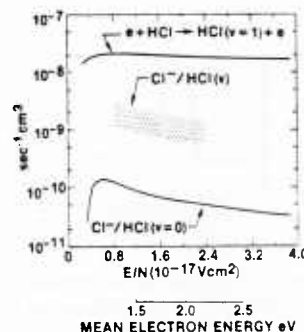


FIG. 1. Rate coefficients for vibrational excitation and dissociative attachment for HCl in the ground vibrational level, computed for a Ne(0.989)-Xe(0.01)-HCl(0.001) laser mixture. The shaded region is indicative of the magnitude of the effective rate coefficient for attachment to vibrationally excited HCl as inferred from the present study.

IV. BASIC PROCESSES IN RARE GAS-HALIDE LASERS

IV-A. KrF(B $\rightarrow$ X) Laser

- Plasma Processes in Electron-Beam Controlled Rare Gas-Halide Lasers
- Influence of Molecular Dissociation and Degree of Ionization on Rare Gas-Halide Laser Properties

## Papers

# Plasma Processes in Electron-Beam Controlled Rare-Gas Halide Lasers

WILLIAM L. NIGHAN

(Invited Paper)

**Abstract**—This paper presents the results of an analysis of plasma properties in an electron-beam controlled KrF\* laser discharge. In this study, special emphasis is placed on establishing the relationship among the numerous kinetic processes influencing the populations of excited species in the laser medium. Important reactions controlling the coupled populations of rare-gas metastable states and higher excited states are discussed in detail, along with the resultant effect of these reactions on KrF\* formation efficiency. It is shown that the rare-gas monohalide production efficiency is approximately 20 percent under typical conditions, and that no single reaction dominates either production or loss of KrF\*. In addition, the very important role of halogen molecule dissociation is treated and the resultant effects of dissociation on the temporal variations of plasma properties and on plasma stability are analyzed.

## I. INTRODUCTION

THE ELECTRICALLY excited rare-gas halide laser is the first *short-wavelength* laser which appears capable of scaling to high pulse energy and high average power. Electrical-optical energy conversion efficiency of approximately 10 percent has been attained [1] for a single-pulse KrF\* laser ( $\lambda = 248$  nm), the most efficient of the rare-gas halide class. There are numerous applications for efficient UV and/or visible wavelength lasers, and for this reason these new laser systems have become the subject of increasing attention [2]. At the time the potential of rare-gas monohalides as laser molecules was first recognized [3], their properties were essentially unknown. For this reason early emphasis was placed on development of a thorough understanding of the structure of such molecules and their reaction kinetics. These efforts have resulted in a relatively complete understanding of rare-gas halide emission spectra [4], and of the dominant formation and quenching processes of these molecules [5]. Additionally, detailed modeling of kinetic processes has provided the insight required to

identify optimum conditions for rare-gas halide laser operation [1], [6], [7].

The plasma medium typical of these lasers is created in a near atmospheric pressure rare-gas mixture containing a small (<1 percent) fractional concentration of a halogen-bearing molecule. Pulsed electrical excitation is provided either by a beam of high energy electrons or by an electric discharge in a manner generally similar to that typical of CO<sub>2</sub> lasers [8], [9]. However, there are several significant features which differentiate rare-gas halide lasers from their IR molecular laser counterparts. These include: 1) a high concentration of "alkali-like" rare gas metastable atoms which, because of their chemical activity [3], exert a dominant influence on all aspects of plasma behavior; 2) a major constituent (the molecular halogen) which dissociates rapidly under the conditions required for laser operation, an effect resulting in very important temporal changes in the gas mixture; and 3) an electron density which is above the level at which electron-electron collisions become important, with the result that the plasma cannot be considered *weakly* ionized. This paper presents the results of a theoretical investigation of these and related plasma processes for conditions representative of KrF\* lasers. Special emphasis is placed on establishing the relationship among the numerous kinetic processes which influence the populations of various excited species. The results presented are qualitatively similar for all rare-gas halide lasers, and should provide useful information relevant to other promising excimer lasers as well.

Section II summarizes the basic processes contributing to the production and loss of rare-gas metastable atoms and of KrF\* molecules. Particular emphasis is placed on analysis of electron-atom excitation and ionization, especially the dependence of rate coefficients for these processes on the fractional concentration of electronically excited species and of electrons. In addition, the potential importance of vibrational excitation and dissociation of F<sub>2</sub> by low energy electron impact and of electron attachment to vibrationally excited F<sub>2</sub> are discussed.

Manuscript received June 26, 1978. Portions of this work were supported by the Office of Naval Research.

The author is with the United Technologies Research Center, East Hartford, CT 06108.

The results of an analysis of plasma properties in an electron-beam controlled  $\text{KrF}^*$  laser discharge are presented in Section III. Therein the important reactions controlling the coupled populations of rare-gas metastable states and higher excited states are discussed in detail along with the resultant effect of these reactions on  $\text{KrF}^*$  formation efficiency. In addition, the very important role of halogen molecule dissociation is treated and the resultant effect of dissociation on plasma stability is analyzed. Important processes requiring improved understanding prior to successful application of rare-gas halide lasers are discussed in Section IV.

## II. PLASMA PROCESSES

### A. $\text{KrF}^*$ Formation and Loss

Rare-gas halide lasers have been excited successfully both by electron beams and by electric discharges [1]. In the latter case either fast pulse discharges or electron-beam controlled discharges have been used. Rare-gas monohalide molecule formation proceeds by way of generally similar processes in each case. The more important features of the  $\text{KrF}^*$  formation and loss sequence in a nominally atmospheric pressure Ar-Kr- $\text{F}_2$  gas mixture are illustrated by the diagram shown in Fig. 1. This figure indicates that there are several pathways resulting in the formation of  $\text{KrF}^*$ . When pure electron-beam excitation is used, the dominant mechanisms are two- and three-body positive and negative ion recombination, the positive ions having been produced by ionization initiated by the high energy primary electrons in the beam, and the negative ions by dissociative attachment reactions involving low energy electrons and  $\text{F}_2$ . Reactions between  $\text{F}_2$  and rare-gas metastable atoms produced by low energy electron impact are the primary source of rare-gas monohalide molecules in electron-beam controlled discharges. Recombination and metastable reactions may make comparable contributions to rare-gas halide formation in fast pulse, self-sustained laser discharges, depending on specific circumstances. Of course there are numerous reactions which tend to interrupt the chain of events illustrated in Fig. 1. Nonetheless, the energy utilization efficiency associated with rare-gas monohalide molecule formation is typically in excess of 20 percent for conditions representative of both electron-beam excited and electron-beam controlled lasers [1]. However, electron-beam controlled-discharge excited lasers, for which most of the energy is provided by the discharge, have greater potential for scaling to high average power than lasers excited by an electron-beam alone.

Fig. 1 indicates that there are several processes contributing to the loss of  $\text{KrF}^*$ ; these are also found to be of comparable importance for typical conditions. In subsequent paragraphs, specific details of the reactions indicated in Fig. 1 will be discussed with emphasis directed toward factors of importance in discharge excited  $\text{KrF}^*$  lasers.

### B. Electron Collision Processes

**Electron-Neutral Energy Transfer:** A fundamental factor contributing to the high efficiency characteristic of discharge excited rare-gas halide lasers is the efficient production of rare-gas metastable atoms for conditions readily attainable experi-

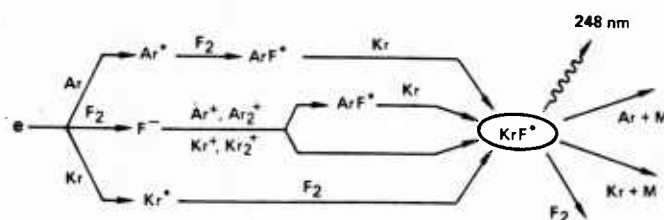


Fig. 1. Illustration of the primary reactions contributing to  $\text{KrF}^*$  formation and loss in an electrically excited Ar-Kr- $\text{F}_2$  mixture at nominally atmospheric pressure.

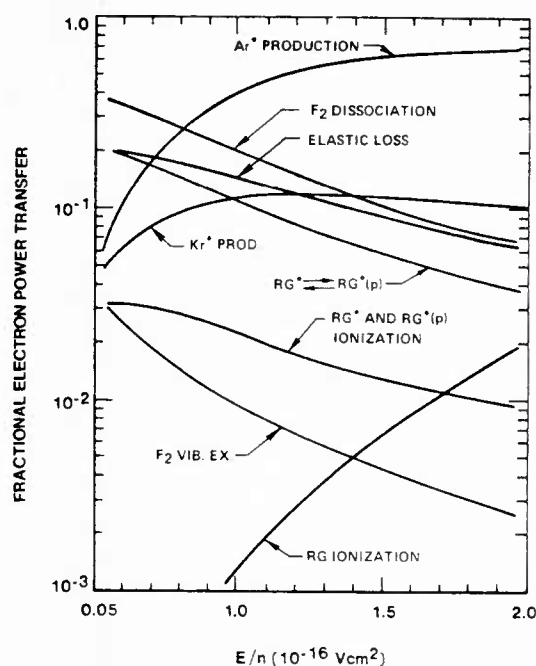


Fig. 2. Fractional contributions to electron-neutral power transfer in an Ar-Kr- $\text{F}_2$  mixture having the proportions 0.945-0.05-0.005. For this example, the fractional ionization, fractional metastable concentration, and fractional concentration of rare gas p state atoms were  $10^{-6}$ ,  $10^{-5}$ , and  $10^{-6}$ , respectively. The notation RG refers to the combined effect of Ar and Kr.

mentally. Shown in Fig. 2 are the computed variations of the processes dominating electron-atom (molecule) energy transfer for conditions typical of an electron-beam controlled  $\text{KrF}^*$  laser. For  $E/n$  values<sup>1</sup> greater than approximately  $1.0 \times 10^{-16} \text{ V} \cdot \text{cm}^2$ , for which the mean electron energy<sup>2</sup> is about 3.25 eV for the mixture indicated, the combined argon and krypton metastable production efficiencies exceed 50 percent, and reach 70 percent for higher  $E/n$  values. Examination of Fig. 2 indicates that the contributions to the undesirable loss of electron energy due to elastic collisions with atoms, excitation of metastable atoms to higher states, and  $\text{F}_2$  dissociation are found to be of comparable importance for the conditions of this example. However, it will be shown that the net effect of electron excitation and deexcitation of rare-gas atoms between their metastable and p states is highly variable, depending on the concentration of metastable atoms. For fractional metastable concentrations greater than the  $10^{-5}$  value typical of this ex-

<sup>1</sup> $E/n$  is the ratio of electric field intensity to total neutral number density.

<sup>2</sup>Mean electron energy as used here is defined as  $\frac{2}{3}$  the average energy.

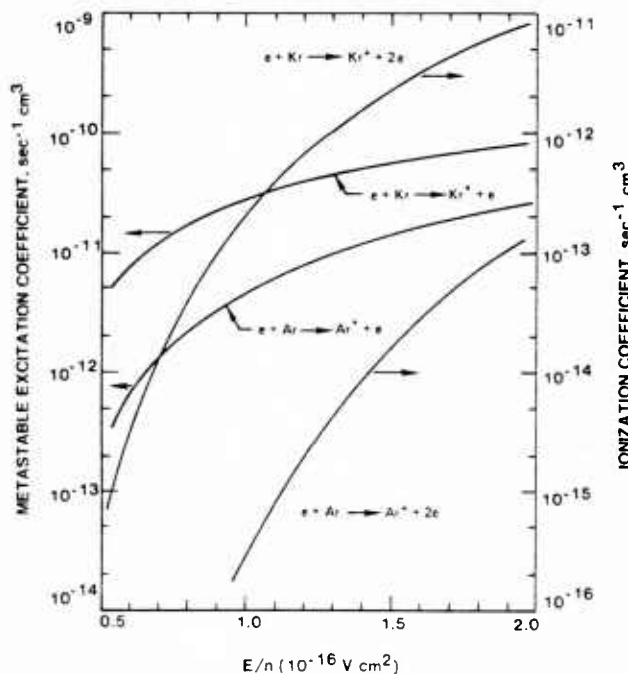


Fig. 3.  $E/n$  variation of the metastable excitation and ionization rate coefficients for ground state Ar and Kr corresponding to the conditions of Fig. 2.

ample, the power loss accompanying this process increases significantly [6], [10]. Although the energy loss associated with ionization of excited states and of ground state atoms is small, these processes make very important contributions to the production of electrons in electron-beam controlled discharges.

Even though the cross sections for electron excitation of  $F_2$  vibrational levels are relatively large ( $\sim 10^{-17} \text{ cm}^2$ ) [11], vibrational excitation does not appear to be an important energy loss process because the energy loss per collision is small ( $\sim 0.1 \text{ eV}$ ) [12]. Although there are no electron cross section data for  $F_2$  electronic excitation, this process may be important because the electron energy loss will be several electron volts. Additionally, there are numerous  $F_2$  electronic states in the 3 to 10 eV range which are repulsive [13] and which would therefore result in  $F_2$  dissociation when excited. In this energy range, there are likely to be excited states of the  $F_2^-$  ion which lie above dissociating states of  $F_2$  in the vicinity of the  $F_2$  equilibrium internuclear separation. Thus, for electron energies of a few electron volts  $F_2$  electronic excitation may be enhanced by resonance processes as is the case with dissociative attachment [14]–[16]. In order to reasonably account for the effect of  $F_2$  electronic excitation, indirect experimental evidence of  $F_2$  dissociation has been analyzed, from which an effective  $e - F_2$  dissociation cross section has been obtained [12]. Based on this provisional cross section, the data of Fig. 2 show that electron energy loss accompanying direct dissociation by electrons is likely to be substantial for halogen molecule concentrations typical of rare-gas halide lasers. In addition, the contribution of this process to  $F_2$  dissociation will also be shown to be significant.

**Electron Rate Coefficients:** Presented in Fig. 3 is the  $E/n$  variation of the electron rate coefficients for metastable excitation and ionization from the ground state corresponding to the conditions of Fig. 2. These data were generated using avail-

able cross section information [17], [18]. With a mean electron energy much lower than the threshold for excitation, only those electrons in the high energy region of the electron energy distribution participate in the metastable production and ionization processes. This accounts for the characteristically strong dependence of the rate coefficients for these processes on  $E/n$  (i.e., mean electron energy). The higher rate coefficients for Kr reflect the fact that the energy thresholds for excitation and ionization of krypton are lower than the respective thresholds for argon.

In most if not all electronically excited excimer lasers, the fractional ionization exceeds  $10^{-6}$  and the fractional metastable concentration exceeds  $10^{-5}$ . For these circumstances, electron-electron [19], [20] collisions and electron collisions with metastable atoms [6] exert an important influence on the electron energy distribution, the former tending to increase the number of high energy electrons and the latter resulting in a decrease in their number. Those electron rate coefficients which are particularly sensitive to the high energy region of the distribution are most affected by such changes. Thus, in addition to their strong dependence on  $E/n$ , the rate coefficients for electronic excitation and ionization of ground state rare gas atoms exhibit a significant dependence on degree of ionization and on fractional metastable concentration. The results presented in Figs. 4 and 5 illustrate this effect for representative KrF\* laser conditions. The influence of electron-electron collisions is particularly striking (Fig. 4), resulting in nearly a two order-of-magnitude increase in the rate coefficient for Kr ionization and a three order-of-magnitude increase for Ar as the fractional ionization increases in the  $10^{-6}$  to  $10^{-4}$  range typical of rare-gas halide discharges.

Fig. 5 indicates that variations in rare gas excitation and ionization rates caused by cooling of the electron energy distribution due to excitation of metastable atoms to higher levels are also significant. Of more importance is the fact that since fractional ionization and fraction metastable concentration generally increase together, the effects illustrated in Figs. 4 and 5 tend to be partially offsetting. In addition, the variation shown in these figures for a fixed  $E/n$  value of  $1.0 \times 10^{-16} \text{ V} \cdot \text{cm}^2$  becomes greater as  $E/n$  is reduced below this level and is smaller for higher  $E/n$  values. Thus, in modeling rare-gas halide laser discharges, it is necessary to evaluate rate coefficients for ionization and excitation from the ground state using self-consistent combinations of  $E/n$ , degree of ionization, and metastable fraction.

Presented in Fig. 6 are the  $E/n$  variations of the rate coefficients for Ar and Kr excitation and deexcitation between the grouped metastable and p states, calculated using available cross section data [21]. Rate coefficients for ionization from both the metastable and p states are also shown [22], [23]. These data exhibit a weak dependence on  $E/n$ , reflecting the fact that the energy thresholds for the processes involved are comparable to (or less than) the mean electron-energy. For this reason the rate coefficients presented in Fig. 6 are practically insensitive to variations in either the degree of ionization or the metastable fraction. However, the magnitude of the rate coefficients for electron-excited state collision processes is exceptionally large as a consequence of the alkali-like structure of the rare-gas excited states [21].

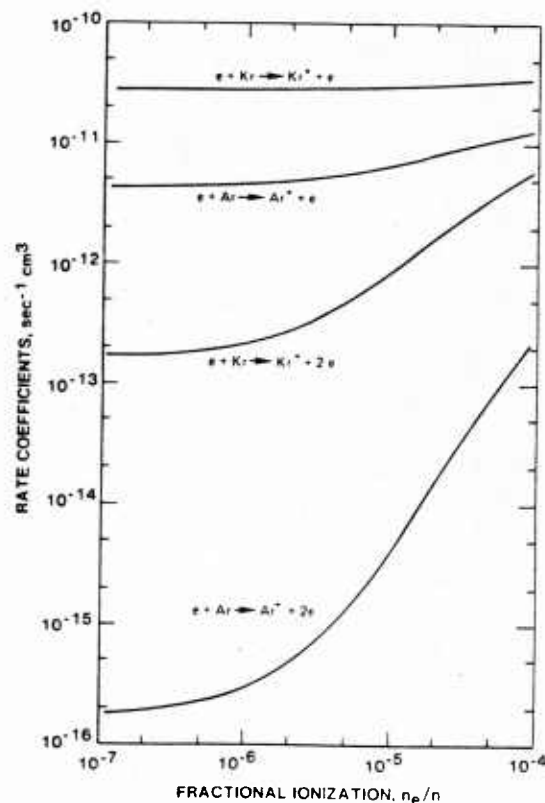


Fig. 4. Variation of Ar and Kr rate coefficients for metastable production and ionization with fractional ionization for an  $E/n$  value of  $1.0 \times 10^{-16} \text{ V} \cdot \text{cm}^2$ . The fractional concentrations of metastable and p state atoms were fixed at  $10^{-5}$  and  $10^{-6}$ , respectively.

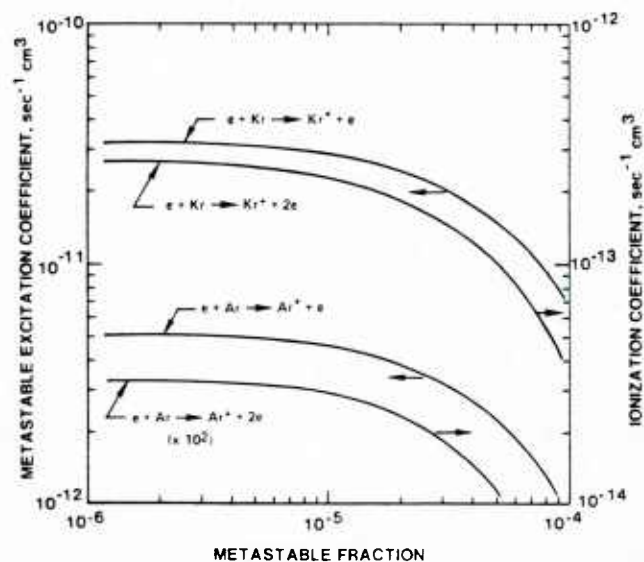


Fig. 5. Variation of Ar and Kr rate coefficients for metastable production and ionization with metastable fraction for an  $E/n$  value of  $1.0 \times 10^{-16} \text{ V} \cdot \text{cm}^2$  and a fractional ionization of  $10^{-6}$ . The fractional p state concentration was increased in proportion to the metastable fraction so that the p state: metastable ratio was always 0.1.

**$F_2$  Vibrational Excitation:** Fig. 6 also shows the electron rate coefficients for  $F_2$  vibrational excitation and for dissociative attachment of  $F_2$  in the vibrational ground state and in the first vibrational level, computed using the theoretical cross sections of [11]. The rate coefficient for vibrational excitation reflects excitation from the ground state to the first ten

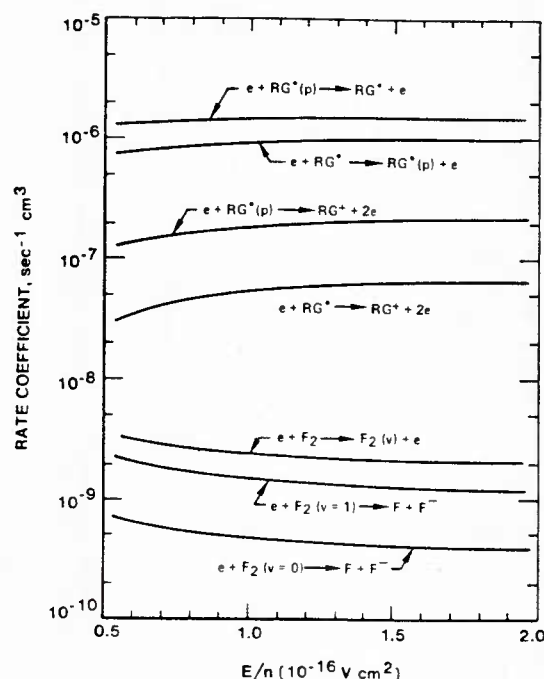


Fig. 6.  $E/n$  variation of electron rate coefficients for excitation, deexcitation and ionization of rare gas p state atoms, along with the rate coefficients for metastable ionization,  $F_2$  dissociative attachment, and  $F_2$  vibrational excitation. The rate coefficients for these processes exhibit very little change in response to variations in fractional ionization or excited state concentration. The notation RG refers to either Ar or Kr.

vibrational levels, each of which has been energy weighted [24] with respect to the first level. The attachment rate coefficient for  $F_2$  in the ground vibrational level is found to be within 5 percent of that computed using recent experimental cross section data [16]. While attachment cross sections for vibrationally excited  $F_2$  have not been measured, this agreement lends support to the theoretical prediction [11] that attachment to vibrationally excited  $F_2$  should proceed at a much faster rate than for  $F_2(v=0)$ . If such is the case, the increasing population of vibrationally excited  $F_2$  during the discharge excitation pulse will result in an increase in electron loss due to attachment, thereby tending to offset the reduction in the attachment loss accompanying the loss of  $F_2$  due to dissociation. Subsequent discussion will show that such an effect could influence the onset of plasma instability.

### C. Excited State Processes

In addition to efficient rare gas metastable production, efficient rare-gas monohalide formation requires that reactions leading to the formation of  $KrF^*$  dominate over competing metastable quenching processes. Thus, reactions between rare-gas metastable atoms and the halogen "fuel" molecule must be the dominant metastable loss process; and the branching ratio for the formation of the desired rare-gas monohalide molecule must be near unity. Setser and co-workers [25] have conducted extensive investigations of rare-gas metastable atom quenching and have found that practically all halogenated molecules have large rate constants. Moreover, diatomic halogens such as  $F_2$  have near unity branching ratio for rare-gas monohalide formation. Thus, energy efficient formation of

rare-gas monohalide molecules is usually assured in discharges in which rare-gas metastables are produced efficiently, and in which an appropriate halogen fuel molecule is present.

With a stimulated emission cross section in the  $1$  to  $5 \times 10^{-16}$   $\text{cm}^2$  range [1], maintenance of optimum gain requires a rare-gas monohalide density of about  $10^{14}$   $\text{cm}^{-3}$ , a relatively high excited state concentration even for an atmospheric pressure glow discharge. Thus, knowledge of rare-gas halide loss mechanisms under various conditions is particularly important. The dominant rare-gas halide quenching processes have been identified by Rokni, Jacob, and Mangano whose detailed analysis and interpretation is presented elsewhere [5]. Certain of their results relevant to  $\text{KrF}^*$  lasers are summarized in Table I along with other related data [26]–[30]. It is worth pointing out that each of the major constituents in the gas mixture collisionally quenches [5]  $\text{KrF}^*$  (Fig. 1, Table I). Additionally, with a radiative lifetime less than 10 ns, spontaneous decay of the rare-gas monohalide laser molecule is always important for the conditions of interest.

**Quenching of Rare-Gas P State Atoms by Neutral Collisions:** Fig. 6 shows that the rate coefficient for electron impact excitation of rare-gas metastable atoms to the higher lying manifold of p states [21] is very large. Indeed, for the conditions encountered in rare-gas halide lasers, this process can compete with the desired metastable- $\text{F}_2$  rare-gas monohalide formation channel. Thus, the significance of p state excitation from the metastable state depends on what happens to the p-state atoms after they are produced. For this reason, a knowledge of p-state quenching processes is particularly important. Recently Chang and Setser [30] reported rate coefficients for collisional quenching of Ar p-state atoms by argon at room temperature (Table I). Their results show that metastable production as a result of p-state quenching by ground state atoms will be very fast for pressures typical of rare-gas halide lasers. Such p-state-metastable transitions can be explained [30] in terms of a curve crossing mechanism among the  $\text{Ar}_2^+$  repulsive states which then dissociate, e.g.,  $\text{Ar}^*(p) + \text{Ar} \rightarrow \text{Ar}_2^+ \rightarrow \text{Ar}^* + \text{Ar}$ . Subsequent discussion will show that this process can dominate p-state atom quenching in rare-gas halide lasers thereby exerting an important influence on both rare-gas halide formation efficiency and plasma stability.

### III. LASER DISCHARGE ANALYSIS

#### A. Temporal Variations

**Plasma Modeling:** Analysis of plasma properties in pulsed rare-gas halide lasers requires modeling of the time dependent variation of electron, ion, and excited state processes for conditions typical of the excitation scheme of interest [1], [6], [7]. In the present work, emphasis has been placed on electron-beam controlled laser discharges operating under conditions similar to those described in [31]. For the most part, the modeling procedures used are similar to those typically employed in such analyses [6], [7]. The principle electron and excited state reactions and rate coefficients used in the present analysis have been discussed in the preceding section and are presented in Figs. 3–6 and in Table I. The dependence of electron-atom rate coefficients on variations in  $E/n$ , fractional ionization and metastable fraction was accounted for by solv-

TABLE I  
RARE GAS AND RARE-GAS HALIDE NEUTRAL REACTIONS AND RATE COEFFICIENTS FOR  $\text{KrF}^*$  LASERS

Reaction	Rate Coefficient <sup>a</sup>	Reference
$\text{Ar}^* + \text{Kr} \rightarrow \text{Kr}^*(p) + \text{Ar}$	5.6 (–12)	26
$\text{Ar}^* + \text{F}_2 \rightarrow \text{ArF}^* + \text{F}$	7.5 (–10)	5
$\text{Kr}^* + \text{F}_2 \rightarrow \text{KrF}^* + \text{F}$	7.8 (–10)	5
$\text{Ar}^*(p) + \text{Ar} \rightarrow \text{Ar}^* + \text{Ar}$	2–6 (–11)	30
$\text{Kr}^*(p) + \text{Ar} \rightarrow \text{Kr}^* + \text{Ar}$	2–6 (–11)	estimated (see 30)
$\text{ArF}^* + \text{Kr} \rightarrow \text{KrF}^* + \text{Ar}$	1.6 (–9)	5
$\text{ArF}^* + \text{Ar} + \text{M} \rightarrow \text{Ar}_2\text{F}^* + \text{M}$	4.0 (–31)	5
$\text{KrF}^* + \text{Kr} + \text{M} \rightarrow \text{Kr}_2\text{F}^* + \text{M}$	6.5 (–31)	5
$\text{KrF}^* + 2\text{Ar} \rightarrow \text{products}$	7.0 (–32)	5
$\text{ArF}^* + \text{F}_2 \rightarrow \text{products}$	1.9 (–9)	5
$\text{KrF}^* + \text{F}_2 \rightarrow \text{products}$	7.8 (–10)	5
$\text{KrF}^* \rightarrow \text{Kr} + \text{F} + h\nu$ (248 nm)	9 (–9)	27
$\text{ArF}^* \rightarrow \text{Ar} + \text{F} + h\nu$ (193 nm)	~ 4 (–9)	29
$\text{Kr}_2\text{F}^* \rightarrow 2\text{Kr} + \text{F} + h\nu$ (400 nm)	181 (–9)	28
$\text{Ar}_2\text{F}^* \rightarrow 2\text{Ar} + \text{F} + h\nu$ (290 nm)	132 (–9)	29

<sup>a</sup> Units: two-body processes,  $\text{sec}^{-1} \text{cm}^3$ ; three-body processes,  $\text{sec}^{-1} \text{cm}^6$ ; radiative processes,  $\text{sec}^{-1}$ . The number in ( ) refers to the exponent of ten.

ing the Boltzmann equation [19], [24] in order to generate a matrix of data similar to those presented in Figs. 3–5. On the basis of the data so obtained, rate coefficients for excitation and ionization from the ground state were represented analytically by an expression of the form,

$$k(E/n, \alpha, \delta) \equiv k_0(E/n) f(E/n, \alpha) g(E/n, \delta),$$

where  $k$  is the rate coefficient for a particular process,  $\alpha$  is the fractional ionization,  $\delta$  is the metastable fraction, and  $f$  and  $g$  are  $E/n$  dependent analytic functions reflecting the numerically determined variations in  $k$  with changes in  $\alpha$  and  $\delta$  (Figs. 4 and 5). Thus,  $k_0$  was determined by specifying an  $E/n$  value in the range of interest. The rate coefficients  $k(E/n, \alpha, \delta)$  were then computed as a function of time using self-consistent values of  $\alpha$  and  $\delta$ .

**Species Concentrations:** Fig. 7 presents the computed temporal variation of selected species for representative experimental conditions [31]. In this example, the external ionization source was increased as a function of time in order to simulate the increase in  $e$ -beam current density typical of pulsed, cold-cathode  $e$ -gun operation [31]. For these conditions, plasma properties reach quasi-steady values in a time less than 0.1  $\mu\text{s}$ . However, Fig. 7 shows that significant changes occur on a longer time scale because of the combined influence of the increasing  $e$ -beam ionization rate and  $\text{F}_2$  dissociation, particularly the latter. Indeed, for this example  $\text{F}_2$  dissociation exceeds 25 percent after about 0.6  $\mu\text{s}$ . The results presented in this figure show that the fractional ionization ( $\alpha = n_e/n$ ) and metastable fraction ( $\delta = n^*/n$ ) are approximately  $4 \times 10^{-6}$  and  $10^{-5}$ , respectively, values for which electron rate coefficients are affected by collisions with other electrons and with metastable atoms (Figs. 4 and 5). In addition, Fig. 7 shows

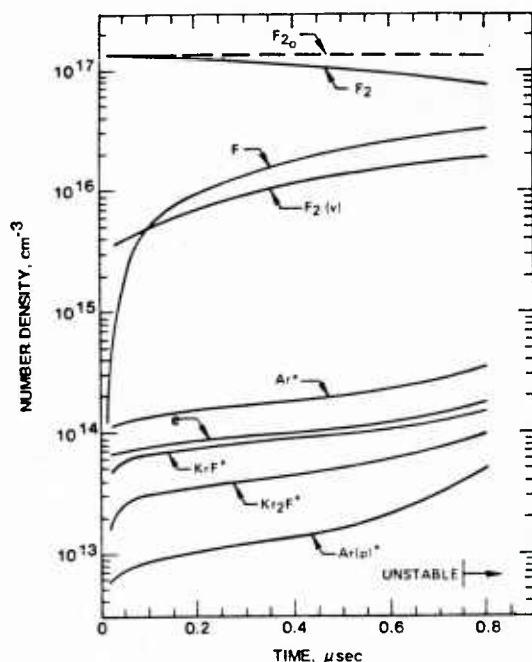


Fig. 7. Temporal variation of selected species in an  $e$ -beam controlled  $\text{KrF}^*$  laser discharge at a pressure of 1 atm;  $\text{Ar-Kr-F}_2$  (0.945–0.05–0.005). For this example the  $E/n$  value was  $1.2 \times 10^{-16} \text{ V} \cdot \text{cm}^2$ ; and the temporal variation of the  $e$ -beam ionization rate was  $160 + 8 \times 10^7 \text{ s}^{-1}$ , resulting in a 50 percent increase in the electron production rate after 1  $\mu\text{s}$ .

that after a few tenths of a  $\mu\text{s}$  the concentrations of vibrationally excited  $\text{F}_2$  and of  $\text{F}$  atoms reach levels corresponding to about one-tenth the initial  $\text{F}_2$  density.

The computed populations of all excited species considered in the present analysis are presented in Fig. 8 for a time 0.4  $\mu\text{s}$  after discharge initiation. This figure shows that the primary excited species are the rare gas metastables,  $\text{Ar}^*$  and  $\text{Kr}^*$ , and the krypton-fluorides  $\text{KrF}^*$  and  $\text{Kr}_2\text{F}^*$ , each having a concentration of approximately  $10^{14} \text{ cm}^{-3}$ . Other excited species have number densities in the  $2 \times 10^{12}$ – $2 \times 10^{13} \text{ cm}^{-3}$  range, with the total excited state fraction in excess of  $2 \times 10^{-5}$  for the conditions of this example. Clearly there are other excited rare gas and rare-gas halide molecules which will probably have concentrations on the order of  $10^{12} \text{ cm}^{-3}$  for conditions typical of rare-gas halide lasers.

**Medium Properties:** Numerical modeling of laser characteristics begins with a study of microscopic processes, analysis of which is the primary source of insight required to optimize and/or improve conditions. However, an equally important objective of such studies is quantitative computation of macroscopic properties of the laser medium which can be directly compared with experimental results. Indeed, comparison between predicted and measured rare-gas halide laser characteristics has been found to be very good [1], [7], [31].

Fig. 9 shows the computed small-signal gain,  $\text{KrF}^*$  production efficiency, total volumetric power density, and discharge:  $e$ -beam power enhancement factor corresponding to the conditions of Figs. 7 and 8. The  $\text{KrF}^*$  production efficiency ( $\eta$ ) as used here includes the quantum efficiency and as such represents the fraction of the total power potentially available for conversion to optical power. The enhancement factor (EF)

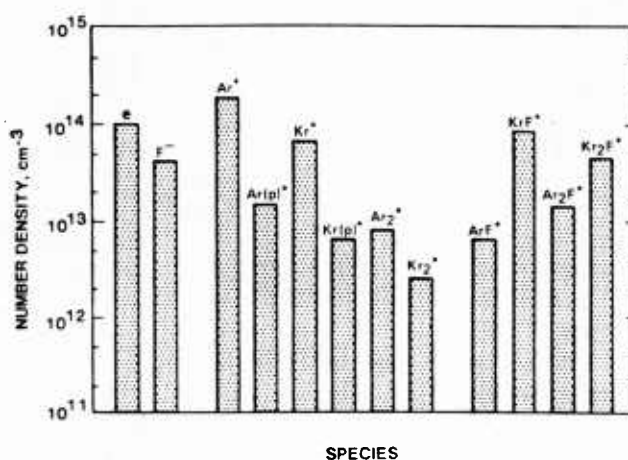


Fig. 8. Particle concentrations corresponding to the conditions of Fig. 7 at a time 0.4  $\mu\text{s}$  after discharge initiation.

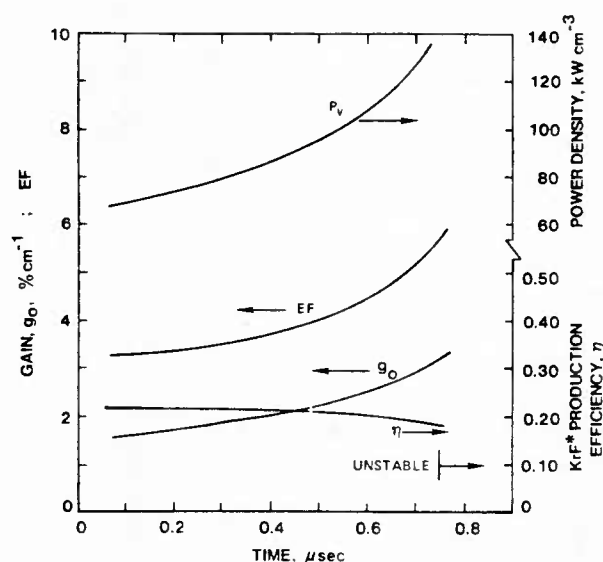


Fig. 9. Temporal variation of total electrical power density ( $P_v$ ), discharge:  $e$ -beam power enhancement factor (EF), small-signal gain ( $g_0$ ), and  $\text{KrF}^*$  production efficiency ( $\eta$ ) for the conditions of Fig. 7.

is simply the ratio of the discharge power to that supplied by the  $e$ -beam. The data of this figure illustrate the high gain and remarkable rare-gas monohalide production efficiency characteristic of rare-gas halide lasers,  $\text{KrF}^*$  in particular. Note, however, that although the power density is dominated by the discharge contribution ( $\text{EF} > 1$ ), the enhancement factor is very much lower than that typical of IR molecular lasers [9]. This is a direct consequence of the high  $e$ -beam power required to maintain the electron density at the necessary level in the presence of the enormous loss rate of electrons due to  $\text{F}_2$  dissociative attachment, a circumstance resulting in significant practical problems related to certain aspects of electron-beam technology. Furthermore, with a total electrical power density of approximately  $100 \text{ kW} \cdot \text{cm}^{-3}$ , the rate of gas temperature rise is well over  $100 \text{ K per } \mu\text{s}$ . This factor, when considered along with the rate of loss of fluorine fuel due to dissociation (Fig. 7), establishes an upper limit for laser pulse duration which is on the order of a few  $\mu\text{s}$ .

Fig. 9 shows that the energy utilization efficiency associated

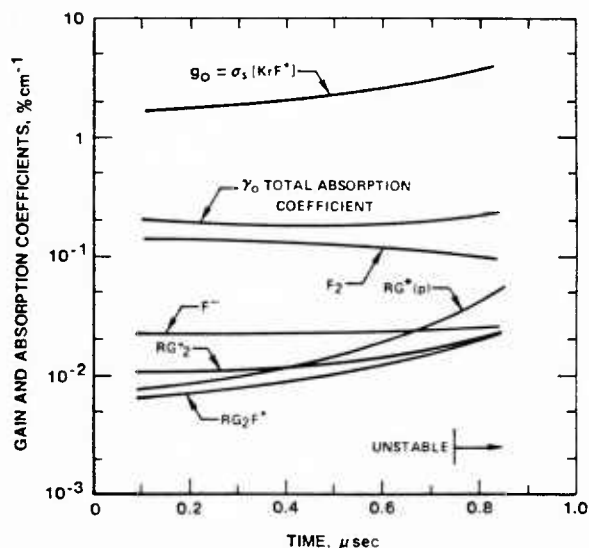


Fig. 10. Temporal variation of small-signal gain and absorption coefficients for the conditions of Fig. 7. The  $\text{KrF}^*$  stimulated emission cross section used was  $2.4 \times 10^{-16} \text{ V} \cdot \text{cm}^2$ ; and the absorption cross sections used for the species indicated were those reported in [32]. In this figure the notation RG refers to the combined effect of Ar and Kr.

with  $\text{KrF}^*$  production can be very high ( $\sim 20$  percent). However, overall laser efficiency is also dependent on optical power extraction efficiency. Analysis shows that optical extraction efficiency can be significantly affected by the presence of electronically excited and/or ion species which absorb at the UV laser wavelength [1], [32], even though the absorption coefficient ( $\gamma_0$ ) may be less than one-tenth as large as the gain coefficient. Indeed, it has been shown [1] that efficient optical extraction requires that  $\gamma_0/g_0 < 0.1$ . Presented in Fig. 10 is the computed temporal variation of the total absorption coefficient at the  $\text{KrF}^*$  laser wavelength (248 nm) corresponding to the conditions of Fig. 7. Also shown are the individual contributions from known absorbing species, computed on the basis of reported cross section data [32]. For the conditions of this example, photodissociation of  $\text{F}_2$  is obviously the dominant laser absorption process. However, the concentrations of ionic and excited species are subject to much greater variation than the  $\text{F}_2$  density, and their combined influence is very significant as indicated in Fig. 10. Analysis of optical extraction efficiency for the conditions of this figure yields a value of about 45 percent for an active medium length of 1 m. When combined with a  $\text{KrF}^*$  production efficiency of 20 percent (Fig. 9), an electrical-to-optical conversion efficiency of almost 10 percent is indicated, in accord with the highest experimental values attained to date under similar conditions [1].

### B. Dominant Processes

As indicated in Section II, numerous processes must be considered in the analysis of rare-gas halide lasers. However, numerical experimentation shows that certain processes such as rare gas metastable loss tend to be dominated by a single reaction. Others such as  $\text{KrF}^*$  formation and loss are affected by several reactions of approximately equal importance. Examination of the relative importance of the various coupled reactions is useful and provides insight helpful to understanding

and improving rare-gas halide lasers. In the following paragraphs, the relative contributions to electron production, metastable and p state loss, and  $\text{KrF}^*$  production and loss for the conditions of Figs. 7-9 will be discussed.

**Electron Production:** Ideally, when electron-beam ionization is employed to provide a stable, large volume plasma medium, ionization is controlled entirely by the external ionization source, effectively decoupling electron production from other plasma properties. Such is the case in IR molecular lasers [9], for example, in which the mean electron energy required for efficient vibrational excitation is much less than that for which electronic excitation and ionization become significant. However, in rare-gas halide lasers (and other excimer lasers as well) the mean electron energy required is several electron volts and the density of electronically excited species is high [9]. Given these circumstances along with the alkali-like structure of rare-gas metastables, significant ionization by low energy plasma electrons is usually unavoidable even when an external ionization source is used.

Fig. 11 compares the various fractional contributions to electron production in a  $\text{KrF}^*$  laser discharge operating under the conditions of Fig. 7. These results show that although ionization by the high energy  $e$ -beam is dominant, low energy electron impact ionization of rare-gas metastable atoms provides almost 20 percent of the ionization, a contribution which increases significantly with time. Indeed, even ionization of argon and krypton p states is important for the conditions of this example. The nonnegligible contribution of ground state ionization is a direct reflection of the increase in the ionization rate coefficient caused by electron-electron collisions.

The relative contributions to the ionization process as indicated by Fig. 11 are typical of the  $e$ -beam controlled rare-gas halide lasers that have been operated to date [1], [31], [33]-[35]. On the basis of these results, it is apparent that such discharges are actually of a hybrid nature in which substantial contributions to ionization are made by both high energy beam electrons and by plasma electrons.

**Metastable and p State Loss Processes:** In  $e$ -beam controlled rare-gas halide discharges, production of rare-gas metastable atoms is dominated by a single process, electron impact excitation of ground state atoms. However, there are several reactions by which metastable atoms are lost. Fig. 12 presents a comparison of the  $\text{Ar}^*$  loss processes for the conditions of present interest. The effect of coupling between the metastable and p states has been grouped as a single process as indicated. Thus,  $\text{Ar}^* \rightleftharpoons \text{Ar}^*(p)$  represents the net effect of electron excitation of the p states from the metastable states, and transitions back to the metastable states caused by both electron and neutral collisions and by radiative decay. This figure vividly illustrates the dominance of the desired metastable-halogen reaction [25] and in part explains why the  $\text{KrF}^*$  laser is so attractive. Although such selectivity is a requirement for efficient  $\text{KrF}^*$  formation, a consequence of the dominance of the  $\text{RG}^*-\text{F}_2$  reaction is that the metastable concentration is particularly sensitive to the loss of  $\text{F}_2$  due to dissociation. Since metastable ionization makes a significant contribution to electron production (Fig. 11), the increased metastable concentration accompanying dissociative loss of  $\text{F}_2$  has a particularly

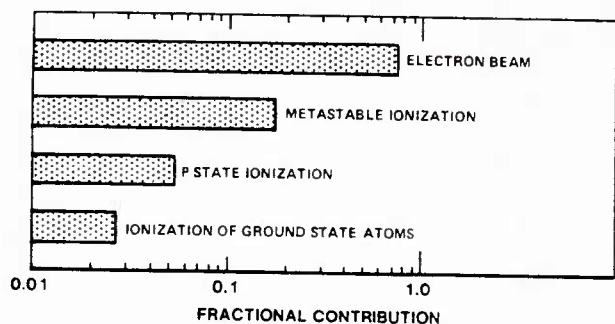


Fig. 11. Fractional contributions to electron production in an  $e$ -beam controlled  $\text{KrF}^*$  laser discharge for the conditions of Fig. 7. These results, and those presented in Figs. 12, 13, and 15-17, refer to the time  $0.4 \mu\text{s}$  after discharge initiation and are representative of conditions in the  $0.2$  to  $0.6 \mu\text{s}$  time range.

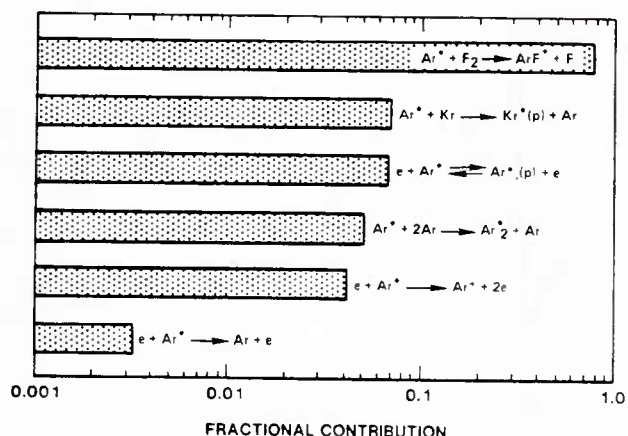


Fig. 12. Fractional contribution to argon metastable loss in an  $e$ -beam controlled  $\text{KrF}^*$  laser discharge for the conditions of Fig. 7.

serious effect on plasma stability, a topic which is discussed in a subsequent section.

For the reasons discussed in Section II, knowledge of the processes by which rare gas  $p$  state atoms are lost is of considerable importance. There are numerous processes resulting in the loss of  $p$ -state atoms including: electron superelastic collisions by which  $p$ -state atoms are converted back to metastable states with no net loss of electron energy, halogen reactions,<sup>3</sup> quenching by neutrals which also results in metastable production [30], electron excitation and ionization, and spontaneous radiative transitions back to the metastable states. Presented in Fig. 13 are the relative contributions of these processes to the loss of argon  $p$ -state atoms. These results show that neutral quenching of  $p$ -state atoms by ground state rare-gas atoms is the dominant  $p$ -state loss process. Thus,  $p$ -state atoms produced by way of electron collisions with metastable atoms are rapidly converted back to metastables by collisions with ground state atoms, with the result that this process has little net effect on the density of metastable atoms. However, the electron energy expended to produce  $p$ -state atoms from metastables is converted to translational energy of neutrals. As long as

<sup>3</sup>In this analysis it has been assumed that  $p$ -state- $\text{F}_2$  reactions result in  $\text{RGF}^*$  formation and proceed at a rate equal to that of the corresponding metastable reaction.

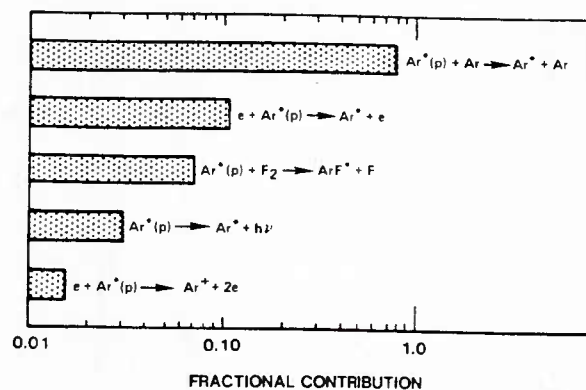


Fig. 13. Fractional contributions to the loss of argon  $p$  state atoms in an  $e$ -beam controlled  $\text{KrF}^*$  laser discharge for the conditions of Fig. 7.

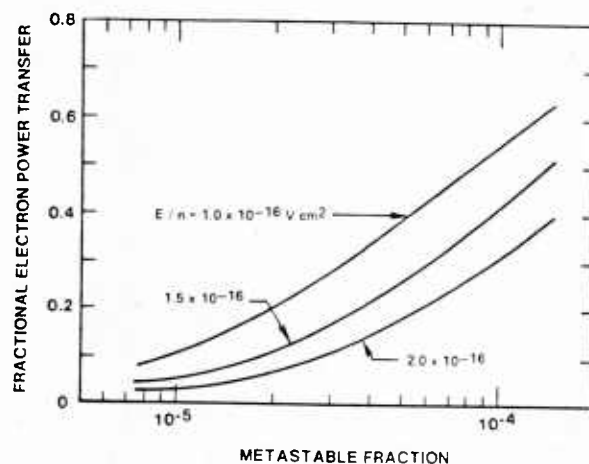


Fig. 14. Fractional loss of electron power resulting from the net effect of excitation and deexcitation of the rare gas  $p$  states in an  $\text{Ar-Kr-F}_2$  (0.945-0.05-0.005) mixture. The fraction of  $p$  state atoms was maintained at a value one-tenth that of the metastable fraction for the purposes of this illustration.

the electron energy loss associated with production of  $p$ -state atoms is not large the laser energy utilization efficiency is not greatly affected by this process. However, Fig. 14 shows that the fractional electron energy loss associated with  $p$ -state excitation depends directly on the metastable density and becomes very significant if the metastable fraction exceeds a value of approximately  $3 \times 10^{-5}$ .

**$\text{KrF}^*$  Formation and Loss:** The mechanisms responsible for rare-gas halide formation and loss have been the subject of extensive experimentation and analysis [1], [5], [25], [27], [28]. As a result, the reactions of primary importance have been identified and a generally complete set of rate data is available for use in analyses such as that described herein. Figs. 15 and 16 present a comparison of the relative importance of  $\text{KrF}^*$  production and loss for the conditions of Fig. 7. For the conditions of this example, the  $\text{ArF}^*-\text{Kr}$  displacement reaction [5] dominates the formation of  $\text{KrF}^*$ . Examination of Figs. 2, 12, and 15 reveals the direct, efficient channel of energy from the electrons to  $\text{Ar}^*$  to  $\text{ArF}^*$ , and finally to  $\text{KrF}^*$ . For typical conditions, the energy channeled through the  $\text{KrF}^*$  molecule represents between 20 and 30 percent of the total discharge energy (Fig. 9). Note, however, that both

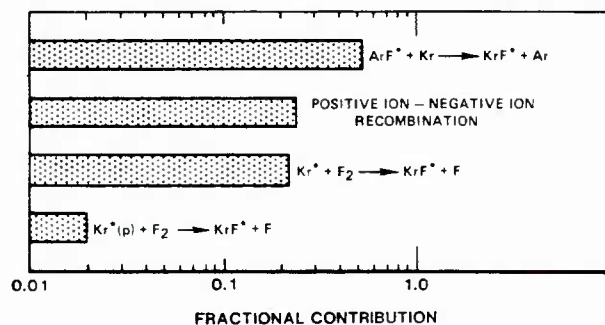


Fig. 15. Fractional contributions to  $\text{KrF}^*$  production in an  $e$ -beam controlled laser discharge for the conditions of Fig. 7.

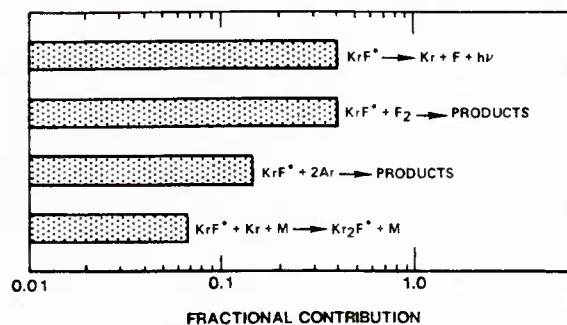


Fig. 16. Fractional contributions to  $\text{KrF}^*$  loss (in the absence of a radiation field) for the conditions of Fig. 7.

the contributions of positive ion-negative ion recombination and of the direct reaction of  $\text{F}_2$  with krypton metastables are also significant. The relative importance of the  $\text{Kr}^*-\text{F}_2$  reaction will be even larger for values of  $\text{Kr}$  fractional concentration larger than the 0.05 considered here.

For the present case in which there is no optical field present, spontaneous decay and  $\text{F}_2$  quenching are both very important loss channels for  $\text{KrF}^*$  as indicated in Fig. 16. However, three-body quenching by  $\text{Ar}$  and  $\text{Kr}$  are also very significant. Indeed, for somewhat higher  $\text{Kr}$  fractions and/or at pressures of a few atmospheres, three-body quenching becomes the dominant  $\text{KrF}^*$  loss process. Under these circumstances the concentration of the triatomic rare-gas halide  $\text{Kr}_2\text{F}^*$  approaches and even exceeds the  $\text{KrF}^*$  density.

Of particular interest is the fact that in  $e$ -beam controlled, discharge pumped lasers, no single process dominates either production or loss of the diatomic rare-gas halide molecule. Of course, efficient laser operation requires conditions such that stimulated emission is the dominant  $\text{KrF}^*$  loss process. With the ratio of gain to absorption ( $g_0/\gamma_0$ ) having a value of about ten, analysis shows that efficient optical power extraction requires an optical flux approximately twice the saturation level [1], the latter having a value of nearly  $1 \text{ MW} \cdot \text{cm}^{-2}$  for the conditions of Fig. 16.

### C. $\text{F}_2$ Dissociation

The results and discussion presented above show that optimum conditions for efficient production of  $\text{KrF}^*$  can be achieved in high-power  $e$ -beam controlled (or  $e$ -beam excited) lasers. In addition it is shown that  $\text{F}_2$  exerts a very important (indeed dominant) influence on the concentrations of electrons, metastable and  $p$ -state atoms, and rare-gas halide molecules. Thus, no single process exerts an influence on laser plasma conditions which is comparable to the effects of  $\text{F}_2$  dissociation. Fig. 7 shows that substantial  $\text{F}_2$  dissociation can occur in a time less than  $1 \mu\text{s}$  in  $e$ -beam controlled discharges. Although plasma conditions are quite satisfactory for the first  $0.5 \mu\text{s}$  for this example (Fig. 9), as a result of dissociation, a substantial variation in properties occurs for times in excess of about  $0.6 \mu\text{s}$ , resulting in the occurrence of plasma instability shortly thereafter.

The various contributions to  $\text{F}_2$  dissociation for these condi-

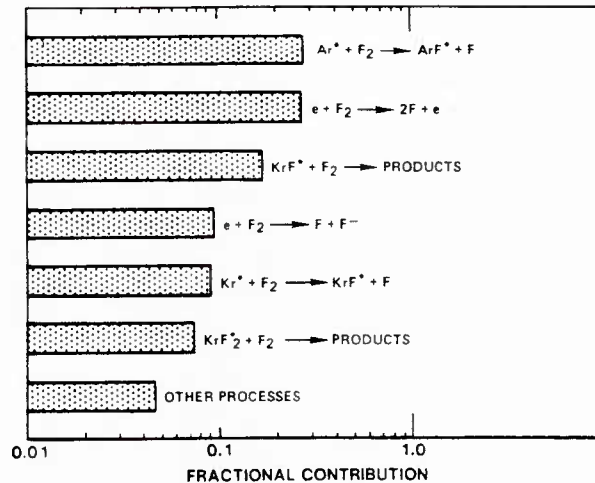


Fig. 17. Fractional contributions to  $\text{F}_2$  dissociation in an  $e$ -beam controlled  $\text{KrF}^*$  laser discharge for the conditions of Fig. 7.

tions are presented in Fig. 17. By far the most important feature of this figure is its indication of the large number of different processes resulting in dissociation. Clearly,  $\text{F}_2$  dissociative reactions are of a fundamental nature in rare-gas halide lasers. Indeed, because of the large number of reactions involved, numerical experimentation shows that the quasi-steady plasma properties discussed in previous paragraphs are relatively insensitive to variations in the rate coefficients used for the reactions indicated in Fig. 17, within known limits of uncertainty. However, since ionization resulting from low energy electron impact is always important (Fig. 11) for the conditions of primary interest, the plasma is only marginally stable. For this reason, the time at which instability actually occurs can vary significantly in response to changes in the  $\text{F}_2$  concentration.

### D. Plasma Instability

For the electrical power density values required for optimum laser performance, the loss of  $\text{F}_2$  due to dissociation, along with gas heating, establishes a maximum limit for discharge pulse length which is on the order of a few  $\mu\text{s}$ . However, the occurrence of plasma instability (current runaway) in a much shorter time actually determines the maximum attainable pulse duration in  $e$ -beam controlled rare-gas halide lasers [1], [31], [33]–[35]. For this reason, plasma instability plays a

uniquely important role in determining the experimentally accessible range of laser discharge operating parameters, especially discharge: *e*-beam power enhancement factor [1] (Fig. 9).

**Electron Density Growth:** Completely self-consistent analysis of rare-gas halide laser stability is a formidable problem, requiring consideration of the temporal response of the electrons, ions, and several excited species to disturbances in plasma properties. However, the mode of instability leading to current runaway in rare-gas halide discharges has been identified as ionization instability [1], [31], [36], [37]. This instability is a manifestation of temporal amplification of electron density disturbances. Therefore, useful insight can be obtained by consideration of the time dependent electron conservation equation alone. For the present purpose, this equation may be expressed in the form

$$\frac{\partial n_e}{\partial t} \approx nS + n_e n k_i + n_e n^* k_i^* + n_e n^*(p) k_i^*(p) - n_e n_{F_2} k_a, \quad (1)$$

where  $n_e$ ,  $n$ ,  $n^*$ ,  $n^*(p)$ , and  $n_{F_2}$  are the densities of electrons, ground state neutrals, metastables, p-state atoms and  $F_2$ , respectively,  $S$  is ionization rate due to the external source, and  $k_i$ ,  $k_i^*$ , and  $k_i^*(p)$  are the rate coefficients for ionization of ground state atoms, metastable atoms, and p-state atoms (Figs. 3-6), and  $k_a$  is the  $F_2$  attachment rate coefficient. If it is assumed that excited species respond to disturbances on a time scale which is shorter than that of the electrons,<sup>4</sup> and that electron density disturbances vary as  $\exp(\nu t)$ , application of first-order perturbation theory results in the following approximate expression for the *maximum* growth rate of electron density disturbances:

$$\nu \approx n k_i \left( 1 + \frac{\alpha}{k_i} \frac{\partial k_i}{\partial \alpha} \right) + 2n^* k_i^* + 3n^*(p) k_i^*(p) - n_{F_2} k_a. \quad (2)$$

The first term on the right-hand side is the contribution of ground state ionization; thus the term  $(\alpha/k_i) \partial k_i / \partial \alpha$  is a dimensionless quantity of order unity which reflects the variation in the ionization rate coefficient with changes in fractional ionization  $\alpha$  (Fig. 4). The second and third terms reflect the influence of metastable and p-state ionization, respectively, the factor-of-two arising because the metastable concentration varies as the square of the electron density, and the factor-of-three because the density of p-state atoms varies as the cube of the electron density. In order to ensure stability ( $\nu < 0$ , electron density disturbances damped), the attachment term  $n_{F_2} k_a$ , must always be larger than the combined contributions to (2) from the various ionization processes.

Presented in Fig. 18 are the temporal variations of the dominant contributions to (2) for the conditions of Fig. 7, i.e., excited state ionization and attachment to  $F_2$  (in the ground

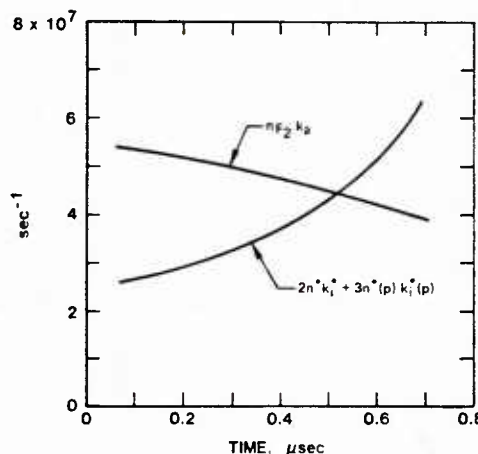


Fig. 18. First-order contributions to the growth (or damping) rate of electron density disturbances resulting from ionization of Ar and Kr excited states and from dissociative attachment to  $F_2$  in the ground vibrational state for the conditions of Fig. 7.

vibrational state). Initially, conditions are such that the contribution due to ionization from excited states is safely below that due to attachment, the latter effectively balanced by ionization provided by the external source (Fig. 11). However, as the  $F_2$  concentration decreases as a result of dissociation, this situation changes significantly with ionization from excited states increasing by about a factor of two in only a few tenths of a  $\mu s$ . Thus, the criterion for ionization stability ( $\nu < 0$ ) is quickly violated, usually in a time less than 1  $\mu s$  after discharge initiation.

Although the stabilizing influence of attachment is initially about twice as large as the terms due to ionization [(2), Fig. 18], the effects on electron density growth of attachment and ionization become equal ( $\nu = 0$ ) as a result of only 25 percent  $F_2$  dissociation (Fig. 7). Analysis of the factors contributing to (2) shows that the ratio of the ionization terms (destabilizing) to the attachment term (stabilizing) varies approximately as  $n_{F_2}^{-3}$ . For this reason, whenever ionization from excited states becomes significant ( $>10$  percent) relative to that provided by the *e*-beam, plasma stability is exceptionally sensitive to the loss of  $F_2$ .

**Current Runaway:** The temporal evolution of discharge current density prior to instability onset and the time at which current runaway actually occurs are both very sensitive to the discharge  $E/n$  value. Fig. 19 presents computed current density profiles for various  $E/n$  values and conditions otherwise similar to those discussed previously. The discharge: *e*-beam power enhancement factor at the leading edge of the pulse is also indicated. Although the current density is uniform and the plasma is stable for over 1  $\mu s$  at an  $E/n$  value of  $1.0 \times 10^{-16}$  V  $\cdot$  cm<sup>2</sup>, at this value the power enhancement factor is only about two. That is, about  $\frac{1}{3}$  of the total power is provided by the *e*-beam ionization source just to maintain the electron density at the required level. Increasing  $E/n$  results in a substantial increase in the discharge power, and therefore in the enhancement factor as is desired. However, Fig. 19 shows that this is accomplished at the expense of stable discharge dura-

<sup>4</sup> Although electrons and metastable atoms often respond to disturbances on the same time scale, the approximation that perturbations in the metastable concentration are quasi-steady significantly simplifies analysis, thereby facilitating development of insight as regards the causes of ionization instability.

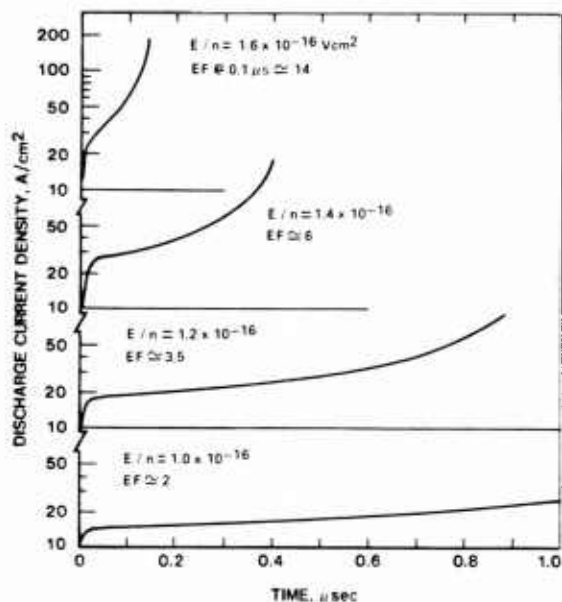


Fig. 19. Temporal variation of discharge current density for various  $E/n$  values and conditions otherwise the same as Fig. 7. The indicated values of discharge: e-beam power enhancement factor refer to the time 0.1  $\mu$ s after discharge initiation.

tion. For  $E/n$  values of  $1.2 \times 10^{-16} \text{ V} \cdot \text{cm}^2$  and higher, current density runaway occurs in a time less than one  $\mu$ s as is evidenced by a rapidly increasing current density derivative.

**Instability Onset Time:** Presented in Fig. 20 is the  $E/n$  dependence of the time at which the computed current density runaway occurs as determined by the present kinetic model for KrF\* laser conditions. Instability onset time determined on this basis is directly comparable with experimental observation of current runaway; and, the computed current runaway time presented in this figure is found to be in good agreement with measured values [31]. Since current runaway is particularly sensitive to the concentration of rare-gas excited states, for which there is no direct experimental measure, agreement between calculated and measured current density profiles serves as a check on the accuracy of the former. Also shown in Fig. 20 is a dashed curve representing the time after discharge initiation at which the theoretical criterion for ionization instability is first satisfied ( $\nu = 0$ ). This time was determined by computing the instability growth (or damping) rate using time varying plasma conditions to evaluate (2). For low values of  $E/n$  the plasma is stable for a relatively long time ( $\sim 1 \mu$ s). Under these conditions, the computed instability onset time based on the theoretical criterion ( $\nu = 0$ ) and on the current runaway time as determined from the complete kinetics calculation are essentially equivalent, reflecting the very short time ( $< 100 \text{ ns}$ ) characterizing ionization growth after the initiation of instability.<sup>5</sup> As  $E/n$  is increased, the time characteristic of stable discharge duration ( $\nu < 0$ ) is reduced dramatically, approaching zero for  $E/n$  values only slightly higher than those shown in

<sup>5</sup>On the basis of this comparison it can also be concluded that the factors dominating ionization instability in rare-gas halide lasers are reasonably represented by the approximate expression for the instability growth rate given in (2).

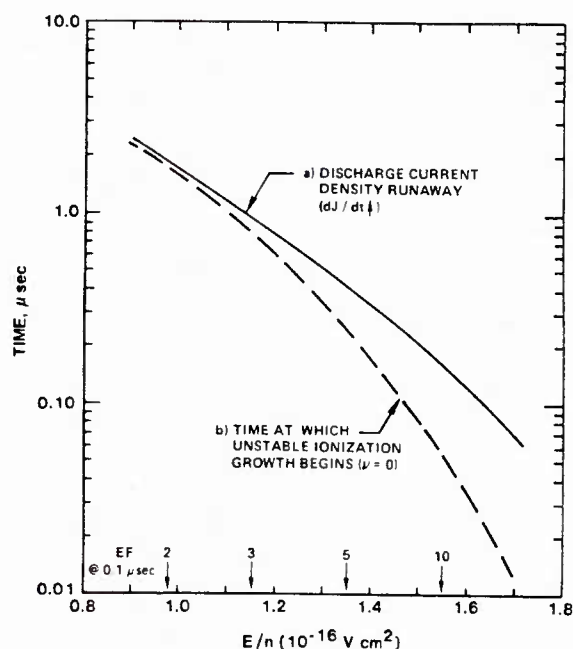


Fig. 20.  $E/n$  variation of the time after discharge initiation at which numerically determined current runaway begins (curve a); and at which exponential growth of electron density disturbances begins, i.e., ionization instability (curve b). In the evaluation of curve b ( $\nu = 0$ ) ionization of ground state atoms and attachment of vibrationally excited  $F_2$  were taken into account. These results correspond to the conditions of Fig. 7.

the figure. That is, for high  $E/n$  values, the plasma is unstable practically from the time of its initiation, based on the criterion that  $\nu$  be less than zero to ensure stability. However, Fig. 20 shows that the actual occurrence of current runaway at high  $E/n$  values is delayed by a time which is approximately equal to the ionization growth time,  $\sim (n^* k_i^*)^{-1}$ . Nevertheless, for the conditions considered here, the duration of the excitation pulse for which the energy enhancement factor can be maintained at a level near ten is limited to approximately 0.1  $\mu$ s as a result of ionization instability.

#### IV. SUMMARY AND DISCUSSION

The analysis and discussion of the preceding sections focuses attention on the relationship among the numerous processes contributing to the formation and loss of the KrF\* molecule in an electron-beam controlled discharge. Therein it is shown that KrF\* can be produced with an efficiency of 20 percent using this scalable excitation technique. In addition, krypton-monofluoride densities in excess of  $10^{14} \text{ cm}^{-3}$  are readily attained which, when combined with a stimulated emission cross section of about  $2.4 \times 10^{-16} \text{ cm}^2$ , results in a gain coefficient of about 1 percent  $\text{cm}^{-1}$ . Thus, it can be concluded that KrF\* kinetic processes are generally very favorable for efficient laser operation under conditions typical of near atmospheric pressure electron-beam controlled discharges.

The plasma required to achieve optimum KrF\* laser excitation is characterized by a mean electron energy of several electron volts, a fractional ionization greater than  $10^{-6}$ , and a fractional metastable concentration in excess of  $10^{-5}$ . Section II shows that under these conditions electron-electron col-

lisions and electron collisions with excited atoms have a very important effect on plasma processes. Further, it is shown that numerous reactions, including rare-gas halide formation, result in dissociation of the fluorine fuel molecules. Since reactions between halogen molecules and both metastable atoms and electrons exert a controlling influence on the population of these species, dissociation of  $F_2$  results in significant changes in plasma properties. Indeed, the results presented here show that as a result of  $F_2$  dissociation,  $KrF^*$  laser properties are continuously changing from the time of plasma initiation until termination due either to the onset of instability or to critical loss of  $F_2$ . For values of discharge:  $e$ -beam power enhancement greater than about three, results obtained to date have shown that plasma instability limits maximum laser pulse duration to a time less than  $1 \mu s$  (Figs. 19-20). However, with  $E/n$  values corresponding to enhancement factors in the 2-3 range, laser pulses of about  $1 \mu s$  have been achieved [1], with eventual loss of  $F_2$  being the factor limiting pulse duration. This general behavior is typical of all electron-beam controlled rare-gas halide lasers [1], [35] and of the closely related mercury-halide [38] lasers as well.

Based on the good agreement between measured and predicted laser characteristics, it is reasonable to conclude that the dominant reactions influencing rare-gas halide formation and loss have been identified and that a satisfactory data base exists. However, operational experience with rare-gas halide lasers has, for the most part, been limited to single pulse experiments [1]. Practical implementation of this unusually promising class of high-power lasers requires dependable, repetitive pulse operation using a flowing, recirculating gas mixture. In addition, many applications will require electron-beam controlled discharge excitation under conditions such that the  $e$ -beam power is a relatively small fraction ( $<0.1$ ) of the discharge power. Past experience with IR molecular lasers indicates that the major obstacles to achieving these objectives will be related to plasma chemical processes and discharge stability [39]-[41]. Solution of these formidable problems will require substantial additions to the existing body of knowledge pertaining to rare-gas halide kinetics. Aside from the primary reactions directly involved in rare-gas halide molecular processes, very little data exist for reactions between halogen molecules (and atoms) and discharge species. For example, there is little or no information pertaining to the reaction of either F atoms or  $F_2$  with rare-gas excited states, electrons, or ions [42]. While reactions of this type may play only a secondary role in rare-gas monohalide molecule formation and loss as it occurs in a single pulse experiment, they are certain to exert an important influence on the chemistry of closed-cycle, repetitive pulse lasers.

Analysis of positive ion reactions in rare-gas halide plasmas is based almost entirely on the premise that rare-gas monomer and dimer ions are dominant. However, in addition to these ions, rare-gas trimer ions, heteronuclear rare-gas dimer ions, and rare-gas halide ions are likely to be present in significant concentrations ( $\geq 10$  percent). It is known that relatively small concentrations of complex ions can significantly influence plasma properties [43] (especially stability [41]) because of their unusually large electron recombination coefficients [44].

In addition, positive ions play a unique role in rare-gas halide lasers as a consequence of their direct involvement in rare-gas halide formation [1], [5] and because they absorb radiation at the laser wavelength [32], [45]. For these reasons, improved knowledge of ion reactions at high pressure and low temperature is also of importance, especially under closed-cycle conditions for which the concentration of neutral species produced by plasma-chemical reactions is likely to become substantial.

Experimental verification [1] of the high energy conversion efficiency predicted for the  $KrF^*$  laser represents a significant milestone in the development of a scalable, high power UV laser, and provides impressive evidence that conditions optimum for efficient laser excitation can be created in a high pressure, chemically active plasma. However, it has also been found that it is exceptionally difficult to maintain the desired plasma properties in a stable, long pulse ( $\sim \mu s$ ) discharge because of significant changes in the gas mixture arising from the rare-gas halide formation process itself. As these systems are scaled for applications requiring high average power, difficulties arising from this circumstances will certainly become more pronounced. For this reason, it is clear that future efforts must be directed toward identification of the dominant ion and neutral chemical reactions occurring under the plasma conditions to be encountered with closed-cycle, respectively pulsed rare-gas halide lasers.

#### ACKNOWLEDGMENT

It is a pleasure to acknowledge the comments of R. T. Brown, which were particularly helpful in the preparation of this paper. Useful discussions with R. H. Bullis, H. H. Michels, L. A. Newman, and W. J. Wiegand are also appreciated.

#### REFERENCES

- [1] M. Rokni, J. A. Mangano, J. H. Jacob, and J. C. Hsia, "Rare gas fluoride lasers," *IEEE J. Quantum Electron.*, vol. QE-14, pp. 464-481, July 1978.
- [2] J. J. Ewing, "Rare-gas halide lasers," *Phys. Today*, vol. 31, pp. 32-39, May 1978.
- [3] J. E. Velazco and D. W. Setser, "Bound-free emission spectra of diatomic xenon halides," *J. Chem. Phys.*, vol. 62, pp. 1990-1991, Mar. 1, 1975.
- [4] P. J. Hay and T. H. Dunning, Jr., "The electronic states of  $KrF^*$ ," *J. Chem. Phys.*, vol. 66, pp. 1306-1316, Feb. 1977.
- [5] M. Rokni, J. H. Jacob, and J. A. Mangano, "Dominant formation and quenching processes in  $e$ -beam pumped  $ArF^*$  and  $KrF^*$  lasers," *Phys. Rev. A*, vol. 16, pp. 2216-2224, Dec. 1977.
- [6] J. H. Jacob and J. A. Mangano, "Modeling the  $KrF^*$  laser discharge," *Appl. Phys. Lett.*, vol. 28, pp. 724-726, June 15, 1976.
- [7] W. B. Lacina and D. B. Cohn, "Theoretical analysis of the electrically excited  $KrF^*$  laser," *Appl. Phys. Lett.*, vol. 32, pp. 106-108, Jan. 15, 1978.
- [8] A. J. DeMaria, "Review of high-power  $CO_2$  lasers," in *Principles of Laser Plasmas*, G. Bekefi, Ed. New York: Wiley, 1976.
- [9] J. D. Daugherty, "Electron-beam ionized lasers," in *Principles of Laser Plasmas*, G. Bekefi, Ed. New York: Wiley, 1976.
- [10] W. L. Nighan, "Influence of molecular dissociation and degree of ionization on rare-gas halide laser properties," *Appl. Phys. Lett.*, vol. 32, pp. 424-426, Apr. 1, 1978.
- [11] R. J. Hall, "Dissociative attachment and vibrational excitation of  $F_2$  by slow electrons," *J. Chem. Phys.*, vol. 68, pp. 1803-1807, Feb. 15, 1978.
- [12] W. L. Nighan, "Influence of electron- $F_2$  collisions in rare-gas halide laser discharges," *Appl. Phys. Lett.*, vol. 32, pp. 297-300, Mar. 1, 1978.
- [13] P. J. Hay and D. C. Cartwright, "Rydberg, ionic and valence in-

- teractions in the excited states of  $F_2$ ," *Chem. Phys. Lett.*, vol. 41, pp. 80-82, July 1, 1976.
- [14] M. V. Kurepa and D. S. Belic, "Dissociative attachment of electrons to chlorine molecules," *Chem. Phys. Lett.*, vol. 49, pp. 608-610, Aug. 1, 1977.
- [15] W. C. Tam and S. F. Wong, "Dissociative attachment of halogen molecules by 0-8 eV electrons," *J. Chem. Phys.*, vol. 68, pp. 5626-5630, June 15, 1978.
- [16] P. J. Chantry, "Attachment measurements in halogen bearing molecules," to be published.
- [17] W. L. Borst, "Excitation of metastable argon and helium atoms by electron impact," *Phys. Rev. A*, vol. 9, pp. 1195-1200, Mar. 1974.
- [18] D. Rapp and P. Englander-Golden, "Total cross sections for ionization and attachment in gases by electron impact. I. Positive ionization," *J. Chem. Phys.*, vol. 43, pp. 1464-1479, Sept. 1, 1963.
- [19] S. D. Rockwood, "Elastic and inelastic cross-sections for electron-Hg scattering from Hg transport data," *Phys. Rev. A*, vol. 8, pp. 2348-2358, Nov. 1973.
- [20] W. H. Long, Jr., "Electron kinetics in the KrF laser," *Appl. Phys. Lett.*, vol. 31, pp. 391-393, Sept. 15, 1977.
- [21] H. A. Hyman, "Electron impact excitation of metastable argon and krypton," *Phys. Rev. A*, to be published.
- [22] D. Ton-That and M. R. Flannery, "Cross sections for ionization of metastable rare-gas atoms ( $Ne^*$ ,  $Ar^*$ ,  $Kr^*$ ,  $Xe^*$ ) and of metastable  $N_2^*$ ,  $CO^*$  molecules by electron impact," *Phys. Rev. A*, pp. 517-526, Feb. 1977.
- [23] Cross sections for ionization of rare gas atoms from their p states were obtained using Gryzinski's formula (*Phys. Rev.*, vol. 138, pp. A336-A358, Apr. 19, 1963). As a check on the validity of this approximation for the conditions of interest, Gryzinski cross sections for ionization of rare-gas metastable states were generated and were found to be in good agreement with those of [22].
- [24] W. L. Nighan, "Electron energy distributions and collision rates in electrically excited  $N_2$ , CO, and  $CO_2$ ," *Phys. Rev. A*, vol. 2, pp. 1989-2000, Nov. 1970.
- [25] J. E. Velazco, J. H. Kolts, and D. W. Setser, "Quenching rate constants for metastable argon, krypton, and xenon atoms by fluorine containing molecules and branching ratios for  $XeF^*$  and  $KrF^*$  formation," *J. Chem. Phys.*, vol. 65, pp. 3468-3480, Nov. 1, 1976.
- [26] L. G. Piper and D. W. Setser, "Electronic energy transfer from metastable argon atoms to krypton atoms," *J. Chem. Phys.*, vol. 63, pp. 5018-5028, Dec. 1, 1975.
- [27] G. P. Quigley and W. M. Hughes, "The radiative lifetime and quenching of  $KrF^*$ ," *Appl. Phys. Lett.*, vol. 32, pp. 627-629, May 15, 1978; also, J. G. Eden, R. W. Waynant, S. K. Searles, and R. Burnham, "New quenching rates applicable to the KrF lasers," *Appl. Phys. Lett.*, vol. 32, pp. 733-735, June 1, 1978.
- [28] —, "Lifetime and quenching rate constants for  $Kr_2F^*$  and  $Kr^*$ ," *Appl. Phys. Lett.*, vol. 32, pp. 649-651, May 15, 1978.
- [29] P. J. Hay and T. H. Dunning, "The covalent and ionic states of the rare-gas monofluorides," *J. Chem. Phys.*, to be published.
- [30] R. S. F. Chang and D. W. Setser, "Radiative lifetimes and two-body deactivation rate constants for  $Ar(3p^5, 4p)$  and  $Ar(3p^5, 4p')$  states," *J. Chem. Phys.*, to be published.
- [31] R. T. Brown and W. L. Nighan, "Instability onset in electron-beam sustained  $KrF^*$  laser discharges," *Appl. Phys. Lett.*, vol. 32, pp. 730-732, June 1, 1978.
- [32] A. M. Hawryluk, J. A. Mangano, and J. H. Jacob, "Gain and absorption measurements in a  $KrF^*$  laser," *Appl. Phys. Lett.*, vol. 31, pp. 164-166, Aug. 1, 1977.
- [33] C. H. Fisher and R. E. Center, "Threshold power density measurements for electron-beam sustained discharge excitation of  $XeF^*$  and  $KrF^*$ ," *Appl. Phys. Lett.*, vol. 31, pp. 106-108, July 15, 1977.
- [34] J. A. Mangano, J. H. Jacob, and J. B. Dodge, "Electron-beam controlled discharge pumping of the  $XeF$  laser," *Appl. Phys. Lett.*, vol. 29, pp. 426-428, Oct. 1, 1976.
- [35] L. F. Champagne and N. W. Harris, "Characteristics of the electron-beam controlled  $XeF$  laser," *Appl. Phys. Lett.*, to be published.
- [36] J. D. Daugherty, J. A. Mangano, and J. H. Jacob, "Attachment dominated electron-beam ionized discharges," *Appl. Phys. Lett.*, vol. 28, pp. 581-583, May 15, 1976.
- [37] W. H. Long, Jr., "Discharge stability in e-beam sustained rare-gas halide lasers," to be published.
- [38] J. H. Parks, "Laser action on the  $B^2\Sigma_{1/2}^+ \rightarrow X^2\Sigma_{1/2}^+$  band of  $HgCl$  at 5576  $\text{\AA}$ ," *Appl. Phys. Lett.*, vol. 31, pp. 192-194, Aug. 1, 1977; also, W. T. Whitney, "Sustained discharge excitation of  $HgCl$  and  $HgBr$   $B^2\Sigma_{1/2}^+ \rightarrow X^2\Sigma_{1/2}^+$  lasers," *Appl. Phys. Lett.*, vol. 32, pp. 239-241, Feb. 15, 1978.
- [39] W. L. Nighan, "Stability of high-power molecular laser discharges," in *Principles of Laser Plasmas*, G. Bekefi, Ed. New York: Wiley, 1976.
- [40] —, "Causes of thermal instability in externally sustained molecular discharges," *Phys. Rev. A*, vol. 15, pp. 1701-1720, Apr. 1970.
- [41] —, "Influence of recombination and ion chemistry on the stability of externally sustained molecular discharges," *Phys. Rev. A*, vol. 16, pp. 1209-1223, Sept. 1977.
- [42] E. W. McDaniel, M. R. Flannery, H. W. Ellis, F. L. Eisele, W. Pope, and T. G. Roberts, "Compilation of data relevant to rare gas-rare gas and rare gas-monohalide excimer lasers: Volumes 1 and 2," U.S. Army Missile Research and Development Command (DRDMI-TI), Rep. H-78-1, Dec. 1977.
- [43] C. W. Werner, E. Zamir, and E. V. George, "Pressure dependence of the electron density in electron-beam-excited rare-gas plasmas," *Appl. Phys. Lett.*, vol. 29, pp. 236-239, Aug. 15, 1976.
- [44] M. A. Biondi, "Recombination," in *Principles of Laser Plasmas*, G. Bekefi, Ed. New York: Wiley, 1976.
- [45] W. R. Wadt, D. C. Cartwright, and J. S. Cohen, "Theoretical absorption spectra for  $Ne_2^+$ ,  $Ar_2^+$ ,  $Kr_2^+$ , and  $Xe_2^+$  in the near ultraviolet," *Appl. Phys. Lett.*, vol. 31, pp. 672-674, Nov. 15, 1977.

# Influence of molecular dissociation and degree of ionization on rare gas-halide laser properties<sup>a)</sup>

William L. Nighan

United Technologies Research Center, East Hartford, Connecticut 06108  
(Received 29 September 1977; accepted for publication 20 December 1977)

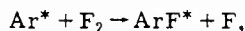
The influence of  $F_2$  dissociation and the accompanying increase in fractional ionization is examined for conditions typical of electron-beam-sustained  $KrF^*$  lasers. It is found that for electron-density- $F_2$ -density ratios greater than about  $10^{-3}$ , rare-gas metastable loss due to electron excitation of higher levels begins to compete significantly with metastable- $F_2$  reactions, thereby leading to a substantial reduction in rare gas-halide production efficiency.

PACS numbers: 42.55.Hq, 52.25.-b, 34.80.Dp

Numerous processes contribute to dissociation of the halogen-bearing molecule in rare gas-halide lasers.<sup>1</sup> In long-pulse ( $\sim 1 \mu\text{sec}$ ) or high-power-density ( $\gtrsim 100 \text{ kW cm}^{-2}$ ) lasers the reduction in halogen molecule density can be substantial ( $> 10\%$ ). Two of the most significant effects accompanying dissociation are (1) an increase in the rare-gas metastable density due to a decrease in the rate of reactions with the halogen molecule and (2) an increase in the electron density due to the combined effects of reduced attachment loss and increased ionization from rare-gas metastable states. In the present paper the influence of these coupled processes on gain and rare-gas-halide production efficiency is examined for conditions representative of electron-beam-sustained  $KrF^*$  laser discharges.<sup>2</sup>

In order to evaluate the effect on laser discharge properties of temporal changes in plasma processes, a numerical kinetics model was developed following procedures generally similar to those described elsewhere,<sup>1,3,4</sup> with the following exceptions: (1) In the present analysis the effects of direct electron impact dissociation and vibrational excitation of  $F_2$  were taken into account<sup>1</sup> and (2) the effects of electron-electron<sup>5</sup> and electron-ion collisions were included in the calculation of the electron distribution function and all electron rate coefficients.

For atmospheric-pressure mixtures of Ar, Kr, and  $F_2$  in which the fractional concentration of Ar is approximately 0.95, on the order of 50% of the total electrical power is utilized in the production of argon metastable states.<sup>1,4</sup> The metastable atoms so produced engage in numerous reactions, with the primary reaction sequence leading to  $KrF^*$  formation,<sup>6</sup> e.g.,



For optimum discharge conditions studies show that this energy pathway can be very efficient with as much as 20% of the total power available for conversion to optical energy. However, the present analysis indicates that significant changes in the nature of rare-gas metastable loss accompany the decrease in  $F_2$  concentration due to dissociation. Presented in Fig. 1 are

computed time-dependent fractional contributions of various argon metastable loss processes in an atmospheric-pressure electron-beam-sustained  $KrF^*$  laser discharge. In this example, the electron-ion pair production rate by the electron beam was set so as to produce an initial electron density of approximately  $10^{14} \text{ cm}^{-3}$ . For these conditions the power input from the e-beam was about one-third of the total power, i.e., the discharge enhancement factor was approximately 3. The results of Fig. 1 show that the two primary loss

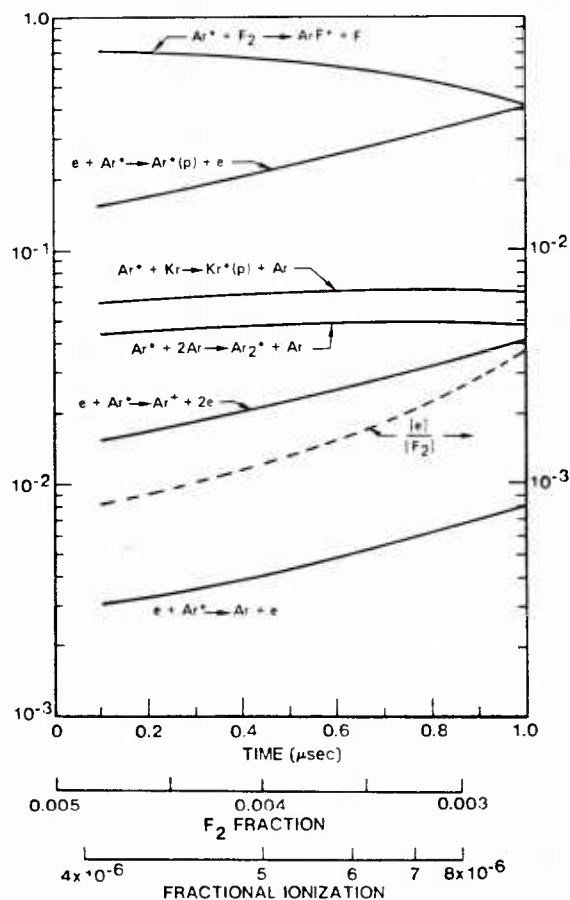


FIG. 1. Fractional contributions to argon metastable atom loss processes in an electron-beam-sustained atmospheric-pressure discharge with an  $E/n$  value of  $1.2 \times 10^{-16} \text{ V cm}^2$ . For these conditions the gas mixture was composed of Ar-Kr- $F_2$  (0.95-0.05-0.005) and the e-beam electron-ion pair production rate was  $250 \text{ sec}^{-1}$ .

<sup>a)</sup> Portions of this work were supported by the Office of Naval Research.

TABLE I. Fractional contributions to  $F_2$  dissociation for the conditions of Fig. 1.

Attachment	$e \rightarrow F_2 \rightarrow F + F^-$	0.14
Direct dissociation	$e + F_2 \rightarrow 2F + e$	0.36
ArF* production	$Ar^* + F_2 \rightarrow ArF^* + F$	0.28
KrF* quenching by $F_2$	$KrF^* + F_2 \rightarrow \text{products}$	0.12
Other processes		0.10
		1.00

processes controlling the density of argon metastables are the desired  $F_2$  reaction resulting in  $ArF^*$  formation and electron excitation of the metastables to the rare-gas  $p$  states.<sup>7</sup> For times up to about  $0.4 \mu\text{sec}$  Fig. 1 shows that  $p$ -state excitation is not particularly significant. However, for longer times electron excitation of metastables to higher states becomes very important. This trend is a direct consequence of the decrease in  $F_2$  concentration due to dissociation which, in turn, results in an increase in electron density. Since the  $Ar^*-F_2$  reaction is a binary process and since the electron- $Ar^*$   $p$ -state excitation rate is very weakly dependent on  $E/n$ , the increasing importance of  $p$ -state excitation relative to  $ArF^*$  formation depends almost solely on the relative concentrations of electrons and  $F_2$  molecules. Note that the electron-density- $F_2$ -density ratio, which is also shown in Fig. 1, increases by almost a factor of 5 in  $1 \mu\text{sec}$ . Based on these considerations the results of Fig. 1 show that metastable loss due to  $p$ -state excitation begins to compete significantly with  $ArF^*$  formation for  $[e][F_2]^{-1}$  ratios greater than about  $10^{-3}$ .

It is worth pointing out that in this example the initial power density level is only about  $70 \text{ kW cm}^{-3}$ , a value not much higher than the measured<sup>2</sup>  $20\text{-kW cm}^{-3}$  laser threshold levels. Further, Table I shows that there are several processes contributing to  $F_2$  dissociation, any one of which would lead to substantial dissociation on a  $\mu\text{sec}$  time scale. Thus, dissociation of the halogen-bearing molecule appears to be of fundamental importance for conditions typical of rare gas-halide lasers. In this regard it is interesting to note that when  $F_2$  is used as the source of fluorine, dissociation results in the gradual elimination of the molecular attaching species. Thus, the resultant effect of dissociation on electron density and electron energy kinetics<sup>1</sup> will be a maximum if a diatomic source of fluorine is used. If a polyatomic fluorine molecule is used, reactions of the type listed in Table I still occur, but they do not appreciably affect the total molecular density, so that the kinetic feedback effects of dissociation on the electrons should be much less. This suggests that more-stable longer-pulse discharges may be attainable using polyatomic sources of F rather than  $F_2$ .

The potential significance of the effects discussed above is vividly illustrated by the results presented in Fig. 2. This figure shows the  $E/n$  dependence of gain and  $KrF^*$  production efficiency at a time  $0.5 \mu\text{sec}$  after discharge initiation. In this example the production rate of electrons by the electron beam was varied from 125 to  $500 \text{ sec}^{-1}$  resulting in an increase in the initial electron density from approximately  $5 \times 10^{13}$  to  $2 \times 10^{14}$

$\text{cm}^{-3}$ ; all other parameters including the initial  $F_2$  concentration were held constant. For fixed  $E/n$  values below about  $1.0 \times 10^{-16} \text{ V cm}^2$ , the gain increases and  $KrF^*$  production efficiency decreases as  $S_E$  is increased, reflecting the effect of increased electron density relative to that of the  $F_2$ . As the electron density increases, the increased electron pumping rate results in an absolute increase in the densities of both the rare-gas metastables and  $KrF^*$  as reflected by the higher gain. However, the overall energy utilization efficiency is reduced because electron excitation of rare-gas metastables to higher levels begins to compete with the metastable- $F_2$  reaction leading to  $ArF^*$  (Fig. 1). Thus,  $\eta$  decreases as  $S_E$  is increased. For a fixed value of the electron-beam ionization rate, increasing  $E/n$  initially results in a substantial increase in both gain and  $KrF^*$  production efficiency due to the strong dependence of rare-gas metastable production on  $E/n$ . However, for  $E/n$  values greater than about  $(1.0-1.2) \times 10^{-16} \text{ V cm}^2$  the combined influence of increased electron production due to metastable ionization and decreased attachment loss accompanying  $F_2$  dissociation results in an electron density increase. The effect of the resultant increase in the ratio  $[e][F_2]^{-1}$  is reflected by a sharp decline in  $\eta$  as rare-gas  $p$ -state excitation becomes an important loss of metastables relative to  $ArF^*$  formation.

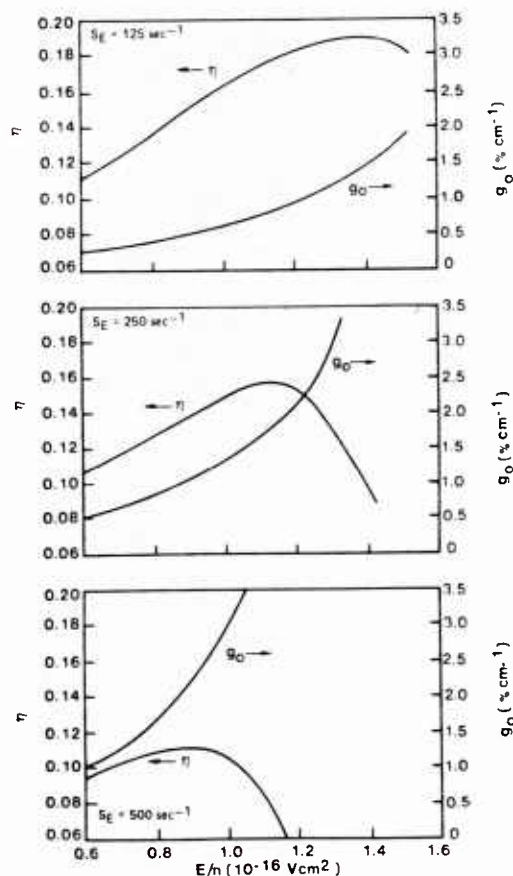


FIG. 2. Computed  $E/n$  variation of small-signal gain and  $KrF^*$  production efficiency for the conditions of Fig. 1 and three values of the e-beam production rate. These results correspond to conditions  $0.5 \mu\text{sec}$  after discharge initiation.

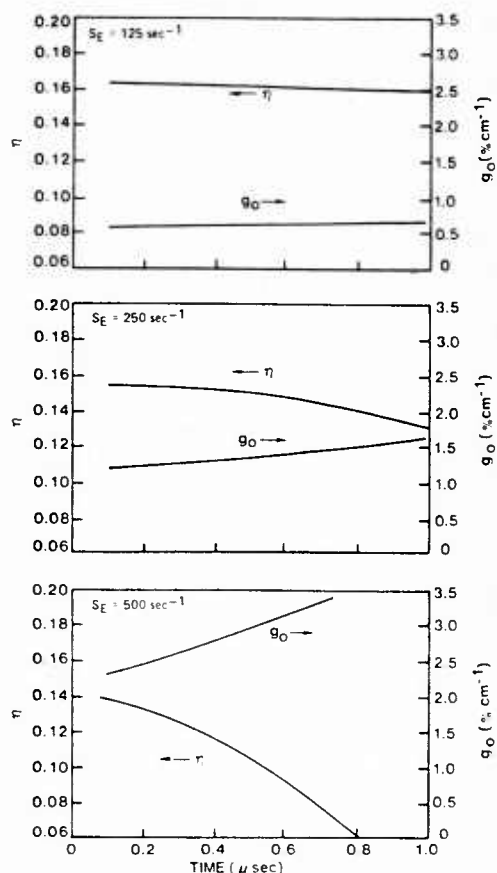


FIG. 3. Temporal variation of small-signal gain and production efficiency corresponding to the conditions of Fig. 2 and an  $E/n$  value of  $1.0 \times 10^{-16}$  V cm<sup>2</sup>.

For purposes of comparison Fig. 3 shows the temporal variation in  $\eta$  and  $g_0$  at a fixed  $E/n$  value of  $1.0 \times 10^{-16}$  V cm<sup>2</sup>. For an  $S_E$  value of  $125 \text{ sec}^{-1}$  the total power density is approximately  $35 \text{ kW cm}^{-3}$  in this example, and both the fractional ionization and  $F_2$  fraction remain sensibly constant at their respective initial values of  $2 \times 10^{-6}$  and  $0.005$  ( $[e][F_2]^{-1} < 10^{-3}$ ). For this reason both the gain and  $KrF^*$  production efficiency exhibit little variation on a  $\mu\text{sec}$  time scale. This is in sharp contrast to the  $\eta$  and  $g_0$  temporal variation when  $S_E$  is increased to  $500 \text{ sec}^{-1}$ . In this situation the fractional ionization and  $F_2$  fraction change from their initial values of  $8 \times 10^{-6}$  and  $0.005$  to  $1.4 \times 10^{-5}$  and  $0.003$  in the first  $0.6 \mu\text{sec}$ . There results an increase in the power density from  $155$  to  $260 \text{ kW cm}^{-3}$ , leading ultimately to plasma instability at approximately  $0.75 \mu\text{sec}$ . The corresponding increase in the ratio  $[e][F_2]^{-1}$  from  $1.6 \times 10^{-3}$  to  $4.7 \times 10^{-3}$  explains the precipitous temporal decline in  $KrF^*$  production efficiency.

The previous discussion is based on the assumption that electron excitation of rare gas metastable atoms to the  $p$  states results in an unrecoverable loss of energy and of useful excited species, a conservative point of view. However, even if Ar and Kr  $p$  states react with  $F_2$  to form  $ArF^*$  and  $KrF^*$ , or if electron and heavy particle deexcitation of  $p$ -state atoms results in repopulation of metastable states, the  $1.5$ – $2.0$ -eV electron energy loss accompanying  $p$ -state excitation from metastable states can be substantial.<sup>1,3</sup> Indeed, for metastable fractional concentrations greater than about  $10^{-5}$   $p$ -state excitation is the dominant electron energy loss process.

The results of this analysis indicate that for  $F_2$  fractions corresponding to a few tenths of a percent, generation of efficient stable long-duration ( $\sim 1 \mu\text{sec}$ ) rare gas–halide laser discharges requires that the fractional ionization be maintained at a level no higher than approximately  $5 \times 10^{-6}$ . For values of fractional ionization of  $10^{-5}$  and above, the selectivity of energy transfer from the electrons through the rare gas metastable states to the rare gas–halide excimer states is substantially reduced. In addition, for values of fractional ionization above this level electron–electron collisions influence the high-energy region of the electron distribution function,<sup>5</sup> resulting in a very significant increase in the rate of ionization of atoms from their ground state. This effect contributes to the premature occurrence of instability in electron-beam-sustained rare gas–halide laser discharges.

It is a pleasure to acknowledge the helpful comments of R. T. Brown, R. J. Hall, and L. A. Newman.

<sup>1</sup>W. L. Nighan, Appl. Phys. Lett. 32, 297 (1978).

<sup>2</sup>C. H. Fisher and R. E. Center, Appl. Phys. Lett. 31, 106 (1977).

<sup>3</sup>J. H. Jacob and J. A. Mangano, Appl. Phys. Lett. 28, 724 (1976).

<sup>4</sup>J. A. Mangano, J. H. Jacob, and J. B. Dodge, Appl. Phys. Lett. 29, 426 (1976).

<sup>5</sup>W. H. Long, Appl. Phys. Lett. 31, 391 (1977).

<sup>6</sup>M. Rokni, J. H. Jacob, and J. A. Mangano, Phys. Rev. (to be published).

<sup>7</sup>In this analysis the rate coefficient for the reaction  $Ar^* + F_2 \rightarrow ArF^* + F$  was taken as  $7.5 \times 10^{-10} \text{ sec}^{-1} \text{ cm}^3$  [J. E. Velazco, J. H. Kolts and D. W. Setser, J. Chem. Phys. 65, 3468 (1976)], and the effective rate coefficient representing the net effect of electron excitation and deexcitation of  $Ar^*$  to and from the  $p$  states was taken as  $2.0 \times 10^{-7} \text{ sec}^{-1} \text{ cm}^3$ . [See J. L. Delcroix, C. M. Ferreira, and A. Ricard, in *Principles of Laser Plasmas*, edited by G. Bekefi (Wiley, New York, 1976)].

#### IV-B. Laser Discharge Stability

- Instability Onset in Electron-Beam-Sustained KrF Laser Discharges
- Stability Enhancement in Electron-Beam Sustained Excimer Laser Discharges

# Instability onset in electron-beam-sustained KrF\* laser discharges<sup>a)</sup>

Robert T. Brown and William L. Nighan

*United Technologies Research Center, East Hartford, Connecticut 06108*  
(Received 2 February 1978; accepted for publication 21 March 1978)

Measurements of instability onset in a spatially uniform electron-beam-sustained KrF\* laser discharge have shown that the time at which instability occurs decreases from about 1 to 0.1  $\mu\text{sec}$  as  $E/n$  is increased in the range required for efficient laser operation. This finding is in good agreement with computed ionization instability onset times determined on the basis of a comprehensive model of the discharge.

PACS numbers: 42.55.Hq, 52.35.Py, 52.80.-s

It has been shown<sup>1,2</sup> that the performance of the KrF\* laser can be improved by operating with electron-beam-sustained discharge pumping rather than with electron-beam pumping alone. Studies<sup>1-3</sup> have also indicated that the occurrence of discharge instability plays an important role in determining the accessible range of operating parameters for such discharges, thereby exerting a direct influence on the overall performance of a given laser system. In order to obtain a better understanding of the factors leading to discharge instability, we have made detailed measurements of several electron-beam-sustained KrF\* discharge properties and have compared the results with predictions of a comprehensive kinetic model. While specifically applicable to externally sustained discharges, the results yield considerable insight and information relevant to the operation of uv-preionized self-sustained discharges as well.

The experiments were carried out using a 1.5 cm  $\times$  2 cm  $\times$  50 cm active volume under conditions typical of those corresponding to optimum KrF\* laser operation. Discharge pulse length could be varied for times up to 1.0  $\mu\text{sec}$ . Great care was taken in designing the experiment so as to maximize spatial and temporal uniformity of the discharge electric field and of the electron-beam power deposition. The electron beam was produced by a cold-cathode diode operated with a nearly constant 300-kV 1- $\mu\text{sec}$  pulse and a slowly increasing current pulse. The discharge voltage was supplied by a low-inductance capacitor circuit. This circuit was switched on 70 nsec after the start of the electron-beam pulse and produced a temporally uniform 800-nsec voltage pulse, which was terminated 130 nsec prior to the end of the electron-beam pulse. Experimental diagnostics included measurements of the electron-beam voltage and current, discharge voltage and current, discharge fluorescence intensity, and time-integrated photographs of the discharge volume. In

<sup>a)</sup>Portions of the analytical work presented here were supported by the Office of Naval Research.

addition, laser cavity experiments were carried out over a range of parameters.

The discharge cell was constructed using stainless steel, aluminum, and Lucite; Viton O-rings were used throughout. A flat stainless-steel screen was used as the discharge cathode and the anode was a Rogowski-profiled aluminum electrode located 1.5 cm from the cathode. The electron-beam window was an unsupported 1-mil titanium foil 1.5 cm×50 cm in cross section located 0.64 cm behind the discharge cathode screen. Prior to filling with the working gas mixture, the cell was fluorine passivated and was then evacuated to  $10^{-5}$  Torr, using a VacLon pump. The working gas mixture was premixed in a passivated stainless-steel gas-handling system and was replaced after each shot.

Total discharge current was measured by monitoring the voltage drop across a series resistor, and the discharge voltage was measured using a low inductance voltage divider connected directly across the discharge electrodes. The KrF\* fluorescence at 248.5 nm was monitored using a fast photodetector (<5 nsec rise time) with a narrow-band (8-nm half-width) filter centered at 248 nm.

Prior to carrying out discharge experiments, a number of tests were performed in order to characterize the electron beam. The diode voltage was monitored using an ammonium chloride voltage divider probe and the total diode current was monitored using a B-dot loop. The electron-beam intensity was measured using both rose cinemoid film and a small scanning Faraday cup and was found to be uniform along the 50-cm dimension to within  $\pm 5\%$ . Measurements in air at 1 atm and at a distance 2 cm from the foil window showed that the transverse beam intensity profile was nearly Gaussian, with a half-width of 2.0 cm. In addition, measurements were made in argon at 1 atm with a 1-cm-diam Faraday cup placed 0.7 cm from the discharge cathode screen. These measurements showed that the current density increased linearly by approximately 50% during the 1- $\mu$ sec pulse and showed small ( $\pm 15\%$ ) fluctuations on a fast time scale (<50 nsec). The measured current density in argon was used to estimate the local electron-beam power deposition by using tabulated stopping powers<sup>4</sup> increased by a factor of 2.5 to account for multiple scattering effects.<sup>5</sup>

In order to identify and understand the primary collisional reactions occurring in the high-pressure ( $\sim 1$  atm) highly ionized ( $n_e/n \sim 10^{-6}$ – $10^{-5}$ ) highly excited ( $n^*/n \sim 10^{-5}$ – $10^{-4}$ ) plasmas of interest, a comprehensive numerical model of the temporal evolution of excited species and discharge properties was utilized.<sup>6</sup> Based on the computed temporal variation of plasma properties, the ionization instability growth (or damping) rate could then be determined for comparison with experiment using procedures generally similar to those described elsewhere.<sup>7</sup>

Typical experimental results, obtained for discharges in a mixture of 94.5% Ar, 5.0% Kr, and 0.5% F<sub>2</sub> at a total pressure of 1 atm, are shown in Fig. 1. For each shot, the electron-beam power deposition (at 0.5  $\mu$ sec and at the center of the discharge volume) was 20 kW/

cm<sup>3</sup>, and the electron-beam pulse duration and the discharge voltage pulse duration (i.e., the time between switch-on and switch-off) were held fixed at 1.0 and 0.8  $\mu$ sec, respectively. The electron-beam voltage and electron-beam current traces indicated a shot-to-shot variation in beam properties of less than  $\pm 5\%$ . Examination of the oscilloscope traces presented in Fig. 1 shows that for  $E/n$  values below  $1.0 \times 10^{-16}$  V cm<sup>2</sup> in this mixture, the discharge was stable for the full 800 nsec of the applied voltage pulse. However, as the  $E/n$  value was incrementally increased in the range  $1.0 \times 10^{-16}$  to  $1.8 \times 10^{-16}$  V cm<sup>2</sup>, discharge instability was observed as indicated by the sharp drop in discharge voltage and KrF\* fluorescence, and by the sharp rise in discharge current. Figure 1 shows that the instability onset time decreased from approximately 750 to 120 nsec as  $E/n$  was increased. Photographs indicated that in each case in which instability occurred during the pulse, one or more large-volume ( $\sim 1$  cm wide) arcs were present and were centered with respect to the transverse (i.e., 2 cm) electron-beam dimension.

Measured and computed values of discharge current density at times prior to the occurrence of instability were found to be in good agreement. In addition, the qualitative trends exhibited by the experimental traces in Fig. 1 were also observed in the calculated current density curves in that for each value of  $E/n$ , a time was reached at which current runaway occurred. Over the  $E/n$  range from  $1.0 \times 10^{-16}$  to  $1.8 \times 10^{-16}$  V cm<sup>2</sup>, for which the average discharge power enhancement relative to that of the electron-beam alone increased from 2 to approximately 6 during the stable portion of the discharge, the KrF\* fluorescence enhancement measured relative to that of pure electron-beam pumping was found to vary from 2.1 to 3.5 (Fig. 1), a finding

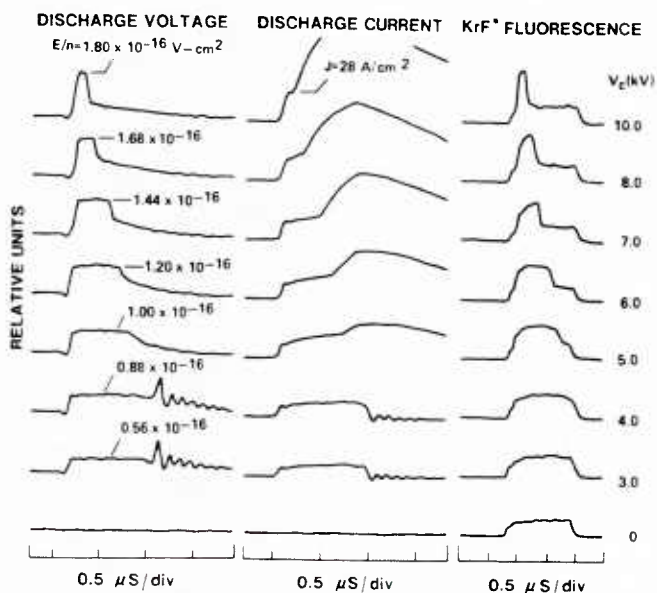


FIG. 1. Discharge voltage, discharge current, and KrF\* fluorescence oscillograms for a range of driver charge voltages  $V_c$ , and an Ar(0.945)–Kr(0.050)–F<sub>2</sub>(0.005) mixture at a pressure of 1 atm.

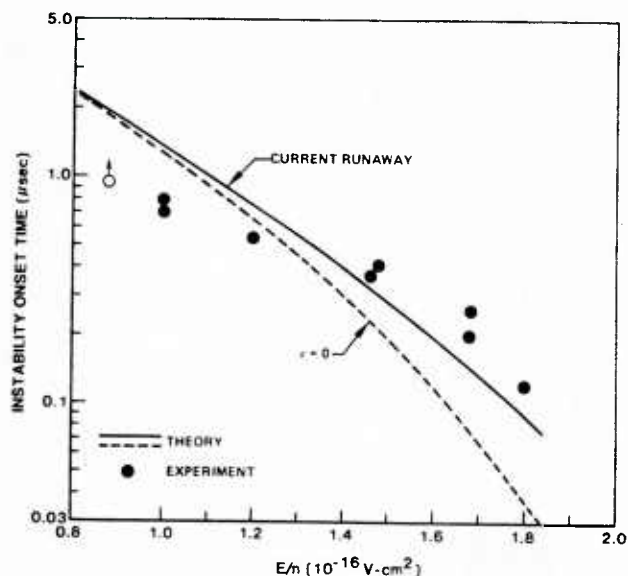


FIG. 2. Instability onset time versus discharge  $E/n$  for the conditions of Fig. 1. For  $E/n = 0.88 \times 10^{-16} \text{ V cm}^2$  the measured onset time exceeded the duration of the applied voltage pulse. The solid curve refers to the time at which runaway of the computed current density occurred, while the dashed curve refers to a self-consistent computation of the ionization instability boundary ( $\nu = 0$ ) as discussed in the text.

which was also in good agreement with predictions of the theoretical model.

Shown in Fig. 2 is the variation of instability onset time with  $E/n$ . The experimental points correspond to the time at which the discharge current was first observed to increase sharply as indicated by the oscillograph traces presented in Fig. 1. The solid curve in Fig. 2 corresponds to the instability onset time as evidenced by the occurrence of a sharp rise in the computed discharge current density. Thus, the time of instability onset determined numerically on this basis is directly comparable to the experimental data and, as seen in Fig. 2, the solid curve is in good agreement with the experimental data.

Plasma instability, as indicated by the occurrence of current runaway in rare gas-halide discharges, is a manifestation of temporal amplification of electron density disturbances, i.e., ionization instability. The cause of this mode of instability can be readily appreciated upon examination of an approximate expression<sup>3</sup> for the instability growth rate  $\nu$ , i.e.,

$$\nu \sim 2n^*k_i^* - n_{F_2}k_a, \quad (1)$$

where  $n^*$  and  $n_{F_2}$  are the number densities of rare gas metastable atoms and fluorine molecules, while  $k_i^*$  and  $k_a$  are the rate coefficients for metastable ionization and electron dissociative attachment, respectively. In electron-beam-sustained KrF\* laser discharges, initial conditions are established so that the metastable ionization rate is well below the attachment rate, with the result that electron density disturbances are damped ( $\nu < 0$ ). However, there are several processes resulting in  $F_2$  dissociation,<sup>6</sup> including rare gas-halide molecule production. Therefore, as the discharge evolves in time  $F_2$  dissociation proceeds, becoming

significant on a time scale less than  $1 \mu\text{sec}$ , with the decreasing  $F_2$  concentration resulting in a reduction in the loss rate of electrons by way of attachment. Consequently, the electron density rises and, additionally, there results an increase in the concentration of rare gas metastables, which are produced by electron impact and lost primarily by reaction with  $F_2$ . The combined influence of these processes leads to a strong temporal increase in the metastable ionization rate which rapidly approaches, and then exceeds, the attachment rate, resulting in ionization instability, i.e.,  $\nu > 0$  [Eq. (1)].

In addition to using the calculated onset of current runaway as a measure of instability, a theoretical criterion for the ionization instability growth (or damping) rate was developed and evaluated as a self-consistent function of plasma properties in the discharge. The effect of ionization of Ar and Kr from their ground states was included in the formulation leading to the expression for the instability growth rate. For the conditions of the present experiment the contribution of ground-state ionization to instability growth was found to be about 10% of that due to metastable ionization. The dashed curve in Fig. 2 represents the  $E/n$  variation of the computed ionization instability boundary, defined by the condition  $\nu = 0$ . Examination of Fig. 2 reveals good agreement between the computed stability criterion (dashed curve) and the numerical indication of current runaway (solid curve). For a relatively long discharge duration ( $\sim 1 \mu\text{sec}$  at low  $E/n$ ), the computed instability onset time and the computed current runaway time are nearly equivalent, reflecting the very short time characteristic of ionization growth ( $< 100 \text{ nsec}$ ). However, as  $E/n$  is increased, the time characteristic of stable discharge duration is reduced to a value comparable to the instability development time ( $\sim \nu^{-1}$ ), and a time delay develops between the onset of instability as defined by the condition  $\nu = 0$  and the observation of current density runaway.

Both theory and experiment show that for the conditions compatible with practical electron-beam-sustained KrF\* laser devices the occurrence of ionization instability is of a fundamental nature, reflecting the loss of  $F_2$  on a  $\mu\text{sec}$  time scale (or less), accompanied by rapid increases in both the metastable and electron densities. Since F atom recombination requires a time much longer than practical KrF\* discharge duration times, elimination or circumvention of this problem will probably require means to control the growth of the concentrations of both the metastables and electrons.

It is a pleasure to acknowledge helpful conversations with L. A. Newman, D. C. Smith, and R. H. Bullis.

<sup>1</sup>J. H. Jacob and J. A. Mangano, *Appl. Phys. Lett.* **28**, 724 (1976).

<sup>2</sup>C. H. Fisher and R. E. Center, *Appl. Phys. Lett.* **31**, 106 (1977).

<sup>3</sup>J. D. Daugherty, J. A. Mangano, and J. H. Jacob, *Appl. Phys. Lett.* **28**, 581 (1976).

<sup>4</sup>M. J. Berger and S. M. Seltzer, *Studies in Penetration of Charged Particles in Matter*, Nuclear Science Series Report No. 10, NAS-NRC Publ. 1133 (National Academy of Sciences,

Washington, D.C., 1964).

<sup>5</sup>G.A. Hart and S.K. Searles, J. Appl. Phys. 47, 2033 (1976).

<sup>6</sup>W.L. Nighan, Appl. Phys. Lett. 32, 297 (1978); 32, 424 (1978).

<sup>7</sup>W.L. Nighan, Phys. Rev. A 15, 1701 (1977); 16, 1209 (1977).

# Stability enhancement in electron-beam-sustained excimer laser discharges<sup>a)</sup>

Robert T. Brown and William L. Nighan

United Technologies Research Center, East Hartford, Connecticut 06108

(Received 9 April 1979; accepted for publication 4 May 1979)

Techniques are described for prolonging the duration of stable e-beam-controlled excimer laser discharges, including: temporal tailoring of either the discharge voltage or the ionization source and kinetics modification by way of additives. Theoretical and experimental results are presented for KrF\* laser discharges.

PACS numbers: 42.55.Hg, 52.35.Py, 52.80. — s

For practical high-power excimer laser systems, it is desirable to utilize electron-beam-sustained discharge excitation rather than electron-beam excitation alone, since for a given laser output power the burden on the electron-beam technology is significantly lower. One of the major obstacles to implementing the e-beam-sustained discharge technique is the onset of ionization instability.<sup>1-3</sup> In this paper a number of techniques for improving excimer laser discharge stability are outlined and theoretical and experimental results are presented for an electron-beam sustained KrF\* laser discharge.

It has been shown<sup>2,3</sup> that the major factor contributing to instability in electron-beam-controlled KrF\* laser discharges is dissociation of the molecular halogen, F<sub>2</sub>, during the discharge pulse. This can be readily appreciated upon examination of the following approximate expression<sup>1-3</sup> for

the instability growth rate  $\nu$ , i.e.,

$$\nu \simeq 2n^*k_i^* - n_{F_2}k_a, \quad (1)$$

where  $n^*$  and  $n_{F_2}$  are the number densities of rare-gas metastable atoms and fluorine molecules, respectively, while  $k_i^*$  and  $k_a$  are the rate coefficients for metastable ionization and electron dissociative attachment, respectively. For conditions typical of KrF\* laser mixtures,<sup>3</sup> the electron conservation equation is well approximated by the relation

$$nS \simeq n_e n_{F_2} k_a, \quad (2)$$

and the metastable conservation equation can be approximated by

$$n_e n k_{ex}(E/n) \simeq n^* n_{F_2} k_Q, \quad (3)$$

where  $n$  is the density of ground-state rare-gas atoms,  $S$  is the ionization rate due to the electron beam,  $k_{ex}(E/n)$  is the metastable production rate coefficient (exhibiting a very strong  $E/n$  dependence<sup>3</sup>), and  $k_Q$  is the rate coefficient for the loss of metastables due to F<sub>2</sub> quenching. Combination of Eqs. (1)–(3) yields the following criterion for discharge sta-

<sup>a)</sup>Supported in part by the Naval Ocean Systems Center and by the Office of Naval Research.

bility (i.e.,  $\nu < 0$ ):

$$\frac{2n^2 k_i^* S k_{ex}(E/n)}{n_{F_2}^3 k_a^2 k_Q} < 1 \quad (4)$$

For the parameter values required for efficient rare-gas-halide laser operation, it has been shown<sup>1</sup> that the left-hand side of this inequality is usually in the 0.1–0.5 range, indicative of a marginally stable situation.

In most e-beam-controlled KrF\* lasers the discharge  $E/n$  value is typically maintained at a relatively constant level throughout the pulse, while the e-beam source function  $S$  tends to increase due to the space-charge-limited mode of operation of cold-cathode e-beam guns. This tendency results in an increase in the numerator on the left-hand side of inequality (4), i.e., reduced stability. More importantly, the form of Eq. (4) indicates that the onset of instability ( $\nu \geq 0$ ) is exceptionally sensitive to the dissociative loss of  $F_2$ . Since  $F_2$  dissociation is primarily a consequence of rare-gas-halide formation itself,<sup>1</sup> invariably a point in time is reached for which electron density disturbances are amplified, i.e., inequality (4) is violated and the discharge becomes unstable. At the high values of  $E/n$  (i.e., higher values of  $k_{ex}$ ) required for effective discharge energy enhancement and high discharge power density, the unstable point is reached earlier in the pulse.<sup>2,3</sup>

The form of the stability criterion [Eq. (4)] discussed above suggests several techniques for increasing the stable duration of the discharge pulse while maintaining laser properties near their optimum values. These include: (1) temporal tailoring of either the discharge voltage ( $E/n$ ), i.e., controlled temporal reduction of  $k_{ex}$ , or of the e-beam ionization source function  $S$  in order to compensate for  $F_2$  loss; (2) modification of the halogen kinetics in such a way that loss of  $F_2$  has a less severe effect on the occurrence of instability.

The stabilizing influence of judicious temporal reduction in either  $S$  or  $k_{ex}$  (i.e.,  $E/n$ ) in order to compensate for the changes in plasma properties caused by the dissociative loss of  $F_2$  is conceptually straightforward. The potential role of halogen kinetics modification is best understood by observing that in conventional KrF\* mixtures reactions involving  $F_2$  control both the electron density [Eq. (2)] and the metastable density [Eq. (3)], a circumstance leading to the cubic dependence on  $F_2$  concentration exhibited by inequality (4). This situation can be favorably altered by use of a two-component halogen mixture in which one species tends to dominate electron loss, while the other (the halogen fuel) dominates metastable processes and therefore excimer formation. Such is the case in certain  $F_2$ - $NF_3$  mixtures, for example. The rate coefficient for electron dissociative attachment in  $NF_3$  is approximately four times larger than that of  $F_2$ , while the  $NF_3$ -rare-gas metastable atom quenching coefficient is about six times smaller than that of  $F_2$ . Thus, addition of a relatively small amount of  $NF_3$  ( $NF_3/F_2 < 0.1$ ) to the conventional KrF\* laser mixture will significantly affect the electron density but should exert little or no influence on other processes. Enhanced stability should result as a consequence of the weakened coupling between the electron and metastable concentrations. Indeed,

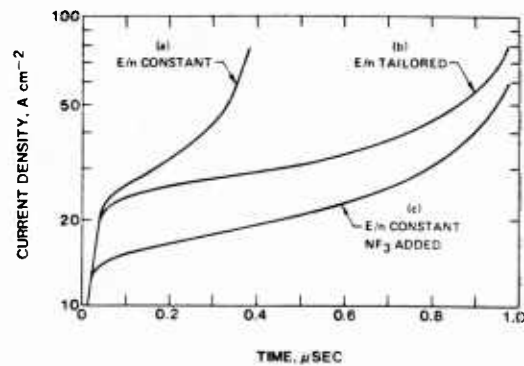


FIG. 1. Computed current density profiles for an e-beam-controlled Ar(0.95)-Kr(0.05)- $F_2$ (0.005) mixture at 1 atm. For each of these examples the initial  $E/n$  value was  $1.4 \times 10^{-16}$  V cm<sup>2</sup> and the e-beam ionization rate  $S$  was  $150 + 7.5 \times 10^7 t \text{ sec}^{-1}$ . (a)  $E/n$  constant; (b)  $E/n$  tailored according to the relation  $1.4 \times 10^{-16} - 0.35 \times 10^{-10} t \text{ V cm}^2$ ; (c)  $E/n$  constant with 0.05%  $NF_3$  added.

with  $NF_3$  controlling the electron loss and  $F_2$  the metastable loss, it is easily shown that the criterion for stability becomes

$$\frac{2n^2 k_i^* S k_{ex}(E/n)}{n_{F_2} k_Q (n_{NF_3} k_a)^2} < 1. \quad (5)$$

Since dissociative  $NF_3$ -metastable reactions will proceed at a much slower rate than the corresponding  $F_2$  reactions, the impact of dissociation on electron density growth (plasma stability) should be lessened substantially as indicated by the linear dependence of Eq. (5) on  $F_2$  concentration. Furthermore, use of  $NF_3$  an acceptable fluorine donor itself, does not introduce processes unfavorable to the efficient formation of KrF\*.

Detailed numerical evaluation of the stability enhancement techniques described above has been carried out using a comprehensive computer model of an e-beam-controlled KrF\* laser discharge.<sup>3</sup> Representative results are presented in Fig. 1, which shows the characteristic temporal runaway of the discharge current density indicative of ionization instability onset [curve (a)].<sup>1</sup> For curve (a),  $E/n$  was maintained at a constant value of  $1.4 \times 10^{-16}$  V cm<sup>2</sup>, a condition for which instability onset occurs approximately 0.3  $\mu\text{sec}$  after discharge initiation. Curve (b) illustrates the effect of a controlled linear reduction in  $E/n$  from an initial value of  $1.4 \times 10^{-16}$  V cm<sup>2</sup> to a value of approximately  $1.0 \times 10^{-16}$  V cm<sup>2</sup> after 1.0  $\mu\text{sec}$ . The predicted improvement in stability as reflected by the temporal variation in discharge current density is dramatic indeed, with the region of stable discharge behavior increasing to about 0.8  $\mu\text{sec}$ , and the total energy deposited in the gas prior to the occurrence of instability increasing by almost a factor of 3. Moreover, the medium properties are sensibly uniform in time, having values compatible with efficient high-power laser operation,<sup>4</sup> e.g., KrF\* production efficiency, 20%, zero-field gain, 2.5% cm<sup>-1</sup>; gain: absorption ratio, 10; electric power density, 110 kW cm<sup>-3</sup>; and time-integrated discharge energy enhancement, 5. Curve (c) illustrates the effect of  $NF_3$  addition for an  $NF_3$ - $F_2$  concentration ratio of 0.1. The initially lower current density level reflects the increased attachment loss of electrons due the presence of  $NF_3$ . However, the im-

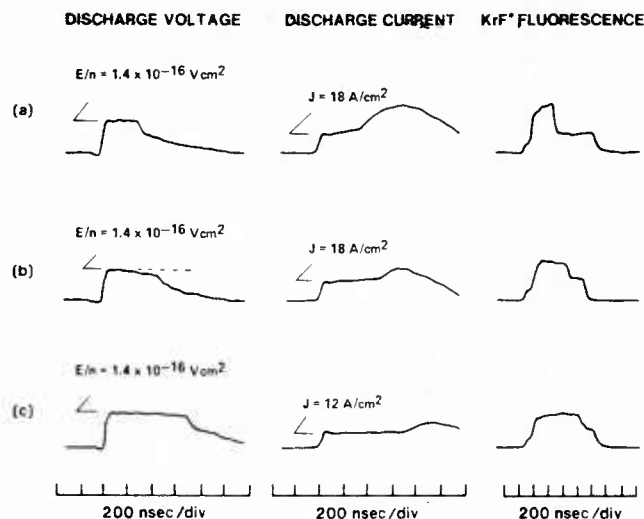


FIG. 2. Measured discharge characteristics for the mixture and e-beam ionization rate of Fig. 1. (a)  $E/n$  constant at  $1.4 \times 10^{-16} \text{ V cm}^{-2}$ ; (b) capacitance of driving circuit reduced resulting in temporal reduction in  $E/n$  similar to that of curve (b) in Fig. 1;  $E/n$  constant at  $1.4 \times 10^{-16} \text{ V cm}^{-2}$  with 0.05%  $\text{NF}_3$  added.

provement in discharge stability as measured by the temporal evolution of the current density is again readily apparent, with the computed energy deposited in the gas approximately twice as large as in the absence of  $\text{NF}_3$  [curve (a)]. In addition, average medium properties are comparable to those of curve (b). Numerous calculations carried out on the basis of a tailored e-beam ionization source, as well as a variety of combinations of the techniques outlined above, produced results generally similar to those of Fig. 1.

The stability enhancement techniques described above were investigated experimentally using an e-beam-controlled discharge<sup>2</sup> having an active volume  $1.5 \times 2.0 \times 50 \text{ cm}$ . Presented in Fig. 2 are discharge current density, voltage, and  $\text{KrF}^*$  fluorescence traces for an  $\text{Ar}(0.95)\text{-Kr}(0.05)\text{-F}_2(0.005)$  mixture at 1 atm. The data of Fig. 2(a) correspond to a constant  $E/n$  value of  $1.4 \times 10^{-16} \text{ V cm}^{-2}$  and exhibit the onset of instability approximately  $0.3 \mu\text{sec}$  after discharge initiation, as indicated by the characteristic sharp rise in current density accompanied by a decrease in both voltage and  $\text{KrF}^*$  fluorescence. The effect of discharge voltage tailoring was evaluated by changing the discharge driving capacitance from 0.9 to  $0.5 \mu\text{F}$ , which resulted in a nearly linear decrease in  $E/n$  from an initial value of  $1.4 \times 10^{-16} \text{ V cm}^{-2}$  in a manner similar to that corresponding to curve (b) in Fig. 1. Figure 2(b) shows that, according to predictions, the onset of instability was delayed until about the  $0.5\text{-}\mu\text{sec}$  point. The influence of  $\text{NF}_3$  addition with constant  $E/n$  is represented by the data of Fig. 2(c). The observed reduction in the initial current density level and the increase in stable discharge duration to about  $0.7 \mu\text{sec}$  are also found to be in good agreement with analytical predictions.

Figure 3(a) shows that an increase in the constant  $E/n$

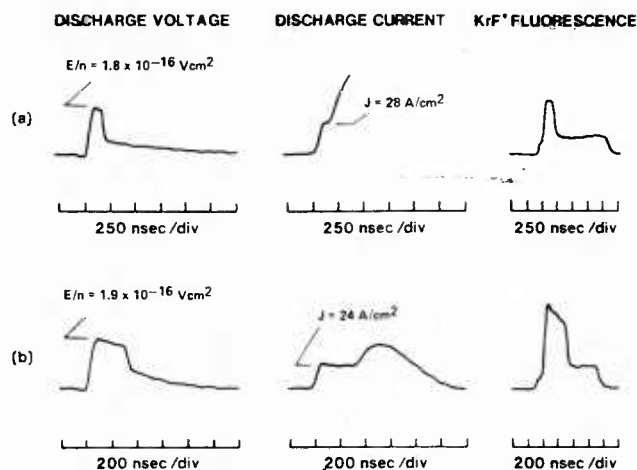


FIG. 3. Measured discharge characteristics for the mixture and e-beam ionization rate of Figs. 1 and 2. (a)  $E/n$  constant at  $1.8 \times 10^{-16} \text{ V cm}^{-2}$ ; (b) temporal reduction in  $E/n$  from an initial value of  $1.9 \times 10^{-16} \text{ V cm}^{-2}$  with 0.025%  $\text{NF}_3$  added.

level to  $1.8 \times 10^{-16} \text{ V cm}^{-2}$  for the indicated  $\text{Ar/Kr/F}_2$  mixture resulted in instability onset in a time less than  $0.1 \mu\text{sec}$ . However, upon introduction of 0.025%  $\text{NF}_3$  ( $\text{NF}_3/\text{F}_2 = 0.05$ ) and by reduction of the discharge driving capacitance from 10.0 to  $0.25 \mu\text{F}$  in order to produce a temporal decrease in  $E/n$ , the stable pulse duration was increased to about  $0.35 \mu\text{sec}$ . For these conditions the discharge power density was  $117 \text{ kW cm}^{-3}$  and the e-beam power deposition density was  $16 \text{ kW cm}^{-3}$  (corresponding to an e-beam current density of  $2.0 \text{ A cm}^{-2}$ ). Thus, the discharge energy enhancement factor was about 7. Code calculations for these conditions indicate a zero-field gain of  $3.4\% \text{ cm}^{-1}$ , volumetric absorption of  $0.2\% \text{ cm}^{-1}$ , and  $\text{KrF}^*$  formation efficiency of 25%, values compatible with efficient high-power laser operation.<sup>4</sup>

The stability enhancement techniques described herein are relatively simple to implement and offer the promise of efficient scalable rare-gas-halide and metal-halide lasers at significantly reduced e-beam current density levels, thereby facilitating operation at high average power. At the present time a more complete reporting of this research is in preparation and work with other excimer lasers is underway.

The authors wish to thank R. Preisach for his excellent technical assistance with the experimental portion of the work.

<sup>1</sup>J.D. Daugherty, J.A. Mangano, and J.A. Jacob, *Appl. Phys. Lett.* **28**, 581 (1976).

<sup>2</sup>R.T. Brown and W.L. Nighan, *Appl. Phys. Lett.* **32**, 730 (1978).

<sup>3</sup>W.L. Nighan, *IEEE J. Quantum Electron.* **QE-19**, 714 (1978), and references cited therein.

<sup>4</sup>M. Rokni, J.A. Mangano, J.H. Jacob, and J.C. Hsia, *IEEE J. Quantum Electron.* **QE-14**, 464 (1978).

IV-C. Electron-F<sub>2</sub> Collision Processes

- Influence of Electron-F<sub>2</sub> Collisions in Rare Gas-Halide Laser Discharges
- Dissociative Attachment and Vibrational Excitation of F<sub>2</sub> by Slow Electrons

# Influence of electron-F<sub>2</sub> collisions in rare gas-halide laser discharges<sup>a)</sup>

William L. Nighan

United Technologies Research Center, East Hartford, Connecticut 06108

(Received 23 September 1977; accepted for publication 20 December 1977)

The influence of F<sub>2</sub> vibrational excitation and direct dissociation by electron impact is examined for conditions typical of electron-beam-sustained KrF\* lasers. For values of F<sub>2</sub> fractional concentration greater than about 0.003 the results of this analysis indicate that the dissociation process  $e + F_2 \rightarrow 2F + e$  may significantly affect electron-metastable atom production efficiency, rare gas-halide excimer production efficiency, and gain.

PACS numbers: 42.55.Hq, 52.20.Fs, 52.20.Hv

Rare gas-halide laser mixtures generally contain fractional concentrations of the halogen bearing molecule in the 0.1–1.0% range. Although there exists almost no electron scattering data for such molecules, there is every reason to suppose that the presence of several tenths of a percent F<sub>2</sub>, for example, will have an effect on electron kinetics other than by way of the well-known dissociative attachment process. This paper analyzes available data relevant to electron-F<sub>2</sub> scattering and examines the potential importance of such collision processes for conditions typical of discharge-pumped KrF\* lasers.

To date the effect of electron-halogen molecule inelastic collisions has not been considered in analyses of rare gas-halide lasers. This is a reflection of the lack of required cross-section data. However, recent

theoretical analysis<sup>1</sup> has shown that vibrational excitation of F<sub>2</sub> by electrons can proceed by way of a resonance mechanism involving the same F<sub>2</sub><sup>-</sup> state which participates in the low-energy dissociative attachment process. The computed energy weighted cross section for vibrational excitation was found to be in excess of 10<sup>-17</sup> cm<sup>2</sup> in the electron energy range of a few electron volts. In addition, measurements<sup>2</sup> of F atom production in an electron-beam-sustained F<sub>2</sub> discharge have shown evidence of enhanced F<sub>2</sub> dissociation as  $E/n$  was increased for average electron energies estimated to be about 1 eV, a value high enough<sup>1</sup> so that dissociative attachment should be a decreasing function of  $E/n$ . While there are several processes<sup>2</sup> which may contribute to F<sub>2</sub> dissociation for the experimental conditions of Ref. 2, direct electron impact dissociation is by far the most likely. Indeed, there are several F<sub>2</sub><sup>-</sup> states which may lie above the repulsive F<sub>2</sub>(<sup>1</sup>π<sub>u</sub>) state in the vicinity of the F<sub>2</sub> ground-state equilibrium separation, so that resonant enhancement of the process  $e + F_2 \rightarrow 2F + e$  is a distinct possibility.

<sup>a)</sup> Portions of this work were supported by the Office of Naval Research.

In order to obtain an estimate for the electron- $F_2$  dissociation cross section based on the observations of Ref. 2, electron energy distributions were computed for  $F_2$  using the vibrational cross sections of Ref. 1 along with a constant momentum transfer cross section having a value of  $10^{-15} \text{ cm}^2$ . The electron- $F_2$  dissociation cross section was assumed to have an apparent threshold of 3.35 eV corresponding to the vertical transition energy from the  $F_2$  ground state to the  $F_2(^1\pi_u)$  state, the lowest electronic state of  $F_2$ . The magnitude and shape of this cross section were then varied in a trial and error fashion. In the experiments of Ref. 2 the production of F atoms was first observed to increase over that due to the electron beam alone for an  $E/n$  value of approximately  $2 \times 10^{-16} \text{ V cm}^2$ . As  $E/n$  was increased to about  $6 \times 10^{-16} \text{ V cm}^2$ , F atom production was enhanced by almost a factor of 2. By using a trial dissociation cross section having a peak value of approximately  $10^{-17} \text{ cm}^2$  at an electron energy of 5 eV, in the present work it was found that the magnitude of the calculated rate of  $F_2$  dissociation (F atom production) by the direct process was a few percent of that due to dissociative attachment for an  $E/n$  of  $2 \times 10^{-16} \text{ V cm}^2$ . Further, the dissociation rate approximately equaled the dissociative attachment rate for  $E/n$  values in the  $5 \times 10^{-16}$  to  $6 \times 10^{-16} \text{ V cm}^2$  range, results consistent with the experimental observations.<sup>2</sup> These findings were not particularly sensitive to the shape of the trial cross section used in the analysis. The direct electron- $F_2$  dissociation rate estimated in this manner is consistent with the limited experimental data available<sup>2</sup> and provides a reasonable basis for an evaluation (albeit provisional) of the potential significance of electron impact excitation of  $F_2$  to repulsive states.

Using this  $F_2$  dissociation cross section and the cross sections of Ref. 1 the electron fractional power transfer

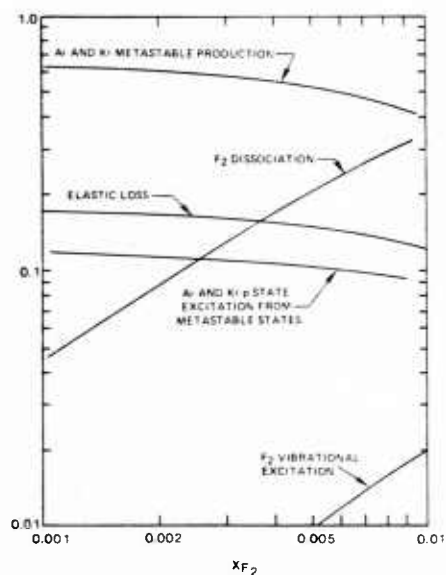


FIG. 1. Contributions to electron fractional power transfer in an Ar-Kr- $F_2$  mixture in which the Ar and Kr fractional concentrations were 0.95 and 0.05, respectively. The calculation was carried out for an  $E/n$  value  $1.0 \times 10^{-16} \text{ V cm}^2$ , a fractional metastable concentration of  $10^{-5}$ , and a fractional ionization of  $10^{-6}$ .

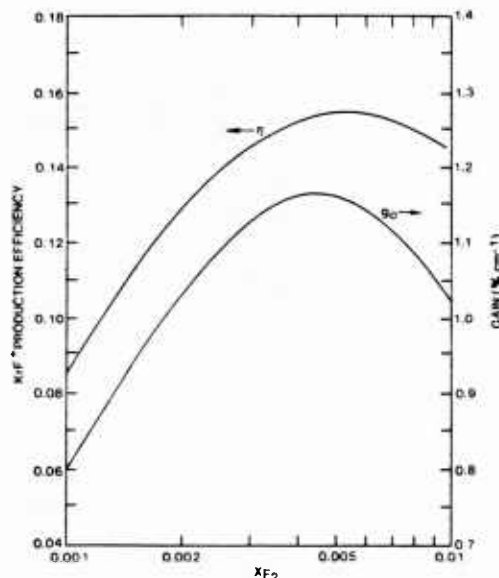


FIG. 2. Small-signal gain and  $KrF^*$  production efficiency in an electron-beam-sustained discharge as a function of  $F_2$  fraction. The computation was made for an atmospheric-pressure Ar-Kr (0.95–0.05) mixture and an  $E/n$  value of  $1.0 \times 10^{-16} \text{ V cm}^2$ . These results refer to conditions 100 nsec after discharge initiation.

was computed for conditions typical of electric-discharge-pumped  $KrF^*$  lasers.<sup>3</sup> The results of this calculation are presented in Fig. 1 as a function of  $F_2$  fractional concentration. For values of  $x_{F_2}$  below about 0.002 electron energy loss due to dissociation is found to be relatively unimportant. However, for higher  $F_2$  concentrations the electron energy loss accompanying dissociation can become very significant, exceeding 10% of the total discharge power. For the conditions of Fig. 1 the rate coefficient for direct dissociation has a value of approximately  $10^{-9} \text{ sec}^{-1} \text{ cm}^3$  and exhibits a weak dependence on  $E/n$ . Since the production of rare gas metastable states is a strong positive function of  $E/n$ , the fractional power transfer associated with the direct dissociation process decreases relative to rare gas metastable production for  $E/n$  values higher than  $1.0 \times 10^{-16} \text{ V cm}^2$  and increases for lower values.

Although the cross sections for  $F_2$  vibrational excitation are relatively large,<sup>1</sup> Fig. 1 shows that the electron energy loss due to vibrational excitation is not likely to be important since the energy loss per collision is small ( $\sim 0.1 \text{ eV}$ ). However, Hall's results<sup>1</sup> indicate that dissociative attachment increases significantly with  $F_2$  vibrational level. In long-pulse<sup>3</sup>  $KrF^*$  laser discharges the fraction of vibrationally excited  $F_2$  will be substantial ( $>10\%$ ). Thus, the degree of  $F_2$  vibrational excitation may affect the electron loss due to attachment, thereby influencing both the quasisteady and stability characteristics of rare gas-halide discharges.

In order to evaluate the influence of the electron- $F_2$  collision processes discussed above, electron distribution functions and all related Ar and Kr rate coefficients were computed as a function of  $F_2$  fractional concentration. The effects of electron-electron, electron-ion, and electron-metastable collisions were taken into

account in the calculation. The data so obtained were then used as input information in a time-dependent KrF\* kinetics model of an electron-beam-sustained discharge,<sup>3</sup> following procedures generally similar to those described elsewhere.<sup>4,5</sup> Figure 2 shows the computed variation of gain and KrF\* production efficiency with F<sub>2</sub> fraction. The results presented refer to conditions 100 nsec after discharge initiation. In the present analysis the KrF\* production efficiency is defined by the relation  $\eta = (\text{KrF}^* \text{ production})h\nu / ([\text{Ar}]S_E u_i + JE)$ , where all the processes contributing to the volumetric rate of KrF\* production are included in the numerator.<sup>6</sup> Also,  $S_E$  is the rate of electron-ion pair production by the electron beam,  $u_i$  is the energy required to produce an electron-ion pair,  $JE$  is the discharge power density, and  $h\nu$  is the photon energy of the KrF\* laser transition. Thus, on this basis  $\eta$  represents the maximum fraction of the total power potentially recoverable from the reaction,  $\text{KrF}^* + h\nu \rightarrow \text{Kr} + \text{F} + 2h\nu$ .

Interpretation of the specific nature of changes accompanying variation in F<sub>2</sub> concentration can be very difficult for the circumstances typical of most experiments since the halogen molecules influence numerous plasma processes. Therefore, in order to assist in interpretation, in the present calculation the e-beam ionization rate,  $S_E$ , was varied from 50 to 500 sec<sup>-1</sup> as the F<sub>2</sub> fraction was increased from 0.001 to 0.01. Thus, the electron density remains approximately constant at 10<sup>14</sup> cm<sup>-3</sup> for the conditions of Fig. 2. In addition, the total power density is sensibly constant, increasing from about 60 kW cm<sup>-3</sup> to 90 kW cm<sup>-2</sup> over the  $X_{F_2}$  range covered.<sup>7</sup> These conditions are representative of recent experiments<sup>3</sup> with electron-beam-sustained rare gas-halide lasers.

As the F<sub>2</sub> fraction is increased above 0.001, Fig. 2 indicates that both the gain and KrF\* production efficiency increase significantly. This reflects the improved efficiency of ArF\* formation from the rare gas metastable states as compared to other metastable loss processes. However, as  $X_{F_2}$  is increased above about 0.005, electron energy loss due to F<sub>2</sub> dissociation becomes increasingly more significant. The resultant cooling of the electrons leads to a 35% decrease in the Ar and Kr metastable production rates for the conditions of this example as  $X_{F_2}$  is increased from 0.001 to 0.01. The combined effect of these related processes is a reduction in the KrF\* production efficiency.<sup>8</sup> Additionally, F<sub>2</sub> quenching of KrF\* exerts an important deleterious influence on the gain at the higher F<sub>2</sub> levels.<sup>9</sup> Results qualitatively similar to those of Fig. 2 were obtained at lower and higher  $E/n$  values, although calculations show that the plasma is unstable for  $E/n$  values above about  $1.2 \times 10^{-16}$  V cm<sup>2</sup> when the F<sub>2</sub> fractional concentration is below about 0.002.

Although the dominant collision processes generally become quasisteady in times much less than 100 nsec for conditions typical of those represented by the results of Fig. 2, the temporal changes in plasma processes resulting from F<sub>2</sub> dissociation can become very significant. The consequences of F<sub>2</sub> dissociation become particularly important for long-pulse discharges (~1 μsec) and/or high-power loading (>100 kW cm<sup>-3</sup>).

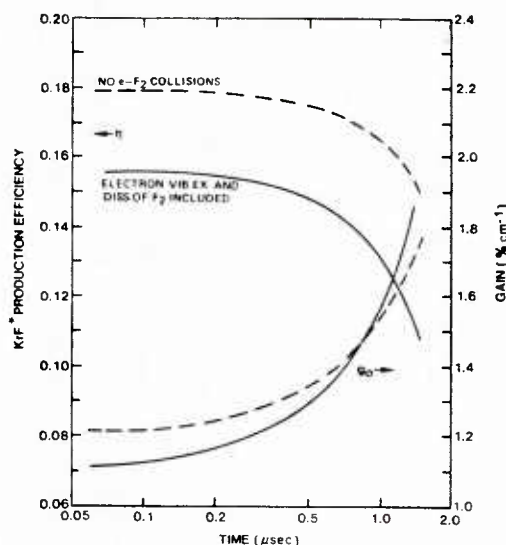


FIG. 3. Temporal variation of KrF\* production efficiency and gain for an F<sub>2</sub> fraction of 0.005 and the conditions of Fig. 2. Also shown (dashed curves) are the results of the same calculation neglecting all electron-F<sub>2</sub> collisions except attachment.

Presented in Fig. 3 are the temporal variations of  $\eta$  and  $g_0$  computed for an  $X_{F_2}$  value of 0.005, i.e., near-optimum conditions in Fig. 2. For purposes of comparison, also shown are  $\eta$  and  $g_0$  computed neglecting the effects of all electron-F<sub>2</sub> collisions except attachment. Clearly, steady-state conditions are attained in a time less than 100 nsec. However, for times greater than about 0.2 to 0.3 μsec significant changes in both  $g_0$  and  $\eta$  resulting from F<sub>2</sub> dissociation become apparent. The decrease in KrF\* production efficiency is a sequence of the increase in electron density accompanying the decrease in F<sub>2</sub> concentration. As the electron density increases, electron excitation of rare gas metastables to higher excited states begins to compete with the desired F<sub>2</sub> reaction leading to the formation of ArF\* and KrF\*. For this reason the energy utilization efficiency associated with conversion of metastable atoms to rare gas-halide excimers decreases. Note, however, that because of increasing electron excitation, the absolute densities of metastable and rare gas-halide states continue to increase as is reflected by the increasing gain. As the data of Fig. 3 indicate, this sequence of events results in rapidly changing  $g_0$  and  $\eta$  for long discharge duration. At the 1-μsec time the F<sub>2</sub> is 35% dissociated for the conditions of this example.

Comparison of the dashed and solid curves in Fig. 3 shows that direct electron impact dissociation of F<sub>2</sub> may result in significant changes in the magnitude and rate of change of both gain and KrF\* production efficiency. However, it is clear that the general trends exhibited by the data in Fig. 3 are not dependent on the inclusion of electron-F<sub>2</sub> collisions. Indeed, at the 1-μsec time only about one-third of the F<sub>2</sub> dissociation results from direct electron impact for the conditions of this example, with ArF\* formation, attachment, and F<sub>2</sub> quenching processes accounting for the other two-thirds.

The results and discussion of this paper focus attention on the role of the halogen-bearing molecule as

regards electron and metastable kinetic processes in rare gas-halide lasers. Conditions typical of electron-beam-sustained laser discharges<sup>3</sup> were examined in detail. The influence of  $F_2$  in  $KrF^*$  lasers was given particular attention because of the availability (albeit limited) of theoretical and experimental data for this molecule. On the basis of this analysis it is reasonable to conclude that electron-halogen processes other than attachment are likely to be important, particularly  $F_2$  electronic excitation leading to dissociation. This finding will most probably have general significance for all rare gas-halide and mercury-halide lasers containing  $F_2$  or other halogenated molecules at fractional concentration levels greater than a few tenths of a percent. Clearly, additional electron scattering data for halogenated molecules would be of considerable value in the modeling and evaluation of rare gas-halide laser properties.

It is a pleasure to acknowledge the helpful comments of R. T. Brown, R. J. Hall, and L. A. Newman.

<sup>1</sup>R. J. Hall, J. Chem. Phys. (to be published).

<sup>2</sup>H. L. Chen, R. E. Center, D. W. Trainor, and W. I. Fyfe, J. Appl. Phys. 48, 2297 (1977).

<sup>3</sup>C. H. Fisher and R. E. Center, Appl. Phys. Lett. 31, 106 (1977).

<sup>4</sup>J. H. Jacob and J. A. Mangano, Appl. Phys. Lett. 28, 724 (1976).

<sup>5</sup>J. A. Mangano, J. H. Jacob, and J. B. Dodge, Appl. Phys. Lett. 29, 426 (1976).

<sup>6</sup>For the conditions of this example the displacement reaction  $ArF^* + Kr \rightarrow KrF^* + Ar$  dominates  $KrF^*$  production (see Ref. 9).

<sup>7</sup>Since the discharge contribution to the total power density was sensibly constant over the entire  $X_{F_2}$  range covered in Fig. 2, the discharge enhancement factor,  $JE([Ar]u_i S_E)^{-1}$  decreased from about 10 to 1 as  $X_{F_2}$  increased from 0.001 to 0.01, reflecting the increase in  $S_E$  required to maintain nearly constant electron density. However, the discharge contribution to the total volumetric power density was dominant over most of the range covered in Fig. 2.

<sup>8</sup>Due to the decrease in enhancement factor corresponding to the increase in  $X_{F_2}$  for the conditions described here, the discharge is relatively less important at high  $F_2$  fractions; this effect also contributes to the reduction in  $\eta$ .

<sup>9</sup>M. Rokni, J. H. Jacob, and J. A. Mangano, Phys. Rev. (to be published).

# Dissociative attachment and vibrational excitation of $F_2$ by slow electrons<sup>a)</sup>

R. J. Hall

United Technologies Research Center, East Hartford, Connecticut 06108  
(Received 2 September 1977)

Self-consistent dissociative attachment and vibrational excitation cross sections for  $F_2$  have been calculated using Herzenberg's theory of resonant electron scattering. It has been found that the observed electron- $F_2$  attachment data can be explained by a low energy shape resonance. Potential parameters for the  $^2\Sigma_u^+$  negative ion were varied in order to fit predicted attachment cross sections to measured rate constant data. The best fit was obtained for a negative ion curve which crosses the  $F_2$  ground state in the vicinity of the equilibrium internuclear separation, in good agreement with an *ab initio* calculation for this state. The associated total vibrational cross section has a peak of about  $2.0 \times 10^{-16} \text{ cm}^2$  at an incident electron energy of 0.45 eV. A strong dependence of attachment rate on  $F_2$  vibrational state is predicted.

## I. INTRODUCTION

Molecular fluorine is an important constituent in several electrically-excited gas lasers.<sup>1,2</sup> However, aside from dissociative attachment,<sup>3-6</sup> little is known about low energy electron impact with fluorine. There is reason to expect that the presence of  $F_2$  in a gas mixture will have some effect on electron energy transfer other than dissociative attachment. Inelastic processes such as  $F_2$  vibrational excitation, direct dissociation, or electronic excitation could have important consequences for electrically-excited lasers employing  $F_2$ . The vibrational excitation cross section in particular is amenable to analysis, because it and the dissociative attachment cross section can be calculated simultaneously from resonance scattering theory.<sup>7-10</sup> A resonance calculation whose validity has been established by comparison with attachment data will yield additional information about the unknown vibrational excitation cross section.

*Ab initio* calculations<sup>11</sup> for the  $^2\Sigma_u^+F_2^-$  ion indicate that the potential energy curve for this state crosses the ground state near the latter's equilibrium internuclear separation. A shape resonance in low energy electron- $F_2$  scattering is likely because the lowest vacant antibonding orbital in  $F_2(\sigma_u 2p)$  possesses nonzero orbital angular momentum. A spherical harmonic expansion of this orbital has only odd components ( $p, f, \dots$  electrons), and thus a centrifugal barrier, the necessary condition for the existence of a shape resonance, will exist.

In low energy electron- $F_2$  scattering, the resonance nuclear wavefunction will consist solely of an outgoing wave because there is no turning point at larger internuclear distance to give rise to a reflected wave. Thus, no interference between outgoing and reflected waves can occur, as in the "boomerang" model,<sup>7</sup> and there will consequently be no structure in the  $F_2$  vibrational cross sections as a function of electron energy. This analysis is limited to consideration of a single resonance,  $F_2(^2\Sigma_u^+)$ . At higher electron energies, there is the possibility of contributions from excited states of  $F_2^-$ .<sup>12</sup> However, until attachment measurements at higher energy provide

evidence that these states are important, it is not advantageous to include them in the calculation.

The details of the resonance scattering theory are presented elsewhere<sup>7,8</sup> with emphasis directed towards  $N_2$  and  $N_2O$ . Thus, only the highlights of the model and those aspects relevant to  $F_2$  are discussed here. The fitting of the theory to attachment data is first carried through in a local potential approximation in which the decay of the resonance is assumed to be proportional to the resonance nuclear wavefunction. Because this approximation may be doubtful at thermal energies, the low incident energy regime is re-examined in a nonlocal formulation.

## II. RESONANT SCATTERING THEORY

Formally, a nuclear wave equation is solved in terms of a complex potential for the compound state,  $F_2(^2\Sigma_u^+)$ . Because little is known about the real and imaginary parts of the compound state potential, these are treated as adjustable parameters. Adjustments are made to the potential parameters in a trial-and-error fashion until the predicted attachment cross sections reproduce experimental rate constants for this process. This process can be expected to give credible results only if the "best fit" potential parameters are physically realistic.

Calculations for  $F_2$  differ mathematically from those for  $N_2$ <sup>7</sup> in several relatively minor respects. Because the assumed  $F_2$  resonance is  $p\sigma$ , the barrier penetration factor required for the calculation of the resonance width should be the expression appropriate to a  $p$  wave, and the vibrational excitation cross section is divided by a factor of 2 because the compound state is nondegenerate [see Eqs. (8) and (12) in Ref. 7]. The boundary condition at infinite internuclear separation is changed from bound state to outgoing wave.

The nuclear wave equation is based upon the adiabatic and local potential approximations. Exchange and spin dependent forces are neglected, leading to

$$\left\{ -\frac{\hbar^2}{2M} \frac{\partial^2}{\partial R^2} + W(R) - E \right\} \xi = \xi'(R) \chi_0(R), \quad (1)$$

where  $-\hbar^2/2M \times \partial^2/\partial R^2$  is the kinetic energy operator for the nuclei;  $W(R)$  is the electronic energy of the com-

<sup>a)</sup>This work was supported by the Office of Naval Research under Contract NO0014-76-C-0847.

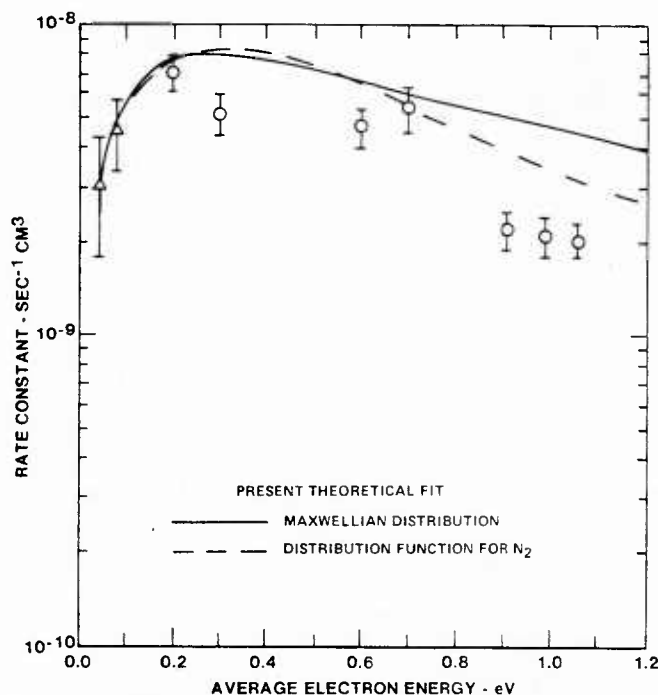


FIG. 1. Fit of resonance scattering theory to experimental attachment data. Solid curve represents rate constant calculated on basis of Maxwellian electron energy distribution. Dashed curve represents use of non-Maxwellian distribution function calculated for  $N_2$ -rich mixture. Theoretical attachment cross section from which these rate constants are derived is given in Fig. 2. Experimental data:  $\circ$ —Ref. 3;  $\triangle$ —Ref. 4.

pound state;  $E$  is the total energy (including the zero-point energy);  $\xi$  is the wavefunction of the nuclei;  $\xi'(R)$  is an entry amplitude for the incident electron; and  $\chi_0(R)$  is the vibrational wavefunction of the target. The compound state energy is represented by

$$W(R) = E^-(R) - \frac{1}{2} i \Gamma(R), \quad (2)$$

where  $\Gamma(R)$  is the autoionization rate multiplied by  $\hbar$ .  $\Gamma$  is assumed to vary with  $R$  in accordance with the penetrability of a  $p$ -wave centrifugal barrier<sup>13</sup>

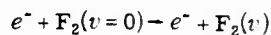
$$\Gamma(R) = \frac{2\gamma(k(R)\rho)^3}{1 + (k(R)\rho)^2},$$

where  $k(R)$  is the wavenumber of the emitted electron,  $\rho$  is the "radius" of the  $F_2^-$  ion, and  $\gamma$  is the reduced width. The expression for the entry amplitude  $\xi'$  is as given in Ref. 7 [Eq. (14)].

The dissociative attachment cross section is given by the expression,<sup>14</sup>

$$\sigma_{DA} = \frac{V_N}{V_0} g_s \frac{1}{|I_0|^2} \lim_{R \rightarrow \infty} |\xi(R, E)|^2, \quad (3)$$

where  $V_N$  and  $V_0$  are the nuclear dissociation and incident electron velocities, respectively;  $g_s$  is a spin degeneracy factor (unity); and  $|I_0|^2$  is the squared amplitude of the incident wave  $(8\pi^3)^{-1}$ . Cross sections for the vibrational excitation processes,



are calculated from the overlap integral,

$$\sigma_{ov} = \frac{V_v}{V_0} \frac{64\pi^5 \mu^2}{\hbar^4} \left| \int dR \chi_v^* \xi \xi' \right|^2, \quad (4)$$

where  $V_v$  is the velocity of the scattered electron,  $\mu$  is the electron mass,  $\chi_v$  is the excited vibrational state wavefunction, and  $\xi$  is an exit amplitude for the electron which is set equal to  $\xi'$ .<sup>7</sup>

The boundary conditions applied to Eq. (1) are

$$\xi(0, E) = 0$$

$$\lim_{R \rightarrow \infty} \left[ \frac{d\xi}{dR} - iK\xi \right] = 0 \quad (5)$$

where

$$K^2 = \frac{2M}{\hbar^2} \lim_{R \rightarrow \infty} (E - E^-(R)).$$

The two-point boundary value problem (1) and (5) was solved by a conventional centered difference method, with numerical accuracy monitored by evaluating both sides of the equation

$$\frac{\hbar^2 K}{M} \lim_{R \rightarrow \infty} |\xi|^2 + \int \Gamma(R) |\xi|^2 dR = -2 \text{Im} \int \xi^* \xi' \chi_0 dR \quad (6)$$

which results from multiplying (1) by  $\xi^*$ , subtracting the complex conjugate, and integrating.

### III. CALCULATED RESULTS

The  $F_2$  ground state potential energy curve was represented by a Morse potential with parameters taken from

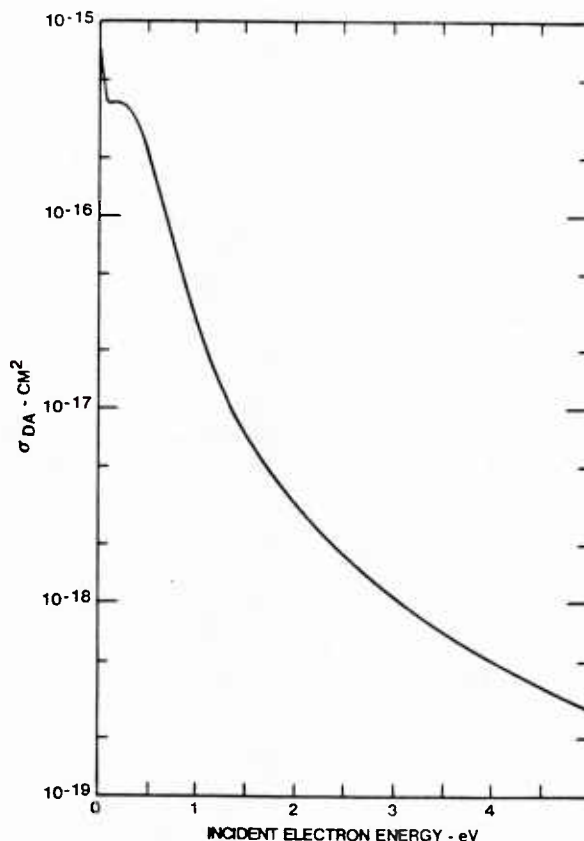


FIG. 2. Best fit attachment cross section as a function of incident electron energy.

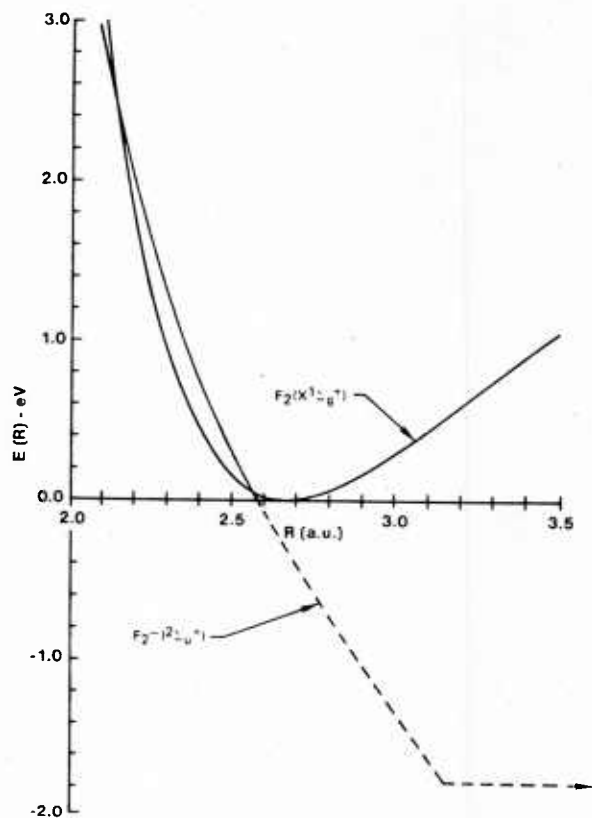


FIG. 3. Real part of best fit compound state potential; ground state represented by Morse potential.

Ref. 15. Morse vibrational wavefunctions were also employed. The real part of the compound state energy was represented by a Taylor series for energies greater than an asymptotic limit deduced from the  $F_2$  electron affinity and ground state well depth.<sup>15</sup>

#### A. Dissociative attachment

The predicted attachment cross sections were found to be quite sensitive to the internuclear distance,  $R_s$ , at which the compound state potential crosses that of the ground state (equilibrium separation  $R_0$ ). For  $R_s \geq R_0$  it was found that the predicted attachment rates, when compared with the data of Refs. 3 and 4, were either too large or had peaks too far displaced from zero electron energy. The best fit, obtained for  $R_s < R_0$ , is shown in Fig. 1. A non-Maxwellian rate constant calculation has been made because electron distribution function effects are important in one of the experiments. The data of Chen and co-workers<sup>3</sup> were obtained in  $N_2$  buffer gas with  $F_2$  mole fractions on the order of  $10^{-3}$ ; departures from Maxwellian due to excitation of the  $N_2$  vibrational mode become important at electron energies around 1 eV. The results of making a non-Maxwellian electron energy distribution attachment rate calculation is shown as the dashed line in Fig. 1.<sup>16</sup> It is apparent that better agreement with the higher energy experimental data is obtained using this distribution function. The fit exhibited in Fig. 1 is judged to be as good as is warranted by the scatter in the available experimental rate data.

The predicted attachment cross section (Fig. 2) has

a value of  $0.7 \times 10^{-15} \text{ cm}^2$  at an incident energy of 0.01 eV and falls rapidly with increasing energy. A bump at 0.2 eV appears to be a consequence of the approach to zero of the incident electron velocity and the entry amplitude,  $\xi'$ .

The real and imaginary parts of the negative ion potential which give this fit are shown in Figs. 3 and 4, respectively. As shown in Fig. 3, the best fit negative ion and ground state curves cross about 0.1 a.u. from  $R_0$ . This result is consistent with the *ab initio* calculation of Ref. 11 in which a crossing at about 2.6 a.u. is predicted. The inferred  $\Gamma(R)$  in Fig. 4 also is quite reasonable for a low energy shape resonance. Averaging  $\Gamma$  with the nuclear wavefunction over the range  $0 < R \leq R_s$  yield values in the range 0.3–0.4 eV. The fact that this width is larger than that for the low energy resonance in  $O_2$  is expected, because this is a *p*-wave resonance, while that in  $O_2$  is *d*-wave.<sup>17</sup> Because of the scatter in the attachment data, these potential parameters must be tentative. More extensive measurements, particularly at the higher electron energies, are needed.

If the compound state potential given in Figs. 3 and 4 is correct, the dissociative attachment cross section is likely to have a strong dependence on the vibrational quantum state of the target  $F_2$  molecule. Replacing the  $v=0$  wavefunction on the right hand side of Eq. (1) with an excited state target wavefunction and modifying the collision energy make it possible to calculate the  $v$ -dependence of the attachment rate. The results of such calculations are presented in Fig. 5, which shows the rates for  $v=0, 1$ , and 2. The predicted  $v$  dependence is very strong, with the peak attachment rate increasing by

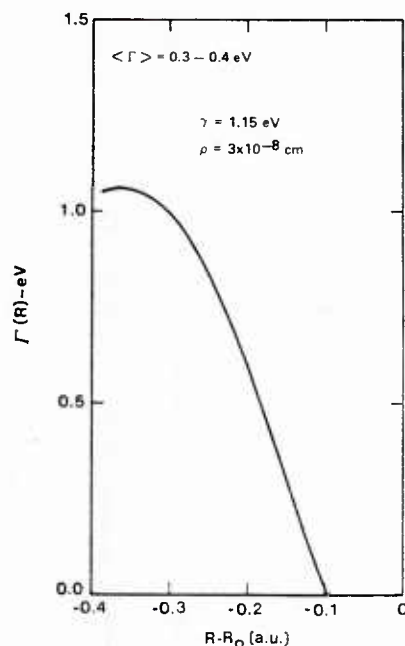


FIG. 4. Imaginary part of best fit compound state potential (the autoionization rate multiplied by  $\hbar$ ).  $\Gamma$  varies with  $R$  in accordance with penetrability of *p*-wave barrier. Averaging  $\Gamma$  over the resonance wavefunction yields values of 0.3–0.4 eV.

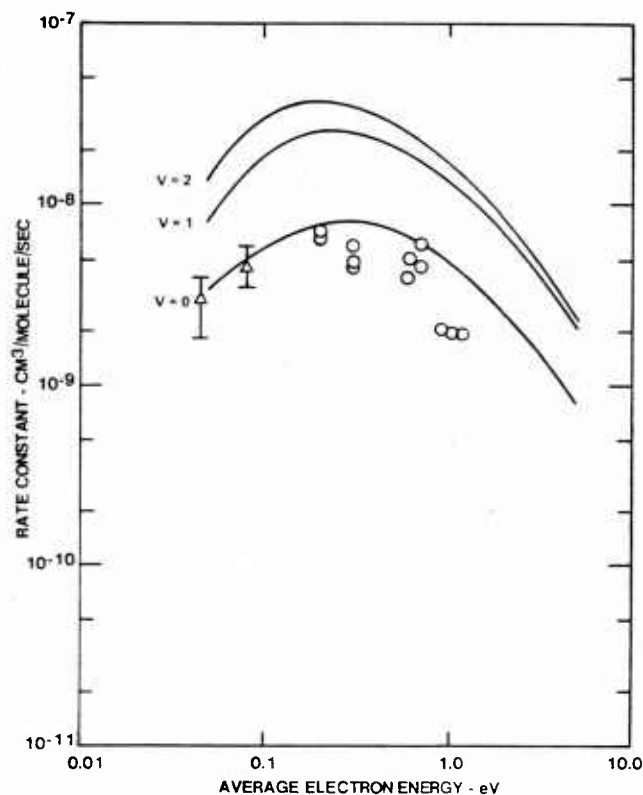


FIG. 5. Predicted dependence of attachment rate on vibrational quantum number of target  $F_2$ . Rate constant calculated for Maxwellian electron energy distribution.

about a factor of 5 from  $v=0$  to  $v=2$ . This prediction is quite sensitive to the value of  $R_s$ ; as  $R_s$  approaches  $R_0$ , the vibrational enhancement is reduced. For  $R_s \approx R_0$ , survival factor is a more important consideration than capture, and the predicted rates decrease with increasing  $v$ . However, at this point a good fit to the  $v=0$  data could not be obtained.

### B. Vibrational excitation

Vibrational excitation cross sections have been evaluated for the best fit attachment case for the process  $e^- + F_2(0) \rightarrow e^- + F_2(v)$ . Figure 6 shows the calculated cross sections for  $v=1, 4, 8$ , and  $12$ , and the sum of the cross sections for excitation up to  $v=15$ . The first vibrational state has a peak cross section value of about  $10^{-16} \text{ cm}^2$ ; at  $v=15$  the maximum has fallen to about 0.001 that of  $v=1$ . Significant excitation of high lying levels is predicted because this is a "strong coupling" case<sup>14</sup>; the ratio of momentum imparted to the nuclei to the initial r.m.s. momentum,  $2a(dE/dR)/\langle \Gamma \rangle$ , is approximately unity. Here  $a$  is the vibrational amplitude of the ground state. The lack of structure in these cross sections is due to the absence of reflected components in the nuclear wavefunction.

Because of the scatter in the experimental attachment data, the sensitivity of the vibrational cross sections to reasonable variations in predicted attachment rates has been examined. Repeating the base case calculation with  $\gamma=2.3$  and  $0.58 \text{ eV}$  ( $\langle \Gamma \rangle \approx 0.7$  and  $0.17 \text{ eV}$ , respectively) gives rise to a variation in predicted attachment rate

that reflects the scatter in the experimental data presented in Fig. 1. The sensitivity of the predicted vibrational excitation cross sections is substantially greater; the cross-section peak at low incident energy is approximately proportional to  $\Gamma$ , with a  $\Gamma^2$  dependence at high energy. For an attachment cross section as large as that reported in Ref. 5, it is estimated that the predicted peak vibrational cross section would be  $O(10^{-14} \text{ cm}^2)$ .

The resonant cross sections shown in Fig. 6 are much larger than those calculated on the basis of direct scattering. Depending on the value assumed for the unknown quadrupole moment derivative, a Born approximation/quadrupole calculation gives a peak cross section of  $10^{-20} - 10^{-19} \text{ cm}^2$  for the 0-1 transition. Raman scattering data<sup>18</sup> yields a value of 0.21 a.u. for the matrix element of the derived polarizability tensor. Using this value in a polarization potential calculation<sup>19</sup> gives a peak cross section of  $10^{-18} - 10^{-17} \text{ cm}^2$ , depending on the cutoff parameter.

### C. Non-local $\Gamma$ correction

The predictions might be improved at thermal energies by employing a nonlocal  $\Gamma$  formulation.<sup>20</sup> In reality, the term  $\Gamma(R)\xi(R)$  in Eq. (1) should be a sum of terms representing negative ion decay to different vibrational states. This effect is accounted for approximately<sup>20,21</sup> by replacing the term  $\Gamma(R)\xi(R)$  in (1) by:

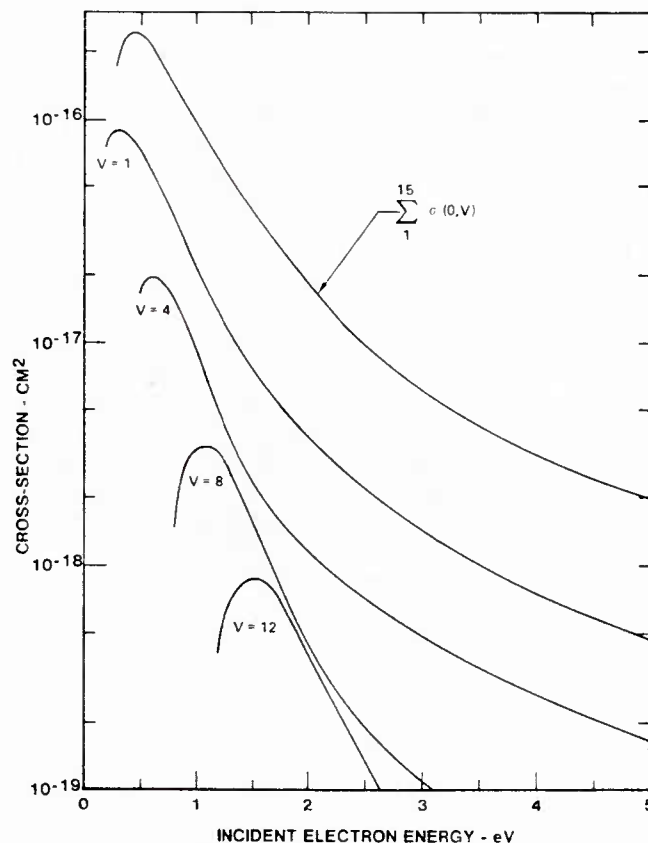


FIG. 6. Predicted vibrational excitation cross sections for target  $F_2$  in  $v=0$  state. Shown are the individual cross sections for excitation of  $v=1, 4, 8$  and  $12$ , and the total vibrational cross section.

$$\sum_v \chi_v(R) \Gamma(E - E_v) \int dR' \chi_v(R') \xi(R', E), \quad (7)$$

where the  $v$  summation extends over open channels and

$$\Gamma(E - E_v) = 2\gamma \frac{(k_v \rho)^3}{1 + (k_v \rho)^2}$$

$$k_v^2 = \frac{2\mu}{\hbar^2} (E - E_v).$$

In the high energy limit the expression (7) returns to  $\Gamma(R) \xi(R)$ . The governing nuclear wave equation (1) thus becomes an integro-differential equation. This equation has been solved iteratively, starting with the  $\xi$  wave from the local  $\Gamma$  calculation, for incident energies up to 0.3 eV. The resulting attachment cross section differs little (10%–15%) from that calculated previously. Presumably this is due to the fact that for very low incident energies the decay term is not very important in either case. Thus, the local  $\Gamma$  approximation appears to be adequate for low energy electron- $F_2$  interactions.

#### IV. CONCLUSIONS

Resonance scattering theory has been applied to electron- $F_2$  interactions to calculate self-consistent dissociative attachment and vibrational excitation cross sections. The observed attachment rate data can be explained in terms of a low energy, shape resonance. For a compound state potential that is consistent with *ab initio* calculations, the theory gives a reasonable fit to attachment rate constant data over the range of average electron energies 0.05–1.0 eV. The associated vibrational excitation cross sections for low lying  $F_2$  states have peaks of approximately  $10^{-16} \text{ cm}^2$  at electron energies of a few tenths eV. A nonlocal  $\Gamma$  analysis for low incident energies has been found to give results not appreciably different from the local  $\Gamma$  calculation.

The cross section predictions are particularly sensitive to the value selected for  $R_s$ . As  $R_s \rightarrow R_0$ , the predicted enhancement of attachment rate by target vibration decreases and changes to a negative dependence at  $R_s = R_0$ . However, the fit to the data of Refs. 3 and 4 that is obtained by decreasing the resonance width becomes unsatisfactory as  $R_s \rightarrow R_0$ . As negative ion potential parameters are varied over wide ranges, peak attachment rates of slightly less than  $10^{-8} \text{ cm}^3/\text{sec}$  are found to correlate with peak vibrational cross sections of about  $10^{-16} \text{ cm}^2$ . Variations in the resonance width which reproduce the scatter in the present attachment

data suggest that the uncertainty in the predicted vibrational cross section is about a factor of 2 at the peak, and a factor of 4 at higher electron energy.

*Note added in proof:* Measurements of electron attachment in  $F_2$ -He mixtures in the average energy range 3–7 eV have recently been made by Nygaard *et al.*<sup>22</sup> When the attachment cross section of Fig. 2 is integrated over an electron distribution function for He, good agreement is obtained with this new data.<sup>23</sup>

#### ACKNOWLEDGMENT

The author is greatly indebted to Professor Arvid Herzenberg for several helpful suggestions.

- <sup>1</sup>S. K. Searles and G. A. Hart, *Appl. Phys. Lett.* **27**, 243 (1975); C. A. Brau and J. J. Ewing, *ibid.* **27**, 243 (1975); J. A. Mangano, J. H. Jacob and J. B. Dodge, *ibid.* **29**, 426 (1976).
- <sup>2</sup>R. Hofland, M. L. Lindquist, A. Ching, and J. S. Whittier, *J. Appl. Phys.* **45**, 2207 (1974); R. L. Kerber, A. Ching, M. L. Lindquist, and J. S. Whittier, *IEEE J. Quantum Electron.*, QE-9, 607 (1973).
- <sup>3</sup>H. L. Chen, R. E. Center, D. W. Trainor, and W. I. Fyfe, *Appl. Phys. Lett.* **30**, 99 (1977).
- <sup>4</sup>G. D. Sides, T. O. Tiernan, and R. J. Hanrahan, *J. Chem. Phys.* **65**, 1966 (1976).
- <sup>5</sup>P. Mahadevan and R. Hofland, *Bull. Am. Phys. Soc.* **21**, 575 (1976).
- <sup>6</sup>J. J. DeCorpo *et al.*, *J. Chem. Phys.* **53**, 936 (1970).
- <sup>7</sup>D. T. Birtwistle and A. Herzenberg, *J. Phys. B* **4**, 53 (1971).
- <sup>8</sup>L. Dube and A. Herzenberg, *Phys. Rev. A* **11**, 1314 (1975).
- <sup>9</sup>M. Zubek and C. Szymkowski, *J. Phys. B* **10**, L27 (1977).
- <sup>10</sup>B. I. Schneider, *Phys. Rev. A* **14**, 1923 (1976).
- <sup>11</sup>L. N. Rescigno and C. F. Bender, *J. Phys. B* **9**, 1329 (1976).
- <sup>12</sup>M. V. Kurepa and D. S. Belic, *Chem. Phys. Lett.* **49**, 608 (1977).
- <sup>13</sup>J. M. Blatt and V. F. Weiskopf, *Theoretical Nuclear Physics* (Wiley, New York, 1966), p. 361.
- <sup>14</sup>J. N. Bardsley, A. Herzenberg, and F. Mandel, *Proc. Phys. Soc.* **89**, 321 (1966).
- <sup>15</sup>E. A. Colbourn *et al.*, *Can. J. Phys.* **54**, 1343 (1976).
- <sup>16</sup>W. L. Nighan, private communication, June 1977.
- <sup>17</sup>D. Spence and G. J. Schulz, *Phys. Rev. A* **2**, 1802 (1970).
- <sup>18</sup>J. M. Hoell *et al.*, *J. Chem. Phys.* **58**, 2896 (1973).
- <sup>19</sup>E. L. Breig and C. C. Lin, *J. Chem. Phys.* **43**, 3839 (1965).
- <sup>20</sup>J. N. Bardsley, *J. Phys. B* **1**, (1968).
- <sup>21</sup>A. Herzenberg, private communication, May 1977.
- <sup>22</sup>K. J. Nygaard *et al.*, "Electron Attachment in Fluorine-Rare Gas Mixtures," 30th Gaseous Electronics Conference, Palo Alto, CA, October 19, 1977.
- <sup>23</sup>W. L. Nighan, private communication, October 1977.

APRIL 1984

REPORTS DISTRIBUTION LIST FOR ONR PHYSICS DIVISION OFFICE  
UNCLASSIFIED CONTRACTS

Director Defense Advanced Research Projects Agency Attn: Technical Library 1400 Wilson Blvd. Arlington, Virginia 22209	1 copy
Office of Naval Research Physics Division Office (Code 412) 800 North Quincy Street Arlington, Virginia 22217	2 copies
Office of Naval Research Director, Technology (Code 200) 800 North Quincy Street Arlington, Virginia 22217	1 copy
Naval Research Laboratory Department of the Navy Attn: Technical Library Washington, DC 20375	1 copy
Office of the Director of Defense Research and Engineering Information Office Library Branch The Pentagon Washington, DC 20301	1 copy
U.S. Army Research Office Box 1211 Research Triangle Park North Carolina 27709	2 copies
Defense Technical Information Center Cameron Station Alexandria, Virginia 22314	12 copies
Director, National Bureau of Standards Attn: Technical Library Washington, DC 20234	1 copy
Director U.S. Army Engineering Research and Development Laboratories Attn: Technical Documents Center Fort Belvoir, Virginia 22060	1 copy
ODDR&E Advisory Group on Electron Devices 201 Varick Street New York, New York 10014	1 copy

Air Force Office of Scientific Research Department of the Air Force Bolling AFB, DC 22209	1 copy
Air Force Weapons Laboratory Technical Library Kirtland Air Force Base Albuquerque, New Mexico 87117	1 copy
Air Force Avionics Laboratory Air Force Systems Command Technical Library Wright-Patterson Air Force Base Dayton, Ohio 45433	1 copy
Lawrence Livermore Laboratory Attn: Dr. W. F. Krupke University of California P.O. Box 808 Livermore, California 94550	1 copy
Harry Diamond Laboratories Technical Library 2800 Powder Mill Road Adelphi, Maryland 20783	1 copy
Naval Air Development Center Attn: Technical Library Johnsville Warminster, Pennsylvania 18974	1 copy
Naval Weapons Center Technical Library (Code 753) China Lake, California 93555	1 copy
Naval Underwater Systems Center Technical Center New London, Connecticut 06320	1 copy
Commandant of the Marine Corps Scientific Advisor (Code RD-1) Washington, DC 20380	1 copy
Naval Ordnance Station Technical Library Indian Head, Maryland 20640	1 copy
Naval Postgraduate School Technical Library (Code 0212) Monterey, California 93940	1 copy
Naval Missile Center Technical Library (Code 5632.2) Point Mugu, California 93010	1 copy

Naval Ordnance Station Technical Library Louisville, Kentucky 40214	1 copy
Commanding Officer Naval Ocean Research & Development Activity Technical Library NSTL Station, Mississippi 39529	1 copy
Naval Explosive Ordnance Disposal Facility Technical Library Indian Head, Maryland 20640	1 copy
Naval Ocean Systems Center Technical Library San Diego, California 92152	1 copy
Naval Surface Weapons Center Technical Library Silver Spring, Maryland 20910	1 copy
Naval Ship Research and Development Center Central Library (Code L42 and L43) Bethesda, Maryland 20084	1 copy
Naval Avionics Facility Technical Library Indianapolis, Indiana 46218	1 copy

U218856